Measurement of the top pair production cross section and the W boson polarization in top dilepton decay in $p\bar{p}$ collisions at $\sqrt{s} = 1.96$ TeV

Chang-Seong Moon

Under the supervision of

Professor Soo-Bong Kim

A Dissertation submitted to

the Graduate Faculty of Seoul National University

in partial fulfillment of the requirement

for the Degree of Doctor of Philosiphy

School of Physics and Astronomy

The Graduate School of Natural Sciences

Seoul National University

Seoul, KOREA

February, 2011

This dissertation is dedicated to my parents.

Abstract

This dissertation presents the results of a measurement of the top pair production cross section and the W boson polarization in top dilepton decay using an 5 fb^{-1} of data obtained at the Collider Detector at Fermilab (CDF) in $p\bar{p}$ collisions at a center-of-mass energy of $\sqrt{s} = 1.96$ TeV. We use $t\bar{t}$ dilepton events reconstructed with 2 high momentum leptons, 2 or more jets from 2 b quarks and initial-final state radiation, and missing transverse energy from the undetected neutrinos.

Assuming $m_t = 172.5$ GeV/c^2, the measured cross section for 343 signal candidate events before the secondary vertex $b-$tagging included with an estimated background of 105.80 ± 17.24 is:

$$\sigma_{t\bar{t}} = 7.40 \pm 0.58(\text{stat}) \pm 0.63(\text{syst}) \pm 0.45(\text{lumi}) \text{ pb.}$$

and the measured cross section for 137 signal candidate events after the secondary vertex $b-$tagging included with an estimated background of 9.75 ± 1.68 is found to be:

$$\sigma_{t\bar{t}} = 7.25 \pm 0.66(\text{stat}) \pm 0.47(\text{syst}) \pm 0.44(\text{lumi}) \text{ pb.}$$

which are consistent with a NNLO prediction of 7.4 ± 0.8 pb.

Meanwhile, in the Standard Model the top quark decays into a W^+ and b quark with a branching fraction above 99%. The V-A structure of the weak interaction of the SM predicts that the W^+ bosons from the top quark decay $t \to W^+b$ are dominantly either longitudinally polarized ($\sim$70%) or left-handed ($\sim$30%), while right-handed W bosons are heavily suppressed and are forbidden in the limit of massless b quarks. Precise measurement of the W boson polarization could reveal new physics beyond the Standard Model. the W boson polarization is reflected in angular (θ^*) distribution between momentum of the charged lepton in the W rest frame and the momentum of the W boson in the top quark rest frame.

We perform 1D measurement of longitudinal (f_0) and right-handed (f_+) fraction as well as model independent 2D measurement. 1D measurements of f_0 constraining f_+ to its Standard Model expected value of 0 give

$$\begin{aligned} \text{Before } b\text{−tagging} \quad &: \quad f_0^{1D} = 0.60 \pm 0.09(\text{stat}) \pm 0.06(\text{syst}) \\ \text{After } b\text{−tagging} \quad &: \quad f_0^{1D} = 0.62 \pm 0.11(\text{stat}) \pm 0.06(\text{syst}) \end{aligned}$$

1D measurements of f_+ constraining f_0 to its Standard Model expected value of 0.7 give

$$\begin{aligned} \text{Before } b\text{−tagging} \quad &: \quad f_+^{1D} = -0.06 \pm 0.04(\text{stat}) \pm 0.03(\text{syst}) \\ \text{After } b\text{−tagging} \quad &: \quad f_+^{1D} = -0.07 \,^{+\,0.06}_{-\,0.05}(\text{stat}) \pm 0.03(\text{syst}) \end{aligned}$$

2D model independents simultaneous measurements of f_0 and f_+ give

$$\begin{aligned} \text{Before } b\text{−tagging} \quad : \quad & f_0^{2D} = 0.73 \,^{+\,0.18}_{-\,0.17}(\text{stat}) \pm 0.06(\text{syst}) \\ & f_+^{2D} = -0.08 \pm 0.09(\text{stat}) \pm 0.03(\text{syst}) \end{aligned}$$

$$\text{After } b-\text{tagging} \quad : \quad \begin{aligned} f_0^{2D} &= 0.78 \,^{+\ 0.19}_{-\ 0.20}(\text{stat}) \pm 0.06(\text{syst}) \\ f_+^{2D} &= -0.12 \,^{+\ 0.11}_{-\ 0.10}(\text{stat}) \pm 0.04(\text{syst}) \end{aligned}$$

All the results are consistent with Standard Model expectations. These results are first measurements of the W boson polarization using cos θ^* distribution in dilepton channel at CDF.

Keywords : **Top quark, W boson polarization, Dilepton, Production cross section, Cos θ*, CDF experiment**
Student Number : **2006-30767**

Contents

List of Figures

List of Tables

Chapter 1

Introduction

This dissertation describes a measurement of the $t\bar{t}$ production cross section and W boson polarization in the top dilepton decay using 5.1 fb^{-1} of Run II data collected at CDF from March 2002 until June 2009. The top quark has been discovered in 1995 at the Tevatron Collider at Fermilab. Since its discovery, the top quark has been the subject of intensive studies by the CDF and D0 experiments in Fermilab because physicists have been mystified by its extremely heavy mass. This has led many scientists to believe that the top quark may shed light on the path to new physics.

The dilepton decay mode occurs when the W bosons created in top quark disintegrations further decay into a charged lepton (electron or muon) and a neutrino. This dilepton final state is rare - only 5 percent of top pairs decay this way - but it is the easiest to identify because not very many other processes can produce such a striking final state even before requiring the identification of one of the jets originating from a b quark. [1] Moreover by requiring at least one b-tagging, the constraint produces an extremely pure signal with a signal to background ratio of 13:1.

In this chapter, theoretical motivations for a measurement of the $t\bar{t}$ production cross section and W boson polarization in the top dilepton decay are briefly described.

1.1 Theoretical Motivation

The top quark, discovered at the Tevatron in Fermilab, completes the third fermion generation in the Standard Model (SM). Accurate measurements of the top pair production cross section ($\sigma_{t\bar{t}}$) play an important role as a test of the quantum chromodynamics (QCD) calculation and can provide probes towards new physics signals involving non-SM $t\bar{t}$ production mechanisms or decays. Since the CKM element V_{tb} is close to unity and m_t is large, the SM top quark decays almost exclusively to a W boson and a b quark, so that the top pair production experimental signatures can be classified with respect to the decay modes of the W boson.

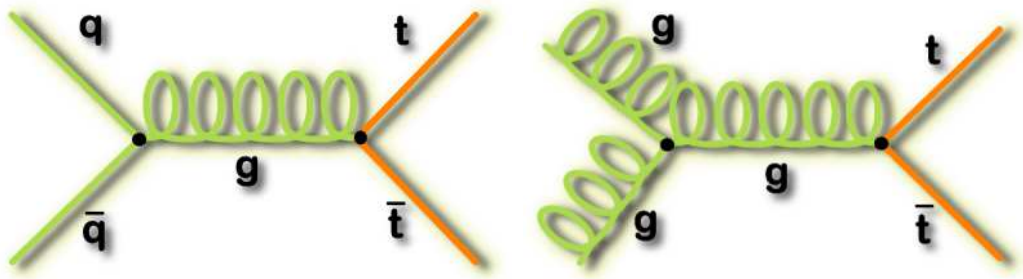

(a) (b)

Figure 1.1: The two $t\bar{t}$ production Feynman diagrams at the Tevatron. (a) is parton-parton annihilation which occurs $\simeq 85\%$, (b) shows the gluon-gluon fusion process which occurs $\simeq 15\%$.

At the Tevatron $p\bar{p}$ collider, at center-of-energy of 1.96 TeV, top quarks are mainly produced in pairs through quark-antiquark annihilation (85%) or gluon-gluon fusion (15%), with a SM predicted cross section at next-to-leading order (NLO) of $\sigma_{t\bar{t}} = 7.4^{+0.7}_{-0.6}$ pb for a reference top quark pole mass of 172.5 GeV/c^2 [2]. Figure 1.2 shows the NLO QCD prediction for the $t\bar{t}$ total cross section at the Tevatron for $\sqrt{s} = 1.96$ TeV.

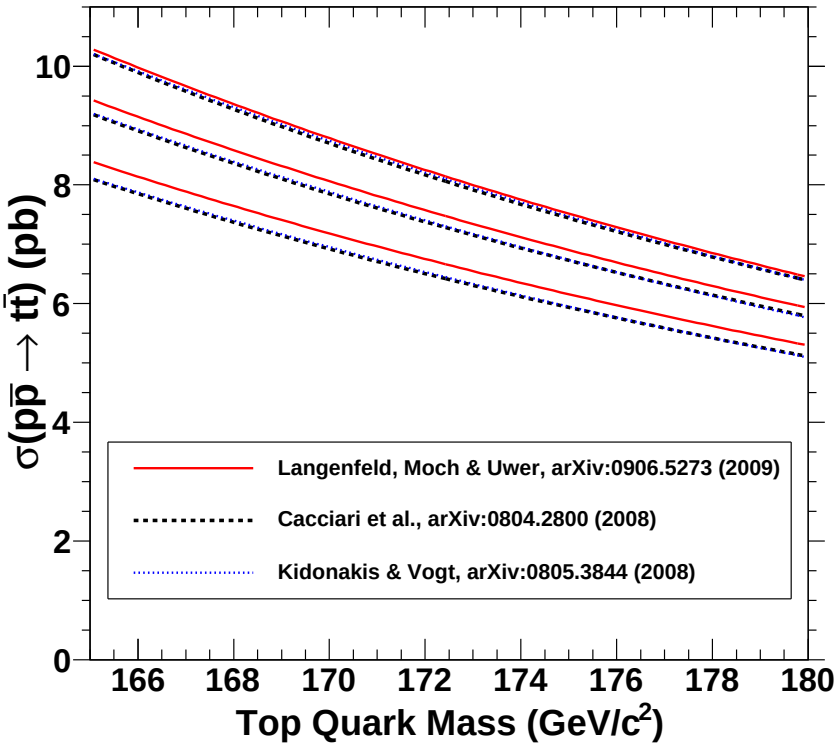

Figure 1.2: NLO calculation of the $t\bar{t}$ cross section dependence as a function of the top mass

In the SM, the Wtb vertex in Eq. (1.1) reduces to $V_L = V_{tb} \simeq 1$ and $V_R = g_L = g_R = 0$ at the tree level. Figure 1.3 shows the top quark decays

to W^+ boson and b quark. Deviations from these values (see for example Refs. [3]-[8]) can be tested by measuring various observables. In particular, the presence of non-zero anomalous couplings V_R, g_L, g_R is probed with good precision by determining the helicity of the W boson in the top quark decay, *i.e.* the relative fractions F_+, F_0, F_- of W bosons produced with helicity +1, 0, -1 [9], and through angular distributions in the top quark rest frame [10] [11] [12].

$$\begin{aligned} \mathcal{L}_{Wtb} &= -\frac{g}{\sqrt{2}}\bar{b}\gamma^{\mu}(V_L P_L + V_R P_R)tW_{\mu}^{-} \\ &\quad -\frac{g}{\sqrt{2}}\bar{b}\frac{i\sigma^{\mu\nu}q_{\nu}}{M_W}(g_L P_L + g_R P_R)tW_{\mu}^{-} + h.c. \end{aligned} \tag{1.1}$$

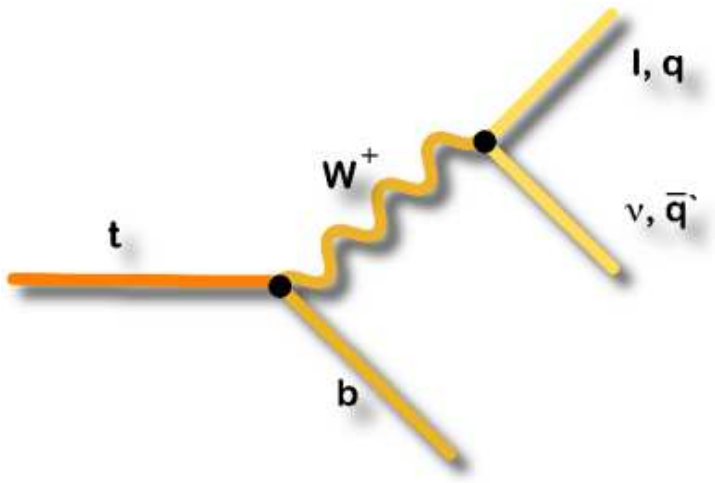

Figure 1.3: Top quark decays to W^+ boson and b quark

A model-independent determination of the Wtb vertex will be important event if it does not lead to new physics discoveries. Even if new physics does

not contribute sizebly to the Wtb vertex and the top quark decays as predicted by the SM, it is crucial to establish this fact in a model-independent way, in order to clearly identify possible new physics in the top quark production, if present [12].

1.1.1 The Standard Model

The Standard Model of particle physics is a theory which describes three of the four known fundamental interactions between the elementary particles that make up all matter. There are three fundamental interactions (the electromagnetic, weak, and strong) and two types of particles that occur in nature, fermions (with half-integer spins) and bosons (with integer spins) Eash fore has at least one force carrier boson. The electromagnetic force is mediated by the $photon(\gamma)$. The strong force is mediated by a set of eight bosons collectively referred to as $gluon(g)$. The weak interaction is mediated by three bosons, W^+, W^-, and Z^0. The electromagnetic and weak interactions are actually the same force at high energies, and has implications for the dynamics associated with them.

The fermions are divided into two categories, quarks and leptons. Quarks are paricipate in the strong interaction. All the fermions participate in the weak interactions, and all the charged particles interact in the electromagnetic interaction. Each fermion is coupled with a partner fermion via the weak interaction. Quarks are coupled with other quarks, and leptons are coupled with other leptons Each pair is called "generation" of particles.

The first generation of particles is composed of the up and down quarks,

		Generation		
		First	Second	Third
Quark	Q = $+\frac{2}{3}$	up (u) $m_u \sim 1.5$ - 4.5 MeV/c^2	charm (c) $m_c = 1.3$ GeV/c^2	top (t) $m_t = 170$ - 180 GeV/c^2
	Q = $-\frac{1}{3}$	down (d) $m_d \sim 5.0$ - 8.5 MeV/c^2	strange (s) $m_s \sim 80$ - 155 MeV/c^2	bottom (b) $m_b = 4.2$ GeV/c^2
Lepton	Q = -1	electron (e) $m_e = 0.511$ MeV/c^2	muon (μ) $m_\mu = 106$ MeV/c^2	tau (τ) $m_u = 1.78$ GeV/c^2
	Q = 0	e neutrino (ν_e) $0 < m_{\nu_e} < 3$ eV/c^2	μ neutrino (ν_μ) $0 < m_{\nu_\mu} < 0.2$ MeV/c^2	τ neutrino (ν_τ) $0 < m_{\nu_\tau} < 18.2$ MeV/c^2

Table I: Fermion family structure.

and the electron and electron-type neutrino. These four particles construct almost all of everyday matter. The up and down quarks combine to make protons and neutrons, which combine to make nuclei. Atoms are made of nuclei combined with electrons, and the neutrino partakes in nuclear decay.

There are two remaining generations, composed of the charm and strange quarks, the top and bottom quarks, the muon and muon-type neutrino, and the tau lepton and the tau-type neutrino. These generations are very discrepancy between the different masses of the fermions seen in nature. The last massive particles, the neutrinos have masses very close to zero but is not zero, while the top quark si as massive as an entire gold atom ($170 \sim 180$ GeV/c^2). Both the leptons and quarks come in six flavors and can be gruoped in three generations as shown in Table 1.1

It is a quantum field theory developed between 1970 and 1973 which is consistent with both quantum mechanics and special relativity. To date, almost all experimental tests of the three forces described by the Standard

Model have agreed with its predictions.

However, the Standard Model falls short of being a complete theory of fundamental interactions, primarily because of its lack of inclusion of gravity, the fourth known fundamental interaction, but also because of the large number of numerical parameters (such as masses and coupling constants) that must be put "by hand" into the theory (rather than being derived from first principles).

The top quark is a fundamental particle in the Standard Model and so characterizing its properities is an important part of studying nature at the most fundamental level. As one of the most recently discovered elementary particles, many of its properties are poorly measured and none are measured as well as would like. In the Standard Model the mass, in the form of the coupling constant of the top quark to the Higgs boson, is a fundamental parameter and so interesting in its own right Further, the enormous mass of the top quark, the most massive elementary particle so far observed and far more massive than the other quarks, hints that the top may have some special role among the elementary particles.

1.1.2 New physics Beyond the Standard Model

There is ample reason to suspect that the Standard Model is not the final theory of nature of the fundamental scale. Since any physics beyond the Standard Model should have high energy manifestations a natural place to look is in the most energetic events available, including $t\bar{t}$ events. Any other model of physics will also have to satisfy the constrains and self-consistency

check of precision physics, and precision electroweak studies will continue to be a powerful tool for future models.

Probably the most popular set of models for physics beyond the Standard Model is supersymmetry. The simplest case is the minimally supersymmetric version of the Standard Model(MSSM). This extension adds a fermionic (particle with half-integer spin) "superpartner" for every boson (particle with integer spin) in the Standard Model and a bosonic superpartner for every fermion. Two Higgs doublets are needed instead of the one doublet of the Standard Model, and a total of five physical Higgs bosons (three neutral and two charged). The MSSM stabilizes the mass of the Higgs boson (eliminating the so-called "gauge hierarchy problem"), aids in the unification of the electroweak and strong interaction, has a dark matter candidate, and is a prerequisite of any string theory.

The implications of precision electroweak physics for the MSSM have been studied in some detail. "Electroweak precision observables in the minimal supersymmetric stanard model" In Figure 1.4 Standard Model and MSSM predictions of M_W as a function of m_t are compared to current and anticipated measurements, which are shown in Table II. For the Standard Model prediction the Higgs mass is the only free parameter while for the MSSM the masses of all superpartners are varied in a coordinated manner. The two models show a small overlap - for light Higgs masses in the Standard Model, and for heavy superpartners in the MSSM. The heavy superpartner regime in the MSSM is the so-called decoupling limit where the supersymmetric content has little impact on low energy physics. Current measurements show a mild preference for the MSSM. The anticipated future measurements give a sense for the discriminating power of precision electroweak measurements at, for

example, an International Linear Collider.

	now	Tevatron	LHC	ILC	ILC with GigaZ
ΔM_W [MeV/c]	34	20	15	10	7
Δm_t [GeV/c^2]	2.9	2.5	1.5	0.2	0.1

Table II: Current and anticipated experimental uncertainties for M_W and m_t. Each column represents the combined results of all detectors and channels at a given collider, taking into account correlated systematic uncertainties. Table adapted from(csmoon)

Another interesting class of theories, those with dynamical electroweak symmetry breaking, do not have fundamental scalar Higgs bosons at all. One possibility is technicolor where the electroweak symmetry is broken by condensates of a new kind of fermions, "technifermions". This symmetry breaking is then communicated to the usual quarks and leptons via a mechanism called extended technicolor which generates the quark and lepton masses. Technicolor theories contain an extended strong interaction which can reduce to two strong interactions at intermediate scales. One can couple to the third generation (t and b quarks) and the other to the other quarks, with the two interactions reducing to the usual strong interaction at low energies. So, it is possible to give the t and b unusually large masses. In other versions of such theories, known as topcolor-assisted technicolor theories(topcolor, csmoon), the top plays an even more unique role. In addition to the technifermion condensates the top quark condenses as well. Technicolor causes most of the electroweak symmetry breaking while the top condensate provides most of the top quark masses and the top-bottom mass splitting. This allows large top and bottom quark masses

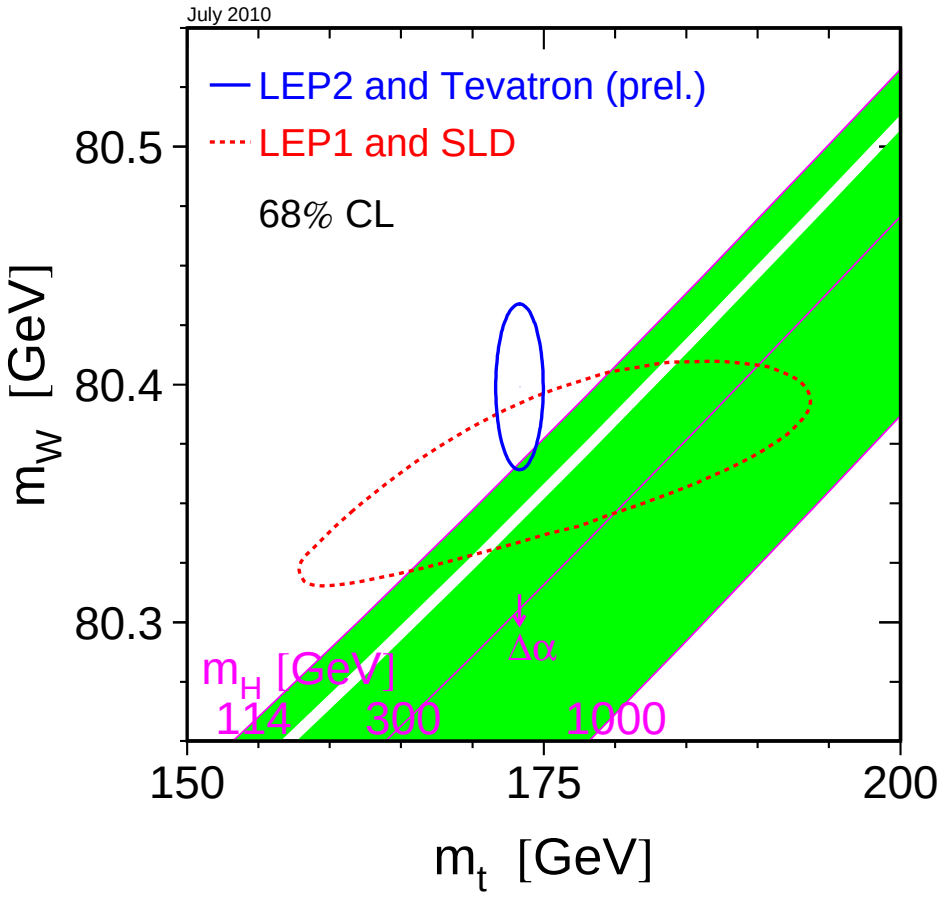

Figure 1.4: The comparison of the indirect constraints on m_W and M_t based on LEP-I/SLD data (dashed contour) and the direct measurements from the LEP-II/Tevatron experiments (solid contour). In both cases the 68% CL contours are plotted. Also shown is the SM relationship for the masses as a function of the Higgs mass in the region favoured by theory (<1000 GeV) and allowed by direct searches (114 GeV to 158 GeV and >175 GeV). The arrow labelled $\Delta\alpha$ shows the variation of this relation if $\alpha(m_Z^2)$ is changed by plus/minus one standard deviation. This variation gives an additional uncertainty to the SM band shown in the figure.

as well as a large top-bottom mass splitting, all while preventing contributions via radiative processes from being unacceptable large. In general any new particles a theory introduces will contribute to processes measurable at low energy via loop diagrams like those of Figures 1.5 and XXX and so precision electroweak measurement place tight limits on new theories. One can search for such theories by looking for resonances in the $b\bar{b}$ and $t\bar{t}$ mass spectra that do not exist for lighter quarks. Such searches have been performed at the Tevatron and will continue there and at the Large Hadron Collider.

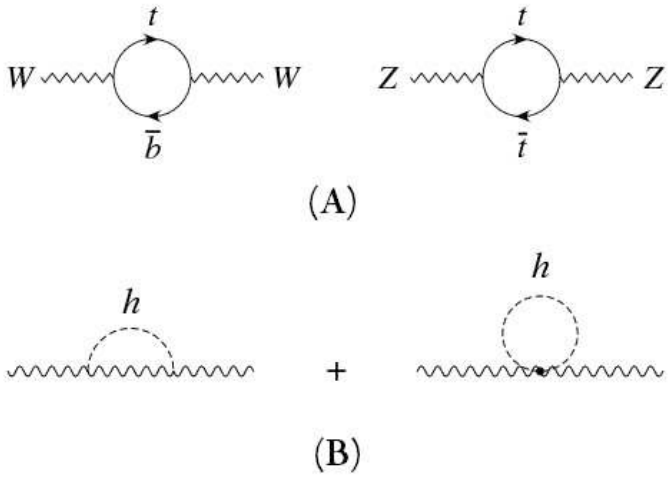

Figure 1.5: (A) One-loop contributions from the top quark to the W and Z masses. (B) One-loop contributions from the Higgs to the W and Z masses.

As one of the highest energy processes currently available for study, top quarks and $t\bar{t}$ events are also a natural place for searches of a general nature for new physics. Top quarks are heavy enough to decay into particles not yet observed, and particles heavier than top could decay into top quarks. For example, in the MSSM a heavy supersymmetric top quark (stop) could decay

into a top quark while if the stop is light the Standard Model top could decay into stop. Heavy intermediate particles from a wide range of theories could decay into $t\bar{t}$ pairs resulting in a possible enhancement in the $t\bar{t}$ cross section and a bump the $m_{t\bar{t}}$ mass spectrum. So, the $m_{t\bar{t}}$ spectrum is under study, with no peaks so far observed. And, the kinematics of top quarks en vents have been, and will continue to be, compared to Standard Model expectations. Any significant deviations would point to new physics - none have so far been observed in Run II.

1.2 Top Quark Production and Decay

1.2.1 top quark production

The top quark can be produced by strong interaction (top pair production) and also electro-weak interaction (single top production). In hadronic collisions which involve large momentum transfer (high Q^2 as compared to the QCD energy scale Λ^2), the processes contributing to the cross section are short-distance interactions which can be described by the parton model. The heavy top quark mass necessarily involves a large Λ^2, thereby ensuring short range interactions, and therefore a small enough α_s for perturbation theory to the valid. There are two leading-order (LO, $i.e$ order of $\mathcal{O}(\alpha_s^2)$ contributions) subprocesses by which $t\bar{t}$ pairs are produced, the $q\bar{q}$ annihilation ($q\bar{q} \to t\bar{t}$) and gluon fusion ($gg \to t\bar{t}$) as shown in Figure 1.1.

$$\sigma(s) = \sum_{i,j} \int_0^1 dx_1 \int_0^1 dx_2 f_i(x_1,\mu) f_j(x_2,\mu) \hat{\sigma}_{ij}(\hat{s}, m_Q, \alpha_s(\mu)), \quad (1.2)$$

where, the sum is over the initial parton states, and the integrations are over the two parton momentum fractions. The terms in Eq. 1.2 have the following meanings.

• $f_i(x_1, \mu)$ is the momentum density (or structure function) for parton i. That is, it represents the probability that parton i is carrying a fraction of the incident hadron momentum between x_1 and $x_1 + dx_1$. Similarly for $f_j(x_2, \mu)$.

• $\hat{\sigma}_{ij}$ is the total short distance cross section for the production of a heavy quark pair from the incident partons i and j. It is calculated from the appropriate Feynman diagrams representing the production of the heavy quark pair.

• μ^2 is the renormalization (or factorization) scale which necessarily results from the inclusion of Feynman diagrams higher than leading order. Essentially, μ^2 defines a reference α_s ($\alpha_s(Q^2 = \mu^2)$) which avoids the infinities appearing in loop diagrams.

• α_s is the strong running coupling constant. It decreases with increasing Q^2 and is therefore small in short-distance interactions.

• $\hat{s}$ is the square of the center-of-mass energy in the $i - j$ parton system and it related to the $p\bar{p}$ center-of-mass energy, s, by $\hat{s} = x_1 x_2 s$.

• m_Q is the heavy quark mass.

The cross sections, calculated from the leading order, or Born, diagrams for $t\bar{t}$ production in Figure 1.1, can be written in terms of the top quark mass, m_t, and $\hat{s}$ as follows.

$\circ$ $q\bar{q}$ annihilation:

$$\hat{\sigma_{q\bar{q}}} = \frac{8\pi\alpha_s^2}{27\hat{s}}\left(1-\frac{4m_t^2}{\hat{s}}\right)^{\frac{1}{2}}\left(1+\frac{2m_t^2}{\hat{s}}\right) \tag{1.3}$$

$\circ$ $q\bar{q}$ annihilation:

$$\hat{\sigma_{gg}} = \frac{\pi\alpha_s^2}{12\hat{s}}\left[\left(\frac{4m_t^4}{\hat{s}}+\frac{16m_t^2}{\hat{s}}+4\right)\ \ln y - \left(7+\frac{31m_t^2}{\hat{s}}\right)\left(1-\frac{4m_t^2}{\hat{s}}\right)^{\frac{1}{2}}\right] \tag{1.4}$$

where,

$$y \equiv \frac{1+\left(1-\frac{4m_t^2}{\hat{s}}\right)^{\frac{1}{2}}}{1-\left(1-\frac{4m_t^2}{\hat{s}}\right)^{\frac{1}{2}}} \tag{1.5}$$

The relative importance of the quark and gluon diagrams depends on the top quark mass m_t. At threshold ($\hat{s} \sim 4m_t^2$), the partonic cross sections become;

$$\hat{\sigma_{q\bar{q}}} = \frac{4\pi\alpha_s^2}{9\hat{s}}\left(1-\frac{4m_t^2}{\hat{s}}\right)^{\frac{1}{2}} \tag{1.6}$$

$$\hat{\sigma_{gg}} = \frac{59\pi\alpha_s^2}{48\hat{s}}\left(1-\frac{4m_t^2}{\hat{s}}\right)^{\frac{1}{2}} \tag{1.7}$$

giving;

$$\hat{\sigma_{q\bar{q}}} : \hat{\sigma_{gg}} \approx 1 : 3. \tag{1.8}$$

However, the $t\bar{t}$ cross section also depends on the parton luminosities (or equivalently, the parton structure functions), which were neglected in calculating the above ratio. A high top mass requires large $x_1 x_2$ and since the gluon to quark ratio decreases with increasing x, the gluon-gluon luminosity decreases relative to the quark-quark luminosity for high top mass. This effect should be properly taken into account by the structure functions in Eq.1.2 when calculating the total $t\bar{t}$ production cross section. It turns out that after folding in the relative effects of the parton luminosities the $q\bar{q}$ annihilation mechanism dominates for $m_t >\sim 100$ GeV for the conditions present at the Tevatron. For $\sqrt{\hat{s}} \approx 4\ m_t$, the relative contribution to the total $t\bar{t}$ cross section from $\hat{\sigma_q q}$ with respect to $\hat{\sigma_{gg}}$ is about $5 : 1$ for a top mass in the region of 175 GeV.

On the other hand, about 30% of the contribution (($\mathcal{O}(\alpha_s^3)$) at $\sqrt{s} =$ 1.96 TeV [13]. Some higher order diagrams for the $q\bar{q}$ annihilation and gluon-gluon fusion process are shown in Figure 1.6. The full calculations were first done in [17] and [18]; a more complete set of contribution diagrams are shown in[18].

An important prediction of the NLO calculation is the possibility of additional hard partons produced in addition to the top quark pair. If one is produced with sufficiently high transverse momentum and large angular separation from other objects in the event, it is detected as a jet.

Initial state gluon bremsstrahlung dominates the NLO corrections [14].

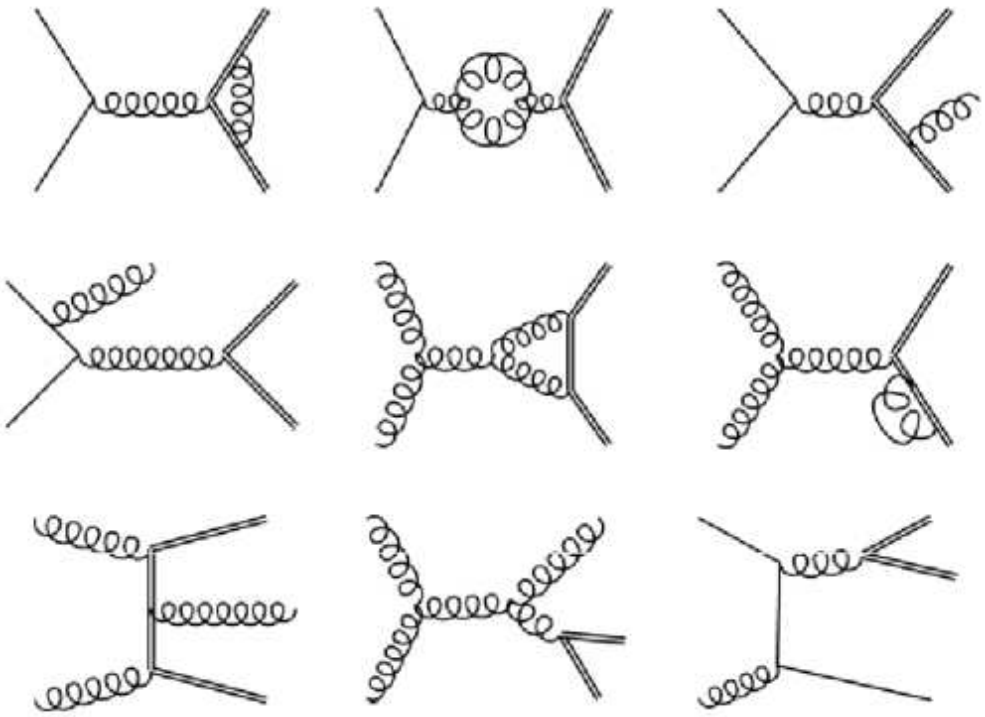

Figure 1.6: Representative subset of diagrams for the next to leading order contribution to top quark pair production at the Tevatron. The double line is the $t\bar{t}$ pair and the single line is a light (u or d) quark.

Other corrections to the partonic cross section at the α_s^3 level include quark-qluon fusion processes in which the final stat gluon split into a $t\bar{t}$ pair.

1.2.2 top quark decay

The $t\bar{t}$ decays can be characterized by the W^+W^- decays, as shown in Figure 1.7. Explicitly, each W boson can decay in the following ways:

$$W^+ \rightarrow (e^+\nu_e)(\mu^+\nu_\mu)(\tau^+\nu_\tau)(u\bar{d})(c\bar{s})$$
$$W^- \rightarrow (e^-\nu_e)(\mu^+\nu_\mu)(\tau^+\nu_\tau)(u\bar{d})(c\bar{s})$$

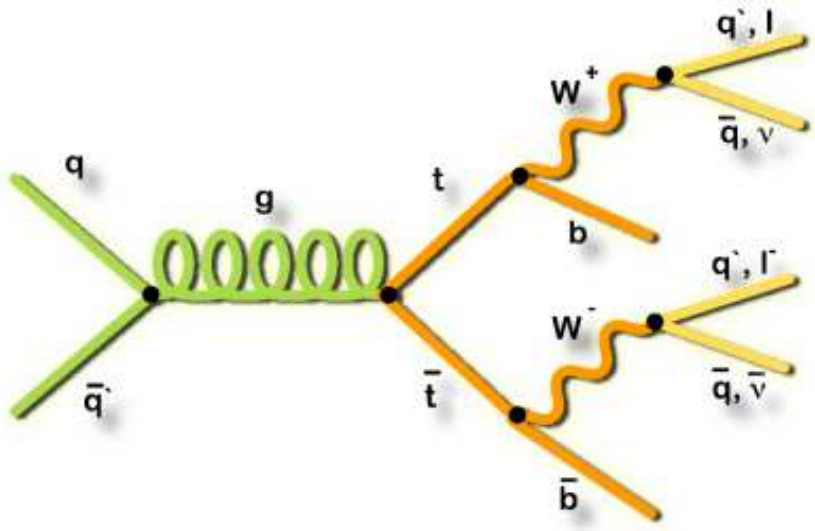

Figure 1.7: Tree level $q\bar{q} \rightarrow t\bar{t}$ production followed by the SM $t\bar{t}$ decay.

The hadronic decay pairs can each appear in 3 different color combinations ($R\bar{R}$, $G\bar{G}$, $B\bar{B}$), giving 9 final state degrees of freedom for each W decay. The $t\bar{t}$ analyses naturally fall into 3 different categories depending on whether

the W decay is leptonic or hadronic. These are summarized in Table xxx. The *dilepton* category for $t\bar{t}$ is represented by the case in which both W decays leptonically and the other hadronically, and the $all - hadronic$ category by the case in which both W bosons decay hadronically. Leptonic decays to τ's are normally excluded in the standard analyses because of the added difficulty in identifying a τ decay from either its leptonic or hadronic decay products above background sources. However, analyses in CDF have been carried out, with some still in progress, that include the τ channels in the dilepton $t\bar{t}$ decay modes.

Category	Decay mode	Branching ratio	
Dilepton	$t\bar{t} \to e\nu be\nu\bar{b}$	1/81	4/81 (5%)
	$t\bar{t} \to \mu\nu b\mu\nu\bar{b}$	1/81	
	$t\bar{t} \to e\nu b\mu\nu\bar{b}$	2/81	
	$t\bar{t} \to e\nu b\tau\nu\bar{b}$	2/81	
	$t\bar{t} \to \mu\nu b\tau\nu\bar{b}$	2/81	
	$t\bar{t} \to \tau\nu b\tau\nu\bar{b}$	1/81	
Lepton + jets	$t\bar{t} \to q\bar{q}be\nu\bar{b}$	12/81	24/81 (20%)
	$t\bar{t} \to q\bar{q}b\mu\nu\bar{b}$	12/81	
	$t\bar{t} \to q\bar{q}b\tau\nu\bar{b}$	12/81	
All-Hadronic	$t\bar{t} \to q\bar{q}bq\bar{q}\bar{b}$	36/81	36/81 (44%)

Table III: $t\bar{t}$ decay modes and their associated branching ratios. The τ decay modes are not considered in the standard $t\bar{t}$ analysis categories.

The all-hadronic decay channel, with 6 jets expected in the final state, has the highest branching ratio, however, it suffers from a large QCD background making it difficult to extract a $t\bar{t}$ signal. However recent success has

been achieved in observing a $t\bar{t}$ signal by requiring tight kinematic cuts on the jets, and with at least on jet required to be tagged as originating from a b quark. A separate CDF analysis requiring *doubletagged* events and a large $\Sigma E_t(jet)$ event cut, has also had success in observing a $t\bar{t}$ signal.

The lepton + jets channel is characterized by a final state with a high -P_t lepton, missing transverse energy ($\not\!\!E_T$) from the undetected neutrino, and four jets, two from the b quarks, and two from the hadronic W decay. The $lepton + jets$ analysis requires events to have at least on $b - tagged$ jet, and a total of least three jets,in association with the high-P_t lepton and $\not\!\!E_T$.

The cleanest channel with respect to signal over background (with an expected ratio of $\sim 2.5 : 1$) is the dilepton channel, though its branching ratio is the smallest. The $t\bar{t}$ dilepton signature is characterized in events by two high-P_t leptons, large missing transverse energy($\not\!\!E_T$) from the neutrinos, and two jets from the fragmentation of the b quarks. The search for this signature is the topic of this thesis, and the requirements imposed form its selection are discussed in Chapter 3.

1.3 Top Pair Production Cross section

The difinition of a cross section is as follows. Consider a reaction

$$A + B \rightarrow FINAL\ STATE \tag{1.9}$$

Then the cross section for this reation is

$$\sigma = \frac{transition\ rate}{incident\ flux} \tag{1.10}$$

The transition rate is the number of times Reaction 1.xx occurs in a small time unit Δt. The incident flux is the number of A and B particles per

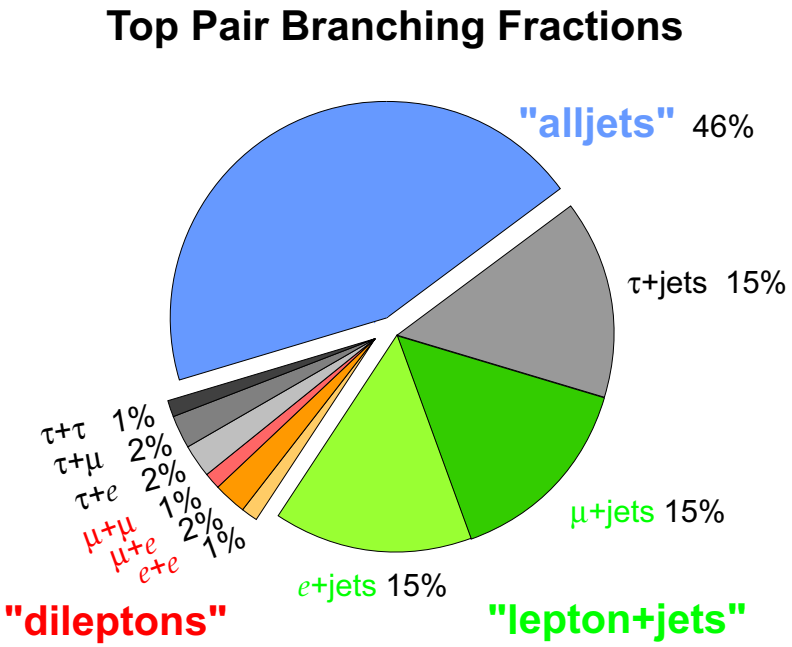

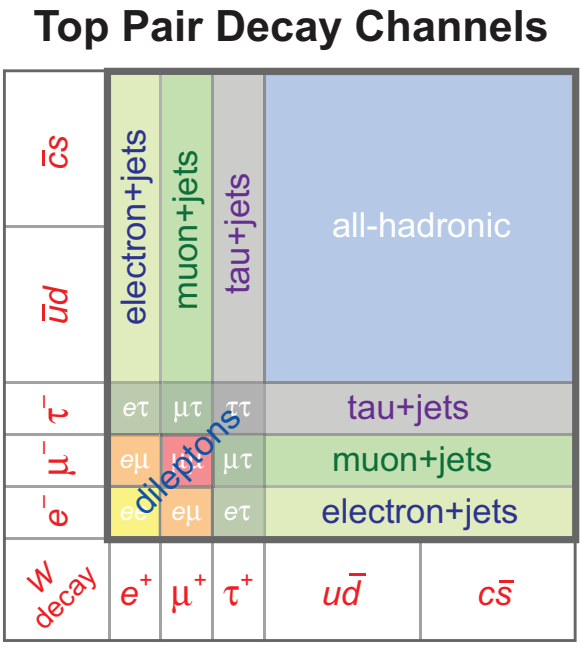

Figure 1.8: $t\bar{t}$ branching fraction and decay modes.

unit area per unit time. Thus, the crosss section has units of area, as expected. Because the length scale accessible to a given probe is inversely proportional to its energy, if a process has a small cross section (i.e. small length scale over which it can occur) it requires a large amount of energy to probe that small length scale.

The typcial cross sections in high energy physics are very small. 10^{-28} m is a comparatively large cross section, so it is called a barn (as in "You couldn't hit the side of a barn!") We often see cross sections on the order of picobarns (pb), for top quark production, or femptobarn (fb), for Higgs boson production.

When one wishes to know about the angular distribution of reaction rates, we use what is called the *diffrential cross section*. This simply modifies our definition to take care of the number of particles that scatter into a solid angle Ω. Thus, we note the differential cross section as

$$\frac{d\sigma}{d\Omega} \tag{1.11}$$

When you integrate over all solid angles, you regain the total cross section.

To obtain the cross section from a quantum mechanical amplitude, the formula for the scattering of particles

$$1 + 2 \rightarrow 3 + 4 + ... + n \tag{1.12}$$

is given by D.Griffiths, Introduction to Elementary Particles, 1987.

$$d\sigma = |\mathcal{M}|^2 \frac{S}{\sqrt[4]{(p_1 \cdot p_2)^2 - (m_1 \cdot m_2)^2}} \left[\prod_{i=3}^{n} \left(\frac{d^3\overrightarrow{p_i}}{(2\pi)^3 2E_i} \right) \right]$$

$$\times (2\pi)^4 \delta^4(p_1 + p_2 - p_3 - p_4 - ... - p_n) \tag{1.13}$$

where $\mathcal{M}$ is the quantum-mechanical amplitude, S is a statistical factor $(1/j!)$ for each group of j identical particles, p_i is the 4-momentum of the ith particle, $\overrightarrow{p_i}$ is the 3-momentum of the ith particle, E_i is the energy of the ith particle, and $\delta^4(x)$ is an energy-conserving delta funtion.

For $2 \to 2$ scattering in the center of mass frame, the differential cross section is

$$\frac{d\sigma}{d\Omega} = \frac{1}{64\pi^2} \frac{S|\mathcal{M}|^2}{(E_1 + E_2)^2} \frac{|\overrightarrow{p_f}|}{|\overrightarrow{p_i}|} \tag{1.14}$$

where $\overrightarrow{p_f}$ is the final momentum of either particle, $\overrightarrow{p_i}$ is the initial momentum, E_1 and E_2 are the energies of the incoming particles, $\mathcal{M}$ is the amplitude, and S is the satistical factor.

Thus, given the matrix element, it is possible to calculate this differential cross section quite easily. We will make use of this to calculate the theoretical prediction for the $t\bar{t}$ production cross section.

The top quark pair production in the standard model proceeds primarily by quark-antiquark annihilations. At the Tevatron the predictions are 85% quark-antiquark annihilations and 15% gluon fusions. At the Large Hadron Collider at $\sqrt{\mathrm{s}} = 14$ TeV the situation is predicted to be very different with 90% of the production being due to gluon-gluon fusion and 10% due to quark-antiquark annihilation.

This thesis present the improvement upon a previous measurements of the cross section using the same dilepton (DIL) selection in a data sample with an integrated luminosity of 0.197 fb^{-1} [15]. Unlike other CDF measurements of the $t\bar{t}$cross section in the dilepton channel [16], where one ℓ is identified as e

or μ while the other is identified by the presence of a high momentum central track, the DIL analysis positively identifies both leptons as either electrons or muons from W decays or as products of semileptonic decays of τ leptons, thus allowing for the comparison of the observed yield of $t\bar{t}$ decays to ee, $\mu\mu$ and $e\mu$ final states with the predictions from lepton universality.

The measurement provides a test of the QCD calculations of the $t\bar{t}$ cross section [2] in a channel which is independent and complementary to other measurements of the $t\bar{t}$ cross section in higher statistics final states where at least one W boson from the top quark is reconstructed via its hadronic decay, $W \to qq'$. The dilepton final state suffers from a lower statistical precision, as the product of the branching ratios of the semileptonic W decay $\mathrm{BR}(W^+ \to \ell^+\nu) \times \mathrm{Br}(W^- \to \ell^-\nu) \approx 5\%$ with $\ell = e$ or μ, but it has a signal to background ratio well above unity even before requiring the identification of one of the jets originating from a b quark. This analysis also requires jets in the events to have secondary vertexes consistent with the presence of a $b-$hadron decay as this selection would further reduce the acceptance by almost 50%. Otherwise it is useful to obtain pure top candidate events.

1.4 W boson polarization in top quark decay

According to the Standard Model the top quark decays into W and $b-$quark with almost 100% probability and very fast ($\tau_{top} \approx 5 \times 10^{-25} s$). Short lifetime prevents the hadronization of top quark therefore its properties are transfered directly to decay products without modification caused by hadronization! This is a unique property of the top quark! Standard Model makes specific prediction about W polarization in case of t $\to$Wb decay. Pre-

cise measurement of W polarization could reveal new physics beyond the Standard Model (if it takes place).

A short description of W helicity expectations in top rest frame predicted by Standard Model is given below.

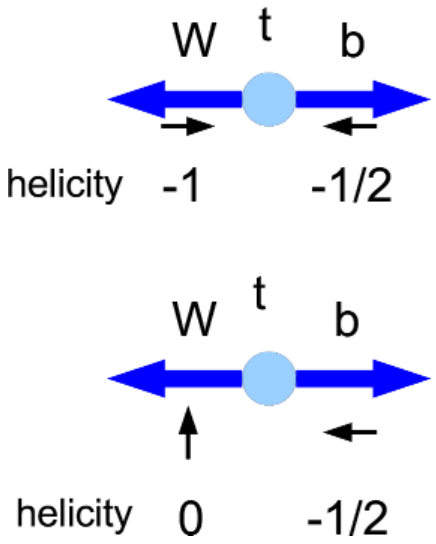

Figure 1.9: Decay of top quark into W and b in top rest frame. Upper part represents top spin projection $+1/2$, W helicity -1 and $b-$quark helicity -1/2 (both left-handed), Lower part represents top spin projection -1/2, W helicity 0 (longitudinal) and $b-$quark helicity -1/2 (left-handed)

WBoson as a vector (spin 1) particle can have projections of spin on the direction of motion (helicity) +1,0,-1, which are right-handed, longitudinal and left-handed helicity states, respectively. In the $b-$quark massless limit in the top quark decay and due to V-A nature of charge current weak interaction responsible for the decay, $b-$quark can be only left handed and $\bar{\text{b}}$-quark (in $\bar{\text{t}}$ decay) only right-handed. Top quark spin is $\frac{1}{2}$. Therefore the only options for W^+ helicity states are left-handed (W_-) and longitudinal (W_0). In case of $\bar{\text{t}}$ decay – W^- helicity states can be right-handed (W_+) and longitudinal

(W_0). These are the only options for W to combine with left-handed $b-$quark to make combined spin projection $\pm 1/2$. Shown in Figure 1.9 is the graphical explanation. Standard Model gives specific prediction about fraction of cases when top quark decays into definite helicity states of W Boson. For example, for the longitudinal fraction f_0 SM predicts (in the tree approximation):

$$f_0 = \frac{\Gamma(t \to W_0 b)}{\Gamma(t \to W_0 b) + \Gamma(t \to W_+ b) + \Gamma(t \to W_- b)} = \frac{M_t^2}{2M_W^2 + M_t^2} \qquad (1.15)$$

In Standard Model $\Gamma(t \to W_+ b)$ is (close to) 0. Naturally, there holds equality

$$f_+ + f_- + f_0 = 1 \qquad (1.16)$$

Therefore for top mass 175 GeV/c^2 SM predicts $f_0 = 0.7$, $f_- = 0.3$ and $f_+ = 0$. The W Boson polarization is reflected in angular distribution of leptons from $W \to l\nu$ decay. Generally, $cos(\theta^*)$ distribution is expressed by:

$$\frac{dN}{dcos(\theta^*)} \propto f_- \cdot \frac{3}{8}(1-cos(\theta^*))^2 + f_0 \cdot \frac{3}{4}(1-cos^2(\theta^*)) + f_+ \cdot \frac{3}{8}(1+cos(\theta^*))^2 \quad (1.17)$$

where θ^* is the angle between momentum of the charged lepton in the W rest frame and the momentum of the W boson in the top quark rest frame. Shown in Figure 1.10 are $cos(\theta^*)$ distributions for different helicity states of W and for SM expectation.

In order to reconstruct $\cos\theta^*$, the full $t\bar{t}$ kinematic chain has to be reconstructed. Since the reconstructed $cos\theta^*$ distribution will be distorted by many factors (selection, reconstruction, etc.) we use the templates for signal and background to fit the data to the $\cos\theta^*$ Monte-Carlo templates to obtain W boson helicity fractions.

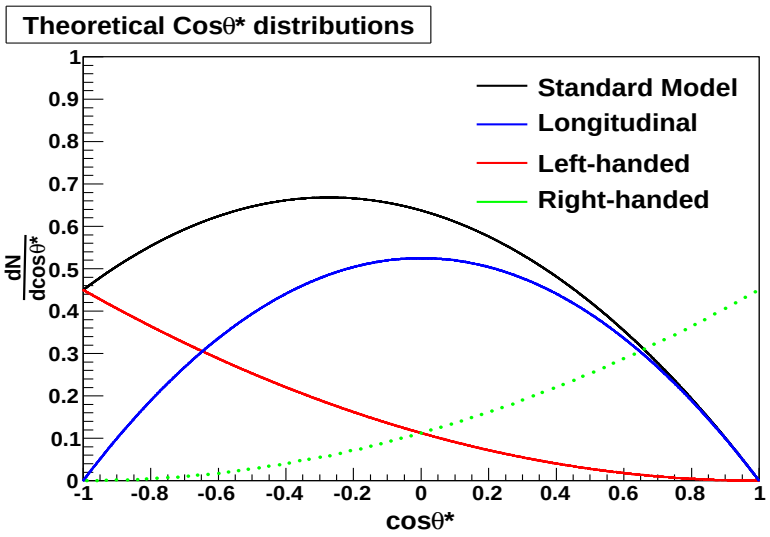

Figure 1.10: Expected angular distribution of leptons in W rest frame in case W_-, W_0, W_+ helicity states compared to SM expectation (see text).

The thesis is structured as following. After the introduction in this section, we will briefly describe the dilepton $t\bar{t}$ event selection we use in section 3. For this round of analysis, we use the DIL selection together with the requirement of at least one SVX b-tagged jet. In the near future, we also plan to make the measurement using pre−tagged sample. In section 7.1 we will describe the method we use for the kinematic reconstruction of $t\bar{t}$ dilepton events. Next, in section 7.2, we present the template method for determining W boson helicity fractions using $\cos\theta^*$ distributions. Various checks performed on simulated Monte Carlo events are presented in section 7.3. Section 7.4 deals with the systematic uncertainties associated with this measurement. Finally, the results which we obtained using 5.1 fb^{-1} (4.8 fb^{-1} on b−tagging) of CDF data are presented in section 7.5 with the conclusion of the work being in section 8.

Chapter 2

Experimental Apparatus

Figure 2.1: An Bird's-eye view of the Fermilab.

The Fermilab Tevatron Collider was till quite recently the world's highest energy accelerator, before the Large Hadron Collider (LHC) have turned

on since 2010, colliding anti-protons with protons at a center of mass energy of $\sqrt{s} = 1.96$ TeV. At present (year 2011) LHC has been started operating since March 2010 at a center-of-energy 7 TeV and will plan to increase the center-of-energy to 14 TeV in 2014. The Tevatron is located about 50 km west of Chicago in Fermilab, a scientific laboratory run by a consortium of universities (URA) and by the University of Chicago ("Fermi Research Alliance") on behalf of the American Department of Energy (DOE). The CDF (Collider Detector at Fermilab) experiment is an international collaboration of about 500 physicists from universities and national laboratories from 12 countries. The CDF II detector is a general purpose detector which measures most of the interesting particles that come out of the $p\bar{p}$ collision. Two intense beams of protons and anti-protons meet head-on in the center of the CDF detector, and a few collisions occur every time 2 bunches cross which happens every 120 ns.

2.1 The Tevatron Accelerator

The Tevatron collider obtained the first collisions in 1985. In the course of time it provided several physics runs as listed in Table I and Figure 2.3. The accelerator complex at Fermilab consists of several key components, that can be conceptually separated into a series of accelerators that prepare the protons, produce and store anti-protons and finally accelerate both protons and antiprotons to a center- of-mass-energy of 1.96 TeV and orchestrate the collisions.

Figure 2.3 shows the schematic view of the accelerator chain to create the world's most powerful particle beams.

Run	Period	Int. Lum pb^{-1}
First Test	1997	0.025
Run 0	1988∼1989	4.5
Run 1A	1992∼1993	19
Run 1B	1994∼1995	90
Run 1C	1995∼1996	1.9
Run 2A	2001∼2004	400
Run 2B	2004∼	>7000

Table I: Integrated luminosity delivered by Tevatron in its physics runs. Run2B is still in progress.

2.1.1 Proton Source

The protons that are used in collisions and to produce antiprotons all begin in a small bottle of hydrogen gas. Hydrogen atoms drawn from this bottle are ionized to form H^- ions. The H^- ions are accelerated from rest to an energy of 750 KeV by a Cockcroft Walton pre-accelerator that applies an electric field to the ions (see Figure 2.4).

The H^- ions are then injected into the Linac (approximately 500 feet long), a linear RF accelerator, which further accelerates them to an energy of 400 MeV. At this point, the electrons are removed from the H^- ions, leaving behind bare protons.

The protons then enter the Booster, a synchrotron with a circumference of 474 m. The Booster utilizes magnets to bend the protons along a circular path while RF cavities accelerate them to an energy of 8 GeV.

At this time, the protons enter the Main Injector, a synchrotron 3 km in circumference. The Main Injector can accelerate the protons either to 150 GeV for injection into the Tevatron, or to 120 GeV for usage in antiproton produc-

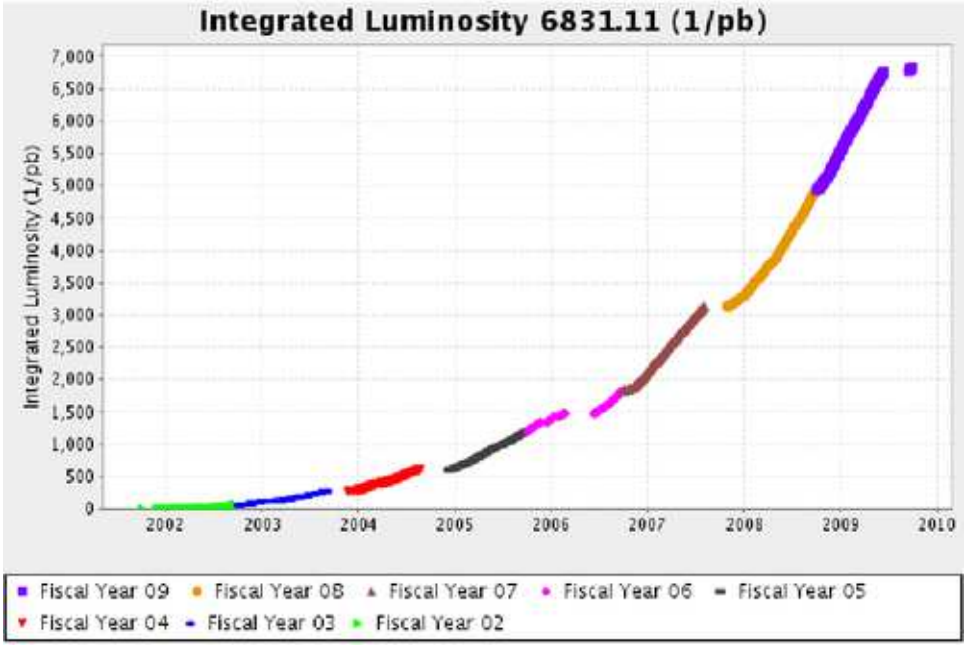

Figure 2.2: The integrated luminosity in Run II. The empty periods of time correspond to Tevatron shutdowns.

tion. The Main Injector can also stack antiprotons produced in the antiproton source and accelerate them to 150 GeV prior to usage in the Tevatron.

2.1.2 Antiproton Source

One of the most technically daunting tasks in the collider operations at Fermilab in the production and storage of antiprotons. Because of its difficulty, the production of antiprotons remains the limiting factor in the luminosity of colliding beams at the Tevatron. The antiproton source at Fermilab consists of a target for production and three accelerators used to cool and store: the Debuncher, the Accumulator and the Recycler (see Figure 2.5).

Antiprotons are produced by striking 120 GeV protons from the Main

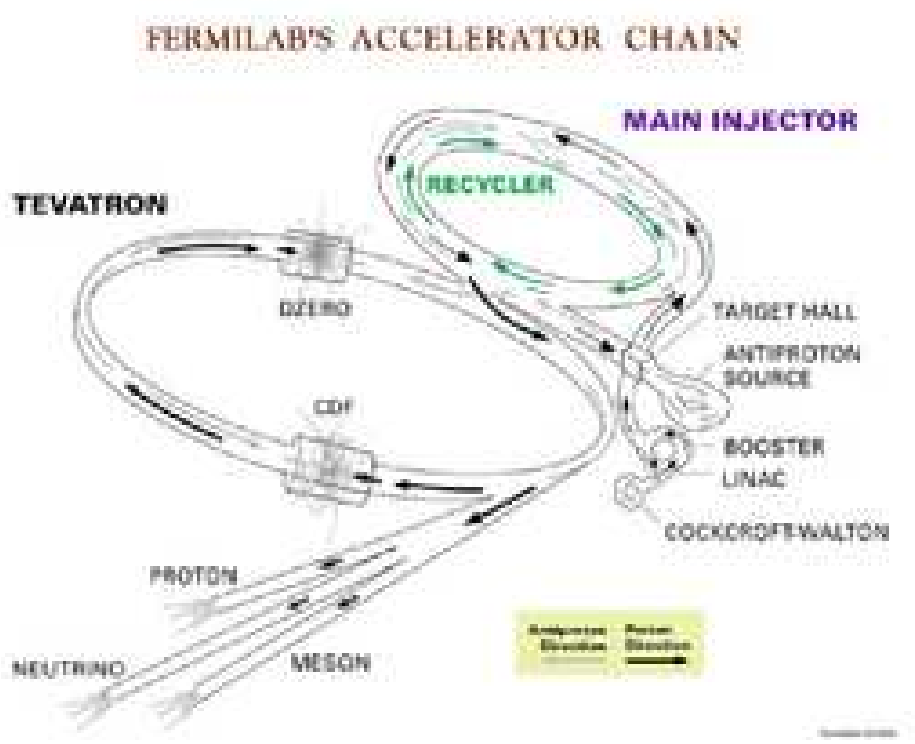

Figure 2.3: Diagram of Fermilab Accelerators

Injector upon a nickel target. These collisions yield a shower of particles from which antiprotons are separated using magnetic spectroscopy. The particles are subject to a magnetic field causing particles of different mass and charge to take paths of different radii. This allows antiprotons to be separated out. Approximately 100,000 protons are needed to successfully produce and store one antiproton. The resulting antiprotons have an average energy of 8 GeV.

The antiprotons produced at the target are then sent to the Debuncher, a triangular synchrotron with a mean radius of 90 m. The beam of antiprotons sent into the Debuncher has a large spread of momenta. The Debuncher is tasked with reducing this spread in momenta, forming a continuous beam.

Figure 2.4: Cockcroft Walton (first stage accelerator)

The antiprotons are sent to the Accumulator, another triangular synchrotron that shares a tunnel with the Debencher. Here, the antiprotons are stored, or "stacked", as more are produced. In addition, a process known as stochastic cooling is used to further reduce the spread in momenta of the antiprotons. When a sufficient number of antiprotons for colliding beam operations have been stacked at the Accumulator, they can then be sent to the Main Injector for further acceleration.

Figure 2.5: A view of the antiproton source

Electron Cooling

Electron cooling is a technique which used a beam of electrons run alongside a beam of antiprotons to reduce the longitudinal momentum of the antiprotons. While the method was first proposed in 1966 and has been utilized for now-energy beams, its implementation at Fermilab in 2005 is the first successful application of electron cooling to a relativistic beam. The electron cooling system in use utilizes a 4.3 MeV beam of electrons that is run alongside a 20 m length of the Recycler. This system has been in operation since late 2005 and is expected to help increase luminosities for the colliding beams by up to 100% from pre-electron cooling peak luminosity.

2.1.3 Linac

The Fermilab Linear Accelerator (Linac) is a negative hydrogen ion, 400 MeV accelerator. It includes a 25 KeV H-minus ion source, a 750 KeV electrostatic accelerating column, a 116 MeV drift-tube (Alverez) linac operating at 201.25 MHz, and a 401 MeV side-coupled cavity linac operating at 805 MHz. Many details can be obtained from the nice picture displays listed in the sidebar to the left (see Figure 2.6).

The Fermilab Linac provides beam for Booster operation at frequencies from 0.1 to 5 Hz. Several times per week, we provide 66 MeV protons to the Fermilab Neutron Therapy Facility (NTF). This outstanding cancer treatment facility has been part of the Linac for over 30 years. We estimate that on the 25th anniversary of the beginning of NTF in 2001, Linac had provided 4.0E21 ("four times ten to the twenty-one") protons to NTF for the generation of the neutrons they use for tumor treatment.

2.1.4 Booster

The Fermilab Booster is a synchrotron accelerator with a circumference of 474 meters. Beam is injected into the Booster from the 400 MeV transport line which carries the 400 MeV beam output from the Linac accelerator. The Booster accelerates a proton beam from 400 MeV to 8 GeV in less than 67 milliseconds for the Main Injector accelerator. Booster also provides beam for the MiniBooNE experiment and the NuMI facility and MINOS experiment (see Figure 2.7).

The FNAL Booster accelerator is approximately 150 m diameter proton

Figure 2.6: Left: A view looking up stream of the 400 MeV (high energy) section of the Linac. Right: Inside view of drift tube in older 200 MeV section of Linac (b).

synchrotron with an injection energy of 400 MeV and an extraction energy of 8 GeV. It is considered a "fast cycling" machine, current waveform to excite the magnets. The Booster is made up of 96 combined function magnets in a series of 24 repeating periods. Their magnetic field varies from about 740 gauss at injection to 7,000 gauss at extraction. The Booster tunnel is a concrete tunnel 8 feet high and 10 feet wide, covered by 15 feet of earth shielding. The 400 MeV line transfers the beam from LINAC to the Booster, bending the beam vertically fifteen feet. A multiple turn system increases the Booster intensity by stacking successive turns of LINAC beam layered on top of each other. RF (radio frequency) energy, delivered by up to 17 ferrite-tuned cavity resonators, accelerates the proton beam over the 33 msec rising portion of the sinusoidal

current waveform. Beam can be extracted from Booster at two locations, depending on its destination. An extraction at Long 13 transfers beam to the Booster dump. An extraction at Long 3, initiated by kickers in Long 2, transfers beam to the Main Injector via the MI-8 line.

Figure 2.7: View of RF Cavity and an Alternate Gradient Magnet in the Booster Accelerator

2.1.5 Main Injector

The Main Injector has been a decade in the making. The initial design work started in 1987, when a small group of physicists undertook a study of how Fermilab could enhance the performance of the Tevatron beyond its original performance goals, by integrating a new accelerator or accelerators within

the existing complex. Funding for the Main Injector Project was approved starting in October 1991. After an extended design and R&D period, the construction really got underway in the spring of 1993. In the spring of 1999 the Main Injector is ready for high energy physics research at Fermilab (see Figure 2.8).

The addition of Main Injector to the Fermilab accelerator complex marks a dramatic increase in the physics capabilities of the Fermilab High Energy Physics Programs.

• There will be a dramatic increase in the number of proton-antiproton collisions that can be created and observed in the Tevatron, by increasing the beam current in the Main Injector, its reliability and the cycling rate over the Main Ring which it replaces, This extends the physics "reach" to higher mass and rarer particles that will, if discovered, expand our understanding of the nature of matter and the forces that hold it together.

• The Main injector will operate simultaneously in fixed target and antiproton production modes. A very intense 120 GeV beam can be extracted. Targeting this beam will create an intense beam of neutrinos that will be used to study the basic question: do neutrinos have mass? An intense beam of K-mesons can also be created and rare decay modes studied.

Greater understanding of the basic quark structure of matter and the nature of the matter-antimatter asymmetry in the Universe will emerge from these studies.

2.1.6 Recycler

The Recycler Ring was added to the Main Injector Project in the spring

Figure 2.8: The Main Injector Tunnel showing the Main Injector (blue magnets on bottom) and the Recycler (green magnets on top).

of 1997. The Recycler Ring will increase the collision rate in the Tevatron collider by a factor of three to five beyond that with the Main Injector alone. Without the Recycler, the precious antiprotons left at the end of a collider "store" (8-12 hour period of time when the beams are in collision) must be thrown away. The Recycler will allow Fermilab to recover these antiprotons and re-use them in a later store. As an added benefit, the Recycler will also allow the existing Antiproton Source to perform more efficiently and produce more antiprotons per hour.

The Recycler is a permanent-magnet 3.3 km antiproton storage ring. It receives 8.9 GeV/c antiprotons from the Accumulator and stores them until the Tevatron is ready for its next store. The Recycler has both stochastic and

electron cooling systems.

Its mission is to prepare antiproton bunches suitable for extraction and transport to the Tevatron. Presently, a typical number of stored antiprotons in the Recycler is 200 - 300e10. The design goal is to store and cool 600e10 antiprotons.

2.1.7 Tevatron

The Tevatron is a 1 km radius circular synchrotron employing superconducting bending magnets, where the protons and antiprotons beams orbit in the same pipe in opposite directions. Undesired bunch crossings are avoided by electrostatic separators.

The beam revolution time is 21 μs. The beams are split in 36 bunches organized in 3 trains each containing 12 bunches. Within a train the time spacing between bunches is 396 ns. An empty sector 139 buckets-long (2.6 μs) is provided in order to allow the kickers to raise to full power and abort the full beam into a dump in a single turn. This is done at the end of a run or in case of an emergency.

The Tevatron receives 150 GeV protons and antiprotons from the Main Injector and accelerates them to 980 GeV, or one Tera electron volt (1 TeV). Traveling only 200 miles per hour slower than the speed of light, the protons and antiprotons circle the Tevatron in opposite directions. The beams cross each other at the centers of the 5000-ton CDF and DZero detectors located inside the Tevatron tunnel, creating bursts of new particles.

2.2 The CDF Coordinate System

The origin of the CDF coordinate system (x,y,z) = (0,0,0) cm (Figure 2.9) is at the nominal point of collision, in the center of the detector. The positive z direction points in the direction of the proton beam (west to east), the positive y direction points upward (south to north) and the positive x direction points out of the ring.

Given that the energy spectrum of quarks inside the protons is very broad, the hard collision rest frame will be boosted, in general, along the beam direction with respect to the lab frame. Therefore it is appropriate to use variables invariant under boosts along z direction. The detector solid angel segmentation, described by the angular coordinates η and ϕ, satisfies this requirement. ϕ is the azimuthal angle about the z-axis. η is the pseudorapidity and is related to the polar angle θ through the relation:

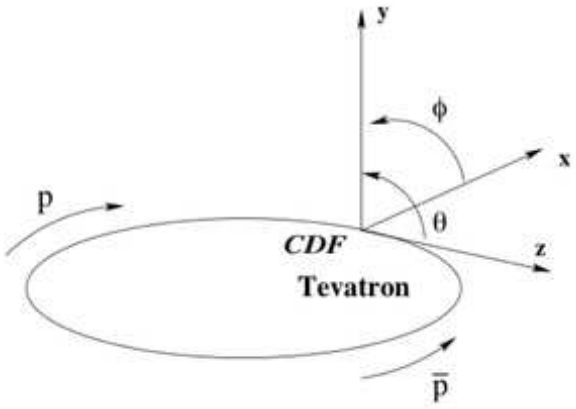

Figure 2.9: CDF Run II coordinate system

$$\eta \equiv -\ln(tan\frac{\theta}{2}) \tag{2.1}$$

Based on this definition, negative η corresponds to the west side of the detector, positive η to the east side of the detector, while $\eta = 0$ is the transverse x-y plane.

The pseudorapidity η is precisely the rapidity of a particle in the limit of m¡¡p, where m is the particle rest mass and p its momentum magnitude. The rapidity is defined as

$$y \equiv \frac{1}{2}\ln\frac{E + P_z}{E - P_z} \tag{2.2}$$

Using the relations between the hyperbolic and trigonometric functions,

$$\sinh\eta = \cot\frac{\theta}{2} \tag{2.3}$$

$$\cosh\eta = \frac{1}{\sin\theta} \tag{2.4}$$

and the notation $\alpha \equiv \mathrm{m}/p_T$, where $p_T = \mathrm{p}\ \sin\theta$, one can rewrite the energy as

$$E = \sqrt{m^2 + \frac{p_T^2}{\sin^2\theta}} \tag{2.5}$$

and further the rapidity as

$$y = \frac{1}{2} ln \frac{\sqrt{\cosh^2\eta + \alpha^2} + \sinh\eta}{\sqrt{\cosh^2\eta + \alpha^2} - \sinh\eta} \tag{2.6}$$

IF m¡¡p, then as $\alpha \to 0$, and the expansion on y in terms of α becomes

$$y \approx \eta - \frac{1}{2}\alpha^2 \tanh\eta + O(\alpha^3) \tag{2.7}$$

So for $\alpha = 0$, $y = \eta$.

Under a Lorentz transformation to another frame moving at velocity β, y transforms as

$$y \to y + \frac{1}{2} \ln \frac{1-\beta}{1+\beta} = y + constant \tag{2.8}$$

This implies that the segmentation in rapidity in Lorentz invariant, $dy \to dy$ under a boost along beam direction. Still, the rapidity is a function of the particle's mass and polar angle. The pseudorapidity is used to define the angular segmentation. It depends only on the polar angle and is approximately Lorentz invariant under z boosts for high pt particles. Also ϕ in invariant under z boosts, as it is a transverse plane variable.

2.3 The CDF II Detector

The CDF II detector, upgraded CDF detector from Run I in 1992 - 1995 period, is an azimuthal and forward-backward symmetric apparatus designed to study $p\bar{p}$ collisions at the Tevatron. It is a general purpose cylindrical detector which combines precision charged particle tracking with fast projective calorimeters and fine grained muon detection. Figure 2.10 shows the detector.

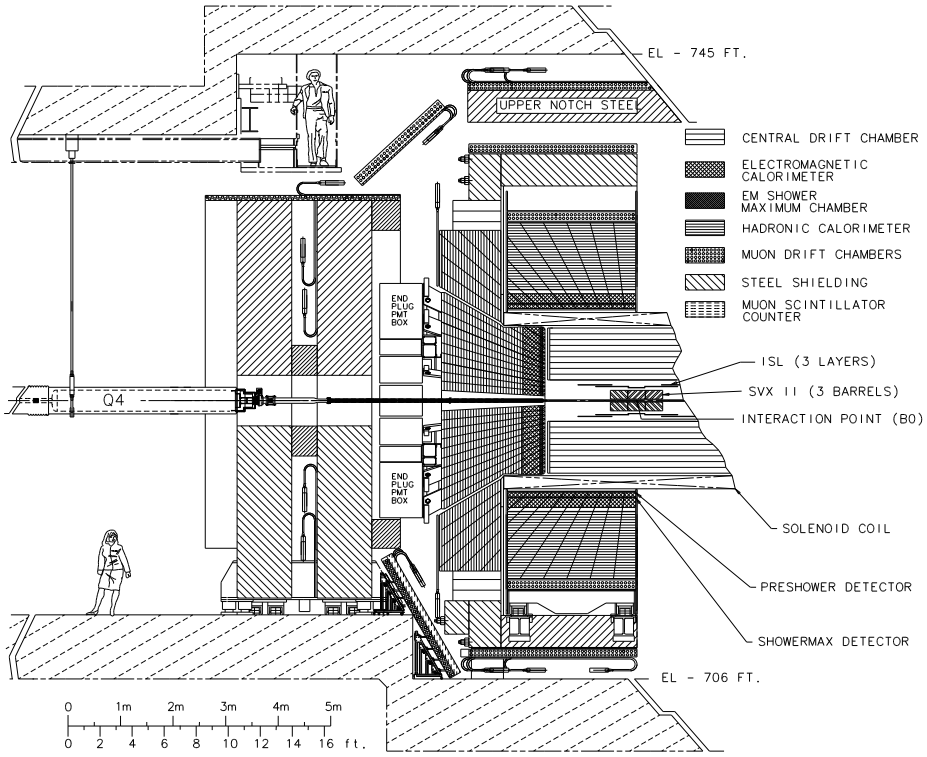

Figure 2.10: Elevation view of one half of the CDF detector.

Tracking systems are contained in a superconducting solenoid, 1.5 m in radius and 4.8 m in length, which generates a 1.4 T magnetic field parallel to the beam axis. Calorimetry and muon systems are all outside the solenoid. The main features of the detector systems are summarized below. I use a

coordinate system where the polar angle θ is measured from the proton direction, the azimuthal angle ϕ is measured from the Tevatron plane, and the pseudo-rapidity is defined as $\eta = -\ln(\tan(\theta/2))$.

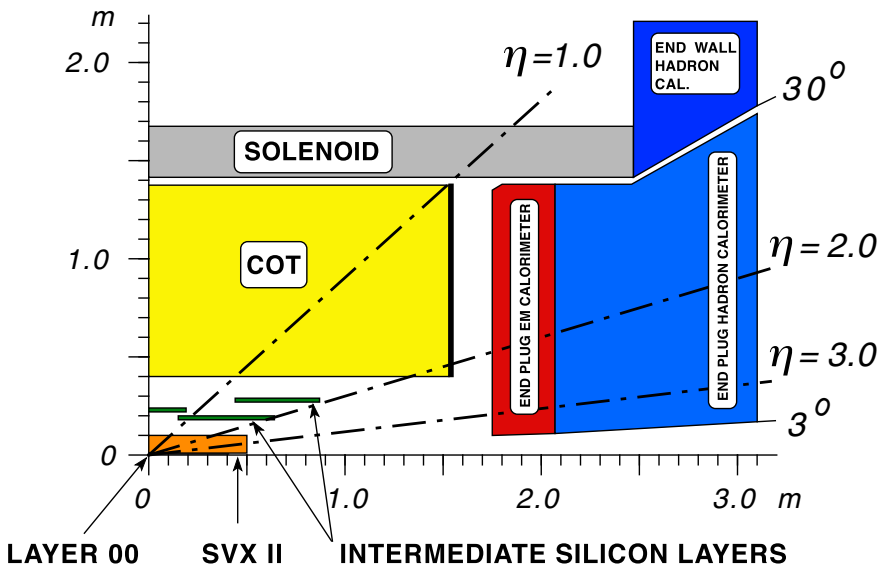

Figure 2.11: A cutaway view of one quadrant of the inner portion of the CDF II detector showing the tracking region surrounded by the solenoid and endcap calorimeters.

2.3.1 Tracking Systems

The tracking system consists of a silicon microstrip system and of an open-cell wire drift chamber that surrounds the silicon system. The silicon microstrip detector consists of seven layers (eight layers for $1.0 < |\eta| < 2.0$) in a barrel geometry that extends from a radius of r = 1.5 cm from the beam line to r = 28 cm.

The core of the CDF II detector is an 8 layer silicon micro-strip tracker. The design of the upgraded silicon system provides improved impact parameter

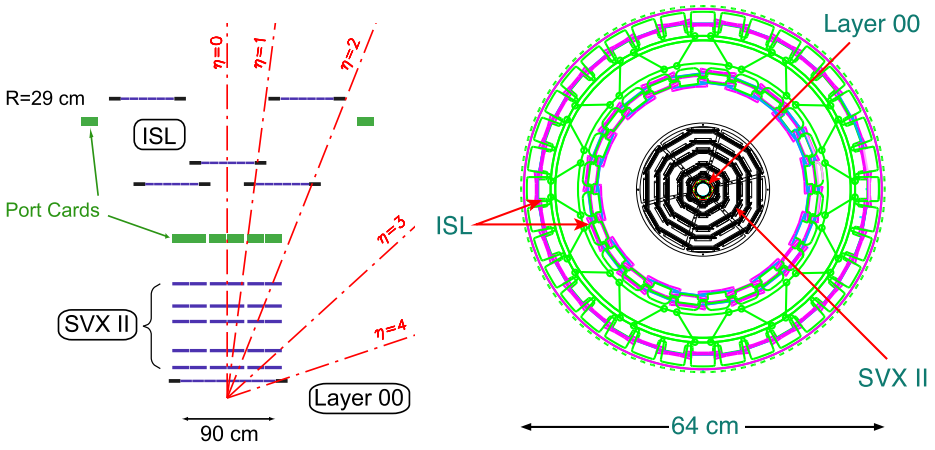

Figure 2.12: Left: A side view of half of the CDF Run II silicon system on a scale in which the z coordinate is highly compressed. Right: An end view of the CDF II silicon system including the SVX II cooling bulkheads and ISL support structure.

resolution and increased acceptance in the forward regions. This translates into better tracking and heavy flavor tagging efficiencies. Of critical importance is also the system's ability to trigger on displaced tracks, enhancing the CDF II B-physics program.

The system is separated into three sub-detectors which share a common infrastructure; the five-layered SVX II for precision tracking and triggering, the innermost Layer 00 (L00) to improve impact parameter resolution, and two Intermediate Silicon Layers (ISL) located between SVX II and the main CDF II tracking chamber. All three detectors use the same custom made front end ASIC, the SVX3D chip, which features deadtimeless operation with separate acquisition and readout cycles. The digitization logic provides 8 bit resolution, dynamic pedestal subtraction and data sparsification which reduces the raw data size of each sub-detector into the DAQ system.

The SVX II is the heart of the silicon detector. Five layers of sensors

are arranged at radii between 2.5 and 10.6 cm, covering 90 cm along the beam direction. The symmetric segmentation in ϕ permits the treatment of each of the 30^o wedges independently. The Silicon Vertex Trigger (SVT), which identifies tracks with large impact parameter, is based on this symmetry, the tight alignment constraints, and the fast readout achieved by reading each wedge in parallel. SVX II uses double sided sensors with axial strips at $\approx 60\mu m$ pitch on one side (layer dependent), and either $90\pm$ strips (at $\approx 140\mu m$) or 1.2^o small-angle stereo strips (at $\approx 60\mu m$ on the other, providing 3D information. The ISL consist of one central (at radius 20 cm) and two forward (at 18 and 29 cm) silicon layers between the SVX II and the tracking chambers, providing track linking between the two systems and extending the silicon tracking to high pseudorapidity ($\eta \leq 2$). The ISL use double sided small angle stereo (1:2) strips, with a strip pitch of $112\mu m$ on both sides. L00, the innermost silicon layer, is mounted directly on the beam-pipe at a radius of 1.4 cm. The sensors are radiation hard, single sided and designed to withstand a high bias voltage ($\approx$ 500V) to allow extended running after type inversion. The strip pitch is 25 m but only alternate strips are read out, this improves spatial resolution without significant degradation in efficiency or two-hit separation. Figure 2.12 shows a schematic view of the CDF II silicon system, the combined detectors have a total of 772,432 electronic channels and 6 m2 of silicon, making it the largest silicon detector in operation.

Central Outer Tracker (COT) is the 3.1 m long cylindrical drift chamber, which covers the radial range from 40 to 137 cm and provides 96 measurement layers, organized into alternating axial and $\pm 2^\circ$ stereo superlayers. Figure 2.3 shows the tracking region. The COT provides coverage of $|\eta| < 1$. The hit position resolution is approximately 140 μm and the momentum res-

olution is $\sigma(P_T)/{P_T}^2 = 0.0015$ (GeV/c)$^{-1}$.

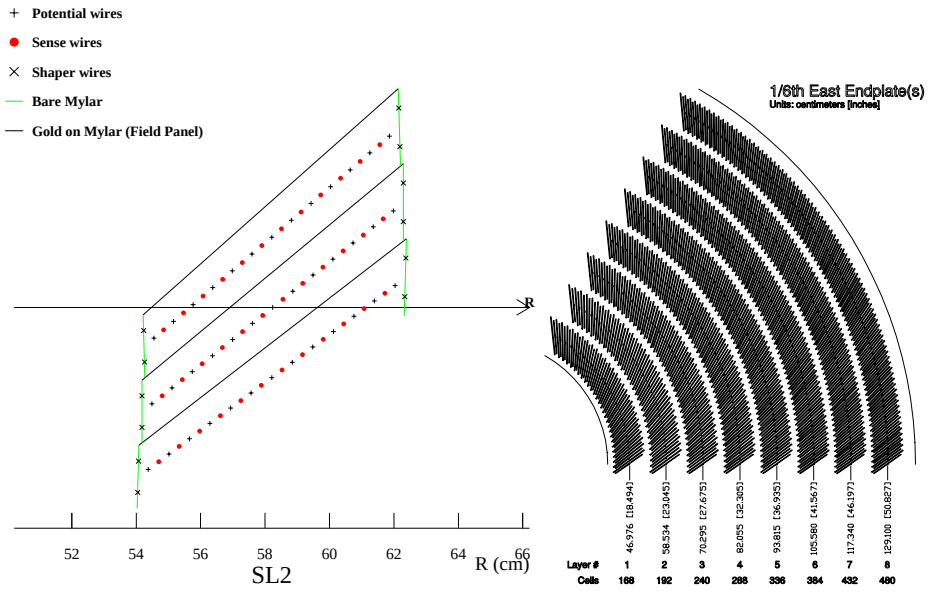

Figure 2.13: Left: Nominal cell layout for SL2. Other superlayers — including stereo — are similar except for the taper. Right: 1/6th view of COT east end-plate

2.3.2 Calorimeter

Outside the solenoid, scintillator-based calorimetry covers the region $|\eta| < 3.0$ with separate electromagnetic and hadronic measurements. The CDF calorimeters measure electron, photon energies and jet energies.

The central calorimeters (and the endwall hadronic calorimeter) cover the pseudo-rapidity of $|\eta| < 1.1(1.3)$ and the plug calorimeters cover $1.1 < |\eta| < 3.6$. It is a scintillator sampling systems with tower segmentation: each tower is 15° in azimuth by about 0.11 in pseudo-rapidity. As seen in Figure 2.14, the calorimeter consists of an electromagnetic (EM) section followed

by a hadronic (HAD) section. The EM sections are all lead/scintillator sampli

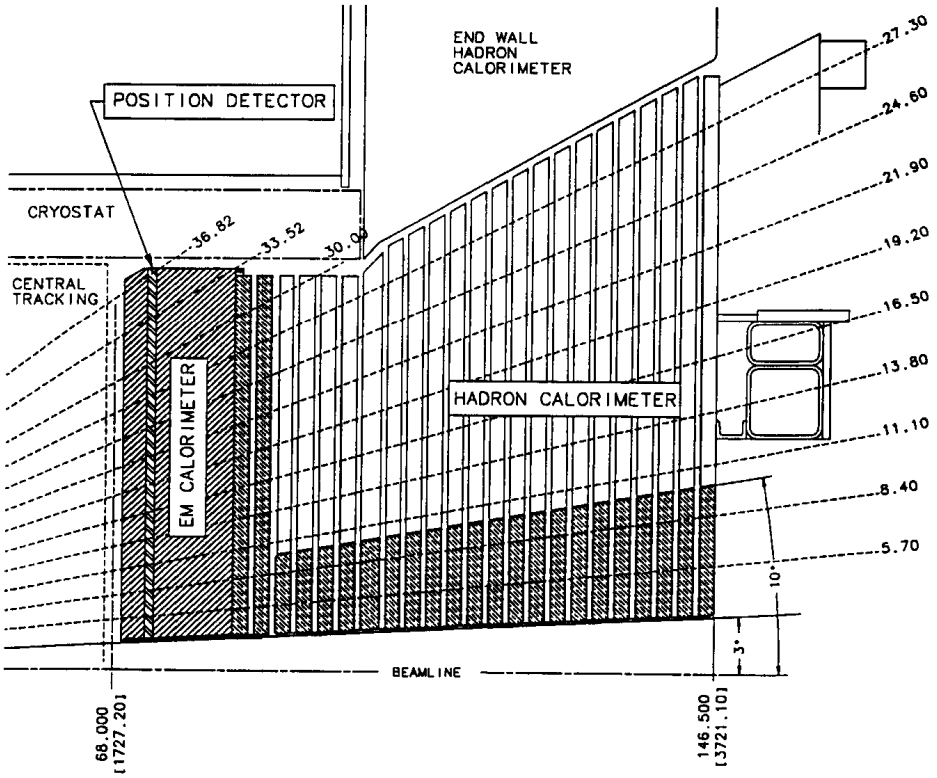

Figure 2.14: Schematic of Towers of the Forward Calorimeter

In both sections the active elements are scintillator tiles read out by wavelength shifting (WLS) fibers embedded in the scintillator. The WLS fibers are spliced to clear fibers, which carry the light out to photomultiplier tubes (PMT) located on the back plane of each endplug. The EM calorimeter is a lead/scintillator sampling device with a unit layer composed of 4.5 mm thick lead and 4 mm scintillator. There are 23 layers in depth for a total thickness of about 21 X_0 (radiation lengths) at normal incidence. The detecting elements are arranged in a tower geometry pointing back towards the interaction region.

The energy resolution of the EM section is approximately $16\%/\sqrt{E}$, where E is in GeV, with 1% constant term. The scintillator tiles of the first layer of the EM section are made of 10 mm thick scintillator and are read out by multi-anode photomultipliers (MAPMTs). They act as a pre-shower detector. A position detector is located at the depth of the EM shower maximum and is made of scintillator strips read out by WLS fibers.

The hadron calorimeter is a 23 layer iron/scintillator sampling device with a unit layer composed of 50 mm iron and 6 mm scintillator. The existing iron of the CDF endplugs is used in the hadron calorimeter: stainless steel disks are attached to the inner 10° cone to extend the coverage to 3°. Two additional stainless steel disks are added behind the electromagnetic section to increase the thickness of the hadron calorimeter. The energy resolution of the hadronic calorimeter is $74\%/\sqrt{E}$ with 1% constant term.

2.3.3 Central Calorimeters

The central region ($0 < |\eta| < 1.1$ or $143° < \theta < 37°$) is the most important to high transverse momentum physics, being at large polar angle with respect to the beamline. For example top pair-production events tend to be central, top and anti-top being produced almost at rest. The central calorimeter (the electromagnetic (CEM) and hadronic (CHA, WHA)) is retained largely unchanged from Run I other than the electronics, new in Run II. Th consists of 2 barrels (one for the positive and one for negative η range) , which are divided azimuthally into 24 wedges, each covering 15° in 15° in ϕ and extending 2.5 m along the beam axis on either side of the detector.

The wedge modules are stacked into four freestanding "C"-shaped arches to allow easy access to the inner components. One module is notched to allow access to the superconducting magnet. This affects tower 9, which is not a full size tower and is not used for election identification in the dilepton analysis. Each wedge module is divided transversely into 10 projective towers, each subtending $\Delta\eta = 0.1$ units in pseudorapidity. Towers are segmented in depth, each depth being read out by separate electronics channels. A CEM module (Figure 2.15) is composed of 31 layers of 3.175 mm thick lead absorber interleaved with 5 mm thick layers of polystyrene scintillator. For each tower there are two wavelength shifters (WLS), one on each side in azimuth η, which guide the green (490 nm) waveshifted light to photomultiplier tubes (PMT). Each tower is read out by 2 PMTs. The signal balance between PMTs allows further determination of η for a single particle to 1° precision. In the Level 1 trigger, the energy is calculated as the average of the two tower energies, while in Level 3 and offline, the tower energy is a geometric mean of the two PMT energies.

The Central Electromagnetic Strip Chamber (CES) (Figure 2.15) is embedded between the eighth lead layer and ninth scintillator layer. It is a proportional wire chamber that measures the positions and the transverse shower shapes of electromagnetic clusters in both r-z and r-ϕ planes. The CES is positioned at the average maximum longitudinal development of an electromagnetic shower, at about 5.9 radiation lengths from the inner radius of the CEM. There are 128 cathode strips that lie perpendicular to the beam direction measuring the z position of the shower. There are 64 anode wires, grouped in pairs, that lie parallel to the proton beam and measure the x coordinate. The position resolution is about 2 mm. The CES also provides

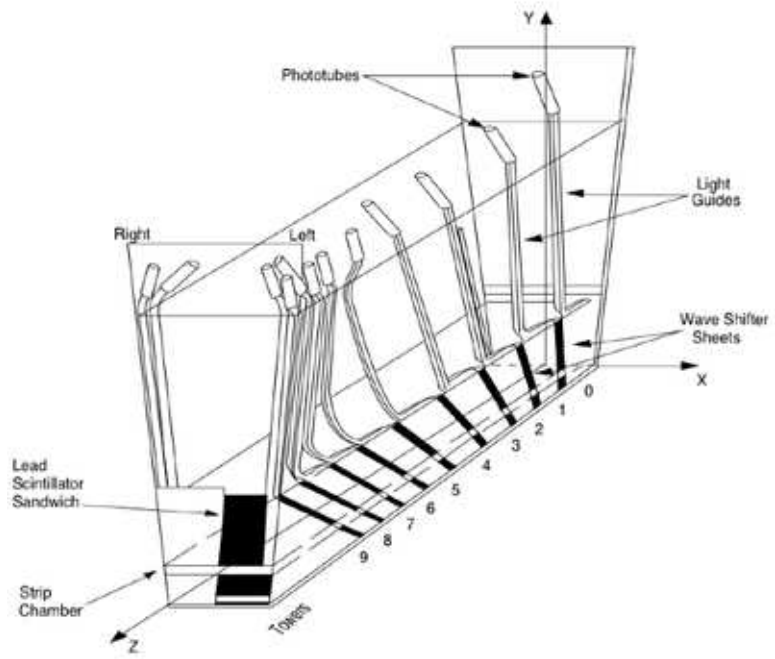

Figure 2.15: A schematic view of one wedge of the Central Electromagnetic Calorimeter (CEM). The Central Electromagnetic Strip Chamber (CES) is embedded at the maximum shower development point. Each wedge module is divided transversely into 10 projective towers.

position information for the identification of photons within particle showers. The detector is mostly unchanged from Run I, but the readout has been modified to accommodate the higher Run II collision rates. The detector has many cracks, or regions with low response. The region -0.05 $< \eta <$ 0.05 near the 90° crack where the detector halves meet, is not used, as the chambers are not fully efficient near the edges. This result in a loss in acceptance of about 5.0 %. For the same reason the showers with a distance less than 1° from ϕ boundary between wedges are not considered. This translates into the requirement that the CES wire cluster closest to the extrapolated electron track be located at less than 21 cm from the center of the strip chamber in the r-ϕ plane. The

loss in the acceptance is $24 \times 2^\circ$ / $360^\circ = 13.3\%$. Also the region $0.82 < \eta < 1.0$, $75^\circ < \phi < 90^\circ$ is explicitly excluded as it is uninstrumented. This is known as *chimneymodule* and is the access point for the cryogenic supply of the superconduction coil. The loss is 0.4 %. The total acceptance loss due to the fiducial requirements is 18.7 % od the geometrical acceptance for the central electron.

The Central Pre-Radiator (CPR) is situated in the gap between the solenoid coil and CEM, at a radius of about 168.0 cm [30]. It is a single plane of multi-wire proportional chamber with 32 sense wires running along the beam direction, providing 32 readout channels per wedge. The readout is split between two chambers, 16 channels at low z (7.9 cm $< |z| <$ 119.7 cm) and 16 channels at high z (123.5 cm $< |z| <$ 235.3 cm). It provides the measurement of the x coordinate only. CPR provides very good differentiation between electrons and minimum ionizing particles, like muons of hadrons. It allows helps to identify electrons from conversion ($\gamma \rightarrow e^+e^-$), taking place inside the coil. However CPR information is not used in this analysis.

2.3.4 Muon Detector

The muon system resides outside the calorimetry. Four layers of planar drift chambers, the Central Muon detector (CMU), detect muons with $P_T >$ 1.4 GeV/c which penetrate the five absorption lengths of calorimeter steel. An additional four layers of planar drift chambers, the Central Muon Upgrade detector (CMP), instrument 0.6 m of steel outside the magnet return yoke and detect muons with $P_T > 2.0$ GeV/c.

The CMU and CMP chambers each provide coverage in the pseudo-

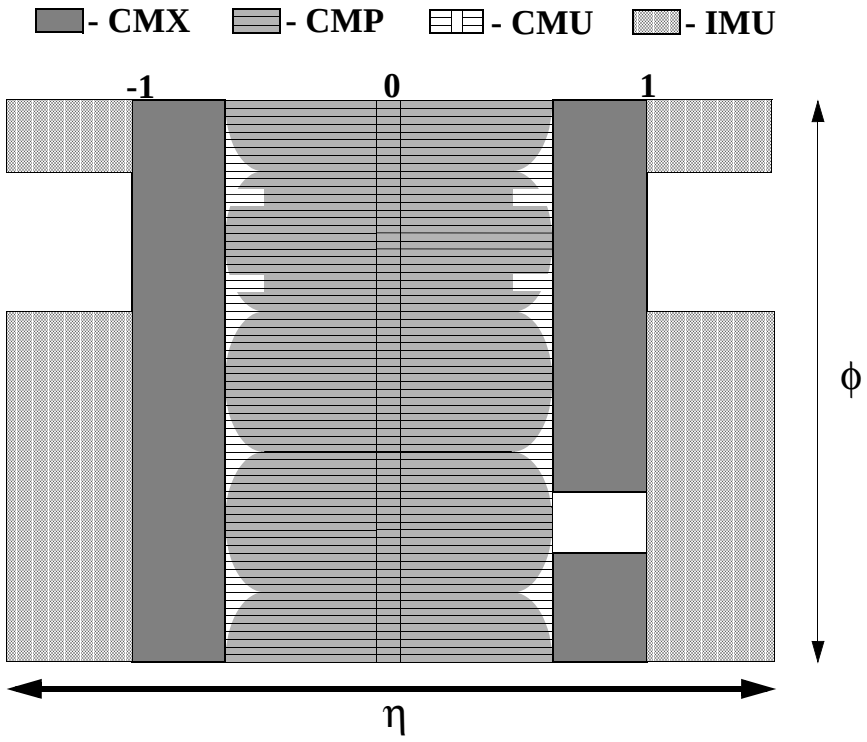

Figure 2.16: The muon components coverage in azimuth ϕ and pseudo-rapidity η.

rapidity range $|\eta| < 0.6$. The Central Muon Extension detector (CMX) covers the range $0.6 < |\eta| < 1.0$. The Intermediate Muon detectors (IMU) are covering the region $1.0 < |\eta| < 1.5$. The IMU provide coverage sufficient to identify isolated high P_T tracks as muons or hadrons. The IMU consists of a barrel of drift chambers and scintillation counters around the toroid steel, with additional counters between the toroids and on the endwall to provide additional projectivity at the trigger level. The IMU counters are virtually identical to the existing central muon detectors and use the same readout electronics.

2.4 Triggers and Data Acquisition

2.4.1 Trigger System

The trigger plays an important role in hadron collider experiments because the collision rate isl to the crossing rate of 7.6 MHz while the tape writing speed will be less than 50Hz The role of the trigger is to efficiently extract the most interesting physics events from the large number of minimum bias events. For example, the total $t\bar{t}$cross section is approximately nine orders of magnitude smaller than the minimum bias cross section.

Due to changes in the detector and the accelerator the entire trigger system used in run must be replaced for run II The primary reason for replacing the trigger electronics along with all CDF front-end electronics, is the reduction in the accelerator bunch spacing from 3.5 μsec to 132-396 nsec. In the past, trigger signals from the calorimeters were sent to the control room, where they were processed, with the trigger decision sent back to the detector before the next beam crossing. As a result, the data from only one crossing needed to be stored on the detector. In run II there will not be enough time to send detector signals to the control room between bunch crossings, let alone make a trigger decision and distribute it back to the detector. In addition most of the old trigger is incompatible with new or upgraded detector elements.

The trigger and data acquisition systems are designed to accommodate the high rates and large data volume of Run II. Trigger systems of CDF consists of three level triggers and the data is decreased by progressing to the next level. Figure 2.17 shows the functional block diagram of the readout electronics. To accommodate 132 ns bunch-crossing time and a 4 μs decision time for the first trigger level, all front-end electronics are fully pipelined, with on

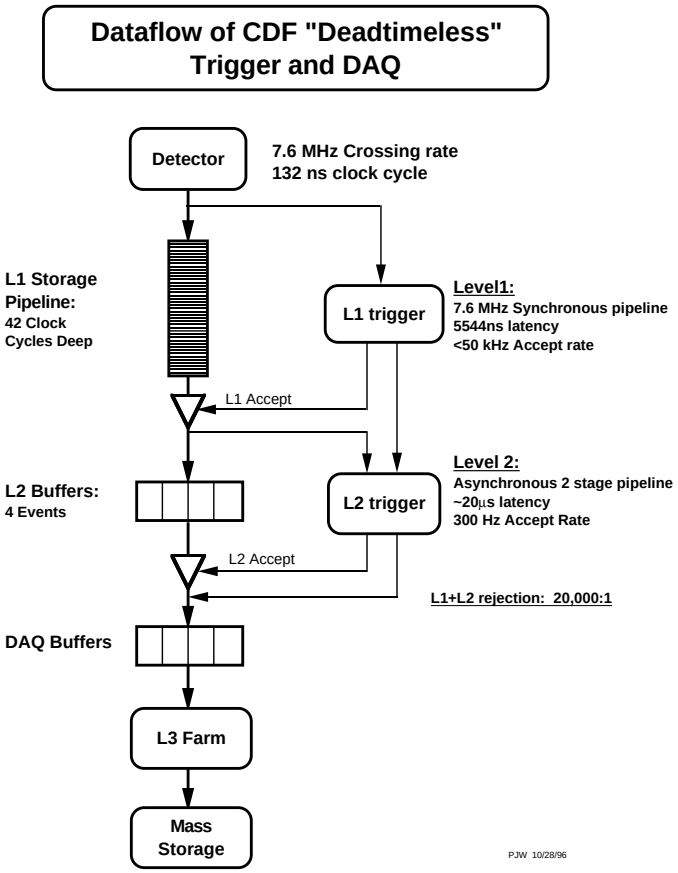

Figure 2.17: Functional block diagram of the CDF II data flow.

board buffering for 42 beam crossings. Data from the calorimeters, the central tracking chamber, and the muon detectors are sent to the Level 1 trigger system, which determines whether a $p\bar{p}$ collision is sufficiently interesting to hold the data for the Level 2 trigger hardware.

The Level 1 trigger is a synchronous system with a decision reaching each front-end card at the end of the 42-crossing pipeline. Upon a Level 1 trigger accept, the data on each frontend card are transferred to one of four local Level 2 buffers. The second trigger level is an asynchronous system with an average decision time of 20 μs. Data are collected in DAQ (Data Acquisition system) buffers and then transferred via a network switch to a Level 3 CPU node, where the complete event is assembled, analyzed, and, if accepted, written out to permanent storage.

CDF II uses a tiered "deadtimeless" trigger architecture. An event is considered sequentially at three levels of approximation, with each level providing sufficient rate reduction for the next level to have minimal deadtime. Level 1 and Level 2 use custom hardware on a limited subset of the data and Level 3 uses a processor farm running on the full event readout. The trigger, like the DAQ, is fully pipelined. The block diagram for the CDF II trigger system is presented in Figure 2.18. Events accepted by the Level 1 system are processed by the Level 2 hardware. The Silicon Vertex Tracker (SVT) provides the ability to trigger on tracks with large impact parameters. The Level 2 system has improved momentum resolution for tracks, finer angular matching between muon stubs and central tracks, and data from the central shower-max detector (CES) for improved identification of electrons and photons. Jet reconstruction is provided by the Level 2 cluster finder. The output of the first level of the trigger is used to limit the rate for accepted events to roughly

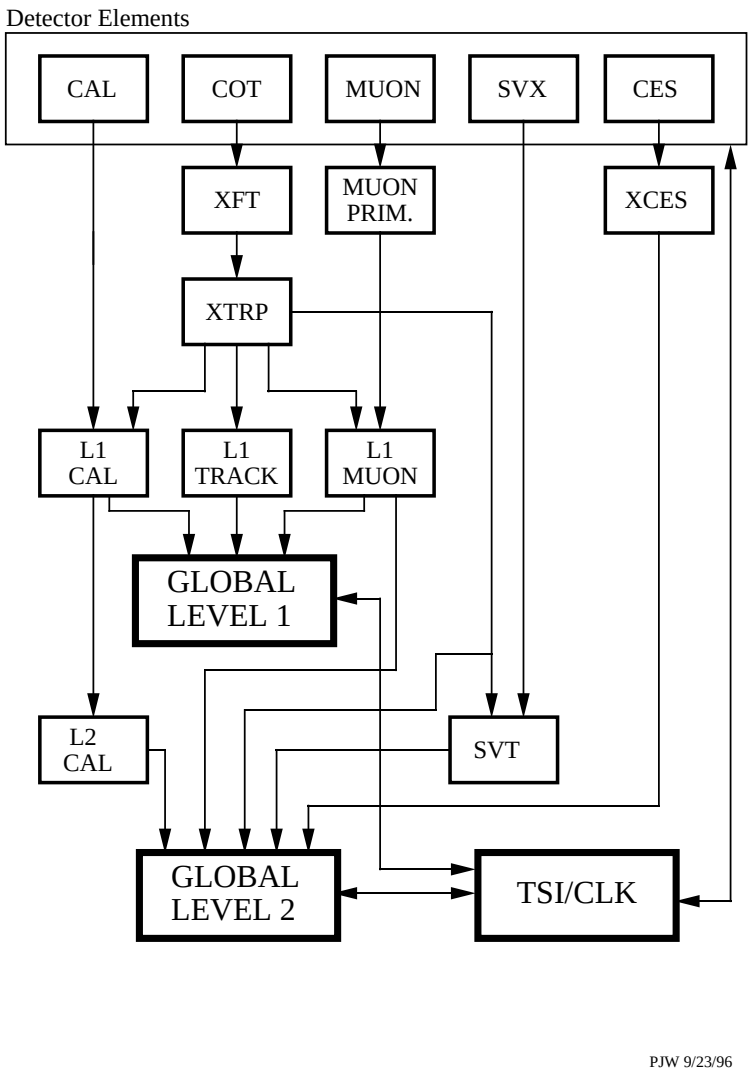

Figure 2.18: Block diagram of the CDF II trigger system.

18 kHz at the luminosity range of $3 - 7 \times 10^{31}\text{cm}^{-2}\text{s}^{-1}$. At the next trigger stage, the rate is reduced further to around 300 Hz. The third and final level of the trigger, with access to the complete event information, uses software algorithms and a computing farm, and reduces the output rate to around 75 Hz, which is written to permanent storage.

Chapter 3

Dilepton Event Selection

3.1 Data Sample and Luminosity

The results presented in this note are obtained by using data collected by CDF from December 2004 to June 2009 and reprocessed with version 6.1.4 of the CDF reconstruction software. For the MC samples, we use events generated with version 6.1.4mc patch "c" in the run range 141544 < run < 277511. This toespond to the 5.1 fb^{-1} of data taking. Physics objects like electrons, muons, jets and missing transverse energy are as defined by the TopEventModule selection code [39] and saved in "topNtuple" format both for data and Monte Carlo events [51] [54].

The data are collected either via the central high p_T electron (`bhelX`, where X = 0d, 0h, 0i, mi, mj, mk or mm) or muon (`bhmu0X`) trigger paths. For this version of the analysis we decided to ignore events triggered by a plug electron plus missing energy (`bpel0X`) as they contributed only a small percentage of the total acceptance ($\sim 4.5\%$) and required an ad-hoc treatment

of the trigger efficiency.

We impose that the events pass the version 31 of the good run list, obtained with bits (1,0,4,1) [40]. This version of the good run list, which includes partially recovered runs, ensures that the CDF detector was in good running condition both for CEM electrons and for CMUP muons. The good silicon requirement slightly reduces the luminosity of our samples and is used when a Phoenix plug electron is reconstructed in the event. The data samples used in this analysis are described in Table I. We use "5.1fb^{-1} " (4.8 fb^{-1} on $b-$tagging) of data.

Data Sample	Low Run	High Run	Luminosity, pb^{-1}	Lumi. with Si, pb^{-1}
Through period 17	141544	261005	2825.95 ± 169.56	2676.13 ± 160.57
period 18	261119	264071	402.03 ± 24.12	304.88 ± 18.29
period 19	264101	266513	208.10 ± 12.49	206.98 ± 12.42
period 20	266528	267718	248.17 ± 14.89	226.92 ± 13.62
period 21	268155	271047	441.05 ± 26.46	435.59 ± 26.14
period 22	271072	272214	268.69 ± 16.12	265.67 ± 15.94
period 23	272470	274055	203.74 ± 12.22	200.65 ± 12.04
period 24	274123	275848	264.68 ± 15.88	252.06 ± 15.12
period 25	275873	277511	227.37 ± 13.64	211.47 ± 12.69
All data (5.1 fb^{-1})	141544	277511	5089.78 ± 305.39	4780.35 ± 286.82

Table I: Run ranges and luminosity for various data taking periods. All of the above luminosities includes the correction factor of 1.019 ± 0.060 [42].

For Monte Carlo events, we use only events for runs in the good electron SI run list, i.e. obtained with bits (1,1,0,1). We also restrict any Monte Carlo

acceptance calculation to events with run $\geq$ 150145, as the CMX detector was not fully functional before that time.

3.2 Event Reconstruction

This chapter describes the reconstruction of physics objects for a proton-antiproton collision, referred to as an event. The Run II reconstruction package uses the C++ Object Oriented programming language(1), and is constructed from a number of independent software modules, each handling the data from a subdetector. Each module communicates with the others through an interface. The modules are executed *sequentially*, in an order specified at run-time, in a tcl file(2). The behavior of a module can also be controlled at run-time through a number of parameters. The logical flow of event reconstruction in CDF is shown in 4.1. The reconstruction process starts with the raw data recorded by the CDF detectors. Then the calibration constants, noise suppression and various corrections are applied, before proceeding to construct higher-level objects, such as Electrons, Muons, Jets or Missing Energy.

3.2.1 Energy reconstruction

The calorimeters are used to measure the electron, photon, jet and net transverse energies. The raw energy in the calorimeter to a calorimeter electronic channel. The wavelength shifters convert the blue scintillator light into green wavelengths which have a larger attenuation length. The green light is transported to the photomultiplier tube via clear light guide bars in the central calorimeters and plastic optical fibers in the plug calorimeters. For each central calorimeter tower, there are two PMTs. For each physical plug

calorimeter tower, there is only a single EMT, The ADC counts are converted to energy (GeV), using detector dependent scale factors, determined using either the test beam data or specific data samples collected during special runs. During the calibration runs, problem channels, such as dead or hot ones, are identified and processed separately For each event, an $\eta - \phi$ array of tower energies is obtained, after the noisy channels are suppressed and spurious sources of energy are properly removed. this $\eta - \phi$ array is used to construct an array of transverse energies, E_T, using the polar angle θ of each tower center, with respect to the event's primary vertex. The event vertex is determined by extrapolating the particle tracks back to the beamline, the details for which are given later in this chapter. The transverse energy in a tower is $E_T = Esin(\theta)$, where E is the energy measured in the tower.

There are two C++ classes of towers in the CDF software, CalTower and PhysicsTower, The CalTowers are the raw experimental towers, i.e. they contain the information that was read by the photomultiplier tubes, while the PhysicsTowers have their transverse energies calculated from a specific vertex and have a four vector associated to them. Therefore, a CalTower will contain, in particular, the energy information , but not the E_T information, which depends on the vertex knowledge. On the other hand, a PhysicsTower will contain the E_T information, and will also have a 4-momentum vector associated to them. The CalTowers are used to create the PhysicsTowerData) from Monte Carlo particles or just plain four-vectors. The electromagnetic and hadronic ET in each tower of the CDF detector can be accessed using an integer representation $(ieta, iphi)$ for the $\eta - \phi$ segmentation of the detectors. There are 9 types of towers in the calorimeter, depending on the rapidity of the tower. the classification of the TowerType is based upon:

1. The number of detectors per tower, e.g. TowerType 1 has CHA and WHA detectors, while TowerType 0 has only a CHA hadronic detector.
2. Different (η, ϕ) granularity of the towers.

The table 4.1 summarizes the characteristics of the tower types [31]. The correspondence between η and IETA is given in the Table 4.2. The tower with IPHI = 0 starts at $\phi = 0$ and IPHI increase as the azimuthal coordinate ϕ. The segmentation in phi depends on the tower type, as shown in Table 4.1.

3.2.2 Track reconstruction

Track reconstruction in CDF is performed using the information provided by the tacking detectors, which are placed in magnetic field. Via curvature, one can determine the charged particle momenta and discriminate between positively and negatively charged particles. The neutral particles do not have traces in the tracking detectors. The algorithms used to reconstruct the tracks depend on the tracking detectors used (COT-only, Silicon-only or both), on the pseudorapidity region (central region, with $—\eta— < 1.0$ or forward region) and on the requirement that the track finding is seeded (4) or not. Thus, the following tracking algorithms were developed in CDF.

• COT-only: histogram tracking (HL) [32] and segment linking tracking (SL) [33]

• Silicon-only: standalone tracking [34] and Phoenix tracking (PHX) [35], the last used only in the forward region, for electrons only;

• COT+Silicon: outside-in [36] and inside-out [37].

IETA(E +)	IETA(W -)	$\mid \eta \mid$ range
26	25	-0.0000-0.1308
27	24	0.1308-0.2595
28	23	0.2595-0.3841
29	22	0.3841-0.5033
30	21	0.5033-0.6162
31	20	0.6162-0.7226
32	19	0.7226-0.8225
33	18	0.8225-0.9160
34	17	0.9160-1.0036
35	16	1.0036-1.1000
36	15	1.1000-1.2000
37	14	1.2000-1.3170
38	13	1.3170-1.4153
39	12	1.4153-1.5231
40	11	1.5231-1.6426
41	10	1.6426-1.7770
42	9	1.7770-1.9311
43	8	1.9311-2.1119
44	7	2.1119-2.3313
45	6	2.3313-2.6113
46	5	2.6113-3.0001
47	4	3.0001-3.6425

Table II: The correspondence between η and IETA.

For this dilepton cross section measurement, $COT-onlytrack$ are used in the central region of the detector, a combination of histogram and segment linking, hit-based, unseeded algorithms; in the forward region, Phoenix tracking, a seeded algorithm, is used. The usage of COT-only tracks in the central region, without silicon information, was preferred, because over time, various beam incidents limited the performance of the silicon detectors. In both cases, to get the reconstructed tracks, a three-dimensional, five parameter fit to a track-helix is performed. Each track is characterized by five track parameters, described below.

• curvature: the 2-D curvature of the track, transverse to the beamline, which is inversely proportional to the transverse momentum, p_T, of the track.

• d_0, impact parameter: the distance of closest approach of the track to the interaction vertex, in the transverse plane.

• cotθ: the cotangent of the polar angle θ.

• z_0: the z coordinate of the point of the closet approach of the track to the interaction vertex, in the transverse plane.

• ϕ_0: the ϕ direction of the track at the point of closest approach.

In the thesis, all track parameters, but cotθ, are used in identification of various objects. The details of the tracking algorithms used in this paper are discussed next.

3.2.3 The COT Pattern Recognition Algorithm

The track reconstruction starts from the hits in the tracking chamber. Then a pattern recognition algorithm[2] is used, in the following order:

• Find the track segments for axial and stereo superlayers: First, the 3-hits from consecutive wires are used to make segment seeds. All good segment seeds from an initial hit are used to make segment seeds. All good segment seeds from an initial hit are used to search for hits on the remaining wires, and only the best segment, with the largest number of his, associated with a hit, is kept.

• Link the axial segments in $r-\phi$ track: The axial pattern recognition consists of two algorithms, Segment Linking (SL) and Histogram Linking (HL), which complement each other very well, to give a high reconstruction efficiency. The axial SL links the axial superlayer segments into 2-D tracks, in $r-\phi$ plane. HL begins from a seed segment position and the beam position, and histograms the hits from the other superlayers as a function of the curvatures. Therefore, the hits corresponding to a track will lie in the same bin and are identified as part of a track.

• Attach the stereo information to make $3-d$ tracks: The stereo pattern recognition consists of two steps: Segment Linking and Hit Linking. The first one, Segment Linking consist of attaching stereo segments to 2-D axial tracks. Once this is done, the event vertices are reconstructed using z_0 of the event tracks. Hit Linking uses the vertices as seeds to try associating stereo hits to axial tracks which failed the Segment Linking step. At the end, a full 3-D 5-parameter fit is performed for the tracks with at least 2 stereo and 12 axial hits.

3.3 Lepton identification

3.3.1 Electron identification variables

We select an electron using the baseline cuts accepted by the Electroweak/Top groups. The variables used to identify an electron are almost identical(except for leakage corrected isolation) with the ones used in Run I:

- E_T :

The transverse electromagnetic energy deposited by the electron in the CEM(central electromagnetic calorimeter) is calculated as the electromagnetic cluster energy multiplied by $\sin(\theta)$, where θ is the polar angle provided by the best COT track pointing to the EM cluster. An electron cluster is made from a seed EM tower and at most one more shoulder tower, passing some well defined requirements. The maximum cluster size could have two towers in pseudorapidity ($\Delta\eta = 0.3$) and one tower in azimuth ($\Delta\phi = 0.1rad$).

- P_T :

The transverse momentum of the COT beam constrained track as measured using the COT track curvature in the magnetic field.

- E_{had}/E_{em} :

(CEM) calorimeter energy for a cluster.

- E/P :

The ratio of the EM cluster transverse energy to the COT track transverse momentum.

• L_{shr} :

The lateral shower profile for electrons. This variable compares the energy in CEM towers adjacent to the seed tower for data and test beam electrons.

• Q * Δx :

The distance in the r-ϕ plane between the extrapolated, beam constrained, COT track and the best matching CES cluster, multiplied by the lepton charge.

• Δz :

The distance in the r-z plane between the extrapolated, beam constrained, COT track and the best matching CES cluster.

• ${\chi^2}_{strip}$:

The χ^2 comparison of the CES shower profile in the r-z view with the same profile extracted from test beam electrons

• z_0 :

The z intersection of the track with the beam axis in the r-z plane. The electron associated track must have passed through at least3 axial and 3 stereo superlayers (SL), each with at least 7 hits out of 12.

Variable	cut
E_T (two-tower Em sum $*\sin(\theta)$ of track)	> 20 GeV
P_T (COR-only beam-constrained track)	> 10 GeV
Fractional Calorimeter Isolation E_T (with PJW leakage Correction)	< 0.1
E/P (for $E_T < 50$ GeV only)	2.0
Track $\lvert z_0 \rvert$	< 60.0 cm
E_{had}/E_{em}	$< 0.055 + 0.00045 * E$
$Lshr$ (using track-based strip cluster, z_0 of track)	< 0.2
charge-signed $\lvert \Delta X \rvert$	-3.0 $< Q_{track} * \Delta X <$ 1.5 cm
$\lvert \Delta z \rvert$	< 3.0 cm
χ^2_{strip}	< 10
Track Type	PADtrack
COT track quality	≥ 3 axial and ≥ 3 stereo SL with > 6 his each
Fiducial	Fidele = 1 (Ces $\lvert X \rvert < 21$ cm, $9 < Ces \lvert Z \rvert < 230$ cm, Tower 9 excluded, most of tower next to chimney included)

Table III: Top Dilepton identification electron selection. Also these selection cuts define a tight electron in DY $\rightarrow e^+e^-$ cross-section measurement

3.3.2 Muon identification variables

The muon id cuts are listed in (Table IV)

• P_T :

The transverse momentum of the COT beam constrained track as measured using the COT track curvature in the magnetic field.

• E_{HAD}, E_{EM} :

The energy the muon candidate deposits in the hadronic, respectively electromagnetic part of calorimeter.

• Q * Δx :

The distance in the r-ϕ plane between the extrapolated track and the muon stub at the chamber radius.

• z_0 :

The muon track impact parameter. If the track has or not silicon hits, the cuts are looser, respectively tighter.

3.4 Event Selection

The DIL selection aims at reconstructing $t\bar{t}$ events with both W's from top decaying leptonically. It requires two fully identified electrons or muons with transverse energy above 20 GeV, $\not\!\!E_T > 25$ GeV and at least two tight jets of $E_T > 15$ GeV. The first, or trigger lepton can be one of three types:

Variable	cut
P_T (COR-only beam-constrained track)	$>$ 20 GeV
Track $\lvert z_0 \rvert$	$<$ 60.0 cm
Cosmic Ray Removal	Cosmic Ray Tagger
E_{had}	$<$ 6 + max(0,0.028 $*$ (p - 100)) GeV
E_{em}	$<$ 2 + max(0,0.0115 $*$ (p - 100)) GeV
Track $\lvert d_0 \rvert$	$<$ 0.02 cm (if track has Si hits) OR $<$ 0.2 cm (if not)
$\lvert \Delta x_{CMU} \rvert$	$<$ 3.0 cm
$\lvert \Delta x_{CMP} \rvert$	$<$ 5.0 cm
$\lvert \Delta x_{CMX} \rvert$	$<$ 6.0 cm
Track Type	PADtrack
COT track quality	$\geq$ 3 axial and $\geq$ 3 stereo SL with $>$ 6 his each

Table IV: Top Dilepton identification muon selection.

CEM electron, CMUP or CMX muon. The second, or loose lepton, can be also non-isolated or an isolated PHX electron or one of the non-trigger muon types: CMU-only, CMP-only and CMIO. Details on the cuts used to identify each lepton category are contained in [43]. Non isolated counterpart of the trigger leptons (i.e. NICEM electrons and NICMUP/NICMX muons) are allowed to trigger the event when they come together with a PHX electron to recover most of the acceptance lost by dropping the plug electron dataset.

The jets are corrected up to hadron level (i.e. up to Level 5) using version "JetCorr06b" of the JetUser module. Unlike previous versions of the DIL analysis, the "Multiple Interactions" or level 4 jet correction is now applied to each event on the basis of the number of good (i.e. quality 12 or higher) z-vertexes in the event. We should mention here that for the purpose of correcting $\not\!\!E_T$ (which is calculated starting from the raw transverse energy deposited in each tower of the calorimeter), we used the jet energy scale calculated ignoring the level 4 correction order to avoid over-correcting $\not\!\!E_T$ for the presence of energy due to extra interactions.

Extra event topology cuts are imposed to improve the purity of the selection:

- Z-veto for ee and $\mu\mu$ events with reconstructed dilepton invariant mass in the 76-100 GeV windo. See details below.

- L-cut in the ($\not\!\!E_T$, $\delta\phi_{min}$) plane to reject Z$\rightarrow \tau\tau$ events and events with mis-measured $\not\!\!E_T$ from jets pointing to cracks in the calorimeter: this cut requires the event $\not\!\!E_T$ to be above 50 GeV is there is any lepton or jet inside 20° of the $\not\!\!E_T$ direction.

- $H_T > 200$ GeV cut to suppress events from an initial state lighter that

$t\bar{t}$

- opposite charge for the two leptons.

The main change between this and previous versions of the DIL selection has been an optimization of the Z-veto cut. Since the 750 pb^{-1} result, we used a Z-veto based on JET significance. JET significance was defined as:

$$JetSig = \frac{\not\!\!E_T}{\sqrt{\sum_i E_{T_i} \cdot \hat{\not\!\!E_T}}} \tag{3.1}$$

where $\hat{\not\!\!E_T}$ is the direction of the corrected $\not\!\!E_T$ and E_{T_i} are the transverse energies of tight jets in the same hemisphere as the $\not\!\!E_T$. An $ee/\mu\mu$ event inside the Z window region was rejected if $JetSig < 8 sqrt GeV$.

As it follows from the JetSig definition, the Z-veto was applied only to events with at least one jet and, even then, only when at least one of the jets in the event was in the same hemisphere of the $\not\!\!E_T$. The idea behind this variable was to penalize events with fake $\not\!\!E_T$ coming from a jet pointing to non-instrumented region of the calorimeter. But its definition made it very hard to plot this variable for all the events and gave one less handle against Drell-Yan rejection for events in the 0-jet control bin. It also made very hard to intuitively predict the effects of a variable which is not only rejecting events based on the magnitude of the missing energy but also on its direction with respect to the jets.

We decided to study the effect of using a more standard Z-veto based on the significance of the missed transverse energy in the event. We defined MET Significance as:

$$MetSig = \frac{\not\!\!E_T}{\sqrt{E_T^{sum}}} \tag{3.2}$$

where E_T^{sum} is the sum of transverse raw energies deposited in all calorimeter towers, corrected for any muon P_T and for the difference between the raw and the non-lv4 corrected energy of tight jets in the event. We find that a cut on $MetSig > 4sqrtGeV$ reduce the background by $\sim 25\%$, mostly in the Drell-Yan channel (which was the dominant background source in 750 pb^{-1} analysis) and reject $\sim 5\%$ of the $t\bar{t}$ events, slightly improving the overall $S/\sqrt{B}$ with respect to the JetSig cut [45].

Other minor technical changes between the previous and the present DIL analysis are listed here:

- Larry correction and plug energy corrections are applied during the generation of the "topNtuple".
- the cut for the track-stub matching distance for CMU Δx_{CMU} has been loosened from 3 cm to 7 cm. This affects both CMUP and CMU muons.
- no stubbed CMIO muons are allowed. Minikey/Keystone muons for run $\geq$ 190697 are considered good CMX muons.
- categories triggered by the PHX electrons, i.e. events with a PHX electron plus a loose non-trigger muon (CMU, CMP or CMIO), are dropped.

The Drell-Yan background from Z^0 decays dominates the dielectron and dimuon envents after the lepton ID and isolation cuts. We remove a large fraction of such backgrounds simply by requiring that the invariant mass of the ee or $\mu\mu$ pairs lies outside the Z^0 mass window: 75 GeV $\geq M_u \geq$ 106 GeV. This cut will be probably removed/replaced in the near future, because we loose 200 % of $t\bar{t}$ events

3.4.1 Isolation cut

Each dilepton event is required to have at least two isolated leptons. For electrons we use the calorimeter leakage corrected isolation fraction (cone R=0.4) $I_{cal} < 0.1$.

Once the lepton isolation cuts are passed, we can categorize the dilepton events based on the lepton types passing the previous cuts, as in Table 4. Requiring that both leptons be isolated we reject the most of the leptons coming from a semileptonic b decay, so the $b\bar{b}$ background is insignificant.

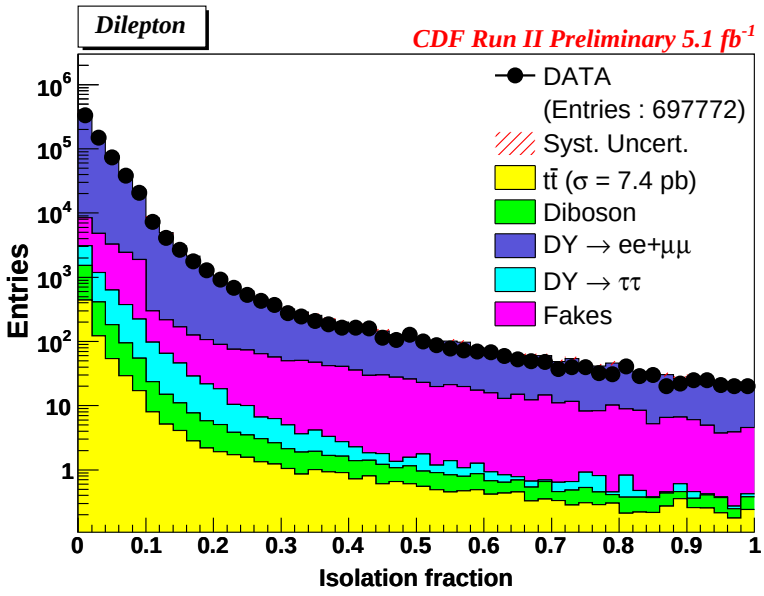

Figure 3.1: Isolation fraction distribution for data and Monte Carlo simulation.

3.4.2 $\not\!\!E_T$ cut

The undetected neutrinos in a $t\bar{t}$ dilepton event will generate large miss-

ing transverse energy ($\not\!\!E_T$). The raw $\overrightarrow{\not\!\!E_T}$ is a 2 dimensional vector ($\not\!\!E_{T\ x}$, $\not\!\!E_{T\ y}$), in the xy transverse plane, equal to the negative of the vector sum of all the transverse energy in calorimeter. We make a cut on the magnitude of $\overrightarrow{\not\!\!E_T}$, denoted as $\not\!\!E_T$. We make the following three corrections to raw $\not\!\!E_T$.

• Primary vertex correction: The raw missing energy stored in CdfMet bank assumes that the events primary vertex is z = 0; we find the primary vertex for the event (for dilepton events we use the z_0 of the highest transverse energy lepton in the event) and then recalculate ($\not\!\!E_{T\ x}$, $\not\!\!E_{T\ y}$).

• Muon correction: The muons are minimum ionizing and they deposited very little energy in the calorimeter; therefore we add back to ($\not\!\!E_{T\ x}$, $\not\!\!E_{T\ y}$) the transverse energy deposited in the calorimeter and subtract the muon transverse energy, (P_{Tx}, P_{Ty}). We correct only for tight muons, passing the id cuts; these could be CMUP, CMP, CMU or CMX.

• Jet correction: In Run I we corrected $\not\!\!E_T$ for change in the raw jet energies after applying the relative corrections only: we apply the same correction for the current study; this is very important for some of the backgrounds($Z \rightarrow \tau\tau$ for example)

3.4.3 "L" cut

The "L" cut is introduced to reject the $Z \rightarrow \tau\tau$ background. This cut removes the events with $|\not\!\!E_T| < 50$ GeV, if the $\not\!\!E_T$ is too close to either a

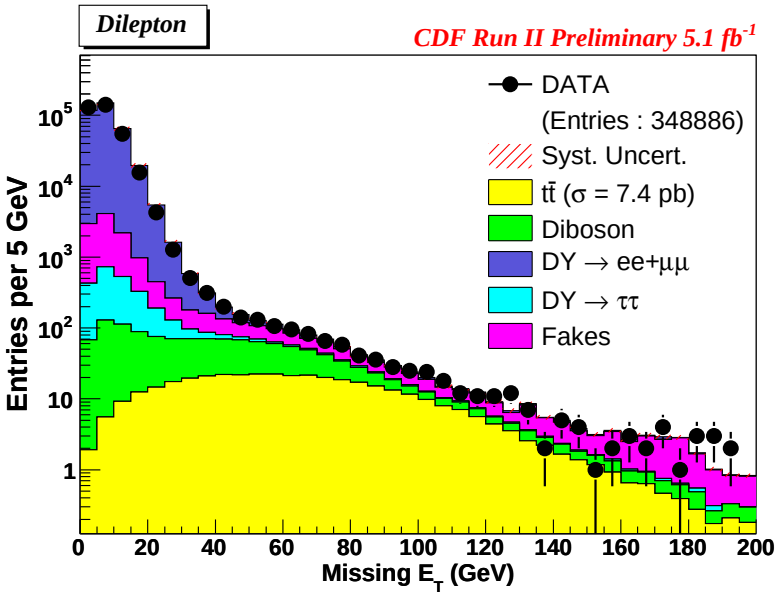

Figure 3.2: $\not\!\!E_T$ distribution for data and Monte Carlo simulation.

lepton or a jet, explicitly $\Delta\phi(\not\!\!E_T$, nearest ℓ or jet) $< 20^o$. This requirement consists of two angular constraints: the angle between the $\not\!\!E_T$ and closest lepton and the angle between the $\not\!\!E_T$ and the nearest jet. The reason both are used is as follows:

• The DY background events have no physical missing energy. The common way fake $\not\!\!E_T$ is "created" is due to a jet being badly measured or lost in the detector crack. So requiring a good separation between $\not\!\!E_T$ and the nearest jet is a very efficient way to reject the DY.

• The $\Delta\phi(\not\!\!E_T$ nearest lepton) cut was used in Run I mainly to reject dilepton from di-tau events and it was preserved for historical reasons.

3.4.4 At least 2 Jets requirement

The dilepton $t\bar{t}$ process give rise to 2 b quarks (a b and a $\bar{b}$), which after fragmentation and hadronization, form streams of particles referred as jets. Extra jets could be produced due to parton showering process. So we ask for at least two jets with $E_{Traw} > 10$ GeV and $|\eta_{detector}| < 2.0$. The detector has cracks and we only reconstruct a fraction of the b energies. Therefore the jets have to be corrected for this any many other effects: (1) calorimeter non-linearities (2) reduced calorimeter response at the tower boundaries (3) loss of low momentum particles inside the magnetic field (4) energy deposited outside the clustering cone (in our case 0.4) (5) contribution from underlying event (beam remnants) of multiple interactions (6) energy loss due to muons or neutrinos (semileptonic decays).

3.4.5 H_T requirement

This variable is a measure of the energy flow in the transverse plane of $p\overline{p}$ collision direction. H_T is currently defined as:

$$H_T = \Sigma E_T(P_T)\ tight\ leptons + \not\!\!E_T + \Sigma E_T\ tight\ jets$$

Note that here the $\not\!\!E_T$ is corrected as described above, the corrected E_T is used in the sum for those leptons passing the id and iso cuts and the corrected jet E_T is used for the jets passing the *tight jet* definition ($E_T^{raw} >$ 10.0 GeV and $|\eta_{detector}| < 2.0$ GeV).

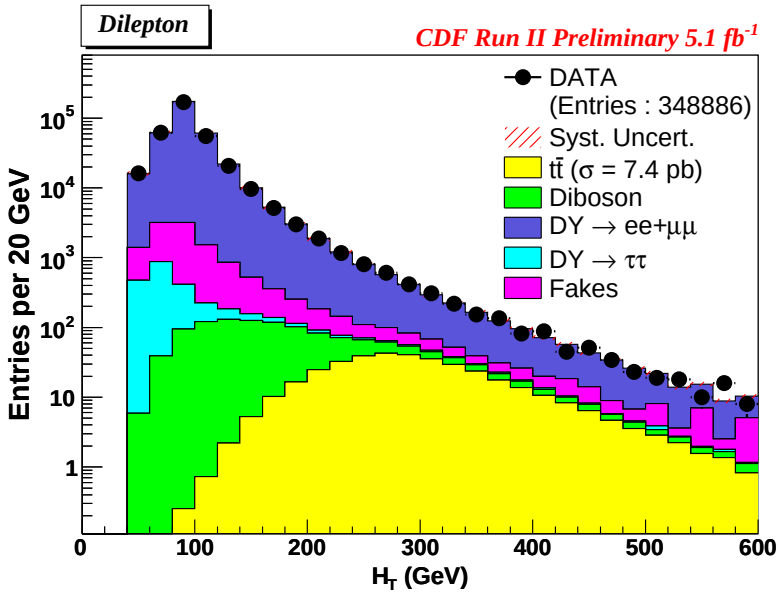

Figure 3.3: H_T distribution for data and Monte Carlo simulation.

3.4.6 Opposite Sign cut

The leptons in a dilepton event are required to have opposite charge. this reduces the fake dilepton background. The same-sign dilepton events have one lepton from a W decay and the other from a semileptonic b decay. In Run II a "trident" is not flagged as a conversion anymore, to reduce the over-efficiency of the conversion find. Therefore the charge of the trident (coming from the highest P_T track) is wrong in some cases and we need to use the curvature of each trident tracks to get the "trident charge" right. This is not available in the software code for the moment.

3.4.7 Cosmic ray removal

We tried applying the Cosmic Ray Removal, but it has a large over-efficiency. The default cuts were tuned using W's and Z's only and this might not be appropriate for a $t\bar{t}$ event, where the track multiplicities are quite different and the topology of the events is very different compared to that of a W $\rightarrow e\nu$ or $Z \rightarrow e^+e^-$ decays. So we decided not to use the Filter for the Monte Carlo samples.

3.4.8 Conversion removal

We reject events with one of the selected electrons being flagged as a conversion. Just as a reminder, the electrons flagged as a "trident" are not vetoed. In Run I the tridents were a smaller problem, because of the lower amount of material in the tracker volume.

3.5 Signal and Background Samples

For Monte Carlo events, we use only events for runs in the good electron SI run list, i.e. obtained with bits (1,1,0,1). We also restrict any Monte Carlo acceptance calculation to events with run $\geq$ 150145, as the CMX detector was not fully functional before that time.

The cross sections for SM processes that we consider as backgrounds and which can be simulated in a MC are given in Table V. The main $t\bar{t}$ signal MC sample is the 6.72 M events of inclusive Pythia 1.884 sample generated at

M_{top}= 172.5 GeV (`ttop25`). In this case, we simulate events up to run 259614, which match the maximum run number accepted for the data. To model the main sources of Standard Model backgrounds to the top dilepton channel we use:

- `alpgen all` $Z(ee)$ `sample` for DY/$Z \to ee$
- `alpgen all` $Z(\mu\mu)$ `sample` for DY/$Z \to \mu\mu$
- `alpgen all` $Z(\tau\tau)$ `sample` for DY/$Z \to \tau\tau$
- `ihht1a`/`jhht1a`/`khht1a` for $WW/WZ/ZZ$ diboson events
- `rewk28`/`rewk29` for $W\gamma$, $W \to e\nu/W \to \mu\nu$ events

All of the backgrounds are generated with Pythia 6.216, with the exception of the Wγ samples which are generated with the Baur Monte Carlo. We used the alpgen+pythia DY/Z samples are generated for $M_{\ell\ell} > 0$ GeV. The ZZ events are generated with $M_{\ell\ell} > 2$ GeV. Their cross section is obtained by multiplying a NLO MCFM calculation for $M_{\ell\ell} > 15$ GeV of 2.1 pb [41] by the fraction of events found with $M_{\ell\ell} < 15$ GeV over the total. A 20% uncertainty is assumed for $\sigma(ZZ)$ given the uncertainty of the extrapolation method. Table V summarizes the NLO cross sections assumed for each MC sample.

The calculation of events with one jet/track faking a lepton uses fake lepton identification rates extracted to the JET50 inclusive jet samples `gjt20X`, where X = d, h, i, j, k or m. Fake rates from the JET20 (`gjt10X`), JET70 (`gjt30X`) and JET100 (`gjt40X`) samples are used to access the systematic uncertainty on the fake estimates.

Process	Cross Section σ (pb)	K-factor
DY/Z$\rightarrow ee/\mu\mu$	355±3	1.4
DY/Z$\rightarrow \tau\tau$	355±3	1.4
WW	12.4±0.8	NA
WZ	3.7±0.1	NA
ZZ	3.8±0.8	NA
Wγ	32±3.2	1.36

Table V: The final NLO cross section are either already quote here as σ or obtained multiplying the σ in the first column by the K-factor in the second column.

Chapter 4

Acceptance and Efficiency

The Top dilepton acceptance is needed to measure the $t\bar{t}$ cross-section in the dilepton channel. As a result of the $p\bar{p}$ collisions, a number of top dilepton events are produced inside the detector. Of these, only a limited number of top dilepton events can be isolated, due to inefficiencies of the triggers or of the various selection criteria, applied to separate the signal from the overwhelming backgrounds. The top dilepton acceptance represents the fraction of produced top dilepton events, which survive the selection process, or the probability that a ttbar dilepton event will pass selection requirements.

The final dilepton acceptance for the pre-tagged candidate dilepton events

$$\mathcal{A} = 0.7558 \ \pm \ 0.0035\% \tag{4.1}$$

and for the b-tagged events is

$$\mathcal{A} = 0.4610 \ \pm \ 0.0027\%. \tag{4.2}$$

4.1 Trigger efficiencies

We estimated the trigger efficiencies for each channel by using the individual efficiencies:

$$CEM : 0.9627 \ \pm \ 0.0007 \tag{4.3}$$

$$CMUP : 0.9151 \ \pm \ 0.0014 \tag{4.4}$$

$$CMX : 0.8906 \ \pm \ 0.0018 \tag{4.5}$$

The trigger efficiencies and identification scale factors for each single lepton in the dilepton pair are reported in Table I. The central value used for each term is the luminosity weighted average of different values measured for the 0d, 0h, 0i, mi, mj, mk and mm periods, as listed in the table. The efficiency of the event for the primary vertex $|z_{VTX}| < 60$ cm cut is also reported in Table I.

4.2 Acceptance

The denominator of the cross section calculation can be written as an acceptance times the luminosity (see section 4 of CDF-8040). The acceptance itself is the convolution of the MC acceptance and of different correction factors estimated from comparing the efficiency predicted by MC and data in independent control samples. For the DIL selection we choose to compute the denominator as:

	Vertex Reconstruction efficiency ϵ_{z_0}
	0.9711 ± 0.0003
Lepton Type	PHX charge fake rate
PHX	1.0065 ± 0.0003
Lepton Type	Trigger efficiency ϵ_{trg}
CEM	0.9627 ± 0.0007
CMUP	0.9151 ± 0.0014
CMX	0.8906 ± 0.0018
Lepton Type	Lepton Identification Scale Factor SF
CEM	0.9760 ± 0.0011
NICEM	0.9848 ± 0.0010
PHX	0.9205 ± 0.0019
CMUP	0.8974 ± 0.0017
NICMUP	0.9070 ± 0.0015
CMX	0.9564 ± 0.0017
NICMX	0.9640 ± 0.0015
CMU	0.9564 ± 0.0035
NICMU	0.9669 ± 0.0032
CMP	0.8662 ± 0.0031
NICMP	0.8755 ± 0.0028
CMIO	0.9844 ± 0.0033

Table I: List by lepton type of vertex reconstruction efficiency ϵ_{z_0}, PHX charge fake rate, trigger efficiency ϵ_{trg}, and lepton identification scale factors SF. For lepton types labelled with a NI means non isolated leptons only.

$$\begin{aligned} \mathcal{A} \times \mathcal{L} &= \sum_i \mathcal{A}_i \times \mathcal{L}_i \\ \mathcal{A}_i &= \mathcal{A}_{\ell_1\ell_2} \times C_{\ell_1\ell_2} \end{aligned} \tag{4.6}$$

where the index i run over all of the DIL selection categories, each made of a pair of leptons, $\ell_1\ell_2$. The Pythia $t\bar{t}$ MC raw efficiencies efficiencies $A_{\ell_1\ell_2}$, calculated as the ratio of the number of dilepton events passing the DIL selection in the `ttop25` MC sample, are multiplied by the dilepton correction factors $C_{\ell_1\ell_2}$ and by the luminosities $\mathcal{L}_i$ appropriate for each lepton pair.

The dilepton correction factors $C_{\ell_1\ell_2}$ are calculated using the following factorization.

$$C_{\ell_1\ell_2} = \epsilon_{z_0} \times (\epsilon_{trg_1} + \epsilon_{trg_2} - \epsilon_{trg_1}\epsilon_{trg_2}) \times SF_1 SF_2 \tag{4.7}$$

where ϵ_{z_0} is efficiency of the cut imposed on all MC events to have the event vertex reconstructed inside a $\pm$60 cm region from the nominal z=0; ϵ_{trg_i} are the trigger efficiencies for the two leptons; SF_i are the identification scale factor, measured as the ratios of the data over the MC lepton identification and muon reconstruction efficiencies.

Table II details all of the inputs to equation 4.6. The total acceptance for the pre−tagged candidate dilepton events is $\mathcal{A}$=0.7558 $\pm$ 0.0035% and $\mathcal{A}$=0.4610 $\pm$ 0.0027% for the b-tagged events. A validation of the factorization model used for $C_{\ell_1\ell_2}$ is obtained by measuring the Z boson cross section for each dielectron and dimuon category. Section 4.3 reports on the results of this validation.

Summing over all of the DIL categories, we obtain a denominator for the 5.1 fb^{-1} DIL cross section of 32.0466 ± 0.1488 pb^{-1} for pre−tagging and 17.5685 ± 0.2375 pb^{-1} for b-tagging, where the uncertainty comes solely from the propagation of the uncertainties of each term in equation 4.7.

4.3 Check of Acceptance Corrections

As a cross-check of our lepton selection, as well as the quoted luminosities, trigger efficiencies and scale factors used in final calculation of $t\bar{t}$ cross section, we measure the cross section of on-shell Z production.

We select the events which have ee or $\mu\mu$ pair in the final state. Cosmic events and events with an identifies conversions are removed. We required the two leptons to have opposite charges and invariant mass in the range 76 GeV/c^2 to 106 GeV/c^2.

The acceptance is calculated using DY/Z $\rightarrow$ ee and $\mu\mu$ Pythia Monte Carlo samples. The MC acceptance is defined by the number of events which pass the selection described above, divided by the number of events in which invariant mass of two leptons satisfies 76 GeV/c^2 $< M_{\ell\ell} <$ 106 GeV/c^2.

Since the CMX trigger rate is changed with jet requirement from run number 226194 in the dataset period 9 to run number 257201 in the period 16. we use two different kind of the CMX trigger for 0jet control bin and 1 jet or more than 1 jet bin. For 0jet bin we use the inclusive high p_T CMX trigger such as MUON_CMX18_DPS or MUON_CMX18_L2_LOOSE_DPS or MUON_CMX18_L2_LOOSE_LUMI_200 or MUON _CMX18_LUMI_250. Meanwhile for 1 jet or more jets, the CMX trigger with JET10 for top quark

Category	$\mathcal{A}_{\ell_1\ell_2}(\%)$	$C_{\ell_1\ell_2}$	$\mathcal{L}_i(\mathrm{pb}^{-1})$
CEM-CEM	0.0958 ± 0.0012	0.9238 ± 0.0021	5089.78
CEM-NICEM	0.0202 ± 0.0006	0.9321 ± 0.0014	5089.78
PHX-CEM	0.0404 ± 0.0008	0.8454 ± 0.0021	4780.35
PHX-NICEM	0.0036 ± 0.0002	0.8530 ± 0.0021	4780.35
CMUP-CMUP	0.0364 ± 0.0008	0.7764 ± 0.0030	5080.48
CMUP-NICMUP	0.0094 ± 0.0004	0.7847 ± 0.0020	5080.48
CMUP-CMU	0.0159 ± 0.0005	0.7627 ± 0.0034	5080.48
CMUP-NICMU	0.0020 ± 0.0002	0.7711 ± 0.0032	5080.48
CMUP-CMP	0.0222 ± 0.0006	0.6908 ± 0.0030	5080.48
CMUP-NICMP	0.0028 ± 0.0002	0.6982 ± 0.0028	5080.48
CMUP-CMX	0.0382 ± 0.0008	0.8257 ± 0.0022	5024.35
CMUP-NICMX	0.0040 ± 0.0002	0.8323 ± 0.0021	5024.35
CMX-NICMUP	0.0042 ± 0.0003	0.7503 ± 0.0024	5080.48
CMUP-CMIO	0.0140 ± 0.0005	0.7851 ± 0.0032	5080.48
CMX-CMX	0.0092 ± 0.0004	0.8776 ± 0.0032	5024.35
CMX-NICMX	0.0015 ± 0.0002	0.8846 ± 0.0021	5024.35
CMX-CMU	0.0067 ± 0.0003	0.7911 ± 0.0036	5024.35
CMX-NICMU	0.0006 ± 0.0001	0.7998 ± 0.0034	5024.35
CMX-CMP	0.0103 ± 0.0004	0.7165 ± 0.0032	5024.35
CMX-NICMP	0.0011 ± 0.0001	0.7242 ± 0.0030	5024.35
CMX-CMIO	0.0062 ± 0.0003	0.8143 ± 0.0035	5024.35
CEM-CMUP	0.1337 ± 0.0014	0.8479 ± 0.0019	5080.48
CEM-NICMUP	0.0185 ± 0.0005	0.8569 ± 0.0017	5080.48
CMUP-NICEM	0.0139 ± 0.0005	0.8555 ± 0.0019	5080.48
CEM-CMU	0.0299 ± 0.0007	0.8727 ± 0.0034	5089.78
CEM-NICMU	0.0034 ± 0.0002	0.8822 ± 0.0032	5089.78
CEM-CMP	0.0409 ± 0.0008	0.7904 ± 0.0031	5089.78
CEM-NICMP	0.0055 ± 0.0003	0.7989 ± 0.0028	5089.78
CEM-CMX	0.0677 ± 0.0010	0.9028 ± 0.0019	5024.35
CEM-NICMX	0.0080 ± 0.0004	0.9109 ± 0.0019	5024.35
CMX-NICEM	0.0060 ± 0.0003	0.9099 ± 0.0018	5024.35
CEM-CMIO	0.0240 ± 0.0006	0.8982 ± 0.0032	5024.35
PHX-CMUP	0.0282 ± 0.0007	0.7389 ± 0.0024	4780.35
PHX-NICMUP	0.0030 ± 0.0002	0.7468 ± 0.0023	4780.35
PHX-CMX	0.0128 ± 0.0004	0.7664 ± 0.0026	4727.11
PHX-NICMX	0.0014 ± 0.0001	0.7724 ± 0.0026	4727.11

Table II: List, by dilepton category, of raw acceptance $\mathcal{A}_{\ell_1\ell_2}$, correction factor $C_{\ell_1\ell_2}$ and luminosity $\mathcal{L}_i$ used to calculate the denominator for the 5.1 fb^{-1} DIL cross section measurement. The raw acceptance uncertainty comes purely from the MC statistics. The error in the $C_{\ell_1\ell_2}$ comes from the propagation of the single lepton efficiency uncertainties reported in Table 2. "NI" means non-isolated leptons only.

such as MUON_CMX18_&_JET10 or MUON_CMX18_&_JET10_LUMI_270 or MUON_CMX18_&_JET10_DPS are used.

We use the inclusive CMX trigger for Z cross section measurement. The measured on-shell Z cross sections are shown in Figure 4.2, 4.3, 4.4 for the $Z \to ee$, $Z \to$ CMUP-any μ and $Z \to$ CMX-any μ channels respectively. We show the Z cross section as a function of run range to check for any time dependence of the overall scale factors. The error bar in the figures reflects uncertainties of data statistics, MC statistics and overall scale factors. The measured on-shell Z cross sections over the whole 5.1 fb^{-1} data sample are shown in Table III and Figure 4.1.

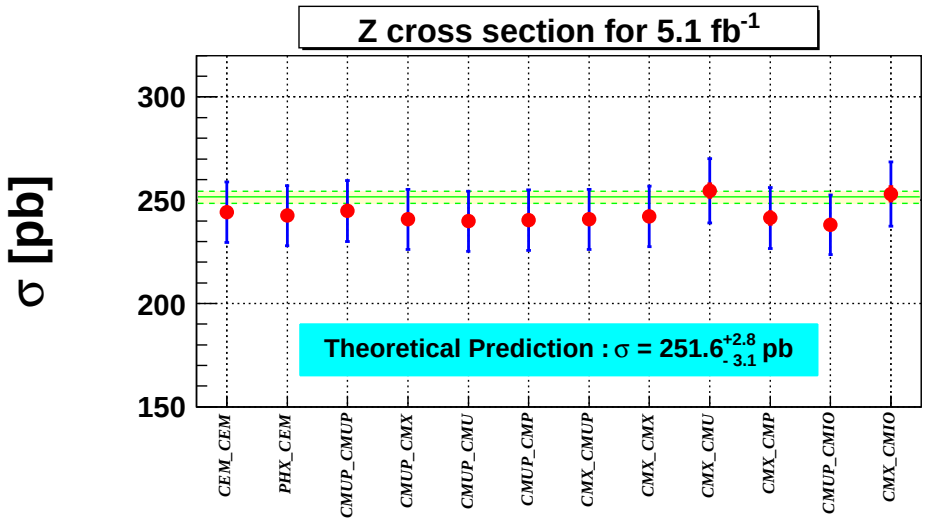

Figure 4.1: A summary of the fitted Z cross section of inclusive dilepton category in 5.1 fb^{-1} . The red line means statistical and systematic error and the blue line shows total error including luminosity error. "(NI)" means inclusive, i.e. both isolated and non-isolated leptons are included.

The categories with two tight leptons (CEM-CEM, CEM-PHX, CMUP-

Category	Z Cross Section (pb) Original	Fitted
CEM-CEM	244.3 ± 14.7	244.3 ± 14.7
(NI)CEM-CEM	244.2 ± 14.7	244.2 ± 14.7
PHX-CEM	244.0 ± 14.7	244.0 ± 14.7
(NI)CEM-PHX	242.5 ± 14.6	242.5 ± 14.6
CMUP-CMUP	243.0 ± 14.7	243.0 ± 14.7
CMUP-(NI)CMUP	244.9 ± 14.8	244.9 ± 14.8
CMUP-CMU	240.1 ± 14.7	249.9 ± 15.3
CMUP-(NI)CMU	239.8 ± 14.6	249.5 ± 15.2
CMUP-CMP	241.1 ± 14.7	236.4 ± 14.4
CMUP-(NI)CMP	240.3 ± 14.6	235.7 ± 14.3
CMUP-CMIO	238.1 ± 14.5	229.6 ± 14.0
CMUP-CMX	240.6 ± 14.5	240.6 ± 14.5
CMUP-(NI)CMX	240.8 ± 14.5	240.8 ± 14.5
CMX-(NI)CMUP	240.8 ± 14.5	240.8 ± 14.5
CMX-CMX	239.8 ± 14.6	239.8 ± 14.6
CMX-(NI)CMX	242.2 ± 14.7	242.2 ± 14.7
CMX-CMU	255.3 ± 15.7	265.7 ± 16.3
CMX-(NI)CMU	254.6 ± 15.6	264.9 ± 16.3
CMX-CMP	240.4 ± 14.8	235.7 ± 14.5
CMX-(NI)CMP	241.4 ± 14.8	236.6 ± 14.5
CMX-CMIO	253.0 ± 15.6	243.9 ± 15.0

Table III: (NI) means inclusive, i.e. both isolated and non-isolated leptons are included.

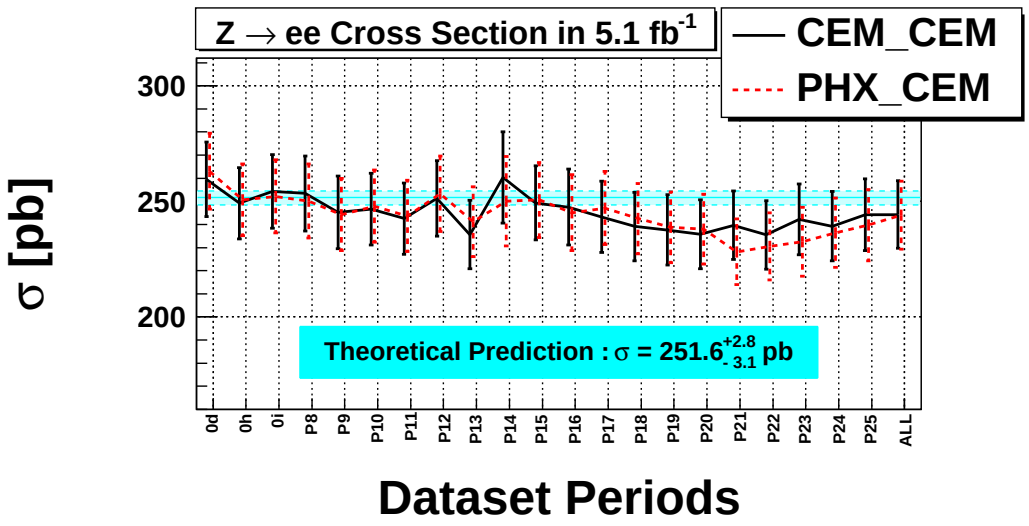

Figure 4.2: Z cross section before applying additional scale factor using $Z \to ee$ channel as a function of run period. "(P8)" $\sim$ "(P25)" means the data from Period 8 until Period 25.

CMUP, CMUP-CMX and CMX-CMX), which are also the ones with the largest acceptance, are consistent with the theoretical prediction of $251.6^{+2.8}_{-3.1}$ pb [44]. Categories with a loose muon (CMP, CMU or CMIO) paired to a tight muon show some residual variation around the average value which is not consistent with statistical fluctuations. In order to find a consistent normalization for all data, we perform a fit to the Z cross sections in the different dilepton categories with three free parameters, corresponding to a multiplicative factor in front of the selection efficiency of each of the three loose muon categories. The fit returns the cross sections reported in the last column of Table III and an average Z peak cross section of 243.1 $\pm$ 14.6 pb, as shown in Figure 4.1.

The free parameters returned by the fit are: $\mathrm{SF}^{Z}_{\mathrm{CMP}} = 0.971 \pm 0.011$, $\mathrm{SF}^{Z}_{\mathrm{CMU}} = 1.052 \pm 0.011$ and $\mathrm{SF}^{Z}_{\mathrm{CMIO}} = 0.967 \pm 0.010$. They are folded into the

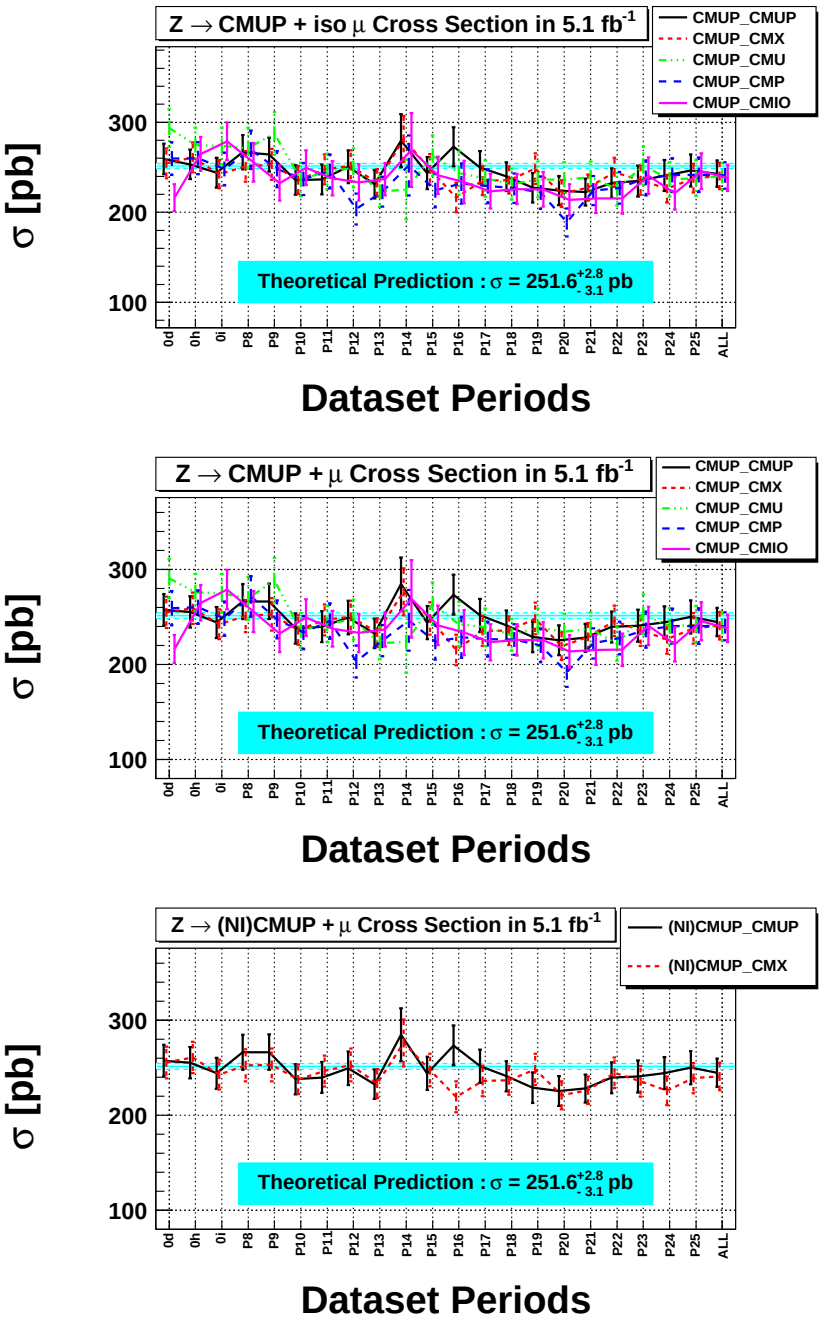

Figure 4.3: Z cross section before applying additional scale factor using $Z \rightarrow$ CMUP-any μ channel as a function of run period. "NI" means inclusive, i.e. both isolated and non-isolated leptons are included.

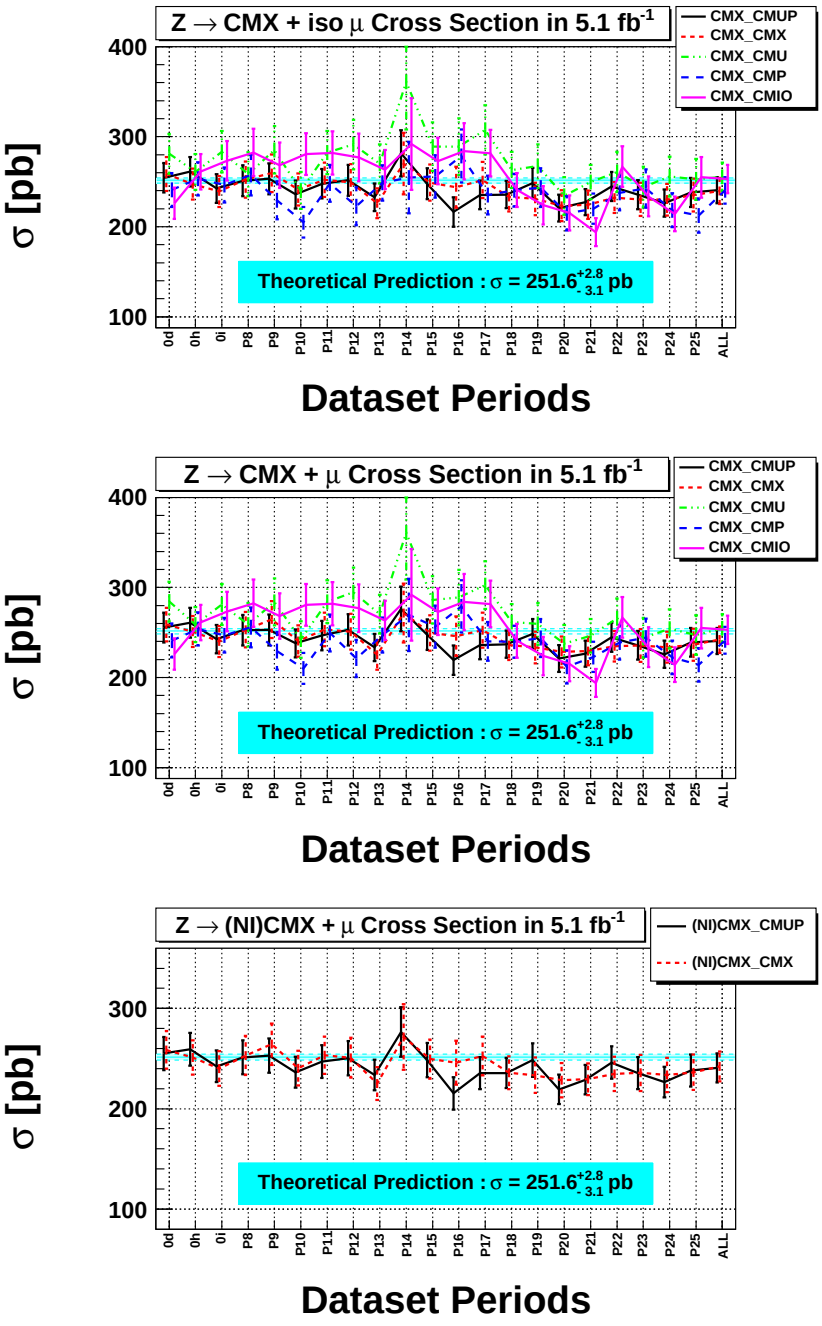

Figure 4.4: Z cross section before applying additional scale factor using $Z \rightarrow$ CMX-any μ channel as a function of run period. "NI" means inclusive, i.e. both isolated and non-isolated leptons are included.

acceptance correction procedure as additional scale factors to be multiplied by the lepton identification scale factors of Table I for the appropriate categories. After the fit, the single Z cross section measurements are consistent with each other within uncertainties, with the possible exception of categories containing one CMIO loose muon for which we observe a maximum deviation equal to 10% of the average value. This systematic deviation affects only 10% of the DIL $t\bar{t}$ raw acceptance, corresponding to the summed contributions of any dilepton pair containing a CMIO muon in Table II. Therefore we estimate a final 1% systematic uncertainty on the acceptance due to the correction procedure. We add this 1% uncertainty into the lepton ID systematic uncertainty.

Chapter 5

Background Estimation

We consider four different sources of standard model processes that can mimic the signature of dilepton plus $\not\!\!E_T$ plus 2 or more jets signature: diboson events (WW, WZ, ZZ or $W\gamma$), Drell-Yan production of tau leptons (DY$\rightarrow \tau\tau$), Drell-Yan production of electrons or muons with additional $\not\!\!E_T$ (if the event is an actual Drell-Yan event, there is no $\not\!\!E_T$ so we refer to this as fake $\not\!\!E_T$) (DY$\rightarrow ee/\mu\mu$) and QCD production of W boson with multiple jets in which one jet is misidentified as a lepton ("W+jet fakes"). The two dominant sources of background are DY$\rightarrow ee/\mu\mu$ and W+jet fakes. These two processes have production cross sections much larger than the $t\bar{t}$, but they can only contaminate the $t\bar{t}$ dilepton signature of two leptons plus jets and large $\not\!\!E_T$ when misreconstructions of the event create either some large fake $\not\!\!E_T$ or a jet misidentified as a lepton. Because it is difficult to use the Monte Carlo simulation to predict the effect of event misreconstruction in our detector, we estimate the background from these two processes using data-based methods, as discussed in Sec. 5.4 and 5.2, respectively. The diboson and DY$\rightarrow \tau\tau$ backgrounds are calculated using Monte Carlo simulation expectation as de-

scribed in Secs. 5.1 and 5.3. Corrections are applied for trigger and lepton ID efficiencies following the same procedure described in Sec. 4.

Our strategy for validating the background estimation is to compare data and background estimates in the 0-jet and 1-jet bins, as discussed in Sec. 6.1 and 6.2.

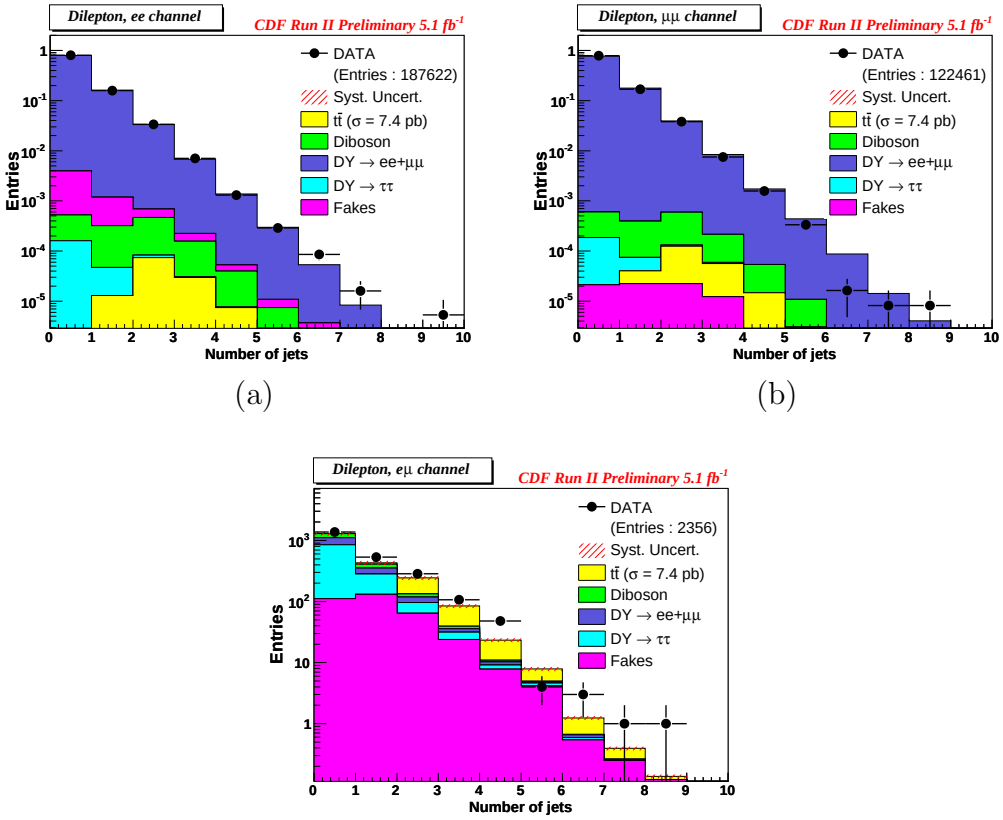

Figure 5.1: Jet multiplicity distribution for data and Monte Carlo simulation in (a) events with ee, (b) $\mu\mu$ and $e\mu$ in the final state

5.1 Diboson backgrounds

The diboson processes, WW, WZ, ZZ and $W\gamma$, can mimic the signature of the $t\bar{t}$ signal via different mechanisms, with real leptons and $\not\!\!E_T$ from W and Z decays and jets produced by boson hadronic decays or initial and final state radiation. For WW events, the two leptons and the $\not\!\!E_T$ are produced when both W's decay semi-leptonically but the jets require some hadronic radiation external to the diboson system. For WZ and ZZ events, the two leptons come from the Z boson while the other W or Z boson provides the jets via their hadronic decays. As these decays do not contain any neutrino, some mechanism to produce fake $\not\!\!E_T$ is required. Finally for $W\gamma$ events, one lepton plus $\not\!\!E_T$ is generated from the semi-leptonc W decay while the second lepton is produced from an asymmetric γ conversion in which one of the two electrons has little energy and is caught spiralling inside the central drift chamber. Like in the WW case, the $W\gamma$ system is accompanied by hadronic jets. Events involving W+jets fake leptons, with a real lepton from W boson paired to a fake lepton from the hadronic decays of the other boson, are removed from the MC to avoid double counting.

Only WW background contribute to the ee, $\mu\mu$ and $e\mu$ final states in the same proportion as the $t\bar{t}$ signal. Diboson processes involving a Z contribute preferentially to the same flavor lepton categories. $W\gamma$ events do not contribute any background to the $\mu^+\mu^-$ category given the negligible probability that the photon will convert to a muon pair.

The WW, WZ and ZZ processes are simulated with the PYTHIA Monte Carlo generator. Their production cross section is taken from the latest next-to-leading order (NLO) MCFM version [23] and CTEQ6 [24] PDF predictions

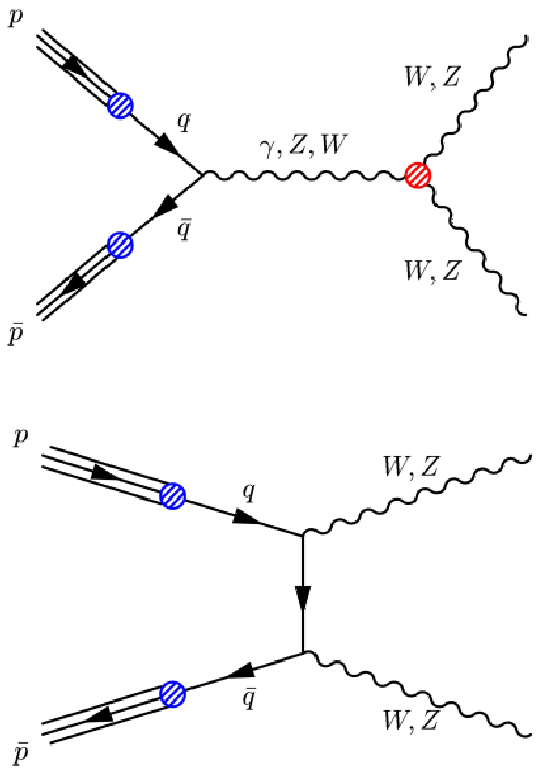

Figure 5.2: Feynman diagram of the tree level processes contributing to $p\bar{p} \to ZZ$.

to be $\sigma_{WW} = 12.4 \pm 0.8$ pb, $\sigma_{WZ} = 3.7 \pm 0.1$ pb. For the ZZ events, a cross section $\sigma_{ZZ} = 3.8$ pb is assumed with an uncertainty of 20%. $W\gamma$ decays are simulated with the BAUR Monte Carlo generator [25]. The leading order (LO) production cross section of $\sigma_{W\gamma} = 32 \pm 3$ pb is assumed, and multiplied by a K-factor of 1.36 [26] to correct for NLO effects. The $W\gamma$ Monte Carlo generator acceptance prediction is multiplied by a conversion inefficiency scale factor of 1.15 ± 0.35 to correct for the imperfect simulation of the tracking variables used in the conversion identification algorithm.

Monte Carlo generators do not correctly model the jet production from hadronic radiation, as is seen by comparing the jet multiplicity spectra of data and MC predictions for ee and $\mu\mu$ events in the Z peak region. Data, even after correcting the jet multiplicity spectrum for other SM contributions, have higher fractions of events in the 2 or more jet bins compared to predictions. We calculate jet multiplicity scale factors C_{Nj} as ratios of data and MC events in each jet bin, after normalizing the MC to the number of data in the Z peak region. These scale factors, shown in Table I, are used to correct the jet multiplicity of WW and $W\gamma$ events. A 5% systematic uncertainty on this correction is assessed by comparing jet multiplicity scale factors calculated with different generators.

5.2 Drell-Yan to $ee/\mu\mu$ background

The contamination from $Z/\gamma^* \to ee/\mu\mu$ decays is calculated using a combination of data based and MC based predictions. We define DIL data samples enriched in DY events after the L-cut by inverting the Z-veto cut and extrapolating the remaining DY contamination in the signal region by

	N_{jet} Scale Factor for WW, Wγ		
	e^+e^-	$\mu^+\mu^-$	$\ell^+\ell^-$
C_{0j}	1.017 ± 0.010	0.999 ± 0.011	1.010 ± 0.010
C_{1j}	0.918 ± 0.012	0.991 ± 0.012	0.948 ± 0.008
C_{2j}	1.056 ± 0.020	1.123 ± 0.020	1.082 ± 0.014

	N_{jet} Scale Factor for DY/$Z \to \tau\tau$		
	e^+e^-	$\mu^+\mu^-$	$\ell^+\ell^-$
C_{0j}	0.994 ± 0.003	1.012 ± 0.005	1.078 ± 0.008
C_{1j}	1.005 ± 0.004	0.976 ± 0.006	1.010 ± 0.010
C_{2j}	0.998 ± 0.003	0.997 ± 0.003	1.050 ± 0.007

Table I: Jet multiplicity scale factors for the 0, 1 and $\geq$ 2-jet bins for $Z \to ee$ and $Z \to \mu\mu$ events. The last column is the weighted average of the two same flavor Z samples and it is used for $e\mu$ reconstructed events. The uncertainties shown here are statistical only.

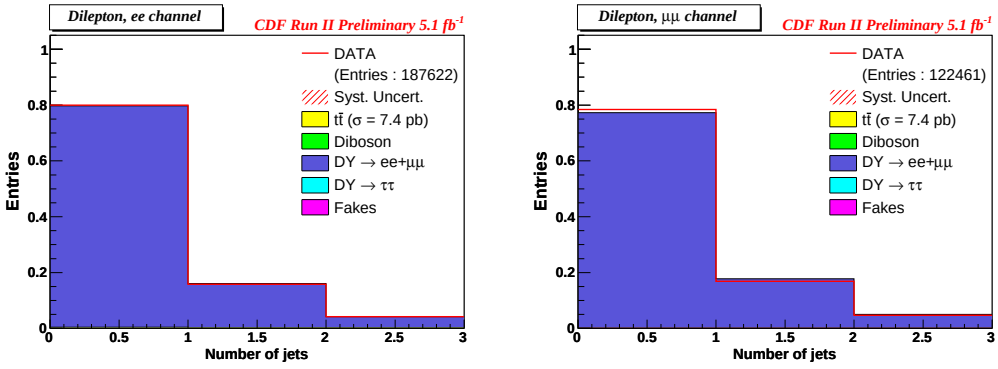

(a) (b)

Figure 5.3: Jet multiplicity distribution for data and Monte Carlo simulation in (a) $Z \to e^+e^-$ and (b) $Z \to \mu^+\mu^-$ events.

using the relative contribution of $Z/\gamma^* \to ee/\mu\mu$ decays passing and failing the Z-veto cut as predicted from MC. The Z-veto cut (see Sec. 3.4) requires that the dilepton invariant mass be outside the Z window region of 76 to 106 GeV/c^2, or, if inside, that the event have missing E_T significance $\not\!\!E_T/\sqrt{E_T^{sum}} >$ 4 GeV$^{(1/2)}$.

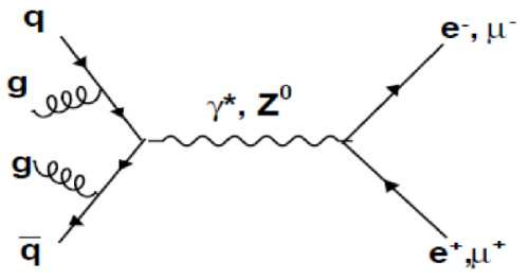

Figure 5.4: Feynman diagram of Drell-Yan processes in association with jets from the initial state radiation (ISR).

We calculate the DY→ee/$\mu\mu$ contamination as the sum of two contributions, one outside the Z window region, N_{out}, and one inside the Z window with high MetSig, N_{high}. The first contribution is calculated as:

$$N_{out} = R_{out/in}(N_{in}^{DT} - N_{in}^{BKG}) \tag{5.1}$$

where N_{in}^{DT} and N_{in}^{BKG} represent the number of events inside the Z-window passing the L-cut in data and in non-DY MC background predictions, respectively. $R_{out/in}$ is the ratio of $Z/\gamma^* \to ee/\mu\mu$ events outside to inside the Z window predicted by the ALPGEN [22] Monte Carlo generator.

The second contributions is calculated as:

$$N_{high} = R_{high/low}(N_{low}^{DT} - N_{low}^{BKG}) \tag{5.2}$$

	0-jet		1-jet		≥2-jets	
	ee	$\mu\mu$	ee	$\mu\mu$	ee	$\mu\mu$
N_{in}^{DT}	178	95	191	123	161	101
N_{in}^{BKG}	53.5±2.3	33.6±2.1	31.9±2.8	20.3±2.7	33.6±2.2	30.6±2.1
$R_{out/in}$	0.33±0.05	0.24±0.06	0.24±0.04	0.17±0.04	0.19±0.02	0.19±0.02
N_{out}	41.29±4.90	14.80±2.58	38.02±3.63	17.89±2.10	24.30±2.49	13.65±2.01
N_{low}^{DT}	157	87	179	116	145	92
N_{low}^{BKG}	21.2±1.1	16.5±1.7	9.6±0.9	7.9±0.7	11.4±0.3	12.5±0.8
$R_{high/low}$	0.038±0.014	0.001±0.000	0.011±0.002	0.009±0.002	0.013±0.001	0.012±0.001
N_{high}	0.48±0.05	0.04±0.01	1.76±0.15	0.94±0.10	1.54±0.15	0.86±0.11

Table II: Inputs to Eqs. (5.1) and (5.2) and for each dilepton flavor and jet multiplicity. N_{out} and N_{high} are the final values of the DY→ ee and $\mu\mu$ background contamination outside the Z peak region and inside the Z peak region with high MetSig, respectively.

where N_{low}^{DT} and N_{low}^{BKG} represent the events inside the Z-window passing the L-cut with MetSig < 4 GeV$^{(1/2)}$ for data and for non-DY MC background predictions, respectively. $R_{high/low}$ is the ratio of events passing/failing the MetSig > 4 GeV$^{(1/2)}$ cut predicted by ALPGEN. Table 5.2 summarizes the inputs to Eqs. (5.1) and (5.2) and the final values of N_{out} and N_{high} for each jet multiplicity bin. For the calculation of $t\bar{t}$ contribution to N^{BKG} we use the prediction of 6.7 pb for the cross section. We later correct this iteratively to the value measured in the data.

The DY contamination in the signal sample is extracted from the N_{out} and N_{high} estimates in the ≥ 2 jet bin, corrected for the efficiency of the $H_T > 200$ GeV and of the opposite sign lepton cuts. The combined efficiency for these two cuts is calculated using ALPGEN simulated Z samples and shown as ϵ_{OS} in Table III.

The contamination of $Z/\gamma^* \to \mu\mu$ to eμ events comes mostly from cases

ϵ_{HT}	ee	$\mu\mu$
After $\not\!\!E_T$ and L-cut	0.42±0.03	0.55±0.04
After $\not\!\!E_T$, L-cut and Z-veto	0.94±0.02	0.98±0.02

Table III: The efficiency is calculated separately for events outside the Z peak region passing the L-cut, and for events inside the Z peak region also passing the MetSig > 4 GeV$^{(1/2)}$ cut.

where one of the final state muon radiates a very energetic photon. These photons, which are almost collinear to the muon, deposit their energy in the EM calorimeter and produce a cluster which is associated to the original muon track and fakes the electron signature. The missed muon gives rise to a sizable $\not\!\!E_T$ in the event, curtailing the effectiveness of the L-cut and Z-veto to reject them. As no data based control sample is available for this contamination, we estimate it using Monte Carlo simulation predictions.

5.3 Drell-Yan $\rightarrow \tau\tau$ backgrounds

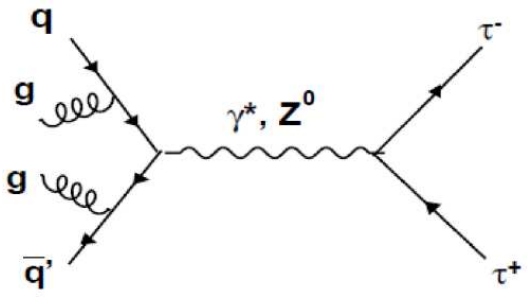

Figure 5.5: Feynman diagram of a $\tau\tau$ production with two jets from ISR.

$Z/\gamma^* \to \tau^+\tau^-$ decays are simulated with the ALPGEN generator. These events can fake the dilepton plus $\not\!\!E_T$ plus 2 or more jets signature when both τ's decay semi-leptonically to $\ell^+\nu_\ell\bar{\nu_\tau}\ell^-\bar{\nu}_\ell\nu_\tau$ and jets from initial and final state radiation are present. The contamination from this process is expected to contribute equally to the e^+e^- and $\mu^+\mu^-$ categories and to be twice as big in the $e^\pm\mu^\mp$ channel. The neutrinos from the semi-leptonic τ decays tend to have lower energy than the neutrinos in the $t\bar{t}$ dilepton sample and align along the direction of the leptonic decay when the Z recoils against the external jets. Hence a big fraction of the $Z/\gamma^* \to \tau\tau$ events are removed by the L-cut, the cut on the event $\not\!\!E_T > 25$ GeV or $\not\!\!E_T > 50$ GeV in case any lepton or jet is closer than 20° to the $\not\!\!E_T$ direction (see Sec. 3.4).

The final contamination from this process is estimated using a Monte Carlo simulation and assumes a $Z \to \tau\tau$ cross section of $251.6^{+2.8}_{-3.1}$ pb [20]. The simulated samples are generated using ALPGEN generator [22] that has built-in matching of the number of jets, coupled with PYTHIA [21] for the shower evolution and EVTGEN [27] for the heavy-flavor hadron decays. All simulated events were run through the full CDF detector simulation. To correct for NLO effects, this value is further multiplied by a K-factor of 1.4 [28]. The MC predictions in the different jet bins are finally rescaled by the C_{Nj} scale factors, as discussed in Sec. V C.

5.4 Fake Lepton background

Events with a single W boson plus jets can simulate the dilepton signature when one of the jets is misidentified as a lepton. The W+jet fake contamination is calculated in two steps: first we extract the probability of a

generic QCD jets faking the signatures of different lepton categories; then we apply these probabilities to weight events in the data containing one and only one high p_T lepton plus jets. Figure 5.6 shows an example of such a process.

The fake probabilities are measured in generic jets from QCD decays by selecting "fakeable" leptons, which are jets passing minimal lepton identification criteria described below. We do not consider separately the heavy flavor contribution to our backgrounds because the probability for a b or c quark to become a well reconstructed high p_T lepton is very small. We define different categories of fakeable lepton, one per high p_T lepton category in the DIL dilepton selection.

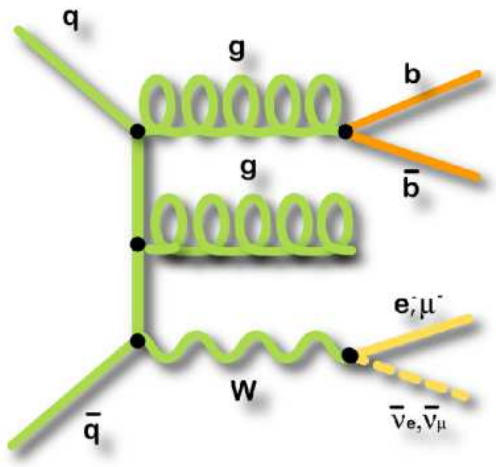

Figure 5.6: Feynman diagram of a W boson production in association with 3 jets. Such event could fake a top dilepton, if W decays leptonically and one of the three final-state fakes a lepton.

Jets with a large fraction of neutral to charged pion production can create signatures with low track multiplicity and large energy deposition in the electromagnetic calorimeter, thus faking the presence of electrons. We de-

fine fakeable electrons as tracks of $p_T > 20$ GeV/c pointing to an electron-like cluster with energy deposition in the electromagnetic section of the calorimeter far exceeding the energy measured in the hadronic section, namely with $\mathrm{E_{HAD}/E_{EM}} < 0.125$. Fakeable electrons are further divided into objects that can fake CEM or PHX electrons depending on whether their clusters belong to the central or plug section of the calorimeter. We label them TCEM and TPHX, respectively. Fakeable for the non isolated electrons do not require isolation for the central cluster and are called NCEM.

Jets whose full hadronic activity is limited to single charged pions or kaons with a late shower development or decay in flight might deposit little energy in the calorimeter but generate hits in the muon chambers, thus faking the signature of a muon. We define fakeable muons as good quality tracks of $p_T > 20$ GeV/c with E/p < 1. Depending on which muon sub-detectors these tracks point to, we label as TCMUP, TCMX, LMIO and LMUO fakeable muons which can fake tight CMUP, tight CMX, loose CMIO or loose CMU/CMP muons, respectively. Fakeable muons that fail the isolation requirement are put together into a single NMUO category as long as they point to any muon sub-detector.

We select fakeable leptons among generic QCD jets collected in four different control samples, whose main trigger requirement is the presence of at least one jet of $E_T^{Trg} > 20$, 50, 70 and 100 GeV, respectively. The simplification of the jet algorithm used in these trigger selection tends to underestimate the energy of the offline reconstructed jets. To ensure a trigger efficiency of 90% or greater we require the trigger jet to have reconstructed E_T greater than 35, 55, 75 and 105 GeV, respectively, in the four jet samples. The resulting probabilities are labeled Jet20, Jet50, Jet70 and Jet100 fake lepton probabili-

ties. To minimize real lepton contamination, we require that fakeables in the denominator of the fake probability fail one or more of the standard lepton identification cuts. For the numerator instead we require that the fakeable leptons pass all of the lepton identification requirements.

The reconstructed fake leptons can be include with real leptons from W, DY, and Diboson. So it is necessary to remove the real lepton contamination in the QCD jet sample. The MC samples for (DY$\rightarrow ee$(zewkad), DY$\rightarrow \mu\mu$(zewk9m), DY$\rightarrow \tau\tau$(zewkat), WW(itopww), WZ(itopwz), ZZ(itopzz))is used to estimate this real lepton contamination. Jet threshold E_T is increased as corresponding to 90% trigger efficiency for the comparison with the MC events. it is possible to mimic the trigger turn on curve by using E_T of 35, 55, 75 and 105 GeV corresponding to the jet20, jet50, jet70 and jet 100 triggers.

Real lepton is calculated using the following equation:

$$\text{RealLepton}_{MC} = \frac{\text{Acc}_{MC} \times \sigma_{MC} \times \text{lum}_{jet}}{\text{EffectivePS}_{jet}} \tag{5.3}$$

"Acc" is each MC's one lepton and more than one threshold E_T jet acceptance. "lum" is luminosity of each QCD jet sample. "Effective PS$_{jet}$" is sum of each run's weighted pre-scale by each run's luminosity. QCD jet sample's detail parameter is Table IV We subtract this real lepton contamination from jet sample's good lepton and fakeable object. Fake Rate is calculated using the following equation:

$$\text{FakeRate} = \frac{\text{GoodLepton}_{jet} - \text{RealLepton}_{MC}}{\text{Fakeable}_{jet} - \text{RealFakeable}_{MC}} \tag{5.4}$$

Where the subscript "jet" refers to number estimated from the QCD jet sample; and the subscript "MC" refers to number from the MC prediction. "GoodLepton" is number of reconstructed lepton in QCD jet sample. "RealLepton" is the number of fakeable in QCD jet sample. "RealLepton" and

"RealFakeable" are number of good lepton and fakeable predicted by MC, i.e. the real lepton contamination.

	jet20	jet50	jet70	jet100
luminosity	5020.76 pb^{-1}	5021.24 pb^{-1}	5021.10 pb^{-1}	5021.24 pb^{-1}
Effective pre-scale	1643.68	70.37	8	1
jet E_T threshold cut	35 GeV	55 GeV	75 GeV	105 GeV

Table IV: Some parameter of QCD jet sample, and jet E_T threshold cut value to ensure 90% trigger efficiency.

We use the fake lepton probability measured in the Jet50 sample as our primary estimator to apply to data events because the jet energy spectrum in the Jet50 sample is the closest to the energy spectrum of jets in the dilepton plus missing E_T sample. The fake probabilities for different lepton categories show a dependence on the transverse energy of the fakeable lepton. To properly account for difference in the p_T spectrum of fakeable leptons in QCD jets vs W+jets, we calculate fake probabilities in six p_T ranges as shown in Table V.

The uncertainties on the fake probabilities in Table V are only statistical. Variations in fake probabilities between the different QCD jet samples are used to estimate a systematic uncertainty in the lepton fake estimate. Figure 5.7 shows a comparison between the number of fake lepton events observed in the Jet20, Jet70 and Jet100 data sample, after integration over the full p_T spectrum, and the number predicted by the Jet50 fake probabilities of Table V. We assess a 30% systematic uncertainty on the ability of the Jet50 fake probabilities to predict electron and muon fake contamination in samples with a wide range of jet energy.

Fakeable	Jet50 Fake Probabilities (%) in p_T range (GeV/c) for period 0 $\sim$ 8					
	[20–30] GeV/c	[30–40] GeV/c	[40–60] GeV/c	[60–100] GeV/c	[100–200] GeV/c	$\geq$ 200 GeV/c
TCEM	0.0490 ± 0.0014	0.0391 ± 0.0011	0.0237 ± 0.0002	0.0274 ± 0.0003	0.0356 ± 0.0016	0.0632 ± 0.0509
NCEM	0.0077 ± 0.0000	0.0053 ± 0.0000	0.0058 ± 0.0000	0.0051 ± 0.0001	0.0046 ± 0.0011	0.0000 ± 0.0000
TPHX	0.1363 ± 0.0013	0.1306 ± 0.0017	0.1213 ± 0.0002	0.1971 ± 0.0003	0.2671 ± 0.0034	0.4830 ± 0.7841
TCMUP	0.0122 ± 0.0007	0.0293 ± 0.0019	0.0412 ± 0.0027	0.0832 ± 0.0056	0.0639 ± 0.0135	0.0000 ± 0.0000
TCMX	0.0105 ± 0.0011	0.0229 ± 0.0032	0.0533 ± 0.0049	0.0961 ± 0.0147	0.0055 ± 0.2219	0.0000 ± 0.0000
LMUO	0.0320 ± 0.0008	0.0426 ± 0.0024	0.0554 ± 0.0046	0.0805 ± 0.0108	0.1461 ± 0.0191	0.0100 ± 0.0059
LMIO	0.1978 ± 0.0013	0.2139 ± 0.0043	0.2110 ± 0.0060	0.3414 ± 0.0140	0.1921 ± 0.0289	0.9250 ± 0.0288
NMUO	0.0053 ± 0.0000	0.0037 ± 0.0000	0.0022 ± 0.0000	0.0020 ± 0.0001	0.0012 ± 0.0007	0.0034 ± 0.0034

Fakeable	Jet50 Fake Probabilities (%) in p_T range (GeV/c) for period 9 $\sim$ 12					
	[20–30] GeV/c	[30–40] GeV/c	[40–60] GeV/c	[60–100] GeV/c	[100–200] GeV/c	$\geq$ 200 GeV/c
TCEM	0.0423 ± 0.0054	0.0232 ± 0.0055	0.0271 ± 0.0005	0.0358 ± 0.0008	0.0255 ± 0.0059	0.0664 ± 0.1319
NCEM	0.0072 ± 0.0000	0.0048 ± 0.0000	0.0055 ± 0.0000	0.0046 ± 0.0002	0.0222 ± 0.0033	0.0000 ± 0.0000
TPHX	0.1302 ± 0.0045	0.1903 ± 0.0061	0.1281 ± 0.0007	0.2230 ± 0.0009	0.2503 ± 0.0112	0.0000 ± 0.0000
TCMUP	0.0086 ± 0.0018	0.0206 ± 0.0042	0.0438 ± 0.0047	0.0689 ± 0.0087	0.0455 ± 0.0121	0.0000 ± 0.0000
TCMX	0.0080 ± 0.0022	0.0293 ± 0.0053	0.0335 ± 0.0067	0.0403 ± 0.0143	0.0032 ± 0.0520	0.0075 ± 0.0079
LMUO	0.0152 ± 0.0021	0.0163 ± 0.0062	0.0330 ± 0.0074	0.0092 ± 0.0406	0.0254 ± 0.0214	0.0000 ± 0.0000
LMIO	0.1951 ± 0.0045	0.2759 ± 0.0119	0.4851 ± 0.0210	0.4904 ± 0.0304	0.4432 ± 0.0460	1.1713 ± 0.0621
NMUO	0.0046 ± 0.0000	0.0036 ± 0.0000	0.0023 ± 0.0001	0.0036 ± 0.0002	0.0063 ± 0.0016	0.0000 ± 0.0000

Fakeable	Jet50 Fake Probabilities (%) in p_T range (GeV/c) for period 13 $\sim$ 17					
	[20–30] GeV/c	[30–40] GeV/c	[40–60] GeV/c	[60–100] GeV/c	[100–200] GeV/c	$\geq$ 200 GeV/c
TCEM	0.0637 ± 0.0050	0.0478 ± 0.0050	0.0242 ± 0.0007	0.0301 ± 0.0011	0.0320 ± 0.0068	0.0000 ± 0.0000
NCEM	0.0065 ± 0.0000	0.0057 ± 0.0000	0.0060 ± 0.0000	0.0044 ± 0.0002	0.0039 ± 0.0047	0.0000 ± 0.0000
TPHX	0.0822 ± 0.0058	0.1186 ± 0.0076	0.1523 ± 0.0009	0.2163 ± 0.0011	0.3018 ± 0.0155	0.0000 ± 0.0000
TCMUP	0.0045 ± 0.0028	0.0103 ± 0.0059	0.0258 ± 0.0067	0.0198 ± 0.0169	0.0129 ± 0.0180	0.0000 ± 0.0000
TCMX	0.0072 ± 0.0025	0.0132 ± 0.0065	0.0535 ± 0.0069	0.0117 ± 0.0281	0.0149 ± 0.0216	0.0078 ± 0.0082
LMUO	0.0148 ± 0.0028	0.0089 ± 0.0085	0.0330 ± 0.0113	0.0608 ± 0.0123	0.0519 ± 0.0178	0.0000 ± 0.0000
LMIO	0.2774 ± 0.0057	0.3499 ± 0.0137	0.2828 ± 0.0209	0.4562 ± 0.0363	0.8478 ± 0.1307	1.2367 ± 0.0589
NMUO	0.0046 ± 0.0000	0.0032 ± 0.0001	0.0025 ± 0.0001	0.0034 ± 0.0003	0.0040 ± 0.0021	0.0000 ± 0.0000

Fakeable	Jet50 Fake Probabilities (%) in p_T range (GeV/c) for period 18 $\sim$ 19					
	[20–30] GeV/c	[30–40] GeV/c	[40–60] GeV/c	[60–100] GeV/c	[100–200] GeV/c	$\geq$ 200 GeV/c
TCEM	0.0686 ± 0.0063	0.0320 ± 0.0079	0.0263 ± 0.0009	0.0275 ± 0.0015	0.0683 ± 0.0066	0.0000 ± 0.0000
NCEM	0.0066 ± 0.0000	0.0052 ± 0.0001	0.0062 ± 0.0001	0.0039 ± 0.0003	0.0109 ± 0.0059	0.0000 ± 0.0000
TPHX	0.1535 ± 0.0146	0.1242 ± 0.0128	0.1207 ± 0.0014	0.1973 ± 0.0017	0.2291 ± 0.0240	0.0000 ± 0.0000
TCMUP	0.0138 ± 0.0024	0.0180 ± 0.0058	0.0192 ± 0.0112	0.0896 ± 0.0125	0.0255 ± 0.0247	0.0000 ± 0.0000
TCMX	0.0030 ± 0.0048	0.0139 ± 0.0093	0.0599 ± 0.0104	0.0246 ± 0.0304	0.0239 ± 0.0268	0.0000 ± 0.0000
LMUO	0.0061 ± 0.0047	0.0125 ± 0.0092	0.0283 ± 0.0145	0.0975 ± 0.0168	0.0000 ± 0.0000	0.0000 ± 0.0000
LMIO	0.2579 ± 0.0062	0.4816 ± 0.0239	0.4524 ± 0.0299	0.8037 ± 0.0603	0.6715 ± 0.0919	1.3156 ± 0.1220
NMUO	0.0052 ± 0.0000	0.0035 ± 0.0001	0.0035 ± 0.0001	0.0034 ± 0.0004	0.0057 ± 0.0030	0.0000 ± 0.0000

Fakeable	Jet50 Fake Probabilities (%) in p_T range (GeV/c) for period 20 $\sim$ 23					
	[20–30] GeV/c	[30–40] GeV/c	[40–60] GeV/c	[60–100] GeV/c	[100–200] GeV/c	$\geq$ 200 GeV/c
TCEM	0.0617 ± 0.0039	0.0482 ± 0.0033	0.0245 ± 0.0005	0.0325 ± 0.0008	0.0248 ± 0.0052	0.1146 ± 0.0965
NCEM	0.0072 ± 0.0000	0.0053 ± 0.0000	0.0059 ± 0.0000	0.0062 ± 0.0001	0.0071 ± 0.0026	0.0000 ± 0.0000
TPHX	0.1067 ± 0.0048	0.1392 ± 0.0053	0.1481 ± 0.0006	0.2244 ± 0.0008	0.2246 ± 0.0093	0.0000 ± 0.0000
TCMUP	0.0045 ± 0.0021	0.0053 ± 0.0055	0.0223 ± 0.0043	0.0238 ± 0.0098	0.0112 ± 0.0139	0.0000 ± 0.0000
TCMX	0.0034 ± 0.0025	0.0154 ± 0.0039	0.0282 ± 0.0058	0.0075 ± 0.0270	0.0080 ± 0.0212	0.0048 ± 0.0052
LMUO	0.0154 ± 0.0019	0.0272 ± 0.0037	0.0337 ± 0.0059	0.0322 ± 0.0119	0.0417 ± 0.0132	0.0000 ± 0.0000
LMIO	0.3080 ± 0.0040	0.4213 ± 0.0111	0.4718 ± 0.0154	0.6868 ± 0.0309	0.7994 ± 0.0443	0.9621 ± 0.0370
NMUO	0.0050 ± 0.0000	0.0033 ± 0.0000	0.0030 ± 0.0000	0.0018 ± 0.0002	0.0026 ± 0.0014	0.0061 ± 0.0062

Fakeable	Jet50 Fake Probabilities (%) in p_T range (GeV/c) for period 24 $\sim$ 25					
	[20–30] GeV/c	[30–40] GeV/c	[40–60] GeV/c	[60–100] GeV/c	[100–200] GeV/c	$\geq$ 200 GeV/c
TCEM	0.0755 ± 0.0073	0.0378 ± 0.0079	0.0334 ± 0.0009	0.0157 ± 0.0027	0.0372 ± 0.0088	0.8880 ± 2.1949
NCEM	0.0068 ± 0.0000	0.0056 ± 0.0001	0.0057 ± 0.0001	0.0052 ± 0.0003	0.0051 ± 0.0057	0.0000 ± 0.0000
TPHX	0.1147 ± 0.0119	0.1283 ± 0.0120	0.1309 ± 0.0015	0.2084 ± 0.0020	0.3316 ± 0.0251	0.0000 ± 0.0000
TCMUP	0.0037 ± 0.0039	0.0046 ± 0.0135	0.0063 ± 0.0207	0.0226 ± 0.0169	0.0340 ± 0.0159	0.0000 ± 0.0000
TCMX	0.0130 ± 0.0037	0.0345 ± 0.0077	0.0004 ± 0.2687	0.0813 ± 0.0159	0.0104 ± 0.0403	0.0000 ± 0.0000
LMUO	0.0139 ± 0.0041	0.0178 ± 0.0111	0.0080 ± 0.0347	0.0427 ± 0.0252	0.0193 ± 0.0216	0.0000 ± 0.0000
LMIO	0.2248 ± 0.0089	0.4458 ± 0.0305	0.4702 ± 0.0339	0.4976 ± 0.0399	1.0773 ± 0.1969	1.2962 ± 0.0851
NMUO	0.0042 ± 0.0000	0.0033 ± 0.0001	0.0022 ± 0.0001	0.0027 ± 0.0005	0.0031 ± 0.0033	0.0000 ± 0.0000

Table V: The uncertainties are statistical only. Due to the definition of fake probability, the denominator can fluctuate to be smaller than the numerator in low statistics high p_T bins, hence fake rate values exceeding 100%.

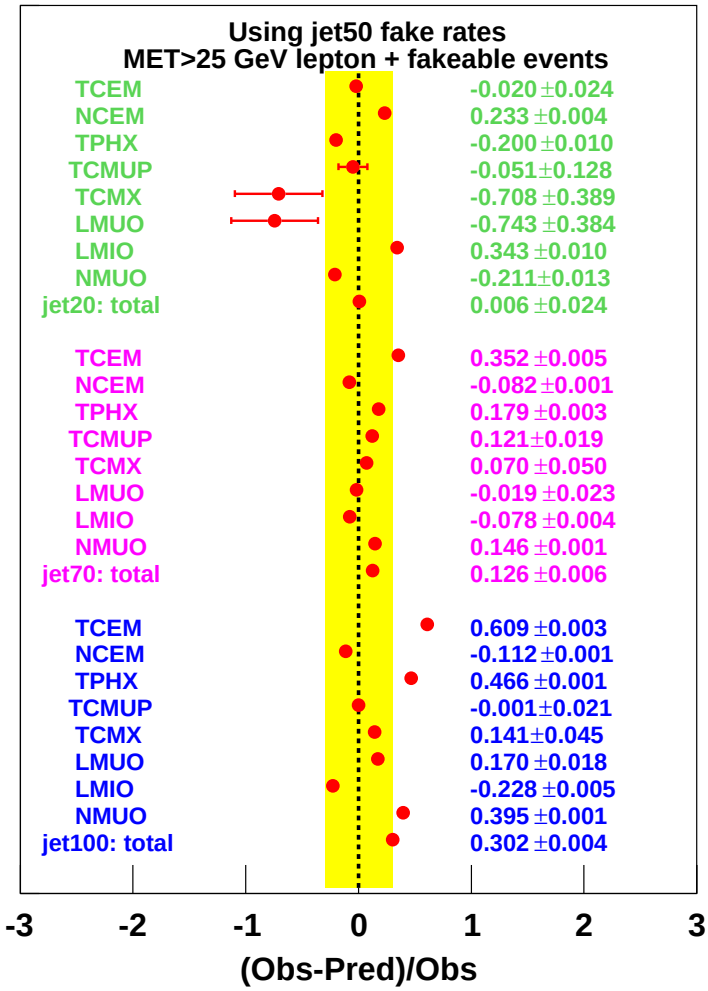

Figure 5.7: Ratio of observed total number of fake leptons for each fakeable category vs the Jet50-based prediction normalized by the number of observed. The predictability of the jet50 P_T dependent fake rate is good at the 30% level, as shown by the band in the plot. When error bars are not shown they are smaller than the dot size.

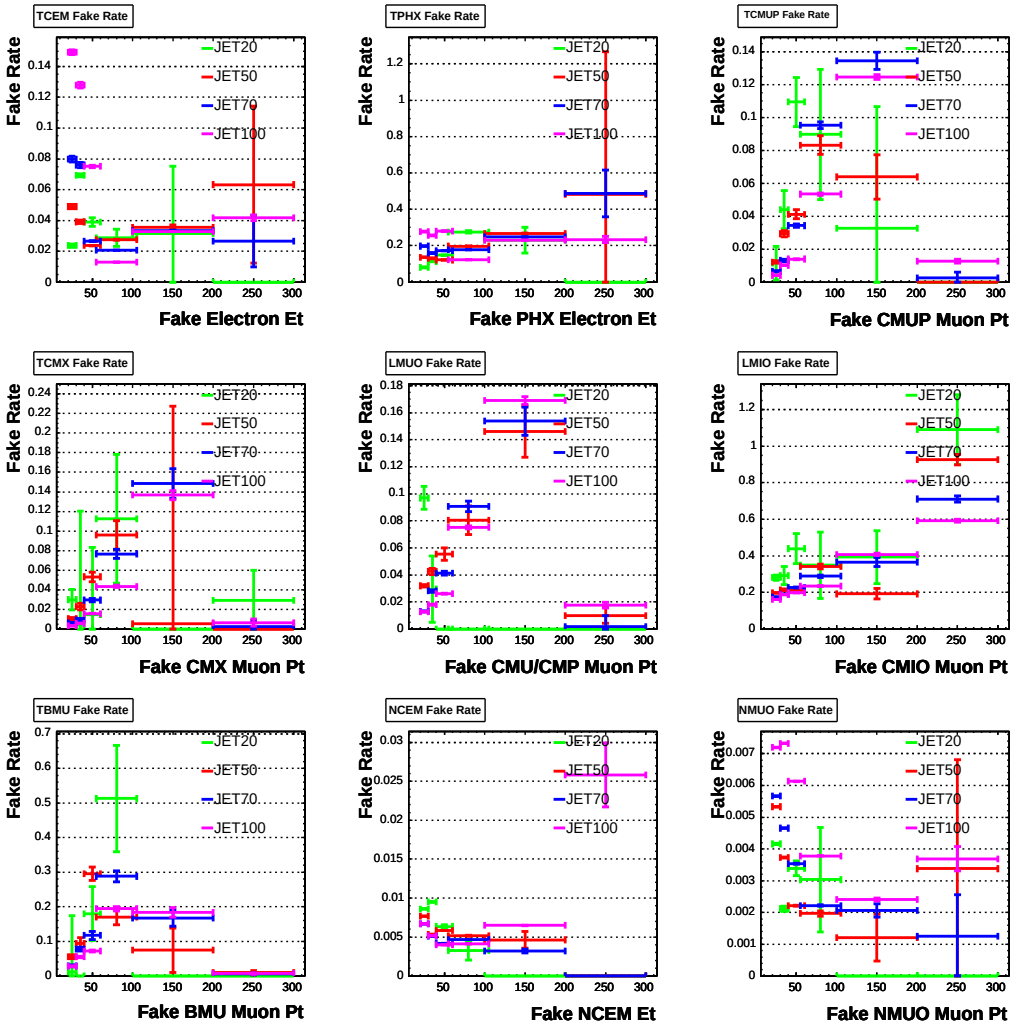

Figure 5.8: Fake rate estimates versus lepton p_T for each fakeable category considered for data period $0 \sim 8$. The JET50 fake rates, shown in red, are compared to the JET20 (green), JET70 (blue) and JET100 (magenta) fake rates. TBMU fakeable objects are not used in this analysis.

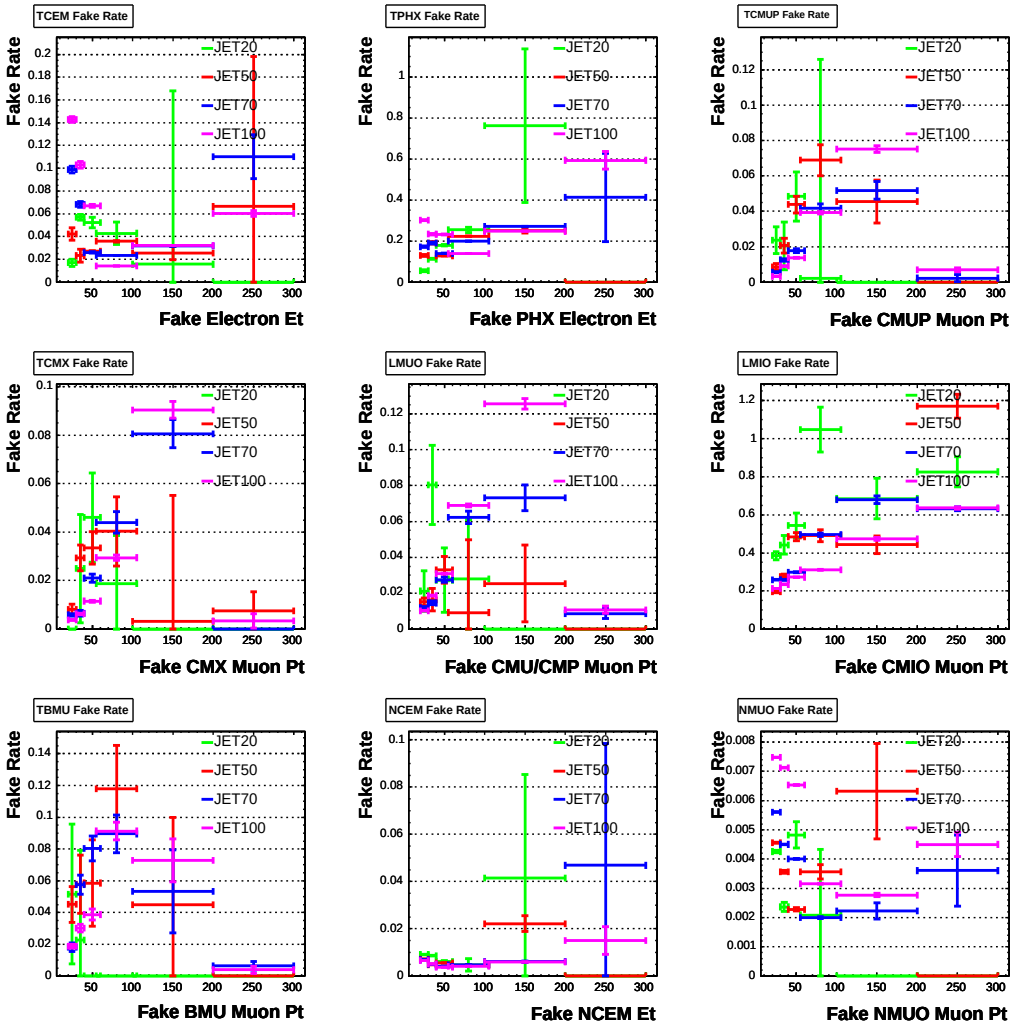

Figure 5.9: Fake rate estimates versus lepton p_T for each fakeable category considered for data period 9 $\sim$ 12. The JET50 fake rates, shown in red, are compared to the JET20 (green), JET70 (blue) and JET100 (magenta) fake rates. TBMU fakeable objects are not used in this analysis.

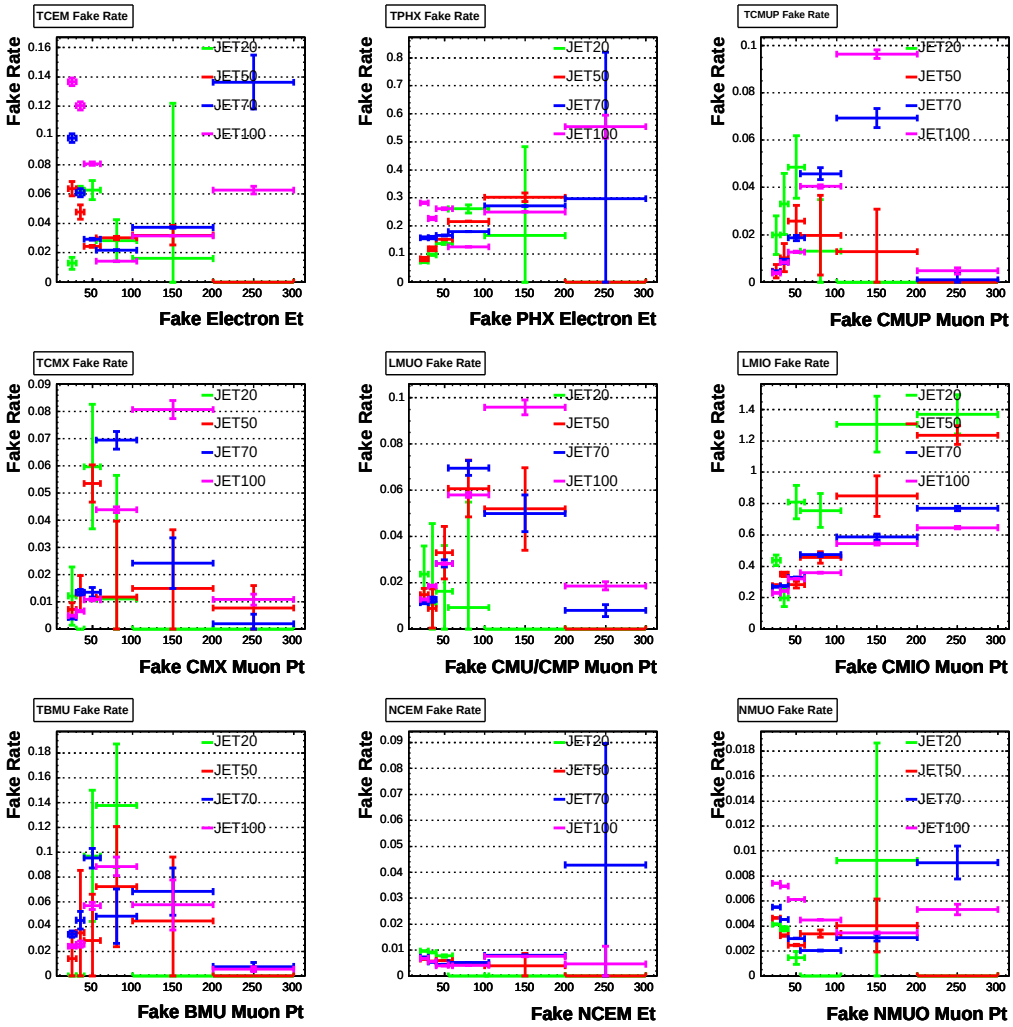

Figure 5.10: Fake rate estimates versus lepton p_T for each fakeable category considered for data period 13 $\sim$ 17. The JET50 fake rates, shown in red, are compared to the JET20 (green), JET70 (blue) and JET100 (magenta) fake rates. TBMU fakeable objects are not used in this analysis.

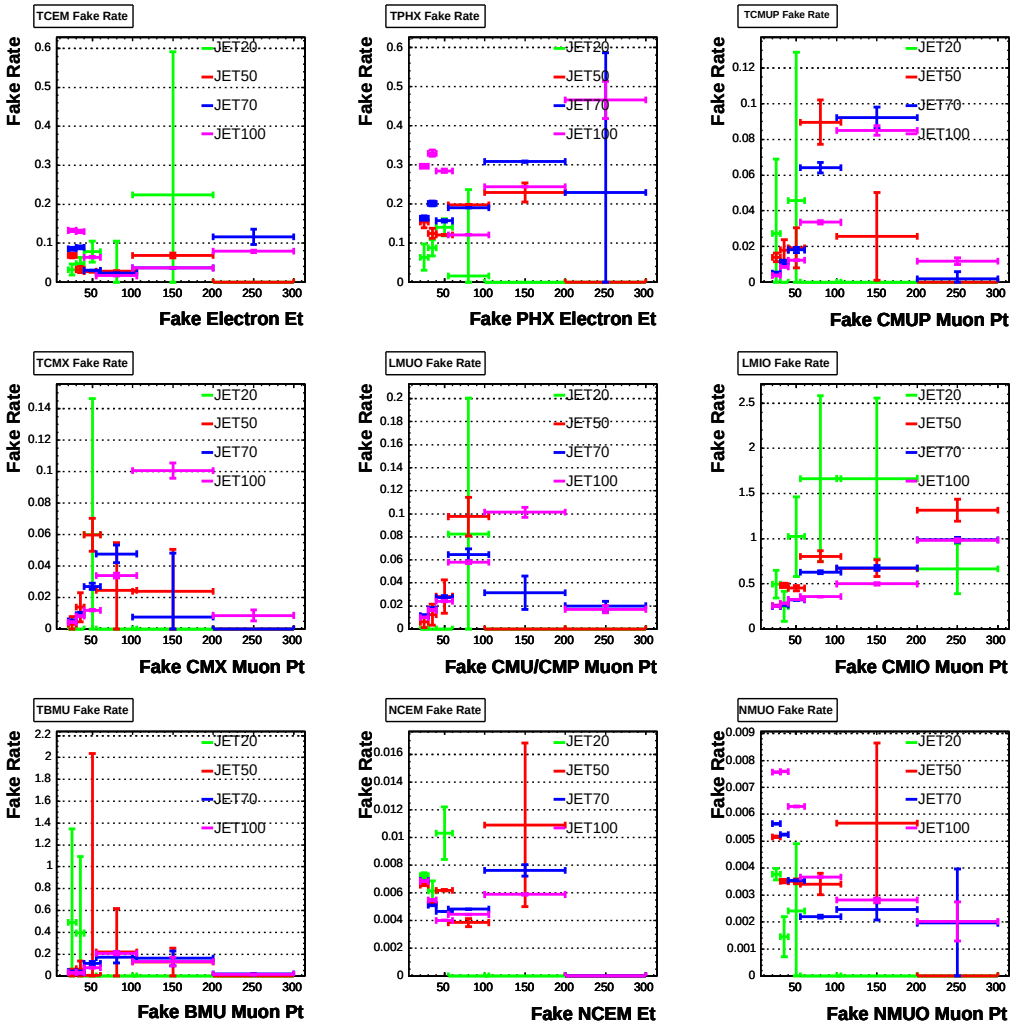

Figure 5.11: Fake rate estimates versus lepton p_T for each fakeable category considered for data period 18 $\sim$ 19. The JET50 fake rates, shown in red, are compared to the JET20 (green), JET70 (blue) and JET100 (magenta) fake rates. TBMU fakeable objects are not used in this analysis.

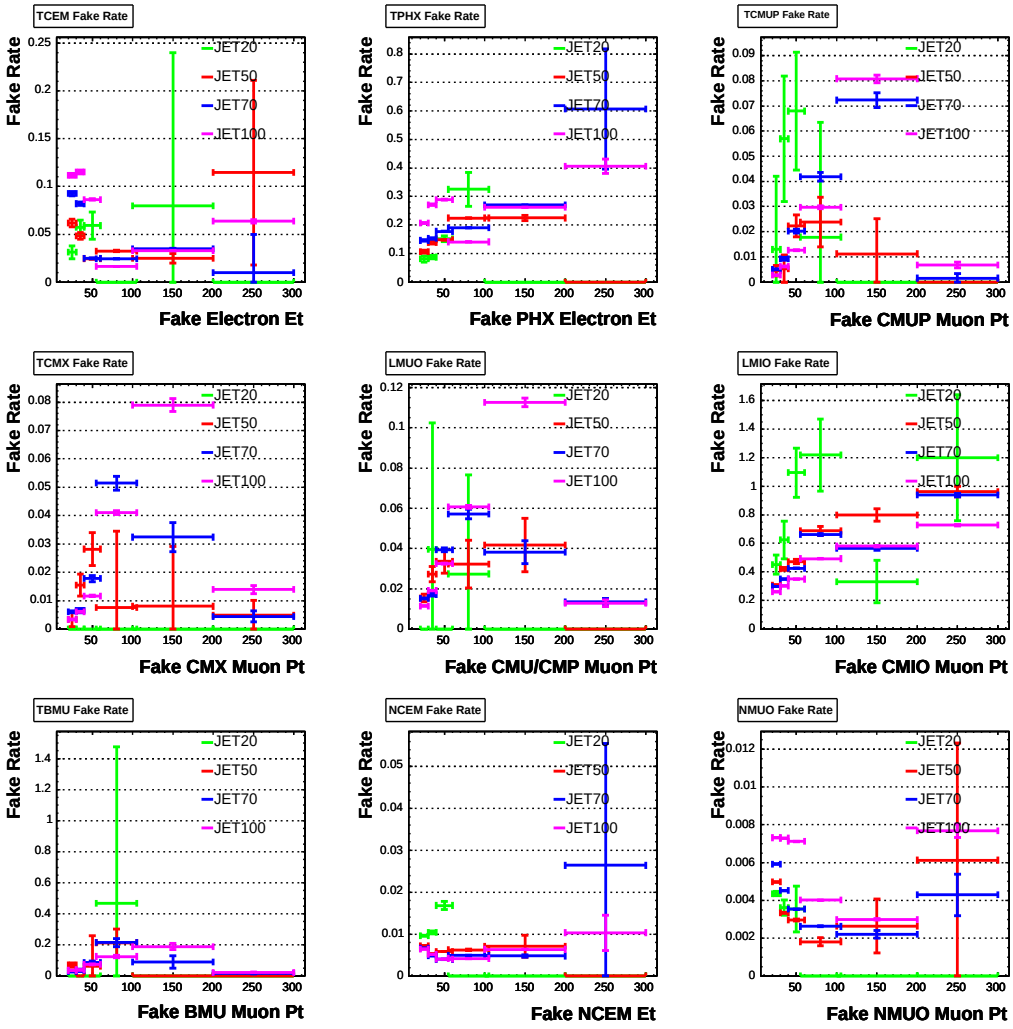

Figure 5.12: Fake rate estimates versus lepton p_T for each fakeable category considered for data period 20 $\sim$ 23. The JET50 fake rates, shown in red, are compared to the JET20 (green), JET70 (blue) and JET100 (magenta) fake rates. TBMU fakeable objects are not used in this analysis.

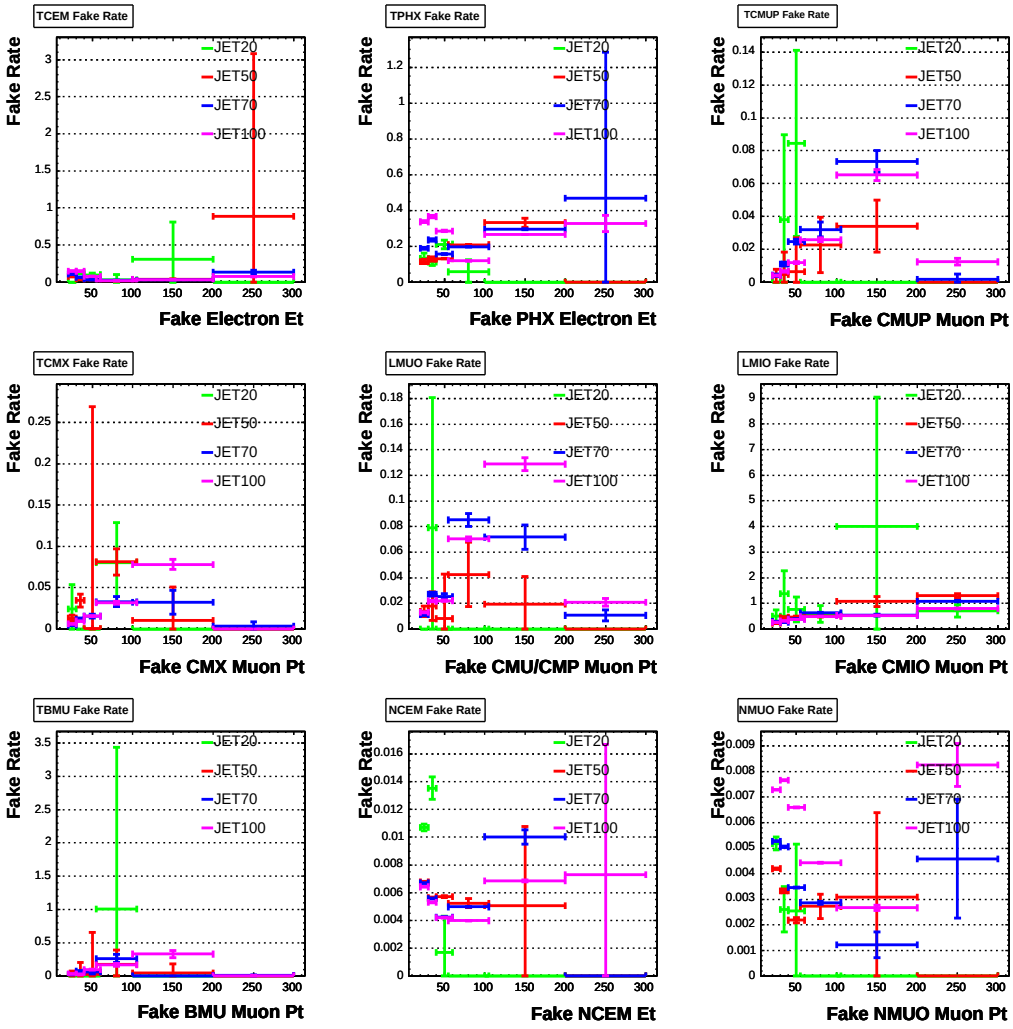

Figure 5.13: Fake rate estimates versus lepton p_T for each fakeable category considered for data period 24 $\sim$ 25. The JET50 fake rates, shown in red, are compared to the JET20 (green), JET70 (blue) and JET100 (magenta) fake rates. TBMU fakeable objects are not used in this analysis.

We define "lepton+fakeable" as those events in the central high p_T lepton data sets with one and only one good high p_T lepton, $\not\!\!E_T$ >25 GeV and a second fakeable object failing at least one standard lepton identification cuts. The fakeable object, which can be from any of the fakeable categories defined above, is paired to the good lepton and treated as the second lepton in the event when calculating any of the kinematic variables used in the top quark DIL selection, such as dilepton invariant mass, corrected $\not\!\!E_T$, and H_T. Jets found in a cone of $\Delta R < 0.4$ around the fakeable lepton are not included in the jet multiplicity count of that event because those jets are associated with the fake lepton in this W+jet fake estimation scheme. The fake lepton contamination is calculated by weighting each "lepton+fakeable" event found in data by the fake probability in Table V. If more than one fakeable object is found in the event, we pair each of them to the good lepton and add their single fake contributions. The fake dilepton background thus calculated contains a statistical component, which is the sum of the fake probability uncertainty itself and the statistics of the "lepton+fakeable" sample.

	ee	$\mu\mu$	$e\mu$	$\ell\ell$
Corrected Candidates in 0 jet	27.32 ± 6.08	15.51 ± 4.36	26.77 ± 6.56	69.59 ± 9.95
Predicted Candidates in 0jet	13.89 ± 4.29	17.52 ± 6.03	31.27 ± 9.75	62.67 ± 19.25
Corrected Candidates in 1jet	13.58 ± 4.47	8.02 ± 3.16	50.05 ± 7.75	71.64 ± 9.49
Predicted Candidates in 1jet	9.17 ± 2.84	12.75 ± 4.21	38.70 ± 11.96	60.62 ± 18.51
Corrected Candidates in jets (≥ 2)	6.38 ± 3.46	2.79 ± 2.00	39.89 ± 6.86	49.06 ± 7.94
Predicted Candidates in jets (≥ 2)	7.24 ± 2.26	13.45 ± 4.39	41.50 ± 12.77	62.19 ± 18.96

Table VI: Comparison between the same sign dilepton fake background prediction using the fake rate tables and the numbers of same sign dilepton candidates found in the signal region, after MC subtraction of standard model contamination sources.

As a check, we compare the same sign "lepton+fakeable" prediction to the number of W+jet fakes with same sign dilepton candidates in the signal regions. We define as fake lepton charge the charge of the track associated to the fakeable lepton. Same sign dilepton candidates are corrected for the presence of same sign pairs coming from $t\bar{t}$, DY or diboson events that are simulated in our Monte Carlo simulations. The results of this check are shown in Table VI. Although the $\mu\mu$ channel shows deviation at the 3 standard deviation level for some jet multiplicity bins, the agreement in the final predictions over all dilepton categories is at the one standard deviation level.

Chapter 6

Measurement of the $t\bar{t}$ Production Cross Section

6.1 Pretag Signal Candidate events

The first step in validating the top DIL selection for the 5.1 fb^{-1} analysis is to produce the background tables for the 0-jet and 1-jet control bins, using a cut on MetSig cut as a Z-veto rejection tool. The results are shown in Tables I. In general we see excellent agreement between data and predictions which give us confidence in the predictability of the methods used to calculate the backgrounds for high $\not\!\!E_T$ events dilepton events. Figures 6.2 show the $t\bar{t}$and background prediction, overlaid to the data, for some kinematic distributions of events in the 0-jet and 1-jet bin, respectively.

Secondly, Tables II give number of 2 jet bin before the H_T and the opposite lepton charge requirement. Figures 6.3 show the $t\bar{t}$ and background prediction of this region.

CDF II preliminary (5.1 fb^{-1})

N$jet = 0$ $t\bar{t}$ Control Sample before H_T and opposite lepton charge requirement				
Source	ee	$\mu\mu$	eμ	$\ell\ell$
WW	61.66±5.67	47.69±4.39	127.36±11.64	236.71±21.58
WZ	4.92±0.37	6.53±0.48	6.68±0.49	18.13±1.29
ZZ	7.14±5.50	6.37±4.91	0.66±0.51	14.17±10.92
Wγ	25.18±8.65	0.00±0.00	23.36±4.47	48.53±12.38
DY$\rightarrow \tau\tau$	2.13±0.67	2.45±0.75	4.87±1.15	9.45±1.67
DY$\rightarrow ee + \mu\mu$	41.77±5.71	14.84±2.78	14.64±2.39	71.25±7.76
Fakes	32.89±9.98	36.18±11.56	70.34±21.45	139.42±36.23
Total background	175.69±25.46	114.06±16.17	247.92±28.03	537.67±63.24
$t\bar{t}$ ($\sigma = 7.4$ pb)	0.36±0.05	0.25±0.04	0.64±0.06	1.25±0.10
Total SM expectation	176.05±25.48	114.32±16.19	248.55±28.06	538.92±63.30
Observed	178	134	237	549

CDF II preliminary (5.1 fb^{-1})

N$jet = 1$ $t\bar{t}$ Control Sample before H_T and opposite lepton charge requirement				
Source	ee	$\mu\mu$	eμ	$\ell\ell$
WW	14.22±1.64	12.36±1.43	30.70±3.49	57.28±6.47
WZ	7.93±0.36	3.99±0.20	6.49±0.30	18.40±0.79
ZZ	2.42±1.87	2.36±1.82	1.46±1.12	6.24±4.81
Wγ	6.53±2.60	0.00±0.00	7.79±1.99	14.32±4.01
DY$\rightarrow \tau\tau$	8.06±1.47	7.31±1.43	15.99±2.85	31.37±5.37
DY$\rightarrow ee + \mu\mu$	39.78±6.99	18.83±3.52	5.97±1.62	64.58±10.64
Fakes	22.53±6.85	27.33±8.52	97.49±29.62	147.35±40.23
Total background	101.47±15.40	72.18±11.51	165.89±31.24	339.54±50.58
$t\bar{t}$ ($\sigma = 7.4$ pb)	7.69±0.42	7.16±0.39	17.23±0.87	32.08±1.57
Total SM expectation	109.16±15.76	79.34±11.84	183.11±32.04	371.62±52.09
Observed	117	89	186	392

Table I: Summary tables for the 5.1 fb^{-1} Inclusive DIL sample with 0-jet (top) and 1-jet (bottom). The top and bottom tables show the total number of background, SM expectation and data candidate events, divided by lepton flavor contribution for 0-jet (top) and 1-jet (bottom) bins. The quoted uncertainties are the sum of the statistical and systematics uncertainty.

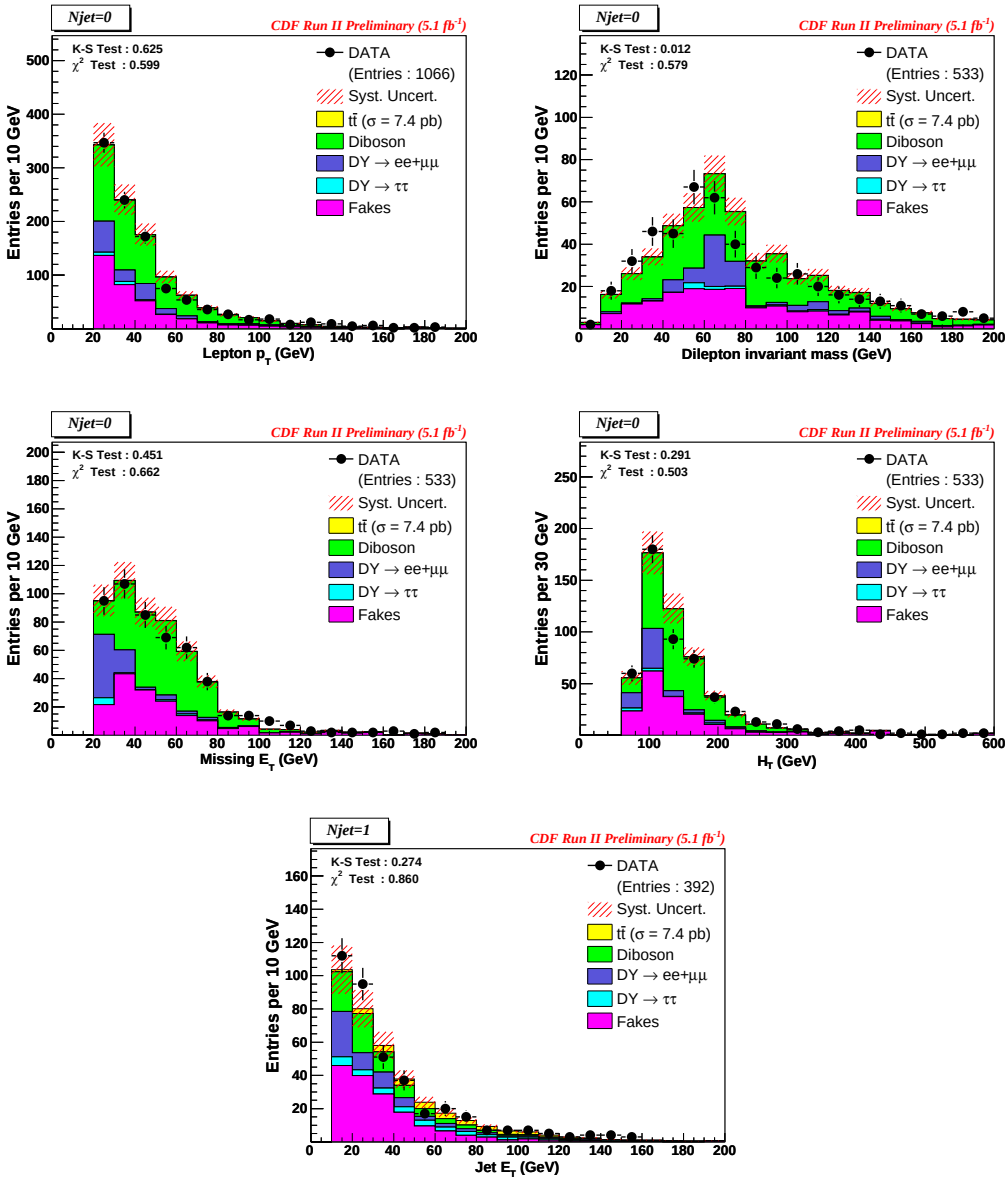

Figure 6.1: From top left to bottom right: background and top signal predictions, overlaid to data, for the lepton transverse energy spectrum, the dilepton invariant mass, $\not\!\!E_T$, H_T and jet transverse energy distributions in 5.1 fb^{-1} 0-jet events.

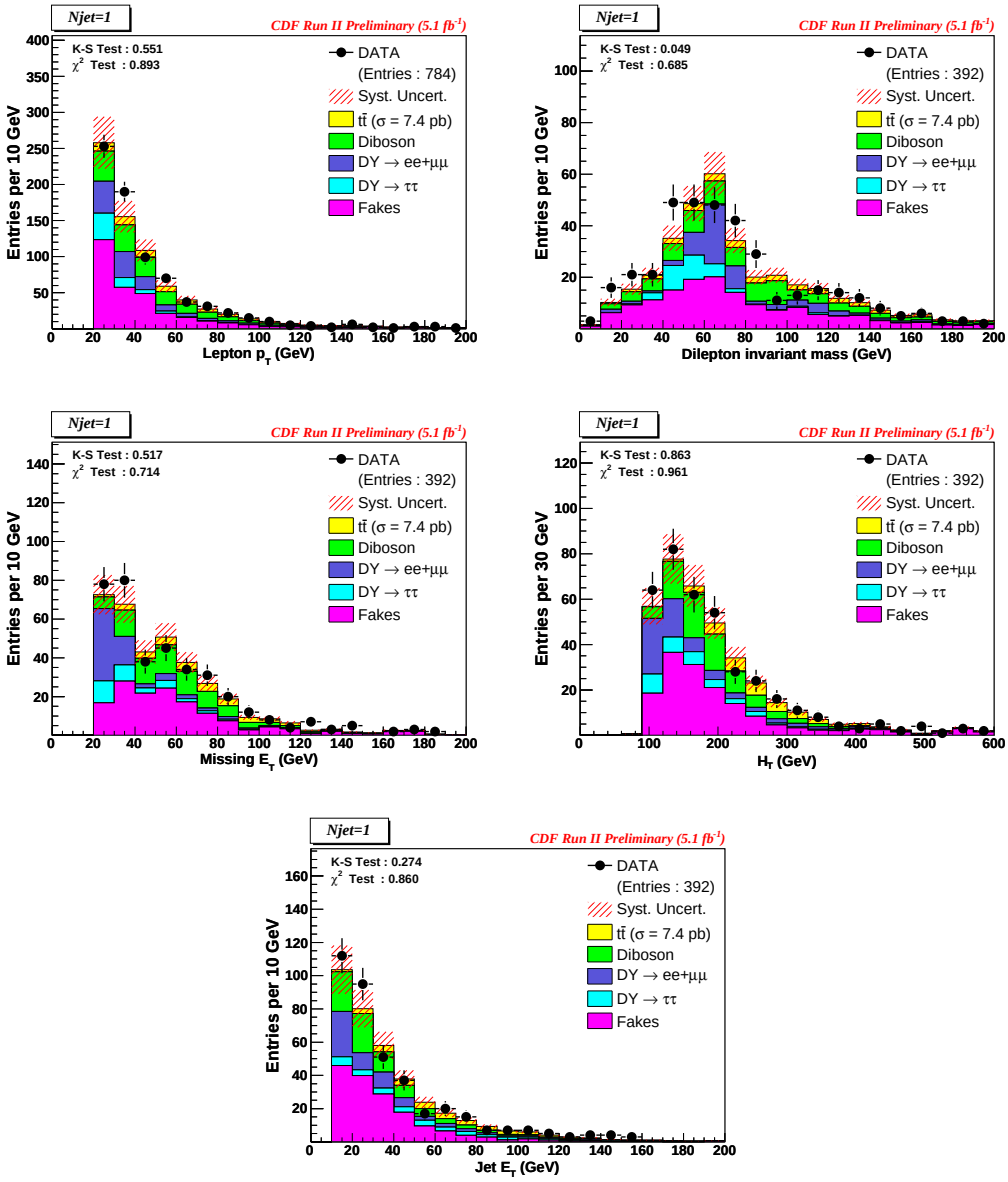

Figure 6.2: From top left to bottom right: background and top signal predictions, overlaid to data, for the lepton transverse energy spectrum, the dilepton invariant mass, $\not\!\!E_T$, H_T and jet transverse energy distributions in 5.1 fb^{-1} 1-jet events.

CDF II preliminary (5.1 fb^{-1})

N$jet \geq 2$ Control Sample before H_T and opposite lepton charge requirement				
Source	ee	$\mu\mu$	eμ	$\ell\ell$
WW	4.92±0.85	3.96±0.69	10.34±1.74	19.22±3.20
WZ	2.66±0.35	1.37±0.18	2.33±0.30	6.36±0.81
ZZ	1.33±1.04	1.00±0.78	0.83±0.65	3.17±2.46
Wγ	1.13±0.75	0.00±0.00	2.25±0.94	3.38±1.33
DY$\rightarrow \tau\tau$	5.61±1.43	6.16±1.57	13.01±3.30	24.78±6.19
DY$\rightarrow ee + \mu\mu$	25.94±7.19	14.32±4.22	3.17±1.32	43.43±11.78
W+jet fakes	19.27±5.78	30.53±9.16	89.31±26.79	139.12±37.63
Total background	60.86±12.42	57.35±11.62	121.24±27.76	239.45±45.11
$t\bar{t}$ ($\sigma = 7.4$ pb)	59.40±2.87	57.59±2.78	135.88±6.50	252.88±12.04
Total SM expectation	120.26±15.20	114.94±14.32	257.12±34.20	492.32±57.08
Observed	111	123	242	476

Table II: Summary table for the 5.1 fb^{-1} Inclusive DIL sample with 2 or more jets. It shows the total number of background, the total SM expectation and data candidate events, divided by lepton flavor contribution, 2 jet bins before the H_T and the opposite lepton charge requirement events. The quoted uncertainties are the sum of the statistical and systematics uncertainty.

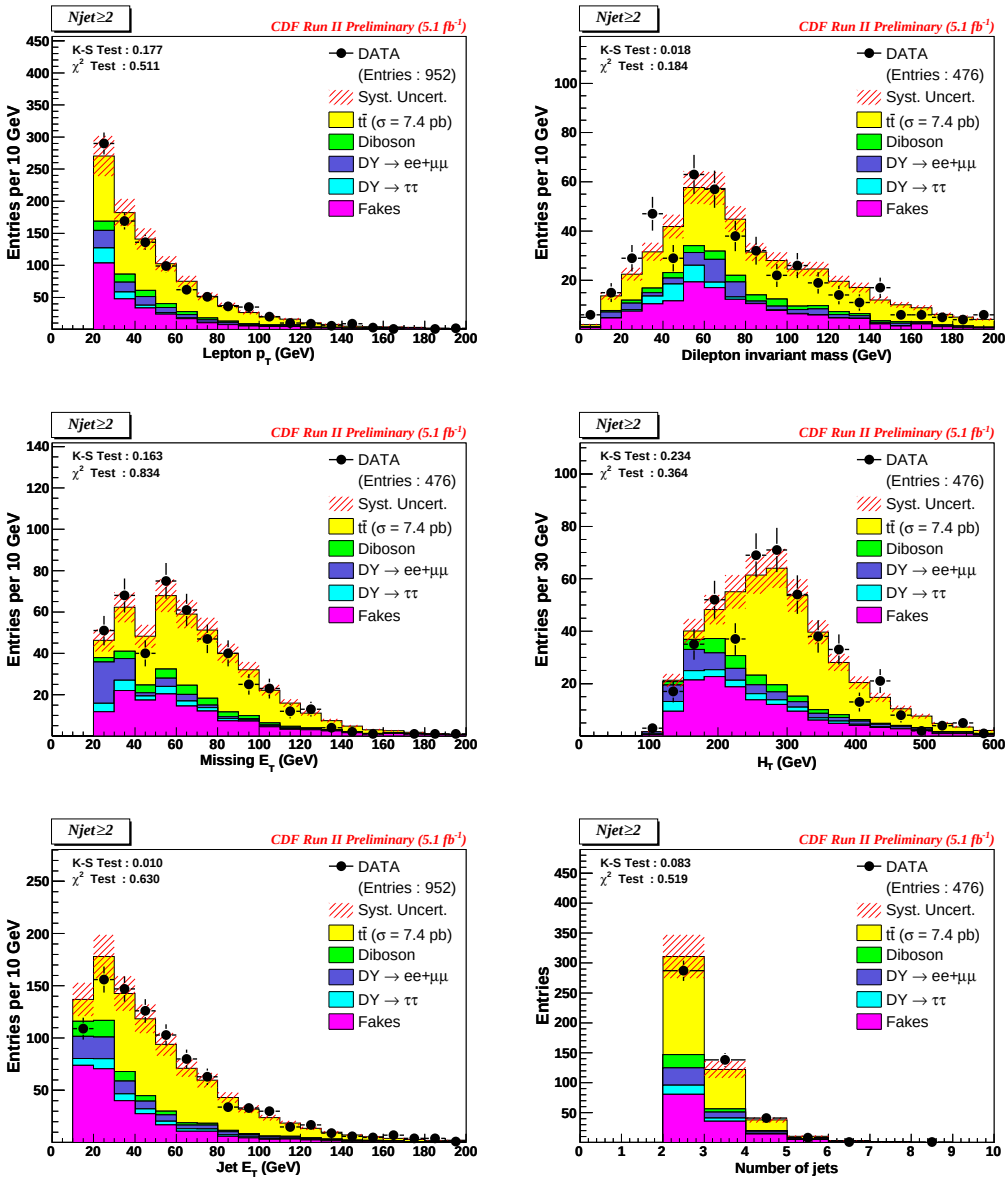

Figure 6.3: From top left to bottom right: background and top signal predictions, overlaid to data, for the lepton transverse energy spectrum, the dilepton invariant mass, $\not\!\!E_T$, H_T, jet multiplicity and jet transverse energy distributions in 5.1 fb^{-1}2-jet before the H_T and the opposite lepton charge requirement events.

Finally, Tables III give the observed number of DIL candidate events versus the background and $t\bar{t}$ signal expectations for the full 5.1 fb^{-1} samples. The total SM expectation is well in agreement with the observed 343 events for the 5.1 fb^{-1} respectively. Figures 6.4 show the $t\bar{t}$ and background prediction, overlaid to the data, for some candidate events kinematic distributions.

CDF II preliminary (5.1 fb^{-1})

$t\bar{t}$ Signal Events per Dilepton Flavor Category before b-tagging				
Source	ee	$\mu\mu$	eμ	$\ell\ell$
WW	3.08±0.64	2.68±0.56	5.96±1.21	11.72±2.36
WZ	1.56±0.25	0.98±0.16	0.93±0.16	3.48±0.55
ZZ	1.02±0.79	0.82±0.64	0.42±0.33	2.25±1.75
Wγ	0.42±0.44	0.00±0.00	0.00±0.00	0.42±0.44
DY$\rightarrow \tau\tau$	2.88±0.55	2.97±0.56	6.42±1.16	12.26±2.18
DY$\rightarrow ee + \mu\mu$	11.54±2.22	8.40±1.62	2.45±1.09	22.40±3.24
Fakes	7.23±2.29	12.85±4.22	33.20±10.25	53.27±14.70
Total background	27.73±4.28	28.69±5.04	49.38±10.85	105.80±17.24
$t\bar{t}$ ($\sigma = 7.4$ pb)	54.65±2.65	54.92±2.65	127.55±6.10	237.13±11.30
Total SM expectation	82.38±6.63	83.61±7.46	176.93±16.80	342.92±28.30
Observed	74	96	173	343

CDF II preliminary (5.1 fb^{-1})

Pre−tagged Control Sample and Signal Events per Jet Multiplicity					
Source	0 jet	1 jet	≥ 2 jet	H_T	H_T, OS
WW	236.71±21.58	57.28±6.47	19.02±4.02	12.04±2.42	11.72±2.36
WZ	18.13±1.29	18.40±0.79	6.37±0.95	5.03±0.79	3.48±0.55
ZZ	14.17±10.92	6.24±4.81	3.17±2.48	2.70±2.10	2.25±1.75
Wγ	48.53±12.38	14.32±4.01	3.26±1.29	0.42±0.44	0.42±0.44
DY$\rightarrow \tau\tau$	9.45±1.67	31.37±5.37	21.95±5.16	12.55±2.23	12.26±2.18
DY$\rightarrow ee + \mu\mu$	71.25±7.76	64.58±10.64	43.53±11.81	22.40±3.24	22.40±3.24
Fakes	139.42±36.23	147.35±40.23	135.37±36.87	94.51±26.07	53.27±14.70
Total background	537.67±63.24	339.54±50.58	232.66±44.46	149.64±27.81	105.80±17.24
$t\bar{t}$ ($\sigma = 7.4$ pb)	1.25±0.10	32.08±1.57	253.10±12.05	243.39±11.59	237.13±11.30
Total SM expectation	538.92±63.30	371.62±52.09	485.77±56.39	393.03±39.23	342.92±28.30
Observed	549	392	476	383	343

Table III: Summary tables for the 5.1 fb^{-1} signal candidate DIL sample. The top table shows the total number of background, SM expectation and data candidate events, divided by lepton flavor contribution. The bottom table shows the same contributions in the 0, 1, 2 jet bins and 2 jet bins after the H_T and the opposite lepton charge requirement. The quoted uncertainties is the sum of the statistical and systematics uncertainty.

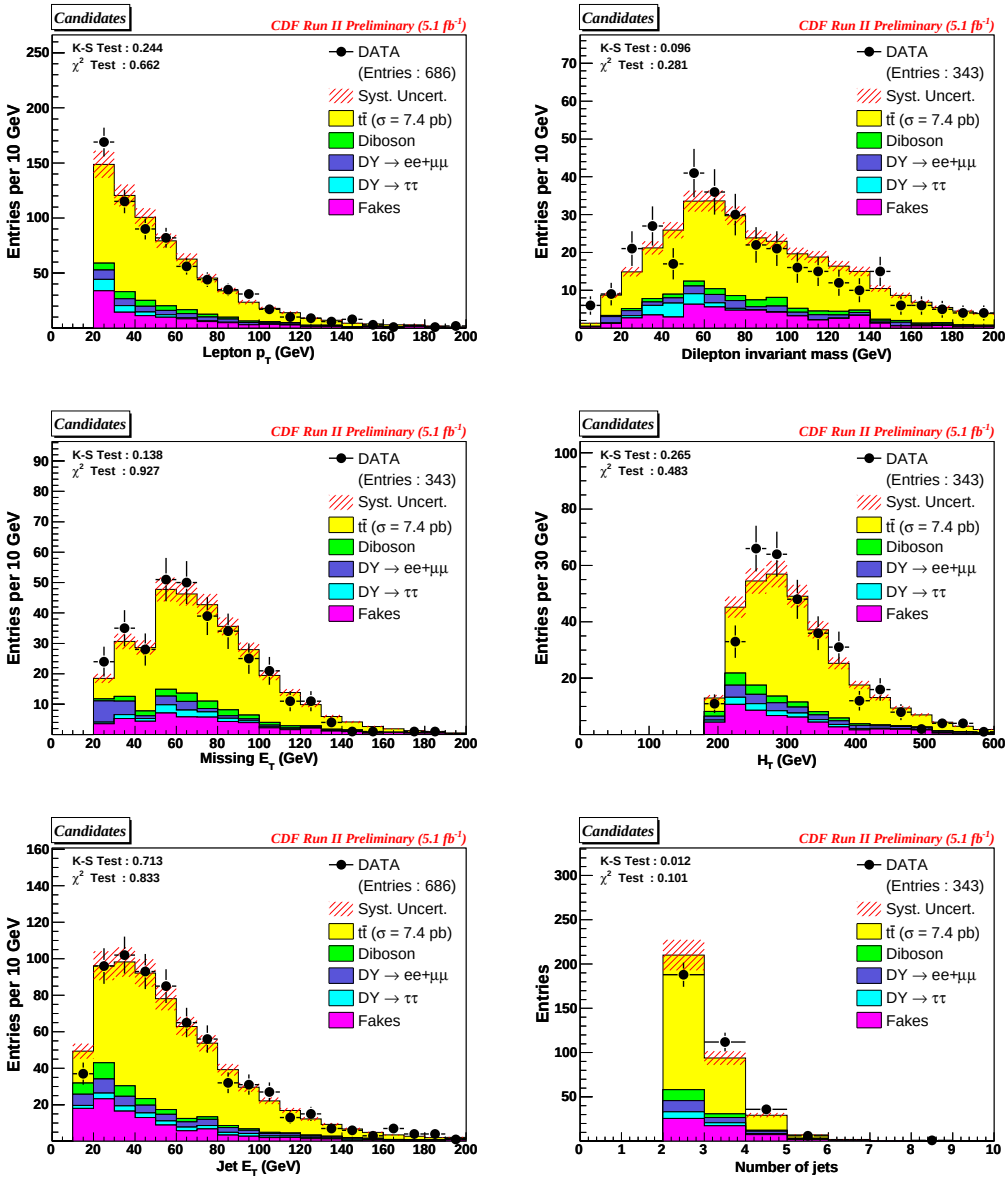

Figure 6.4: From top left to bottom right: background and top signal predictions, overlaid to data, for the lepton transverse energy spectrum, the dilepton invariant mass, $\not\!\!E_T$ and H_T distributions in 5.1 fb^{-1} top DIL candidate events.

6.2 b-tagged Signal Candidate Events

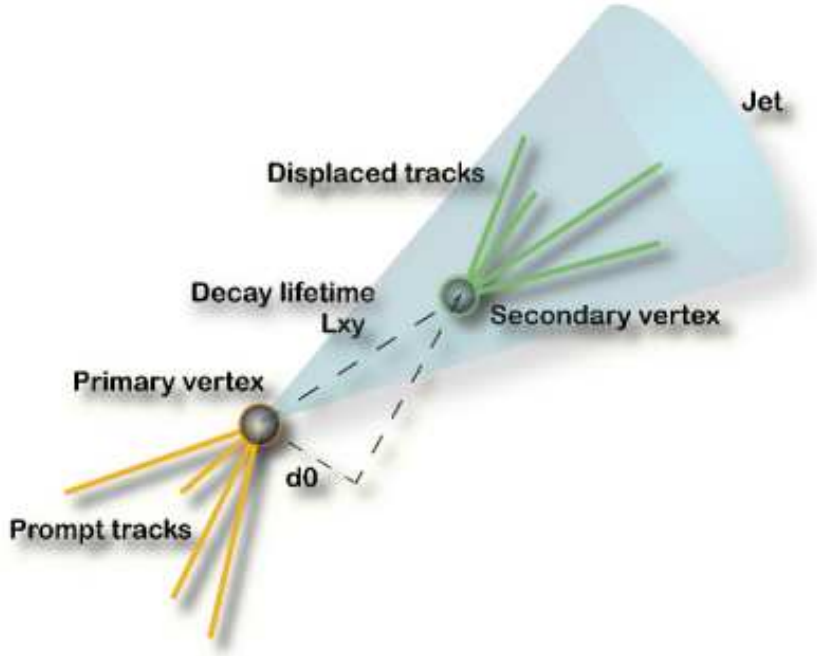

Figure 6.5: Illustration of the secondary vertex $b-$tagging

In this section we describe how to apply the Tight SecVtx $b-$tagging from the pretag samples. Figure6.5 shows the secondary vertex $b-$tagging in the transverse plane of a single top quark event forward jet escapes down beampipe. Secondary vertices are reconstructed by selecting tracks within the jet that have a large impact parameter and satisfy some tracking quality requirements. In a first pass, the algorithm attempts to reconstruct vertices with at least 3 tracks. If none is found, it tries to reconstruct 2 track vertices with more stringent cuts on the track selection. A jet is $b-$tagged if a secondary vertex is reconstructed with a significant decay length in the transverse plane.

The Method II approach is used to estimate the Z+Light Flavor using mistag matrix applied to Alpgen Monte Carlo events. We take the mistag matrix of jetMistagJun2009.

The heavy flavor scale factor is applied as the below table from the analysis of stop search in the dilepton channel(CDF note 9417). Due to technical difficulties we were not able to generate the Drell-Yan + c$\bar{c}$ events below the Z mass peak region, thus we used only $b\bar{b}$ Monte Carlo to represent Z + heavey flavor events and then rescale heavy flavor background using these scale factors. For the heavy flavor rescale method, the kinematic distributions before missing E_T cut and Zveto cut are shown in Figure 6.6. The data is consistent with our expectation. The Heavey Flavor scale factors in Table IV are used from Stop quarks search analysis in dilepton channel [47]. And the scale factor for the tight SecVtx tag is taken from CDF High P_T $b-$tag ground as 0.95 $\pm$ 0.04.

	1 jet	$\geq$ 2 jet
ee	2.31$\pm$0.10	1.44$\pm$0.10
$\mu\mu$	2.90$\pm$0.11	1.43$\pm$0.10
Total	2.57$\pm$0.15	1.44$\pm$0.07

Table IV: Jet bin correction factors for Z + heavy flavor events without Z + c$\bar{c}$ events. The uncertainty on the total scale factor takes into account statistical uncertainty added in quadrature to half of the discrepancy between ee and $\mu\mu$ channels.

Table V and Table VI shows the signal and background after SecVtx $b-$tagging for 1-jet control events and signal candidate events respectively. We

CDF II preliminary (4.8 fb^{-1})

N$jet = 1$ Control Sample with the tight SecVtx $b-$tag				
Source	ee	$\mu\mu$	eμ	$\ell\ell$
WW	0.13±0.04	0.14±0.04	0.24±0.06	0.51±0.09
WZ	0.03±0.01	0.04±0.01	0.03±0.01	0.10±0.02
ZZ	0.03±0.02	0.03±0.02	0.01±0.01	0.06±0.05
DY+LF	0.54±0.04	0.12±0.01	0.36±0.03	1.02±0.08
DY+HF	0.45±0.04	0.27±0.02	0.16±0.01	0.88±0.07
Fakes	0.16±0.06	0.18±0.09	1.42±0.57	1.77±0.63
Total background	1.34±0.13	0.79±0.12	2.22±0.58	4.35±0.69
$t\bar{t}$ ($\sigma = 7.4$ pb)	2.82±0.21	2.71±0.20	6.18±0.42	11.71±0.76
Total SM expectation	4.15±0.32	3.51±0.29	8.40±0.92	16.06±1.37
Observed	4	6	6	16

Table V: Top table of background estimates, $t\bar{t}$ predictions and observed events in data corresponding to an integrated luminosity of 4.8 fb^{-1} for 1 jet control sample with SecVtx $b-$tagging before H_T and opposite lepton charge requirement. The quoted uncertainties are the sum of the statistical and systematics uncertainty.

take the Tight SecVtx $b-$tagging scale fator 0.95 ± 0.04 from CDF high p$_T$ $b-$tag group.

When we apply $b-$tagging, the total background number 111.59 ± 17.33 in the pretag signal candidate events is significantly reduced by 8.30 ± 1.68. Total expected signal candidate is 138.32 ± 9.77 and we observed signal candidate event 137.

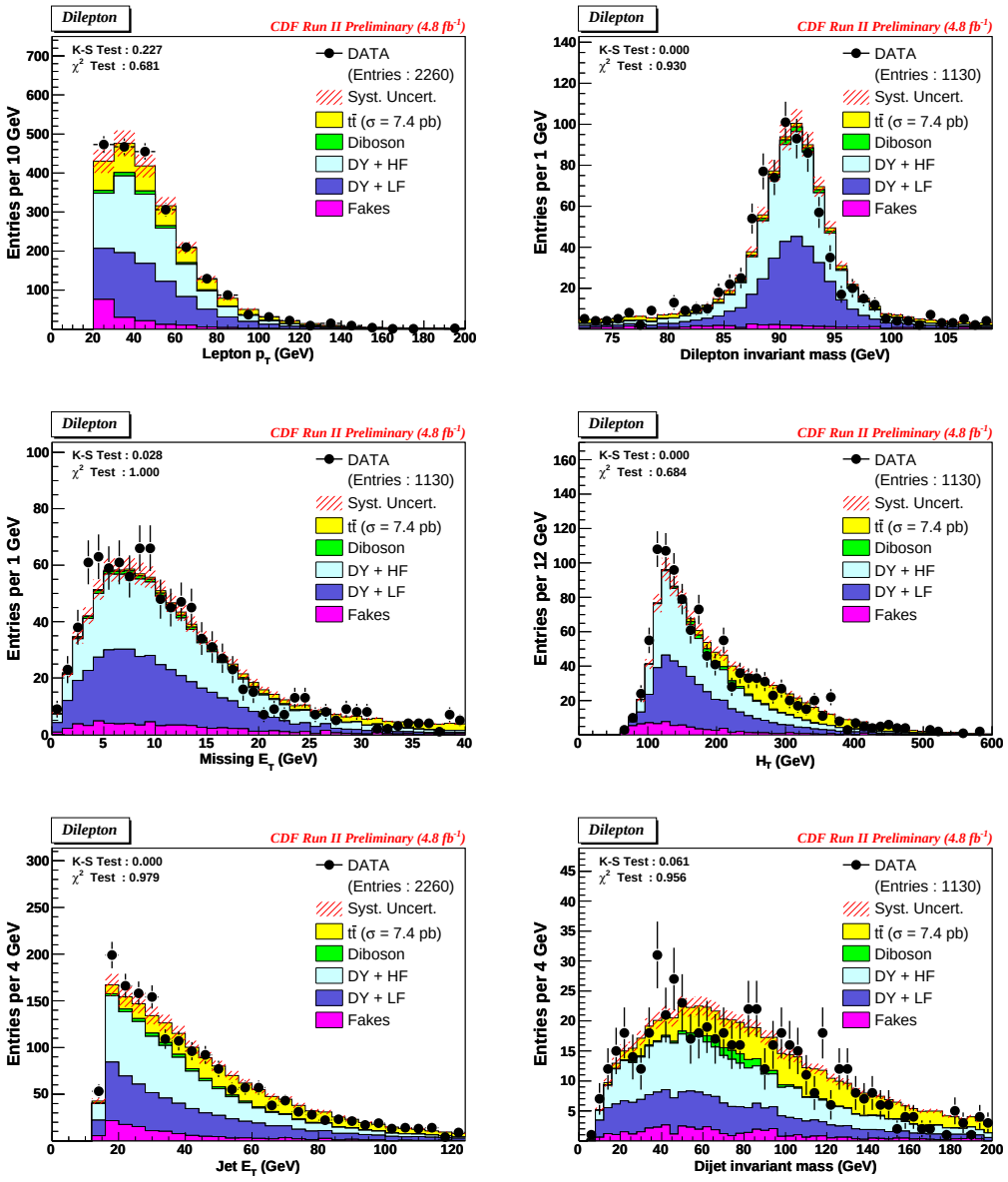

Figure 6.6: From top left to bottom right: background and top signal predictions, overlaid to data, for the lepton transverse energy spectrum, the dilepton invariant mass, $\not\!\!E_T$, H_T, jet multiplicity and jet transverse energy distributions in 4.8 fb^{-1} top DIL signal candidate events with the Tight SecVtx $b-$tag.

CDF II preliminary (4.8 fb^{-1})

$t\bar{t}$ Signal Events with the tight SecVtx $b-$tag				
Source	ee	$\mu\mu$	eμ	$\ell\ell$
WW	0.08±0.03	0.09±0.04	0.21±0.06	0.37±0.10
WZ	0.02±0.01	0.03±0.01	0.03±0.01	0.08±0.02
ZZ	0.08±0.06	0.07±0.06	0.02±0.02	0.17±0.14
DY+LF	0.51±0.05	0.60±0.05	0.28±0.03	1.39±0.12
DY+HF	0.51±0.04	1.41±0.11	0.37±0.03	2.28±0.18
Fakes	1.17±0.48	0.90±0.39	3.39±1.12	5.46±1.59
Total background	2.36±0.51	3.10±0.46	4.29±1.13	9.75±1.68
$t\bar{t}$ ($\sigma = 7.4$ pb)	30.22±1.91	29.63±1.87	70.10±4.38	129.96±8.10
Total SM expectation	32.59±2.32	32.73±2.25	74.39±5.42	139.71±9.66
Observed	22	44	71	137

Table VI: Summary table by lepton flavor content with SecVtx $b-$tagging, of background estimates, $t\bar{t}$ predictions and observed events in data corresponding to an integrated luminosity of 4.8 fb^{-1} for $t\bar{t}$ signal events. The quoted uncertainties are the sum of the statistical and systematics uncertainty.

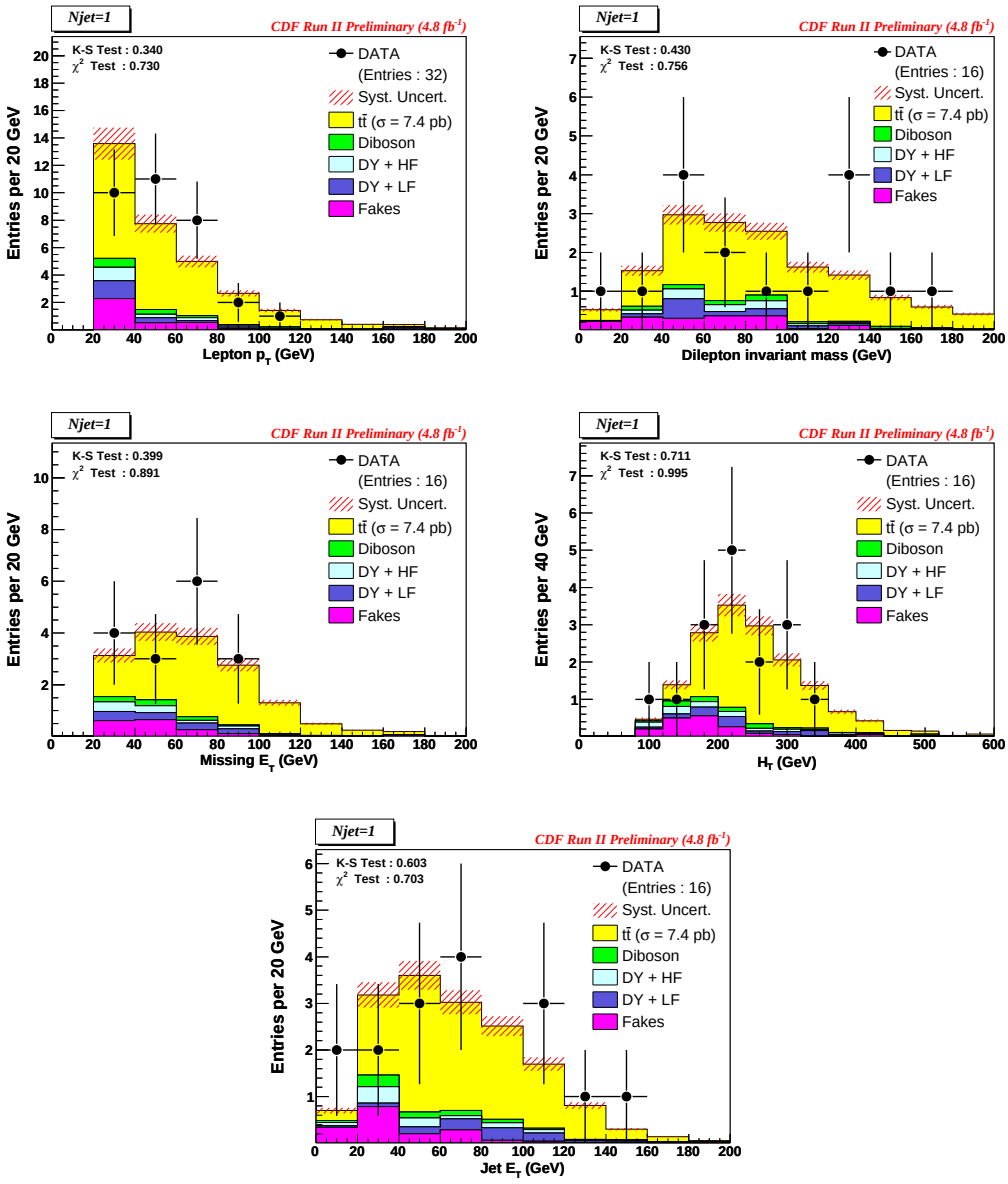

Figure 6.7: From top left to bottom right: background and top signal predictions, overlaid to data, for the lepton transverse energy spectrum, the dilepton invariant mass, $\not\!\!E_T$, H_T and jet transverse energy distributions in 4.8 fb^{-1} 1-jet $b-$tagged evensts.

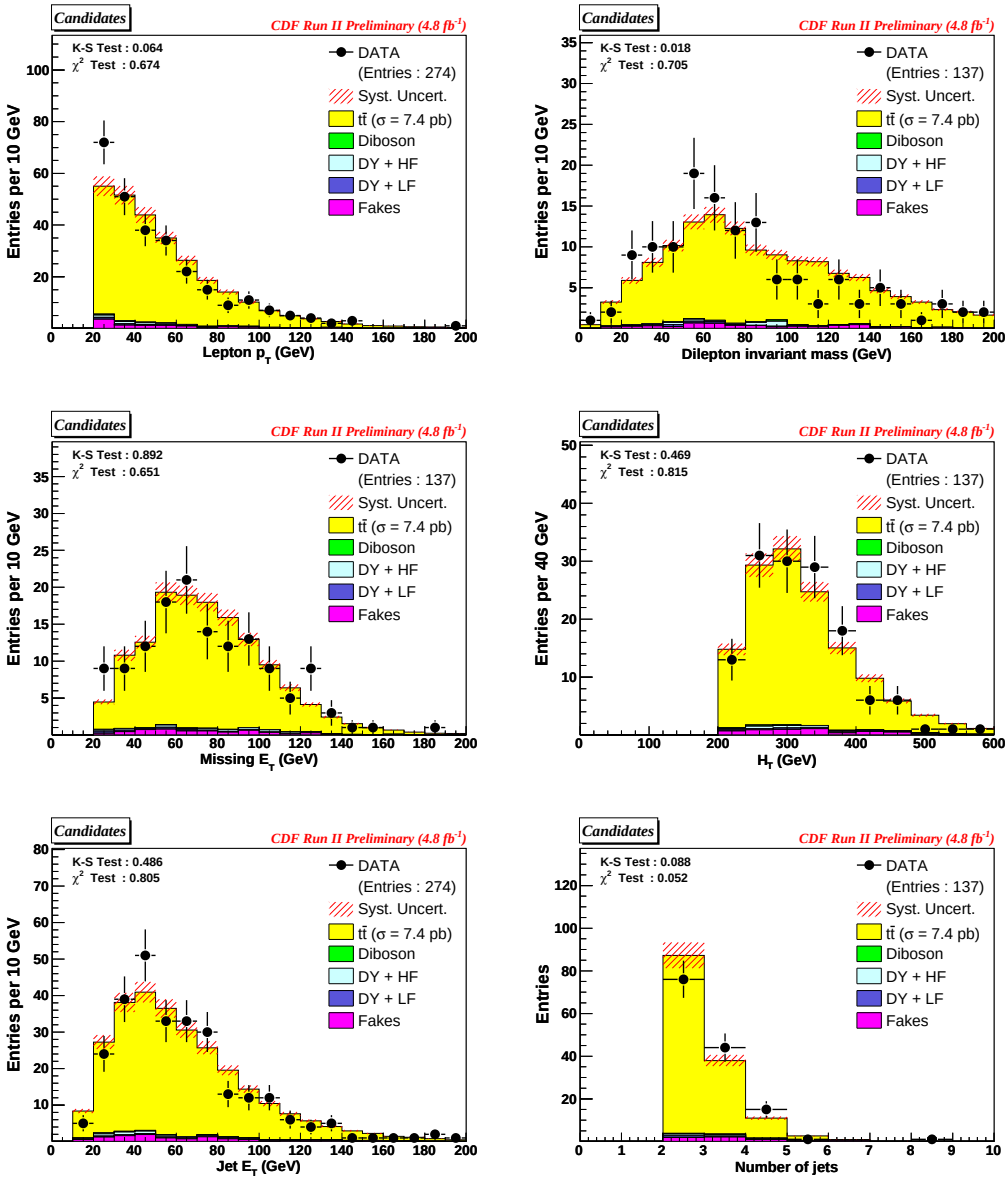

Figure 6.8: From top left to bottom right: btagged background and top signal predictions before the missing E_T cut and Zveto cut, overlaid to data, for the lepton transverse energy spectrum, the diljet invariant mass, $\not\!\!E_T$, H_T, jet multiplicity and jet transverse energy distributions in 4.8 fb^{-1} top DIL signal candidate events with $b-$tag.

6.3 Systematics Uncertainties

6.3.1 Lepton ID Uncertainties

In this section we briefly review the systematics studies performed for the signal and backgrounds MC estimates.

A common systematics to signal and background MC estimates comes from the uncertainty on the lepton ID scale factors. These factors are measured in Z events, which have a limited jet activity. CDF-8503 limit possible systematic variations in the lepton scale factor due to extra-jet activity to 1.1%. We assign a conservative systematic of 2% to the lepton ID scale factors of table I and assumed that it is 100% correlated among the different MC samples. So the total lepton ID systematic uncertainty turn to be 2.2% by adding 0.1% systematic uncertainty due to the additional scale factor for CMP, CMU, CMIO.

6.3.2 Jet Energy Scale

Another common systematics comes from jet energy scale uncertainties. This is measured using the change in the default acceptance obtained from shifting the jet corrections up and down by 1σ of their systematic uncertainty. Although the central value for this systematic source is calculated separately for each MC background sample and, within each sample, for each jet multiplicity bin (see Table VII), a 100% correlation is assumed when propagating this systematic uncertainty to final cross section.

A final source of correlated systematic, this time affecting only MC-based backgrounds, is the uncertainty on the N_{jet} scale factor.

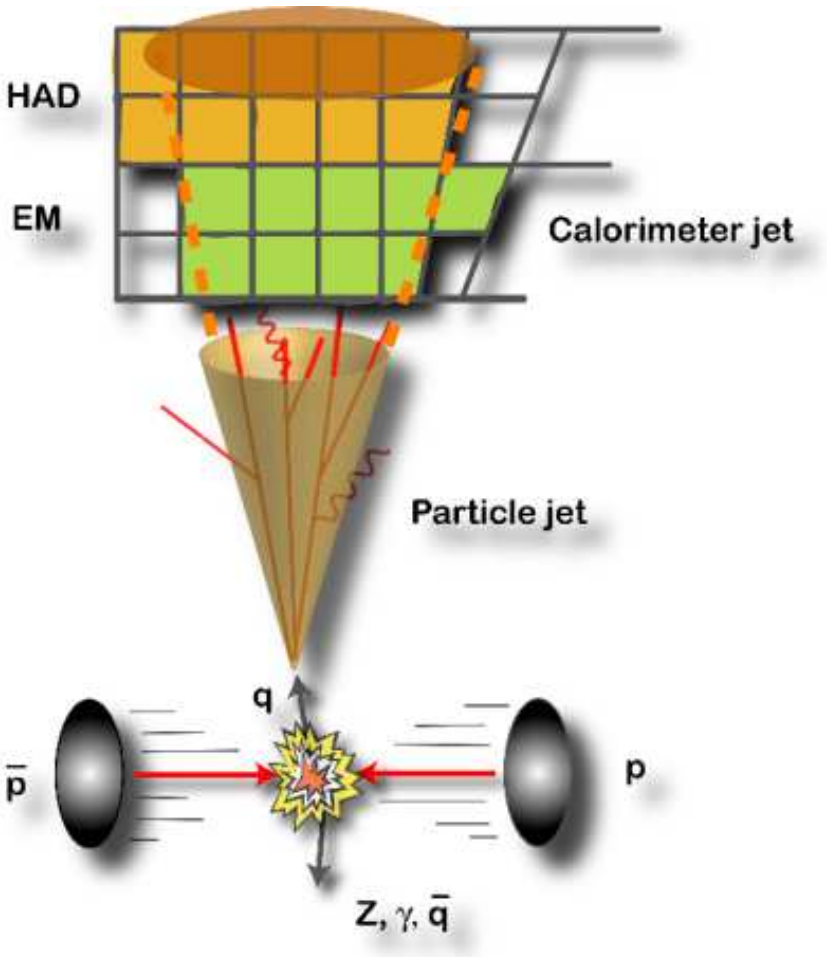

Figure 6.9: Jet energy deposit in EM and HAD calorimeter

Source	0j(%)	1j(%)	$\geq$ 2j(%)	H_T, OS(%)
`ttop25`	30.0	13.3	2.6	3.3
`DY/`$Z \to \tau\tau$`(Alpgen)`	7.3	15.4	22.5	16.3
`ihht1a`	3.2	7.3	19.1	17.9
`jhht1a`	6.1	2.1	14.3	15.2
`khht1a`	3.6	3.0	12.7	12.5
`rewk28/29`	2.7	5.6	10.0	10.0

Table VII: Systematics uncertainties, as percentage of the raw Monte Carlo acceptance, due to JES systematic variation for the different Standard Model processes.

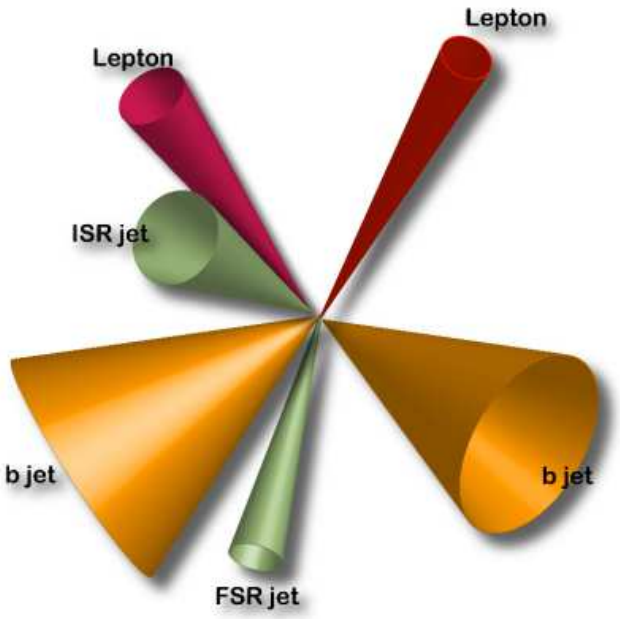

Figure 6.10: Jets due to the $t\bar{t}$ decay and to the ISR and FSR

Uncorrelated sources of systematic uncertainties are the jet fake systematics, the cross section uncertainties and a 30% systematic uncertainty on the conversion rejection scale factor. For the signal acceptance, we estimated systematic uncertainties due to multiple effects: MC generator, ISF/FSR variations, PDF's uncertainty and Color reconnection. The first two components are calculated by comparing the raw MC acceptance of the default $t\bar{t}$ sample (`ttop25`) to specialized MC samples. Details on the PDF's uncertainty calculation are contained in the next section. And the systematics uncertainty due to the Color reconnection(CR) is just added in this analysis. We compare two different CR sample such ad Tune Apro (`ctopsd`) and the Tune ACRpro (`ctopse`). A summary tables of the systematic uncertainties affecting the $t\bar{t}$ acceptance is shown in Table X.

6.3.3 Systematics due to PDF uncertainties

The CTEQ5L parton distribution function (PDF) are used in the default "ttop25" Pythia sample. To evaluate the systematics due to PDF uncertainties, we calculate the acceptance variation from the default acceptance when we use different PDF sets, namely MRST72, MRST75, CTEQ6L, CTEQ6L1 and CTEQ6M. To calculate the dependence of the acceptance on the different PDF sets, we adopt the weighted MC method [46]. In this method, we reweigh each event of a MC sample we already have, instead of generating a different set of MC events for each different PDF sets. We first obtain the parton momentum fractions x_1 and x_2 and Q^2 for each $t\bar{t}$ MC event, next we calculate the relative probability of the event for the PDF set we are considering by dividing it by the probability of the same event for the default PDF

set (CTEQ5L). We use the relative probability as a weight for each event, and the sum of these weights for accepted events over the sum of the weights for the whole generated sample gives a rough estimate of the acceptance with each different PDF set. Table VIII summarizes the resulting acceptances and variations from the default acceptance using CTEQ5L.

We estimate the effect of different PDF set to be $\pm 0.1441\%$ by comparing the acceptance of MRST72 with CTEQ5L which gives the largest effect on the acceptance in the table. Likewise, we estimate the effect of α_s uncertainty to be $\pm 0.1633\%$ by comparing MRST72 with MRST75.

PDF	Acceptance(%)	Difference(%)	Description
CTEQ5L	0.7558	—	default PDF set
MRST72	0.7568	0.1441	default MRST
MRST75	0.7581	0.3076	MRST lower α_s
CTEQ6L	0.7567	0.1289	different α_s
CTEQ6L1	0.7561	0.0450	different α_s
CTEQ6M	0.7570	0.1686	

Table VIII: Signal acceptance for different PDF sets evaluated using the weighted MC method. Differences from the default "ttop25" acceptance using CTEQ5L are also listed.

In the next step, we estimate the effect due to the variation of 20 independent parameters of the CTEQ6M PDF fit. We evaluate the acceptance, calculated using the weighted MC method as well, by shifting up and down by 1σ the uncertainties of 20 eigenvector directions within CTEQ6M. Table IX summarizes the central value for the acceptances using the weighted MC method and its percentage difference with respect to the default CTEQ6M

Eigenvector index	Acceptance(%) $+1\sigma$ up	Diff.(%)	Acceptance(%) -1σ down	Diff.(%)
# 1	0.7573	0.0400	0.7567	-0.0402
# 2	0.7570	-0.0073	0.7571	0.0073
# 3	0.7571	0.0136	0.7569	-0.0122
# 4	0.7570	-0.0021	0.7571	0.0029
# 5	0.7569	-0.0120	0.7571	0.0116
# 6	0.7577	0.0897	0.7564	-0.0893
# 7	0.7561	-0.1234	0.7579	0.1115
# 8	0.7583	0.1705	0.7559	-0.1515
# 9	0.7576	0.0756	0.7565	-0.0687
# 10	0.7574	0.0511	0.7566	-0.0507
# 11	0.7570	-0.0091	0.7570	-0.0083
# 12	0.7566	-0.0609	0.7570	-0.0058
# 13	0.7576	0.0819	0.7562	-0.1108
# 14	0.7574	0.0460	0.7569	-0.0141
# 15	0.7580	0.1232	0.7534	-0.4763
# 16	0.7566	-0.0503	0.7568	-0.0366
# 17	0.7569	-0.0129	0.7565	-0.0730
# 18	0.7571	0.0151	0.7572	0.0166
# 19	0.7560	-0.1378	0.7570	-0.0079
# 20	0.7567	-0.0489	0.7573	0.0402

Table IX: Signal acceptance using the the CTEQ6M PDF's shifted up and down by 1σ along 20 eigenvector directions. Each acceptance is evaluated using the weighted MC method. The percentage difference with respect to the CTEQ6M central value acceptance of 0.7570% is also listed.

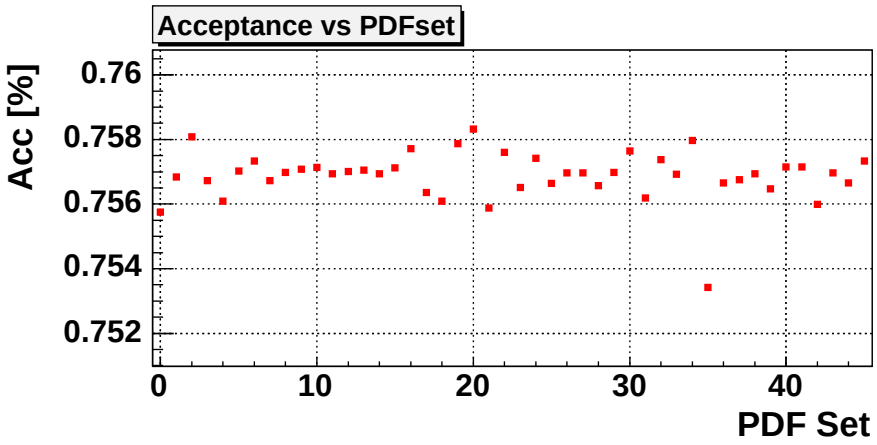

Figure 6.11: Measured acceptance in the 46 PDF-weighted ttop25 samples. The first point shows the default CTEQ5L's acceptance. And from 2nd to 6th points are for MRST72, MRST75, CTEQ6L, CTEQ6L1, CTEQ6M PDF set. From 7th to 46th points are corresponding to the PDF sets which have the 20 different eigenvector shifts with respect to the default CTEQ6M.

acceptance for each of the 20 eigenvector shifts.

The sum in quadrature of the all of the positive and negative variations gives us a value of $+0.2938\%$ and -0.5730%, respectively, for the systematic uncertainty due to uncertainties in 20 parameters of PDF.

The sum in quadrature of the systematics from the uncertainty of MRST, α_s, and 20 parameters is $+0.3363\%$ to the positive side and -0.5960% to the negative side. We quote 0.596% which is larger one as the systematic due to PDF uncertainties.

6.4 Results of the $t\bar{t}$cross section measurement

For pre−tagged signal candidate events, using the numbers in Table III

Source	Systematic Error (%)
Lepton ID	2.2
MC Generator	1.9
ISR/FSR	1.3
PDF's	0.6
Color Reconnection	1.2
Jet corrections	3.3
Total	4.8

Source	Systematic Error (%)
Lepton ID	2.2
MC Generator	1.9
ISR/FSR	1.3
PDF's	0.6
Color Reconnection	1.2
Jet corrections	3.3
b-tagging	4.1
Total	6.3

Table X: The left table shows Summary of systematic uncertainties for pre−tagged events and the right table for b-tagged events. The total error is the sum in quadrature of each contribution

for the numerator and the denominator quoted in Section 4.2, we measure:

$$\sigma_{t\bar{t}} = 7.40 \pm 0.58 \pm 0.63 \pm 0.45 \text{ pb} \tag{6.1}$$

for the 5.1 fb^{-1} data sample, after propagating the acceptance and background systematics uncertainties.

The last error is 6% uncertainty coming from luminosity measurement.

For $b-$tagged signal candidate events, using the numbers in Table VI, we measure:

$$\sigma_{t\bar{t}} = 7.25 \pm 0.66 \pm 0.47 \pm 0.44 \text{ pb} \tag{6.2}$$

for the 4.8 fb^{-1} data sample, after propagating the acceptance and background systematics uncertainties.

In the Figure 6.12, the left plot shows the number of candidate events in 0, 1, $\geq$2jet events together with a histogram representing the component of the background for the pre$-$tagged events. And the right plot shows the number $b-$tagged events in 1jet control region and signal candidate events. The yellow band gives the $t\bar{t}$ contribution for a cross section of 7.4 pb. The red hatched area is the uncertainty in the total background estimate.

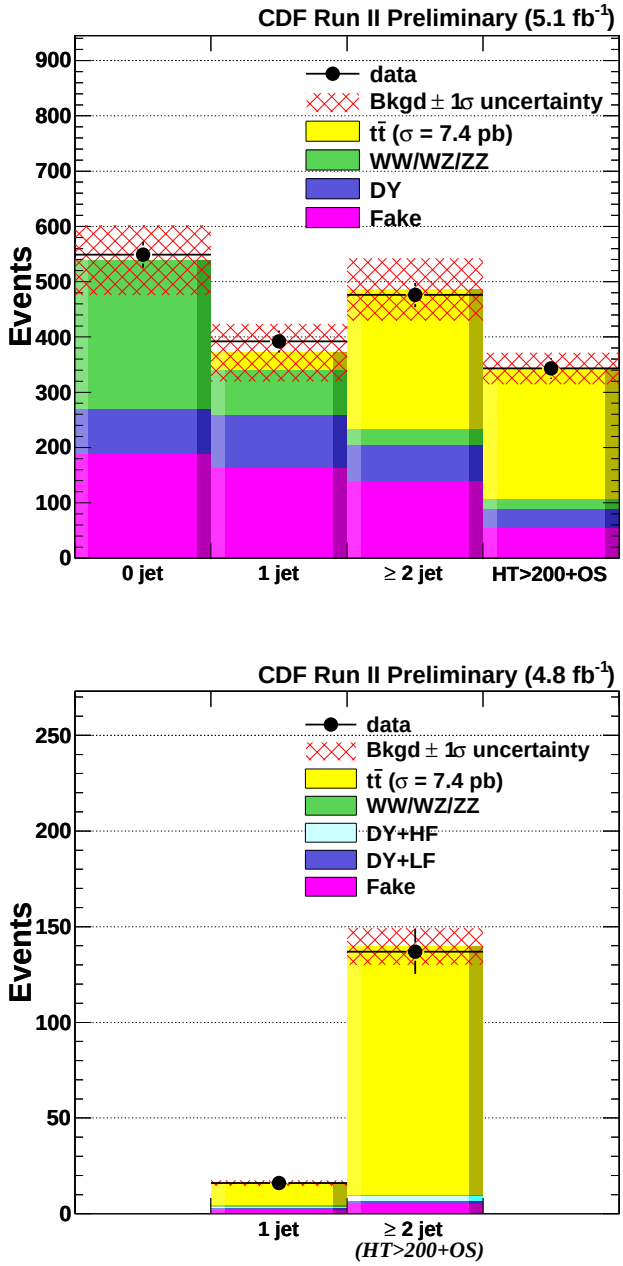

Figure 6.12: Observed dilepton candidate events (black point) by jet multiplicity for pre−tagged (top) and b−tagged (bottom) events. The colored histogram represents the background contribution for an assumed $\sigma_{t\bar{t}} = 7.4$ pb. The red hatched area is the uncertainty in the total background estimate.

Chapter 7

Measurement of W boson polarization in top quark decay

7.1 Reconstruction of t and $\bar{t}$ four vectors

Method for reconstruction of t and $\bar{t}$ four vectors has it's origin in the top mass kinematic reconstruction method in dilepton channel [48] [52] [53]. Along the years there were made a little modifications when used at CDF for top mass reconstruction in above channel.

Kinematic top mass reconstruction in dilepton channel is challenging because the number of kinematic constraints is smaller by one than the number of independent variables. We assume that top quark mass is known therefore number of kinematic constraints matches number of independent variables and t and $\bar{t}$ can be at least in principle reconstructed. There are additional complications as in case of top mass reconstruction - like number of solutions and choice of correct pairing of leptons and $b-$jets and they are handled in

the same way as in the case of top mass reconstruction. Let's describe the kinematic reconstruction mathematically.

Assumptions:

Top mass M_t fixed and mass of $M_w = 80.4$ GeV/c^2.

Four vectors for top, lepton $b-$jet, W and neutrino are denoted t, l, b, W, and ν respectively.

Kinematic equations:

$$\begin{aligned}
(W_1 + b_1)^2 - M_t^2 &= 0 \\
W_1^2 - M_w^2 &= 0 \\
l_1 + \nu_1 &= W_1 \\
(W_2 + b_2)^2 - M_t^2 &= 0 \\
W_2^2 - M_w^2 &= 0 \\
l_2 + \nu_2 &= W_2 \\
\vec{\nu_{1t}} + \vec{\nu_{2t}} &= \vec{\not{E}_T}
\end{aligned}$$

These equations are solved by numerical method(Newton's method). In case one solution is known second solution can be found using the same Newton's

method applied on following set of equations:

$$\begin{aligned}
\Delta_i &= \nu_i^1 - \nu_i^0 \\
2(l_1 + \nu_1^0).\Delta_1 + (\Delta_1)^2 &= 0 \\
2(l_2 + \nu_2^0).\Delta_2 + (\Delta_2)^2 &= 0 \\
b_1.\Delta_1 &= 0 \\
b_2.\Delta_2 &= 0 \\
\vec{\Delta}_{1t} &= -\vec{\Delta}_{2t}
\end{aligned}$$

Where ν_i^0 are four vectors of two neutrinos for the first solution.

There is placed cut on minimal top mass difference between solution to consider these solutions as different. There can be in principle 4 solutions but most probable situation is just two solution and that's what our procedure is set for. If two solutions are found our final choice will be solution with smallest effective mass of t and $\bar{t}$.

Kinematic characteristics of leptons can be considered precise however resolution effects for $b-$jets and $\not{E}_T$ cannot be ignored. $b-$jets momenta are smeared according to expected resolution (same for $\not{E}_T$) and procedure of reconstruction t and $\bar{t}$ is repeated a given number of times (100) for the two choices of pairing $b-$jets and leptons. Pairing which has larger probability of reconstruction is considered as a correct choice.

When pairing ambiguity is solved reconstructed t and $\bar{t}$ four vectors are either reconstructed four vectors with nominal input (no smearing applied) or (in case when nominal input has no solution) first solution with randomly smeared $b-$jets and $\not{E}_T$ variables.

One can make a cut on reconstruction probability (to select only events

where $t\,\bar{t}$ is greater than some preset value) but at present any reconstruction probability greater than 0 was accepted.

Figure 7.1 and 7.2 shows kinematic distributions for the events passing the kinematic reconstruction before and after $b-$tagging requirement.

7.2 Template method for W helicity fractions reconstruction

Reconstructing $t\bar{t}$ kinematic chain using method described in previous section (Sec. 7.1), we are able to reconstruct $\cos\theta^*$ and from this information we will determine W boson helicity fraction.

The reconstructed $\cos\theta^*$ distribution will be shifted from the theoretically predicted (Eq. 1.17) due to various reasons: selection will introduce some bias (e.g. requiring isolation on leptons cause the deficit of events with $\cos\theta^* \simeq -1.0$, requiring leptons to pass cut $p_T > 20$ GeV will also have impact due to fact that lepton from right-handed W tend to have larger p_T than lepton from left-handed W, etc.), reconstruction method can also cause some bias (e.g. in events with more than 2 jets, you have possibility to use the jets from ISR/FSR instead of jets coming from b-quark hadronization, etc.). Therefore, we can not simply fit the resulting reconstructed $\cos\theta^*$ distribution by theoretical formula. The solution how to resolve this complication is to use the template method: create the templates for reconstructed $\cos\theta^*$ using Monte-Carlo samples and at the end fit reconstructed $\cos\theta^*$ from data to these templates. As long as we apply your procedure consistently for the data and MC, we should get unbiased estimate of W boson helicity fractions even if

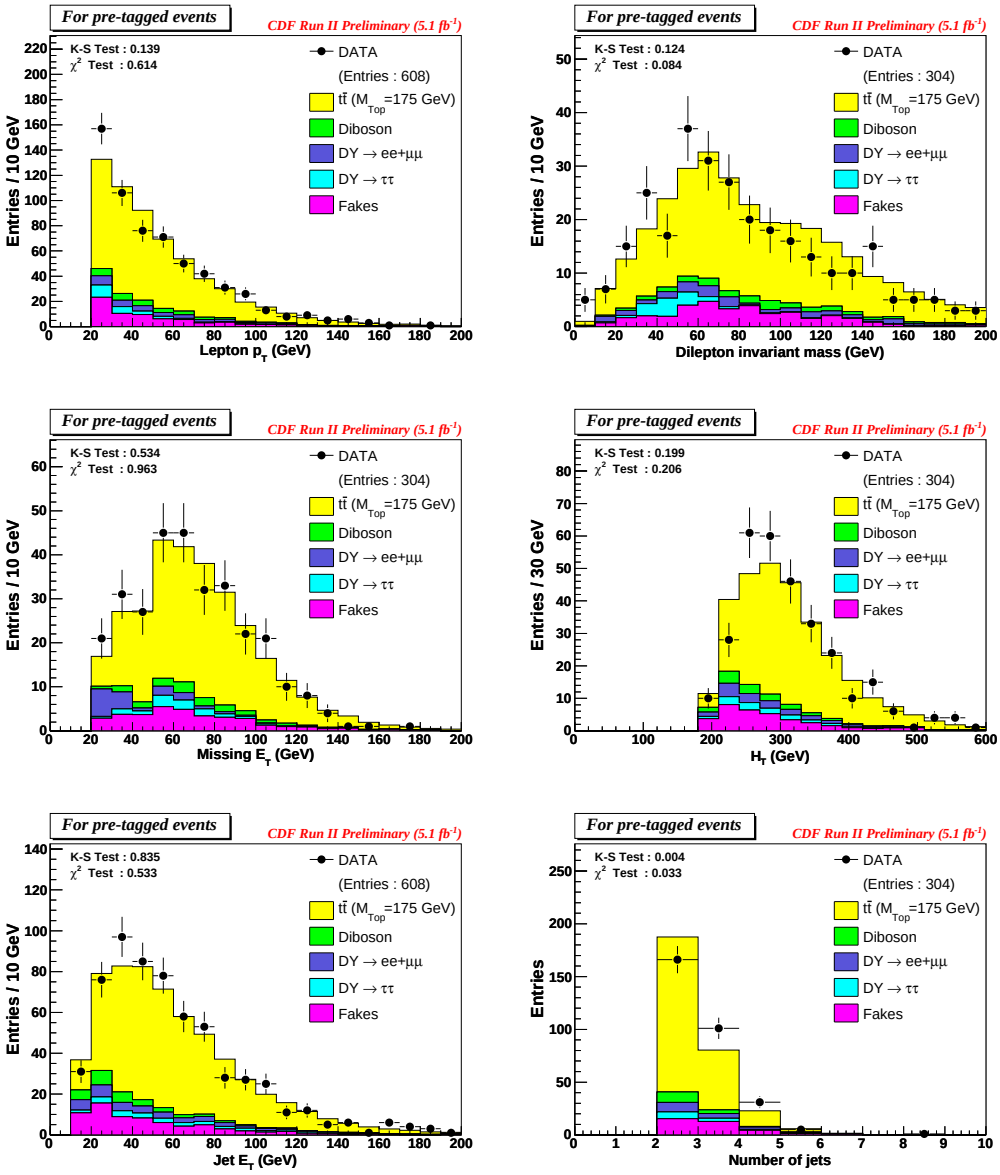

Figure 7.1: Kinematic distributions for the events passing the kinematic reconstruction before $b-$tagging requirement.

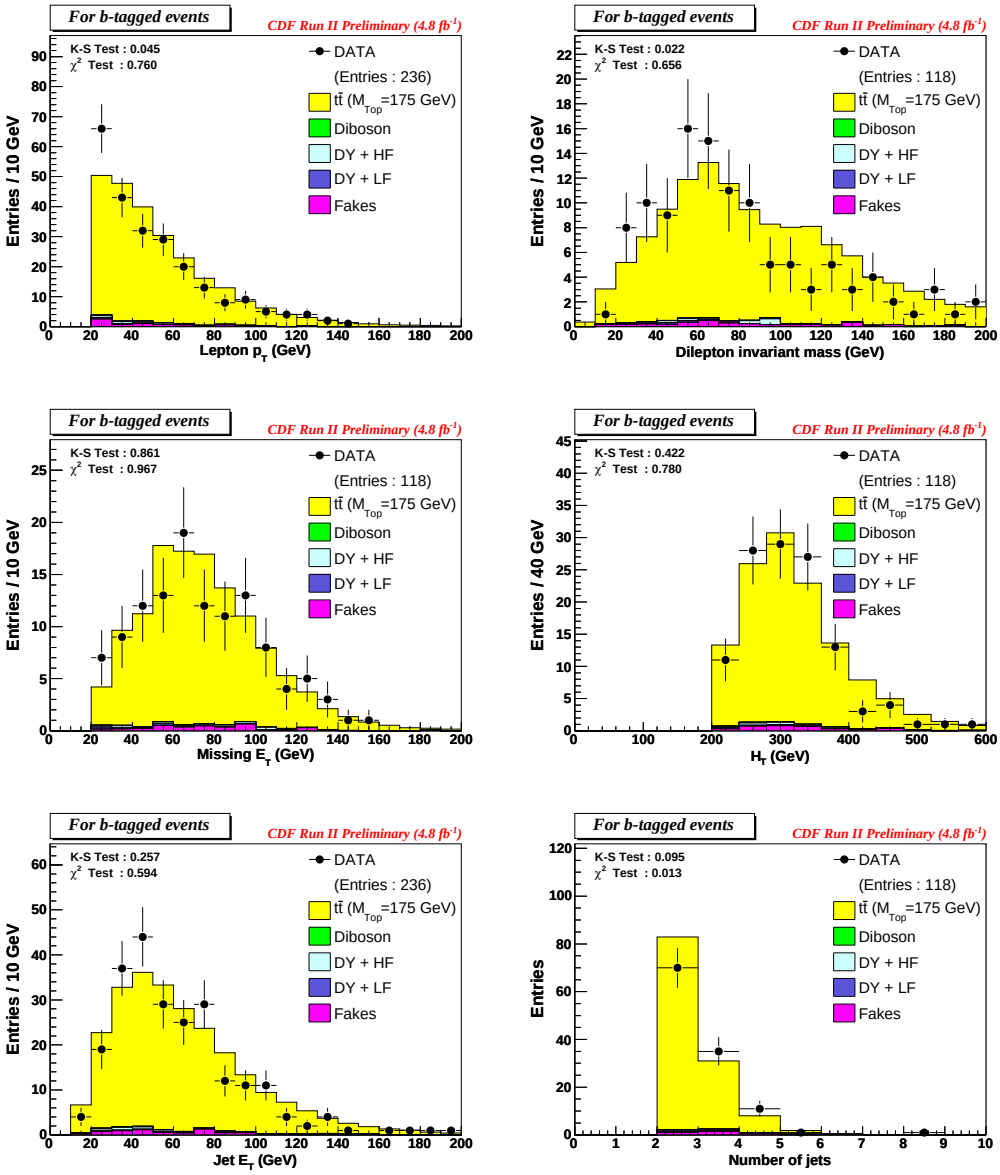

Figure 7.2: Kinematic distributions for the events passing the kinematic reconstruction after $b-$tagging requirement.

the $\cos\theta^*$ distributions themselves are shifted from theoretical distributions. Depending on how well a given method can separate different W helicity fractions, it can loose/gain some sensitivity in the measurement.

7.2.1 Signal templates

We create three different templates for different W boson helicity states: left-handed (f_-^{sig}), longitudinal (f_0^{sig}) and right-handed (f_+^{sig}). For that, we use GGWIG samples [1] with input $M_{top} = 175$ GeV listed in Table I. The detailed information about used GGWIG samples can be found in reference [49].

The distributions of $\cos\theta^*$ for left-handed, longitudinal and right-handed W bosons created by using GGWIG samples (utop0j, utop2j, utop1j) are shown in Figure 7.3 together with simple polynomial fits which we will use as probability distribution functions.

The combined signal template (f^{sig}) is given by the following formula

$$\begin{aligned} f^{sig}(\cos\theta, f_0, f_+) &= \sum_{i=-,0,+} b_i * f_i^{sig} \\ b_i &= \frac{\sum_{j=-,0,+} acc_{i,j} * f_i * f_j}{\sum_{i,j} acc_{i,j} * f_i * f_j} \end{aligned} \tag{7.1}$$

where $f_- = 1 - f_0 - f_+$ and $acc_{i,j}$ is the acceptance for the case of one W having helicity 'i' and other W in the same event is 'j'. This is determined by using samples with different helicities of W bosons (see Table I).

The formula takes into account the fact that the acceptance is different for the events with different combination of helicities of W bosons from top

[1] GGWIG is just customized HERWIG generator which enables one to set input W boson helicity fractions

Sample ID	helicity states of (W^+, W^-) bosons	acceptance (in %)
utop0j	(LH, LH)	0.577 ± 0.007
utop1j	(RH, RH)	0.745 ± 0.008
utop2j	(LO, LO)	0.815 ± 0.009
utop3j	(LH, LH)	0.580 ± 0.007
utop4j	(RH, RH)	0.733 ± 0.008
utop5j	(LO, LO)	0.804 ± 0.009
utop0k	(LH, LO)	0.704 ± 0.013
utop1k	(LH, RH)	0.714 ± 0.013
utop2k	(LO, LH)	0.686 ± 0.013
utop3k	(LO, RH)	0.791 ± 0.013
utop4k	(RH, LO)	0.753 ± 0.013
utop5k	(RH, LH)	0.708 ± 0.013

(a)

Sample ID	helicity states of (W^+, W^-) bosons	acceptance (in %)
utop0j	(LH, LH)	0.350 ± 0.006
utop1j	(RH, RH)	0.446 ± 0.007
utop2j	(LO, LO)	0.493 ± 0.007
utop3j	(LH, LH)	0.358 ± 0.006
utop4j	(RH, RH)	0.442 ± 0.007
utop5j	(LO, LO)	0.493 ± 0.007
utop0k	(LH, LO)	0.432 ± 0.010
utop1k	(LH, RH)	0.448 ± 0.011
utop2k	(LO, LH)	0.426 ± 0.010
utop3k	(LO, RH)	0.458 ± 0.011
utop4k	(RH, LO)	0.451 ± 0.011
utop5k	(RH, LH)	0.427 ± 0.010

(b)

Table I: The list of GGWIG samples used to create signal $\cos\theta^*$ templates and also the "cross-samples" used for the acceptance correction. The acceptance is the product of DIL $t\bar{t}$ event selection acceptance (with $b-$tagging requirement)and the kinematic reconstruction probability for pre$-$tagged (a) and $b-$tagged (b) samples.

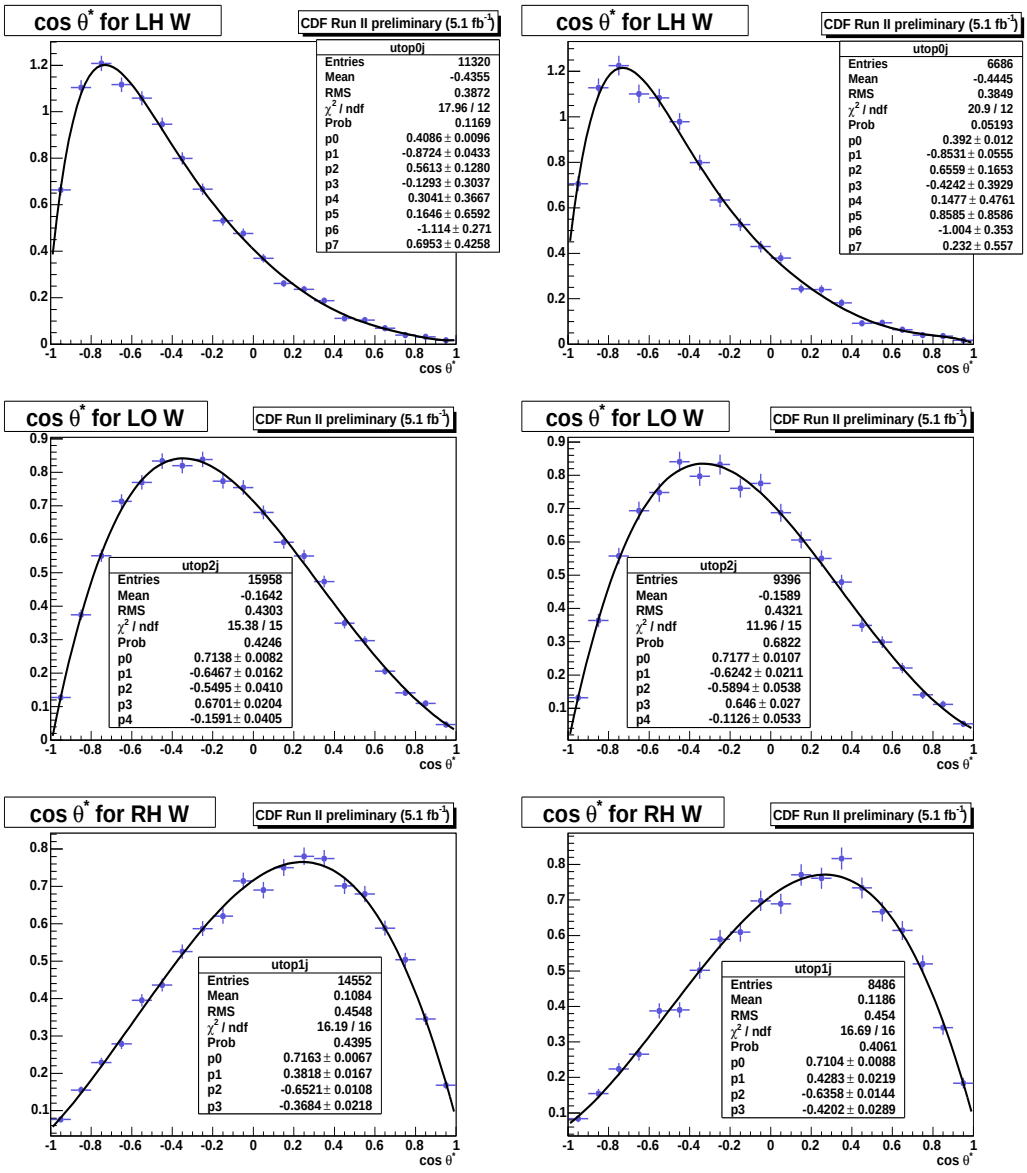

(a) (b)

Figure 7.3: The $\cos\theta^*$ distributions for left-handed, longitudinal and right-handed W bosons together with the polynomial fits for pre−tagged (a) and b−tagged (b) background.

decays.

1-dimensional and 2-dimensional negative log-likelihood fitting test is performed using ttop75 Pythia signal Monte Carlo sample which is generated with the longitudinal fraction is 70% and the left handed fraction is 30% for pre−tagged and b−tagged events. Figure 7.4 and Figure 7.5 show the negative log-likelihood fitting results.

7.2.2 Background templates

Similarly as for $t\bar{t}$ signal events, we create also $\cos\theta^*$ templates for all the background processes. In the end, we combine them into one final background template which we will use in the subsequent fit to determine W boson helicity fractions. The samples we used to produce the background templates together with their reconstruction probabilities are listed in Table II.

The signal and background template comparison for pre−tagged and b−tagged events can be found in Figure 7.8.

The $\cos\theta^*$ distributions for individual backgrounds are presented in Figure 7.6 with the combined background template being in Figure 7.7.

The templates from the individual background processes are combined together into the final combined background template according to the expected yield after kinematic reconstruction for each process. This means scaling each individual background template according expected number of DIL b−tag selected events (see Table VI) in Sec. 6 and also scaling by the kinematic reconstruction probability (see Table II).

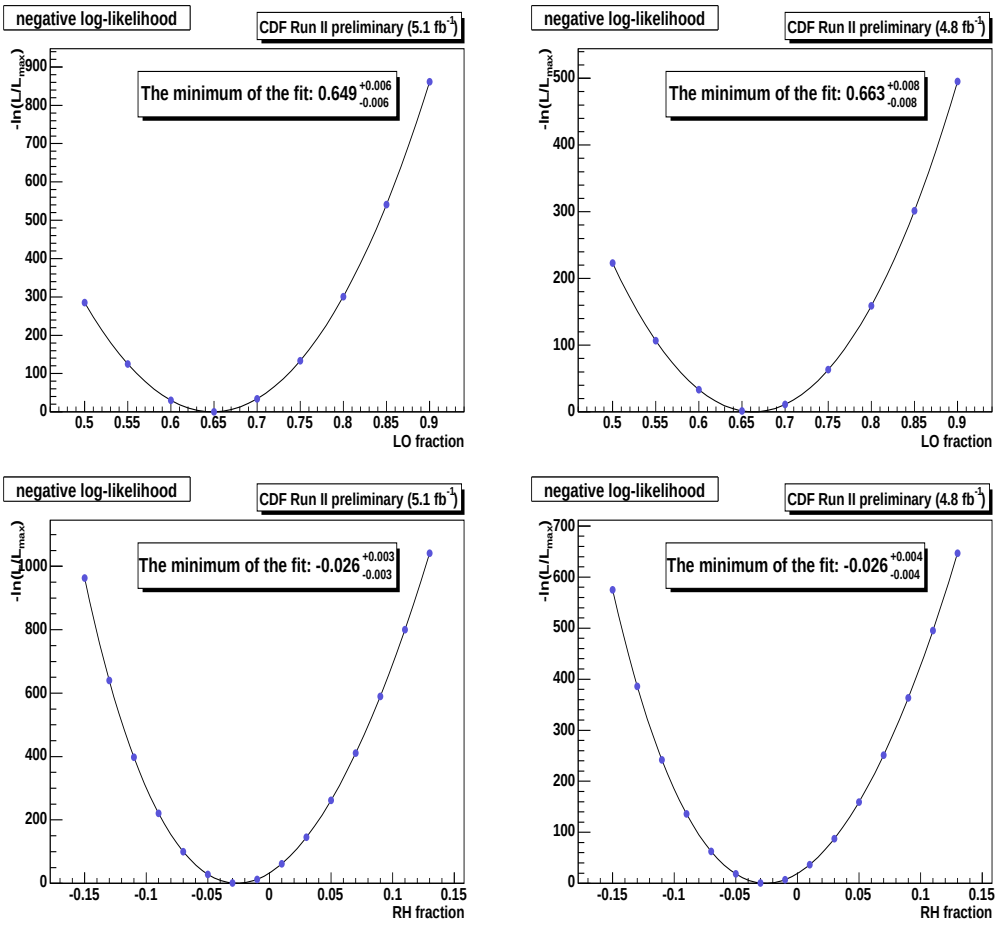

(a) (b)

Figure 7.4: 1D negative log-likelihood fitting test using ttop75 Pythia signal Monte Carlo sample for pre−tagged (a) and b−tagged (b) events.

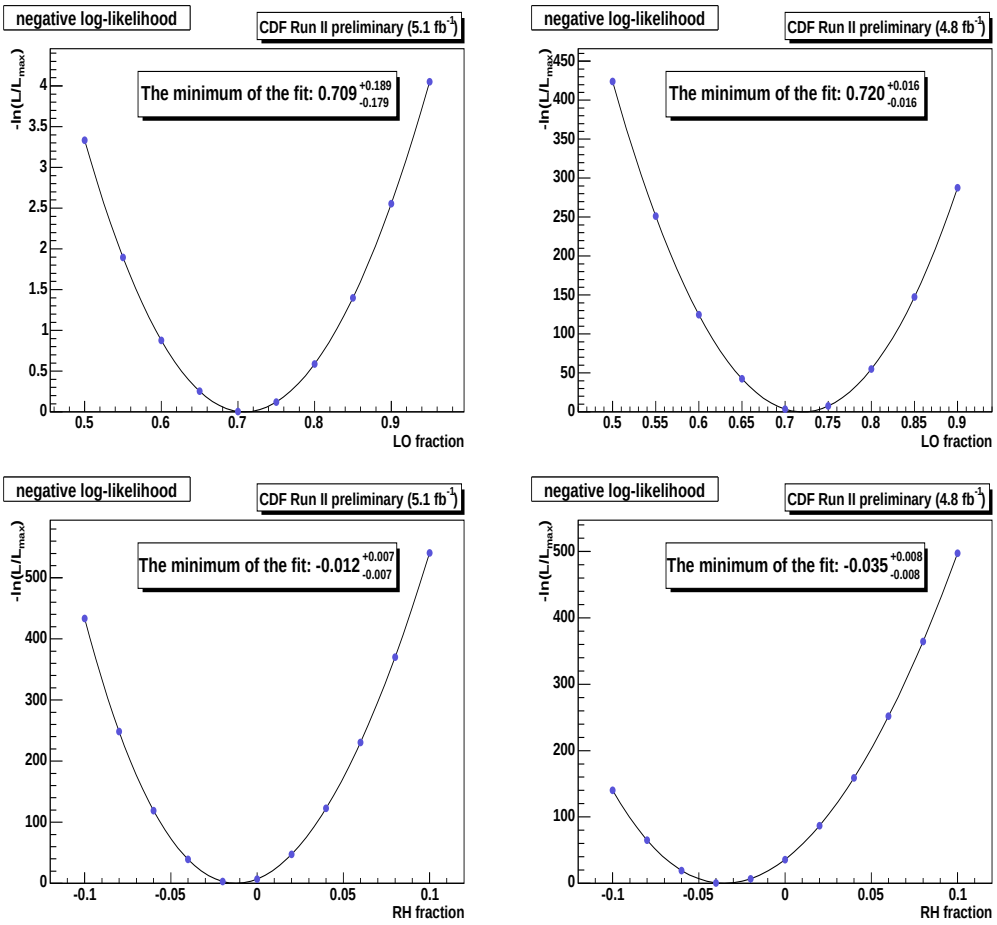

(a) (b)

Figure 7.5: 2D negative log-likelihood fitting test with ttop75 Pythia signal Monte Carlo sample for pre−tagged (a) and b−tagged (b) events.

backgroud	sample types (datasets)	recon. probab.
WW	Pythia - ihhp1a	0.833 ± 0.062
WZ	Pythia - jhhp1a	0.679 ± 0.088
ZZ	Pythia - khhp1a	0.552 ± 0.065
DY$\rightarrow ee + \mu\mu$	Alpgen + Pythia	0.712 ± 0.385
DY$\rightarrow \tau\tau$	Alpgen + Pythia	0.733 ± 0.308
Fakes	Fakeable data	0.637 ± 0.202
Total		0.676 ± 0.214

(a)

backgroud	sample types (datasets)	recon. probab.
WW	Pythia - ihhp1a	0.833 ± 0.062
WZ	Pythia - jhhp1a	0.679 ± 0.088
ZZ	Pythia - khhp1a	0.552 ± 0.065
DY+LF	Alpgen + Pythia (DY + 1-4 partons)	0.712 ± 0.385
DY+HF	Alpgen + Pythia (DY + bb/cc + 1-4 partons)	0.733 ± 0.308
Fakes	fakeable data	0.637 ± 0.202
Total		0.676 ± 0.214

(b)

Table II: The samples used to create background $\cos\theta^*$ templates for pre−tagged (a) and b−tagged (b) background.

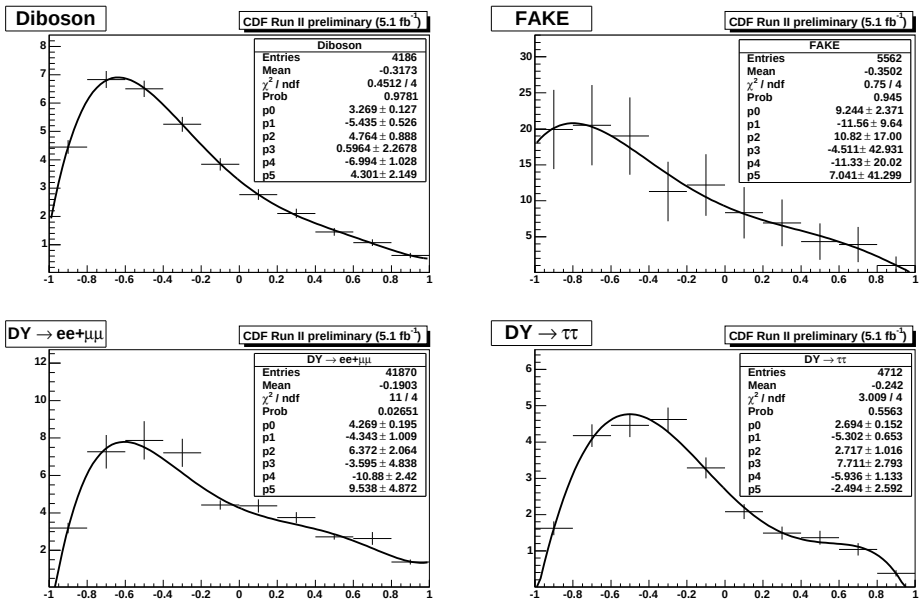

(a)

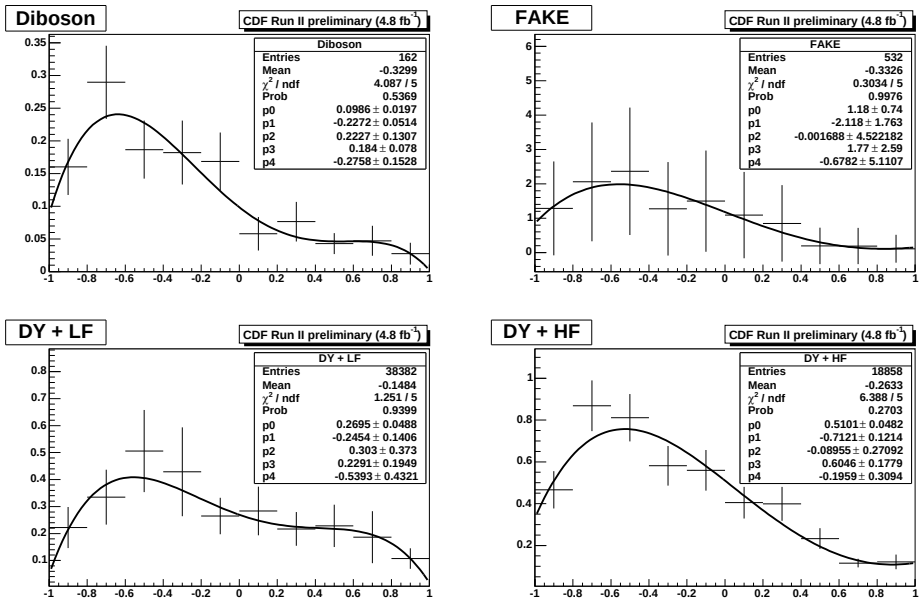

(b)

Figure 7.6: The $\cos\theta^*$ distribution for individual background processes for pre−tagged (a) and b−tagged (b) events.

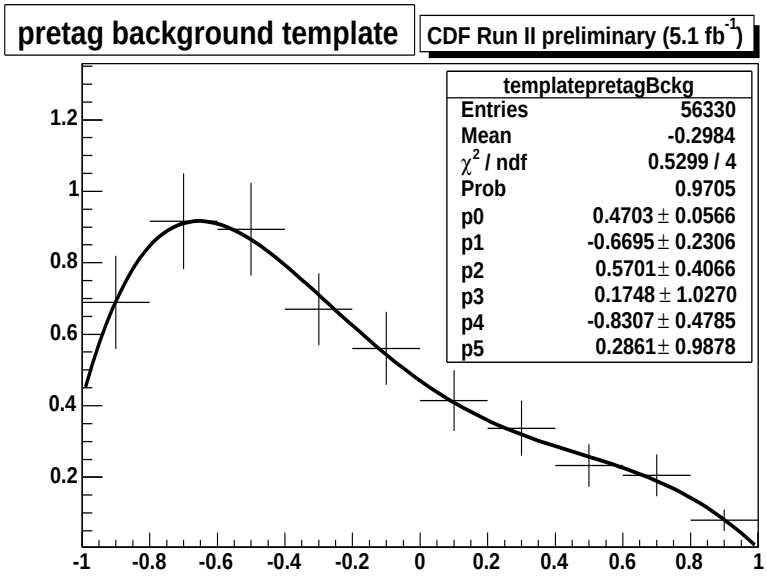

(a)

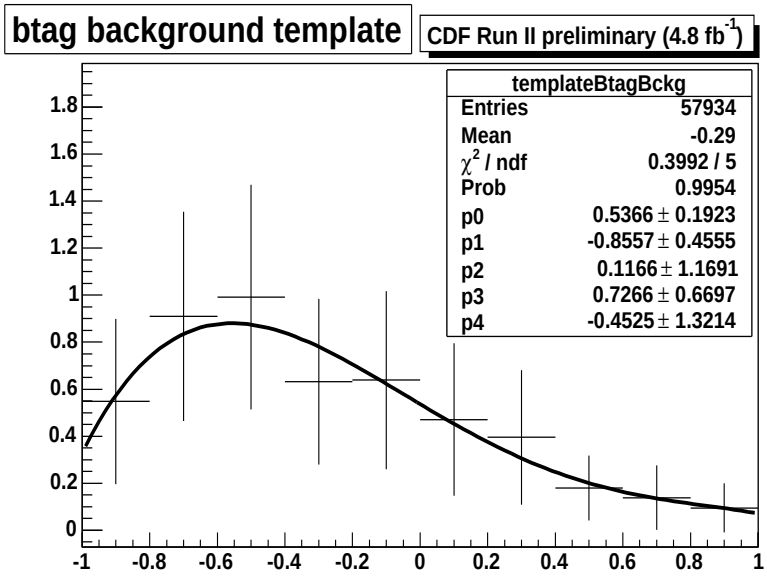

(b)

Figure 7.7: The $\cos\theta^*$ distribution for total background for pre−tagged (a) and b−tagged (b) events.

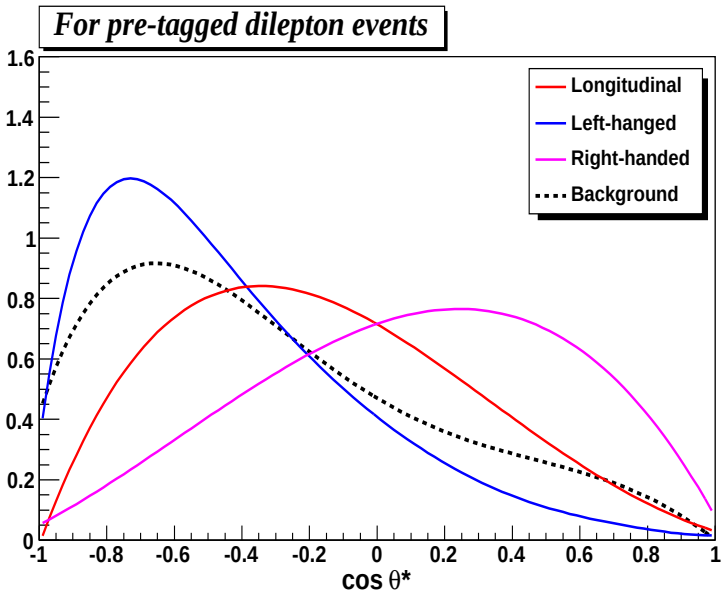

(a)

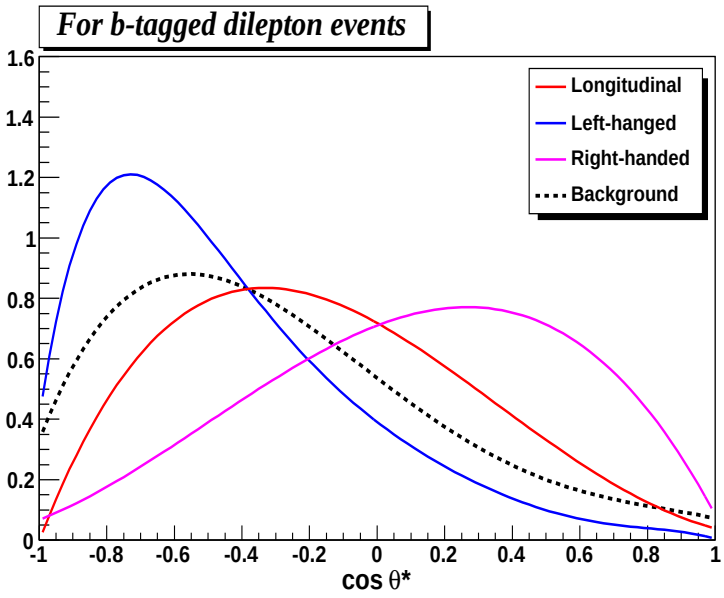

(b)

Figure 7.8: The $\cos\theta^*$ distribution for signal and background for pre−tagged (a) and b−tagged (b) events.

7.2.3 Determination of W boson helicity fractions

We perform the likelihood fit of the data to the combination of three signal templates and one background $\cos\theta^*$ template in order to determine W boson helicity fractions. The exact formula of the likelihood is given as follows

$$\begin{aligned}
\mathcal{L}(f_0, f_+, n, n_b) &\equiv \mathcal{L}_{shape} \times \mathcal{L}_{nev} \times \mathcal{L}_{bg} \\
\mathcal{L}_{shape} &\equiv \prod_{i=1}^{N} \frac{n_s \times f^{sig}(\cos\theta_i{}^{rec}, f_0, f_+) + n_b \times f^{bckg}(\cos\theta_i{}^{rec})}{n_s + n_b} \\
\mathcal{L}_{nev} &\equiv \frac{e^{-(n_s+n_b)}(n_s+n_b)^N}{N!} \\
-\ln\mathcal{L}_{bg} &\equiv \frac{(n_b - n_b^{exp})^2}{2\sigma_{n_b}^2},
\end{aligned} \tag{7.2}$$

where the sum of the number of signal and background events is constrained by Poisson distribution in $\mathcal{L}_{nev}$ and $\mathcal{L}_{bg}$ was introduced to constrain the number of background events around its expected value by Gaussian distribution. The W boson longitudinal fractions, longitudinal (f_0) and right-handed (f_+), the number of background events n_b and the number of signal events n_s are free parameters in a likelihood function and are returned as a result of the fit. The fractions f_0 and f_+ which minimize $-\ln\mathcal{L}$ will be taken as the final estimate for a given sample. The statistical uncertainty on f_0 and f_+ is given by the difference between the result at the minimum and the values at $-\ln(\mathcal{L}/\mathcal{L}_{max}) = 0.5$.

In order to be able to use the above likelihood formula, we need to know:

- N - number of reconstructed events in data sample and their recon-

structed $\cos\theta^*$ values $\cos\theta_i^*$. These we obtain by reconstruction procedure introduced in Sec. 7.1.

- n_b^{exp} - estimate of number of expected background events in the sample and also error on this estimate σ_{n_b}
- $f^{sig}(\cos\theta_i{}^{rec})$ - combined probability density function for $t\bar{t}$ signal sample given by Eq. 7.2
- $f^{bckg}(cos\theta_i{}^{rec})$ - function which will parametrize the background template. This is given in Figure 7.7.

Note, variables in the likelihood formula, which correspond to number of events (N, n_s, n_b, n_b^{exp}), mean the number of events after kinematic reconstruction. This means N is not the total number of DIL $t\bar{t}$ candidates we see in the data, rather just the number of events in the data which $\cos\theta^*$ is reconstructed for. Similarly, the n_b^{exp} is the number of expected background events after the kinematic reconstruction, i.e. number of expected background events (according Table VI) in Sec. 6 multiplied by the probability of reconstruction (see Table II).

7.3 Tests performed on MC

Before we proceed to apply our reconstruction method on real physics data, we want to check the method on MC samples to prove that we are unbiased or in case we see the bias to derive necessary correction. Also, we want to check whether the method returns proper statistical uncertainty and how large uncertainty we should expect in data.

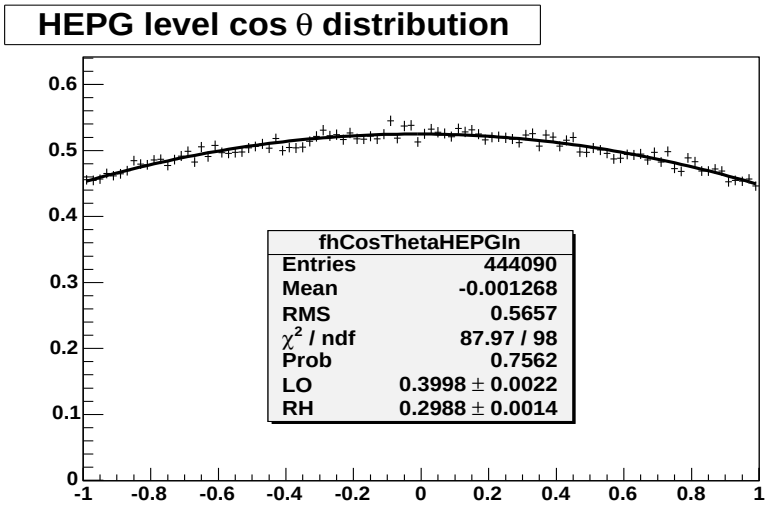

Figure 7.9: The HEPG $\cos\theta^*$ distribution for utopal sample used for reweighting.

Since it would require lots of MC samples to generate in order to perform the checks within full 2D space (f_0, f_+), we decided instead to use the reweighting method to perform MC checks. The nominal sample (utopal) has about the flat HEPG $\cos\theta^*$ distribution ($f_- = 0.3, f_0 = 0.4, f_+ = 0.3$), see Figure 7.9. We perform the reweighting (in order to assign the weights to the individual events) in such way, that HEPG distribution of reweighted sample correspond to our desired W helicity fractions. This way we obtained 861 reweighted MC samples for each possible (f_0, f_+) combination where $f_0 \in < 0, 1 >$ and $f_+ \in < 0, 1 >$ and both f_0 and f_+ are increased in 0.025 steps. After that, we performed the tests the standard way, where each event is weighted in $-\ln\mathcal{L}$.

7.3.1 The 1D measurement of f_0

The negative log-likelihood fitting is tested using non reconstructed bias

samples which are generated from combination cos θ^* distribution between signal templates in Figure 7.3 for the left-handed, longitudinal and right-handed W bosons. The 1D measurement of f_0 result is shown that the fitted f_0 fraction is well matched with the input f_0 for fixed $f_+ = 0$ in Figure 7.10.

Next, we perform the reconstruction for the samples which have full range of f_0 values while keeping the input value of f_+ being equal to SM expected value (0).

The reconstruction is performed on full sample. The dependence of reconstructed f_0 fraction on input f_0 fraction for fixed $f_+ = 0$ is shown in Figure 7.11. The slope and the offset of the dependence are a little bit shifted from the expected values and we will use the slope and offset of this dependence to correct the results.

The pseudo-experiments is performed in order to check the reconstructed uncertainty for each value of input f_0 (again f_+ is always kept at 0. We plot the dependence of the of pull width as a function of input f_0 in Figure 7.12 where the pull is defined as:

$$pull = \frac{\tau_g - \tau_m}{\sigma_m}$$

where τ_g is generated value, τ_m is the measured value and σ_m are the MINOS errors. In average, the pull width is consistent with expected value of 1.0 and so our estimate of uncertainty is appropriate.

The distribution of the uncertainty for f_0^{1D} (for the expected number of signal and background events expected in data) is shown in Figure 7.13. We determine the expected uncertainty for f_0^{1D} to be 0.9 for pre$-$tagged, 0.10 for

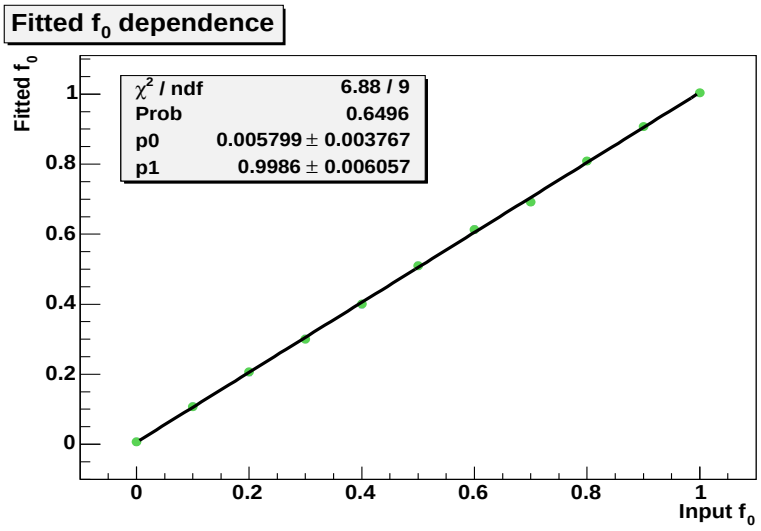

(a)

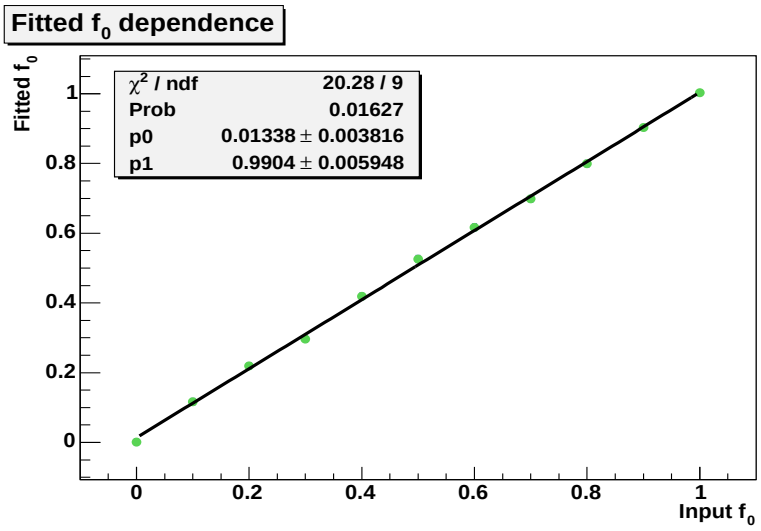

(b)

Figure 7.10: Method test of for the fitted f_0 fraction on input f_0 for fixed $f_+ = 0$ using non-reconstruction bias samples: (a) is plot for pre−tagged and (b) is plot for b−tagged events.

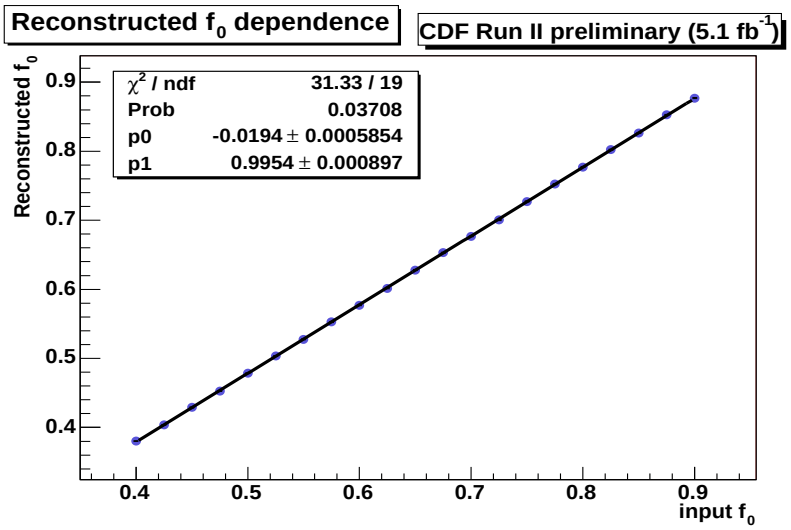

(a)

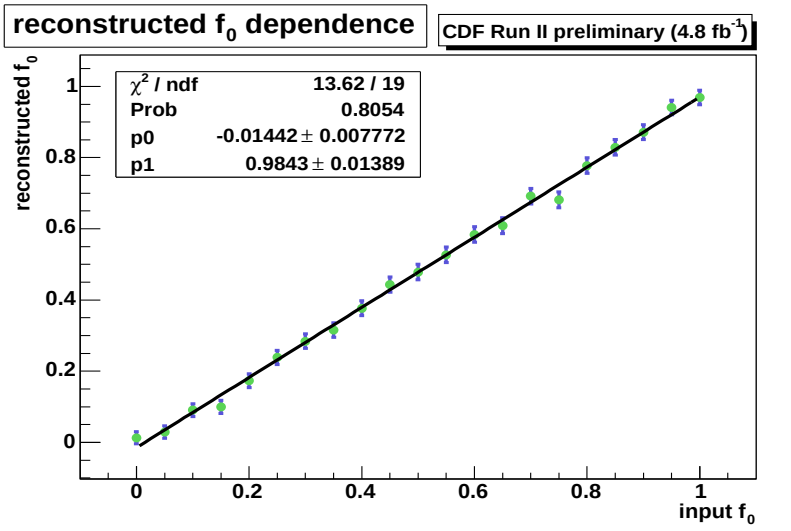

(b)

Figure 7.11: The dependence of reconstructed f_0 fraction on input f_0 for fixed $f_+ = 0$: (a) is plot for pre−tagged and (b) is plot for b−tagged events.

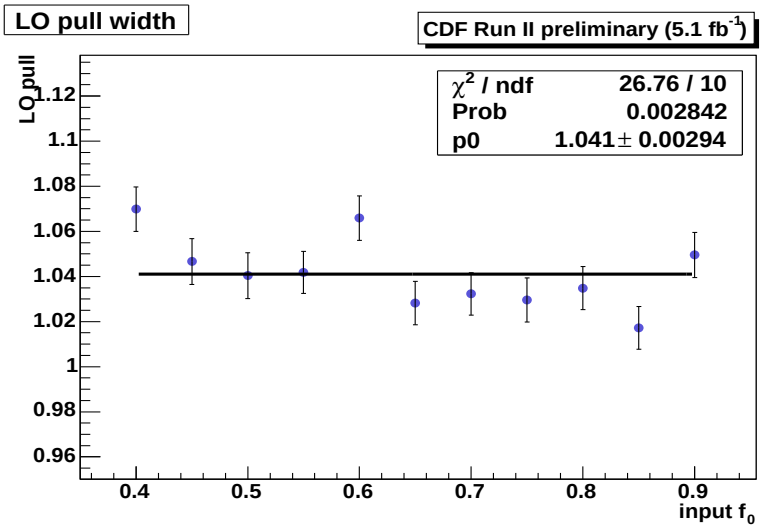

(a)

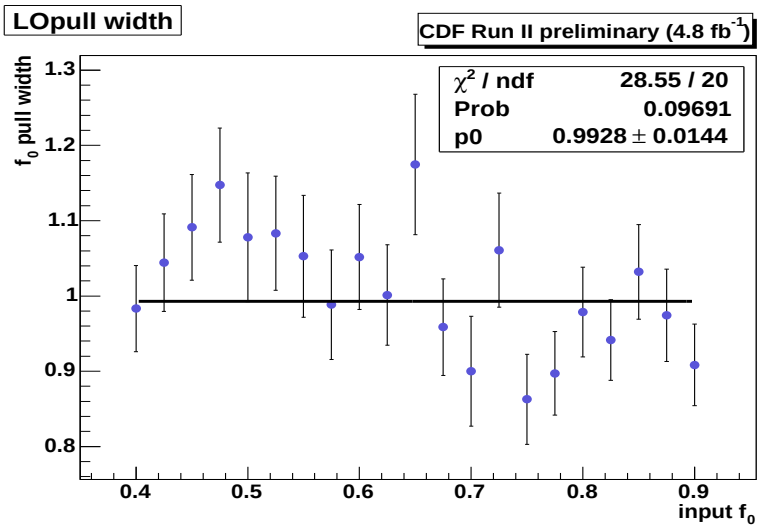

(b)

Figure 7.12: The pull width dependence for pre−tagged (a) and b−tagged (b) events as a function of input f_0 for fixed $f_+ = 0$.

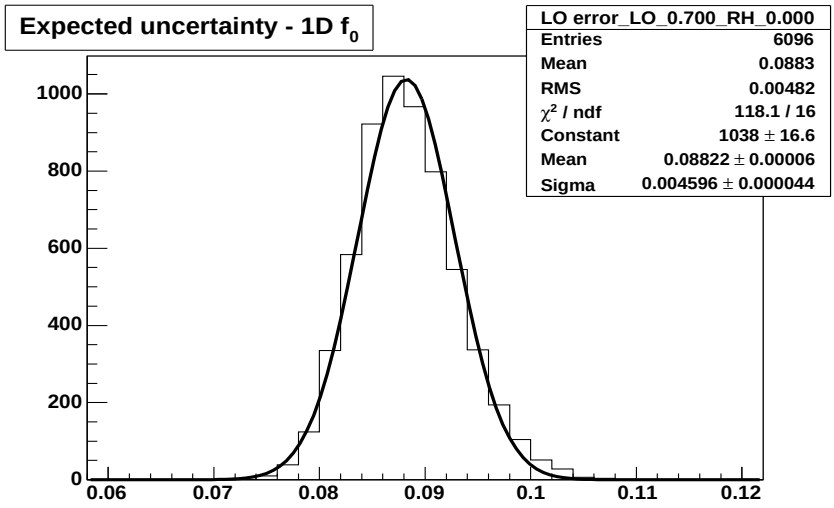

(a)

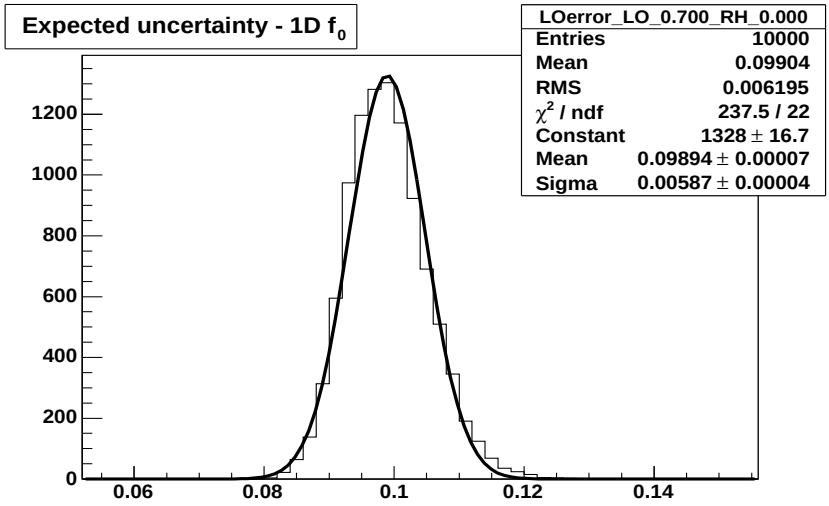

(b)

Figure 7.13: The expected uncertainty distribution for f_0^{1D} of pre−tagged (a) and b−tagged (b) events.

$b-$tagged events (mean value of the fit to the distribution).

7.3.2 The 1D measurement of f_+

The fitting method is tested using non reconstructed bias samples for the 1D measurement of f_+. The 1D measurement of f_+ result is shown that the fitted f_+ fraction is well matched with the input f_+ for fixed $f_0 = 0.7$ in Figure 7.14.

We perform the reconstruction for the samples which have full range of f_+ values while keeping the input value of f_0 being equal to SM expected value (0.7).

The reconstruction is performed on full sample. The dependence of reconstructed f_+ fraction on input f_+ fraction for fixed $f_0 = 0.7$ is shown in Figure 7.15. The offset is a little bit shifted from zero, so we will again use this dependence to make the correction.

We perform the pseudo-experiments in order to check the reconstructed uncertainty for each value of input f_+ (again f_0 is always kept at 0.7). We plot the dependence of the of pull width as a function of input f_+ in Figure 7.16 where the pull is defined the same way as in f_0 case. In average, the pull width is a little bit shifted from the expected value of 1.0 and we will use the average shift to correct the uncertainty.

The distribution of the uncertainty for f_+^{1D} (for the expected number of signal and background events expected in data) is shown in Figure 7.17. We determine the expected uncertainty for f_+^{1D} to be 0.05 for pre$-$tagged and $b-$tagged events (the mean value of the fit to the distribution).

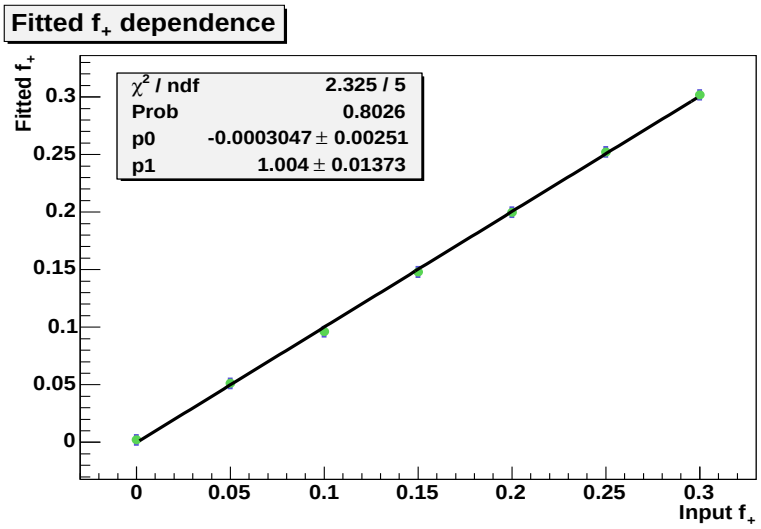

(a)

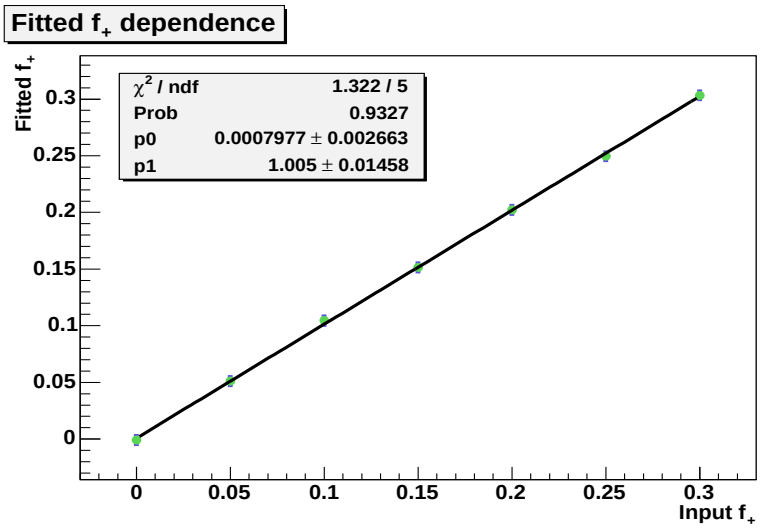

(b)

Figure 7.14: Method test of for the fitted f_+ fraction on input f_+ for fixed $f_0 = 0.7$ using non-reconstruction bias samples: (a) is plot for pre−tagged, (b) is plot for b−tagged events.

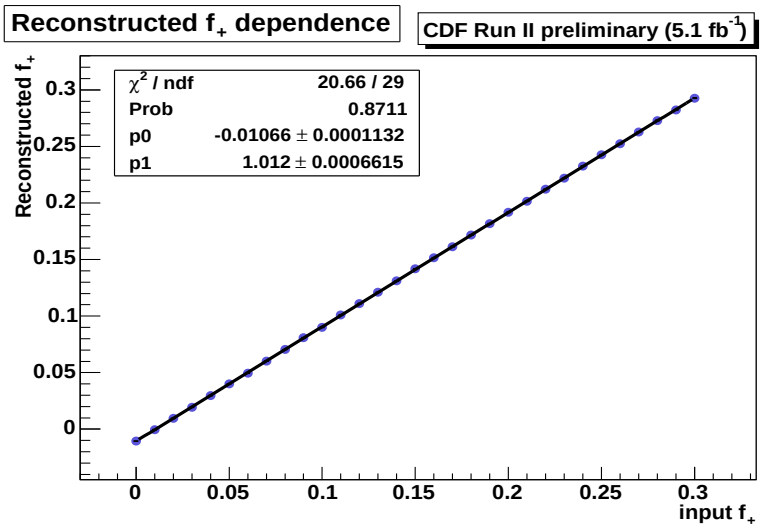

(a)

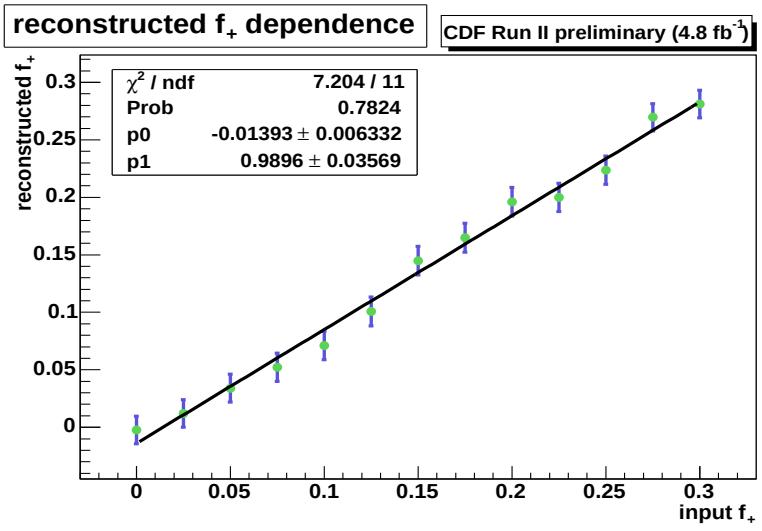

(b)

Figure 7.15: The dependence of reconstructed f_+ fraction on input f_+ for fixed $f_0 = 0.7$: (a) is plot for pre−tagged and (b) is plot for b−tagged events.

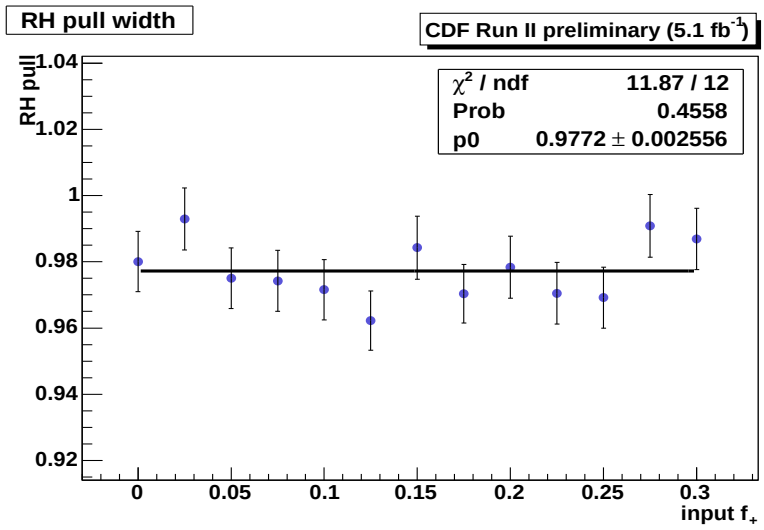

(a)

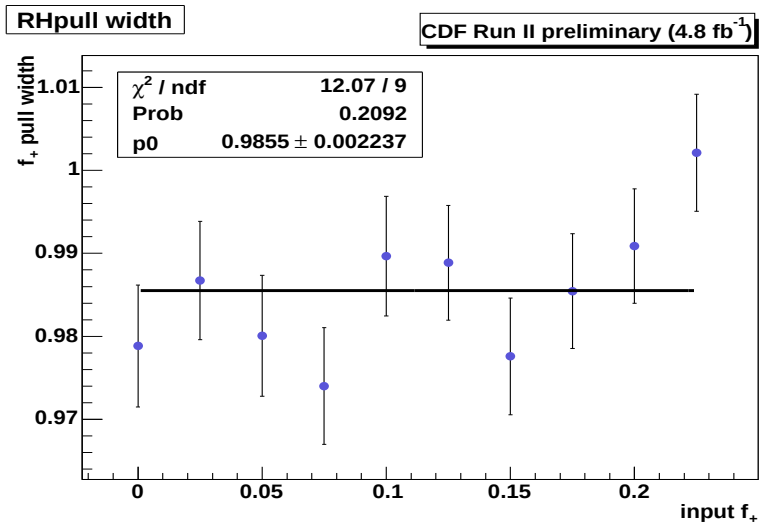

(b)

Figure 7.16: The pull width dependence for pre−tagged (a) and b−tagged (b) events as a function of input f_+ for fixed $f_0 = 0.7$.

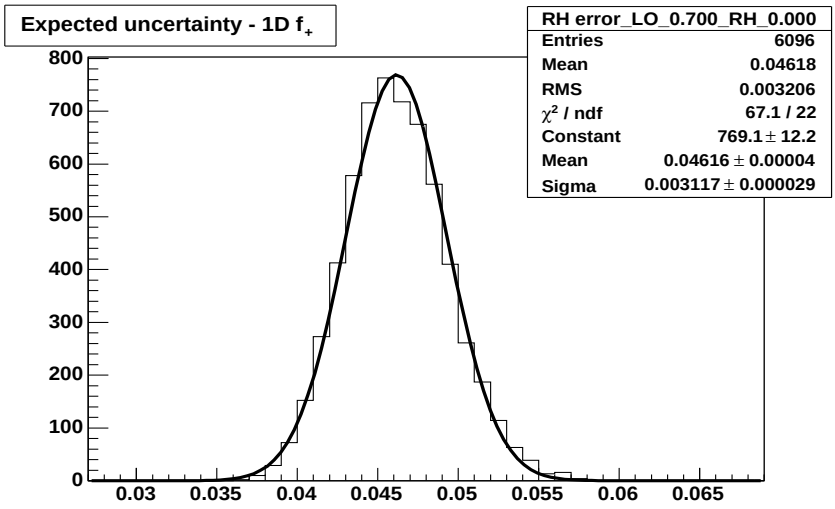

(a)

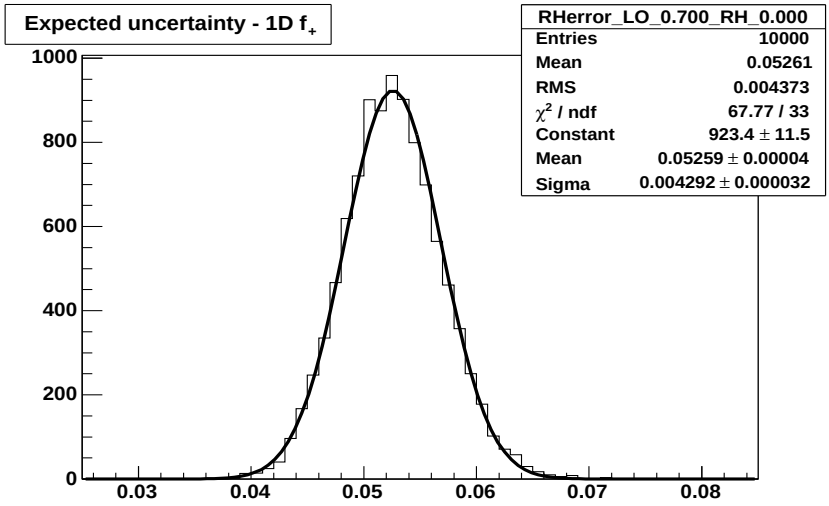

(b)

Figure 7.17: The expected uncertainty distribution for f_+^{1D} of pre−tagged (a) and b−tagged (b) events.

7.3.3 The simultaneous 2D measurement of f_0 and f_+

We perform the reconstruction within full space of $(f_0, f+)$ input values.

The reconstruction is performed on full sample. For a given input value of f_+ (f_0) we perform the simultaneous fit of (f_0, f_+) and plot the dependence of reconstructed f_0 (f_+) on input value of f_0 (f_+). Fitting such dependence by straight line we get the slope and offset value of linear dependence for a given value of input f_+ (f_0). The dependences of slope and offset of f_0 and f_+ linear dependence as a function of input f_+ and f_0 fraction for pre$-$tagged and $b-$tagged events are shown in Figure 7.18, 7.19, 7.20 and 7.21. The slopes and the offsets are constant over large range of input values. Again there is a little shift from expected values and we will use it to correct the results.

We perform the pseudo-experiments in order to check the reconstructed uncertainty for each pair of input values (f_0, f_+). We plot the dependence of the pull widths for pre$-$tagged and $b-$tagged events as a function of input f_0 (for different input values of f_+) in Figure 7.22 and 7.26. The same plot for f_+ dependence is plotted in Figure 7.23 and 7.27. The results of the fits to these dependences are summarized in the Figure 7.24 and 7.28 and Figure 7.25 and 7.29. The dependeces are nicely constant except the last couple of points where the physics constraint (sum of all fractions is being 1.0) plays the role.

In average, the pull widths are a little bit smaller than expected value of 1.0 for both f_0 and f_+ and we will use these values to correct the result from data.

The distribution of the uncertainty for f_0^{2D} and f_+^{2D} (for the expected number of signal and background events expected in data) is shown in Figure 7.30 and Figure 7.31. We determine the expected uncertainty for f_0^{2D}

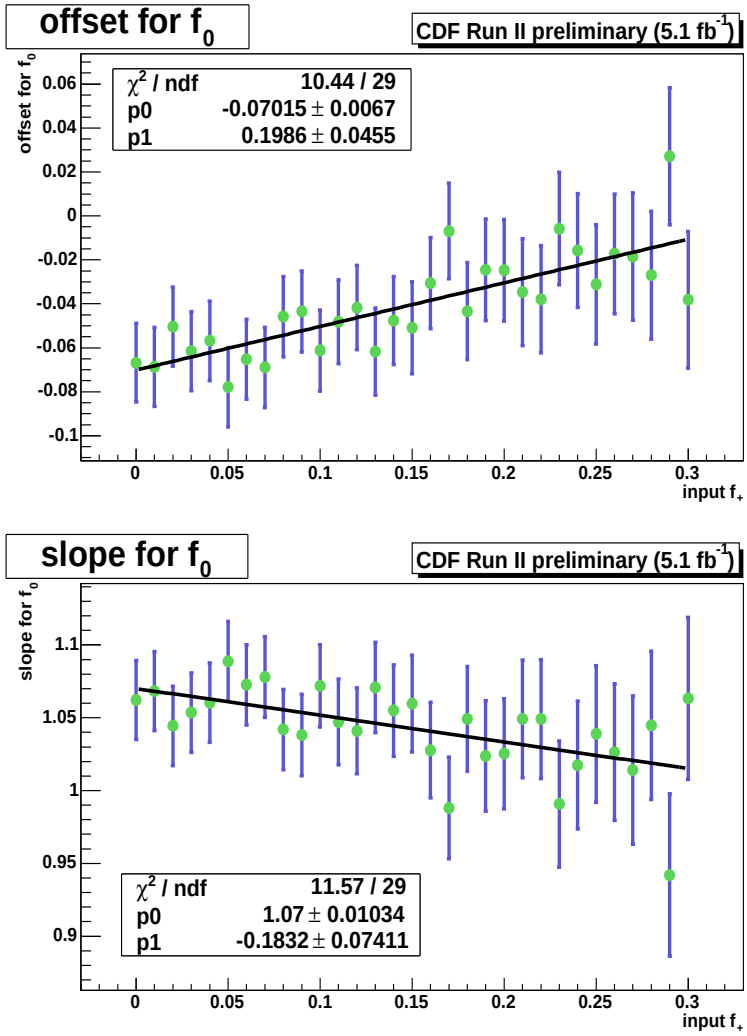

Figure 7.18: The dependence of slope and offset for f_0 fraction of pre−tagged events as a function of input f_+.

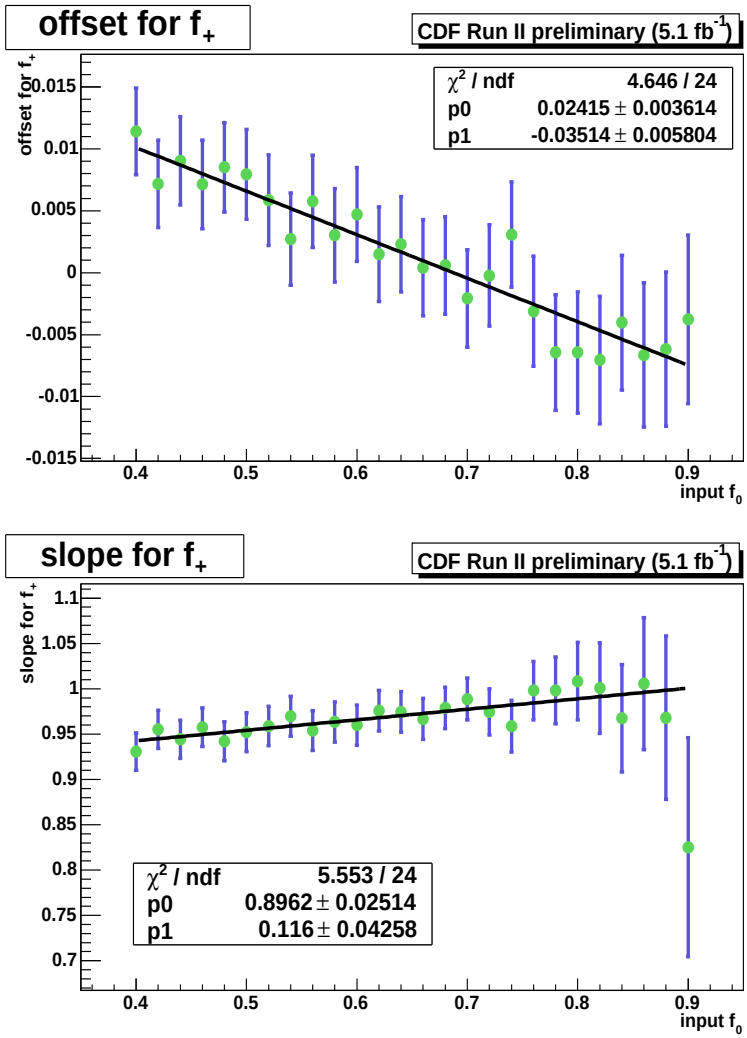

Figure 7.19: The dependence of slope and offset for f_+ fraction of pre−tagged events as a function of input f_0.

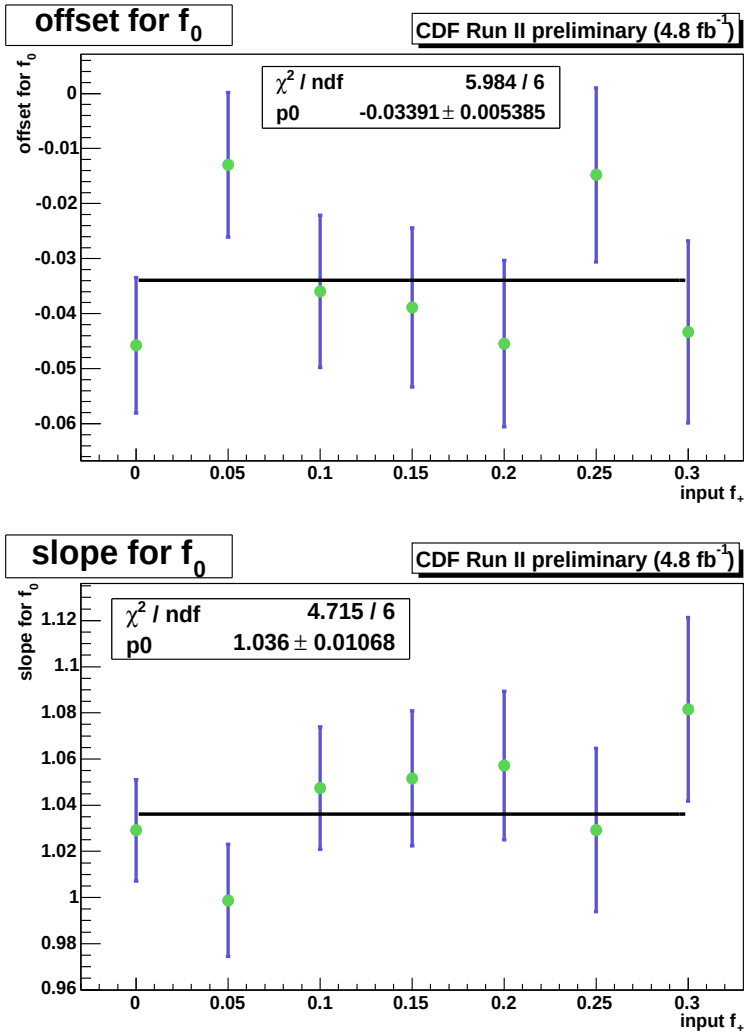

Figure 7.20: The dependence of slope and offset for f_0 fraction of $b-$tagged events as a function of input f_+.

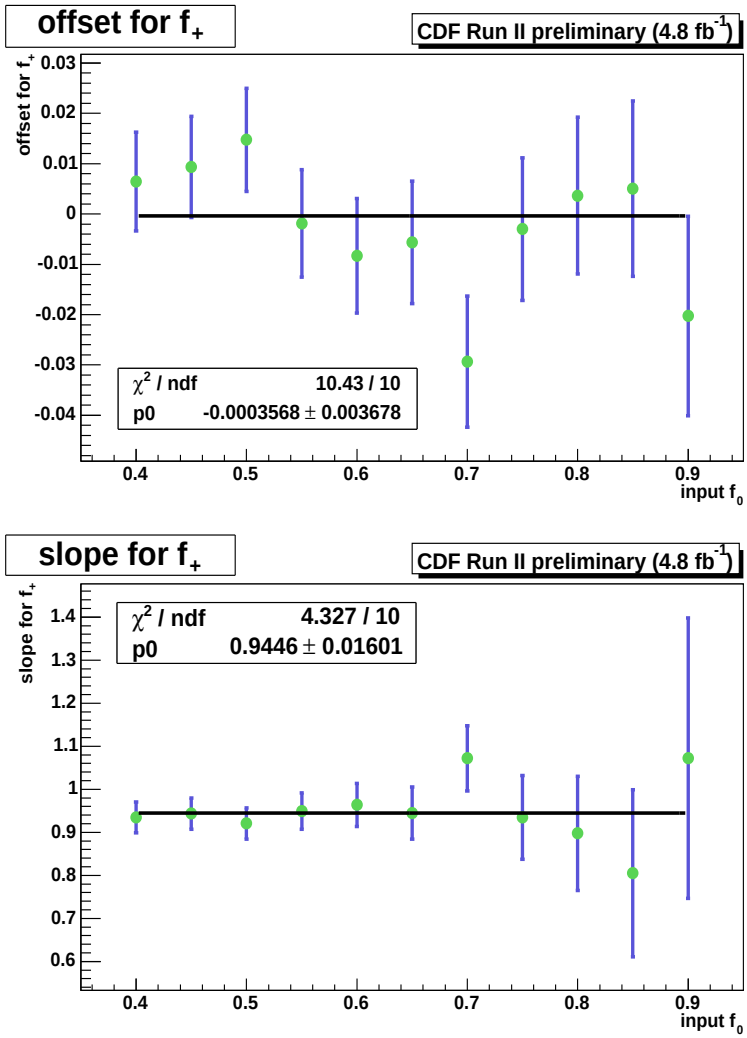

Figure 7.21: The dependence of slope and offset for f_+ fraction of $b-$tagged events as a function of input f_0.

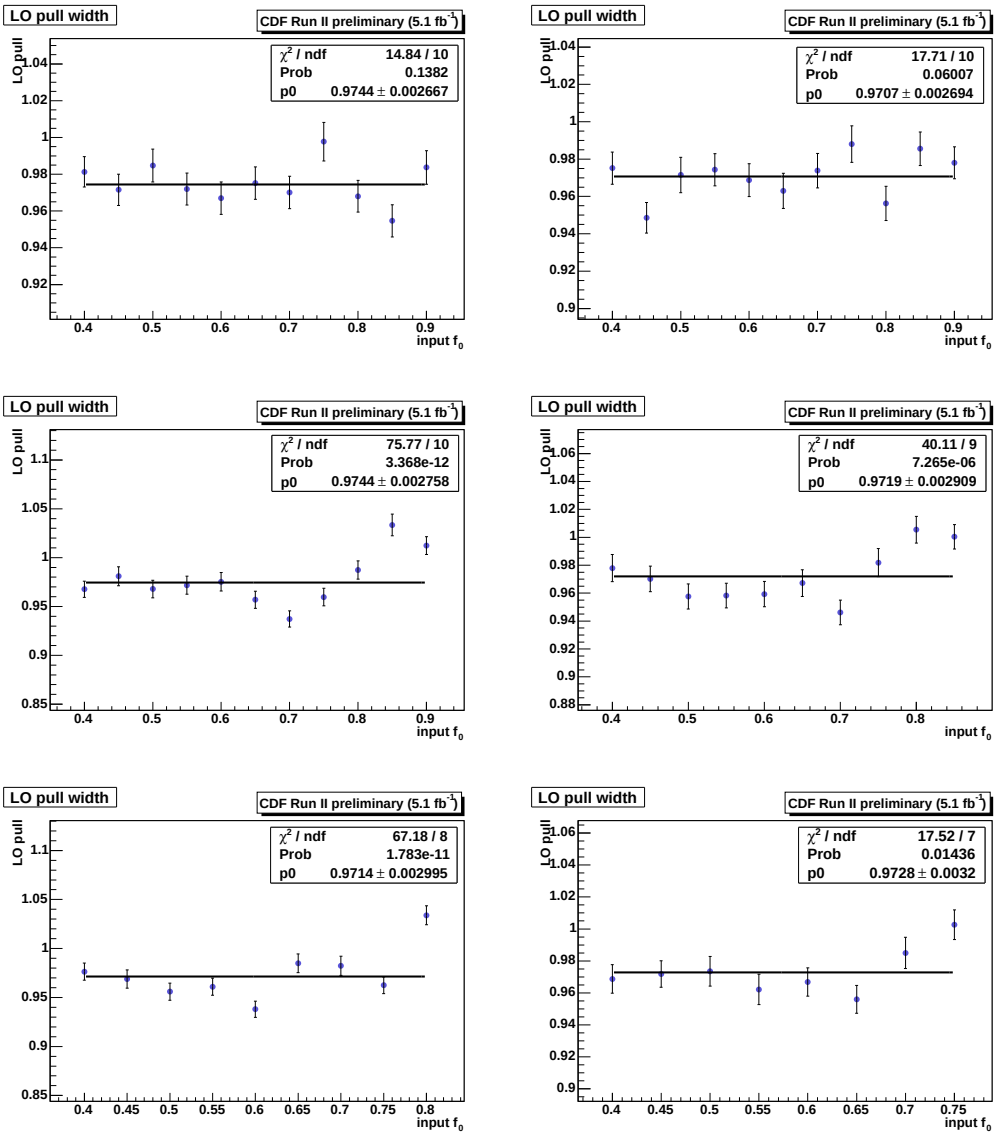

Figure 7.22: The f_0 pull width dependence for pre−tagged events as a function of input f_0 for input values of $f_+ = 0.00, 0.05, 0.10, 0.15, 0.20, 0.25$ (from top to bottom and left to right).

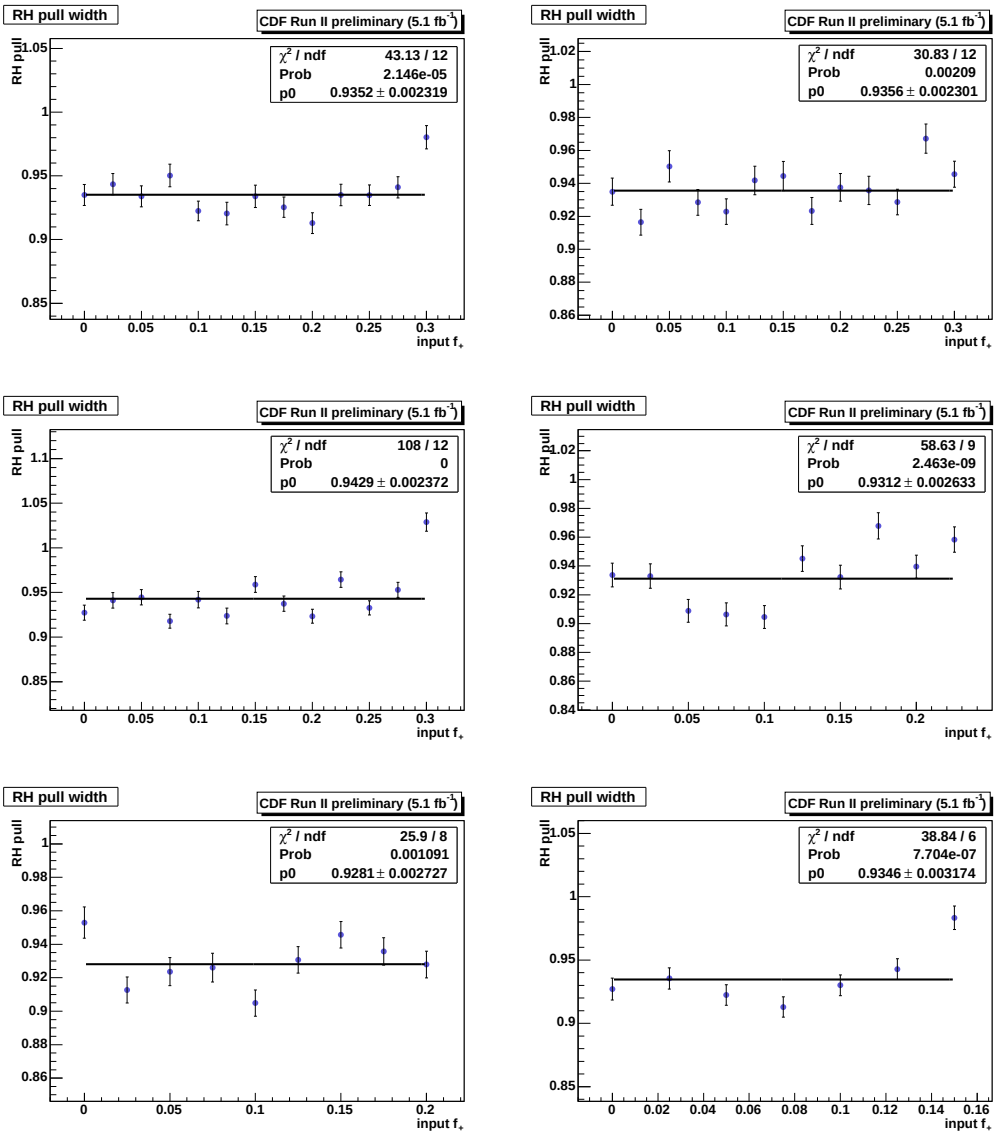

Figure 7.23: The f_+ pull width dependence for pre−tagged events as a function of input f_+ for input values of $f_0 = 0.600, 0.650, 0.700, 0.750, 0.800, 0.850$ (from top to bottom and left to right).

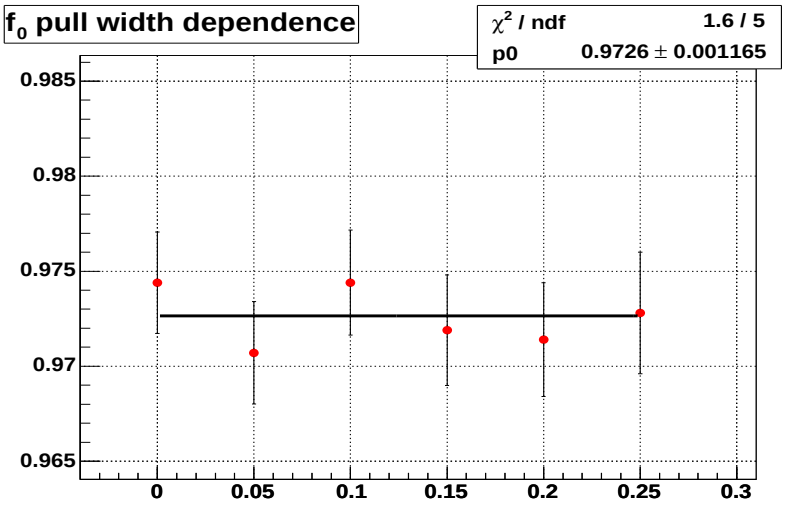

Figure 7.24: The dependence of constant fits to the pull widths dependences for f_0 of pre−tagged events.

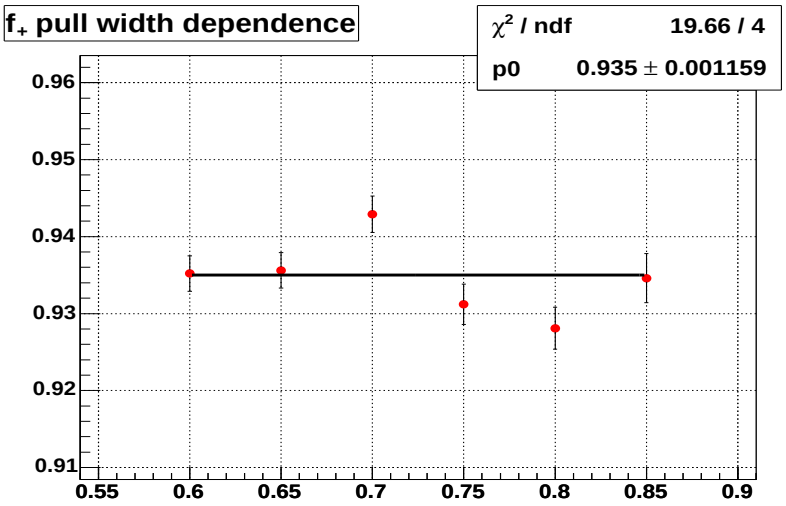

Figure 7.25: The dependence of constant fits to the pull widths dependences for f_+ of pre−tagged events.

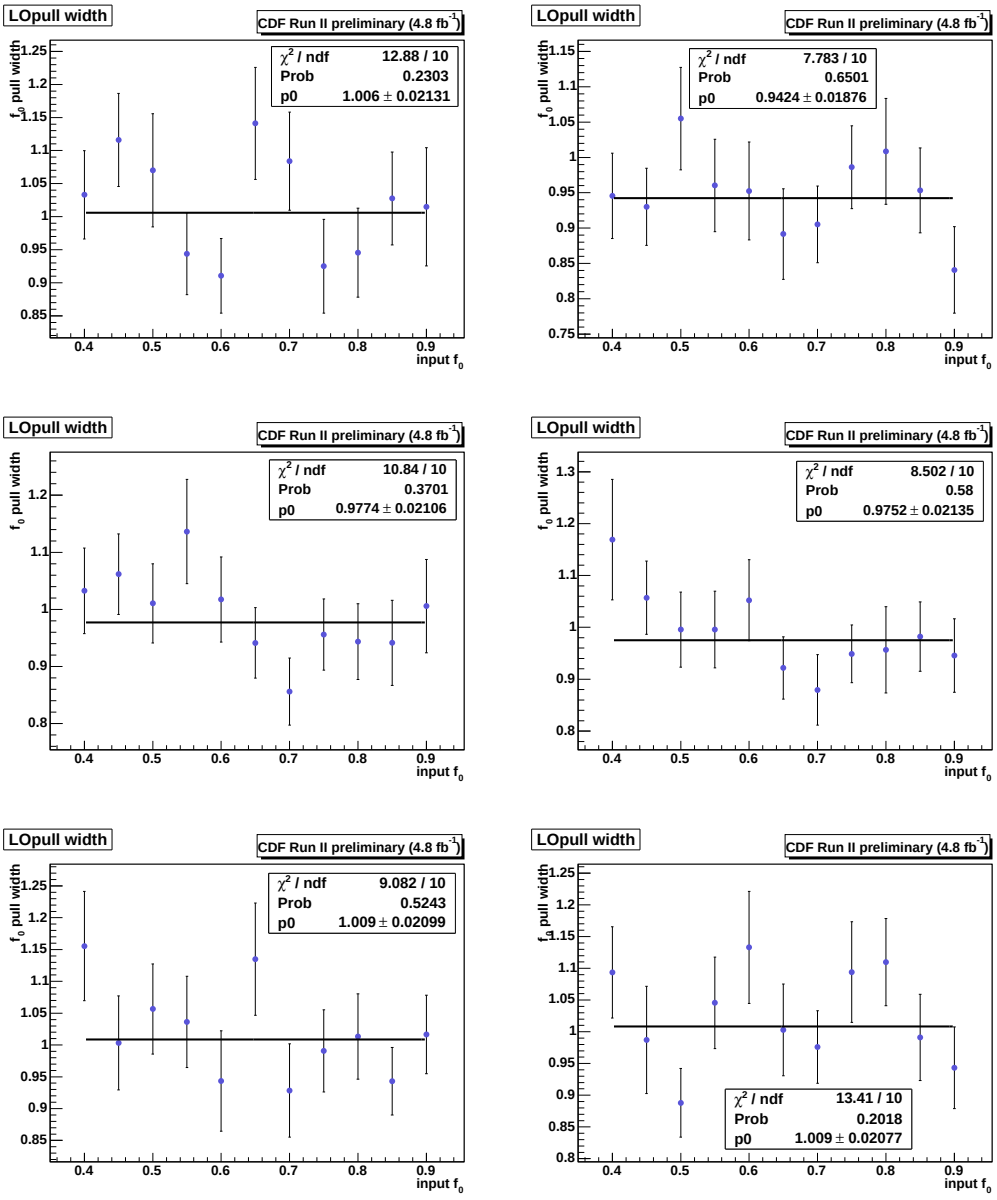

Figure 7.26: The f_0 pull width dependence for $b-$tagged events as a function of input f_0 for input values of $f_+ = 0.000, 0.025, 0.050, 0.075, 0.100, 0.125$ (from top to bottom and left to right).

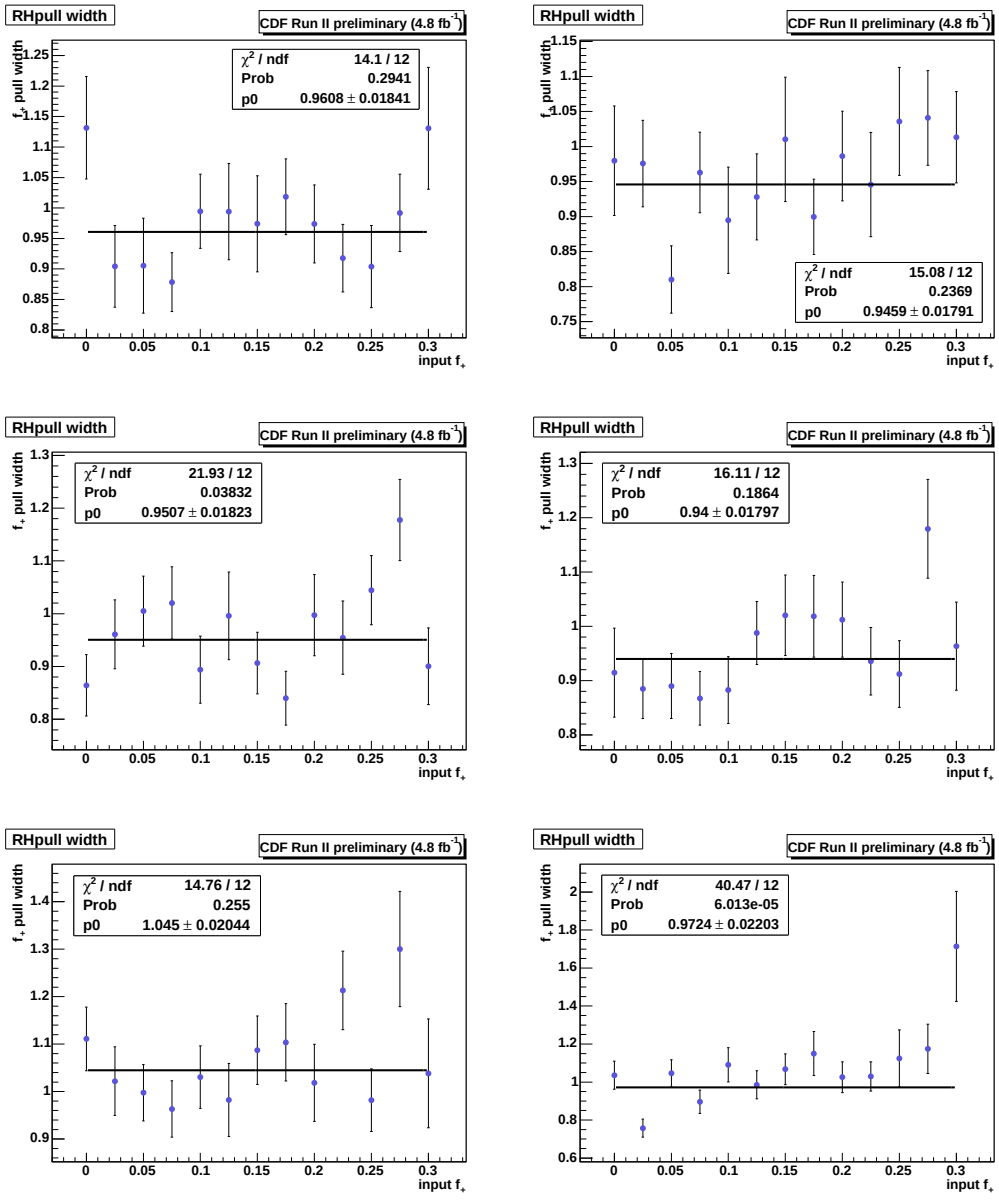

Figure 7.27: The f_+ pull width dependence for $b-$tagged events as a function of input f_+ for input values of $f_0 = 0.650, 0.700, 0.750, 0.800, 0.850, 0.900$ (from top to bottom and left to right).

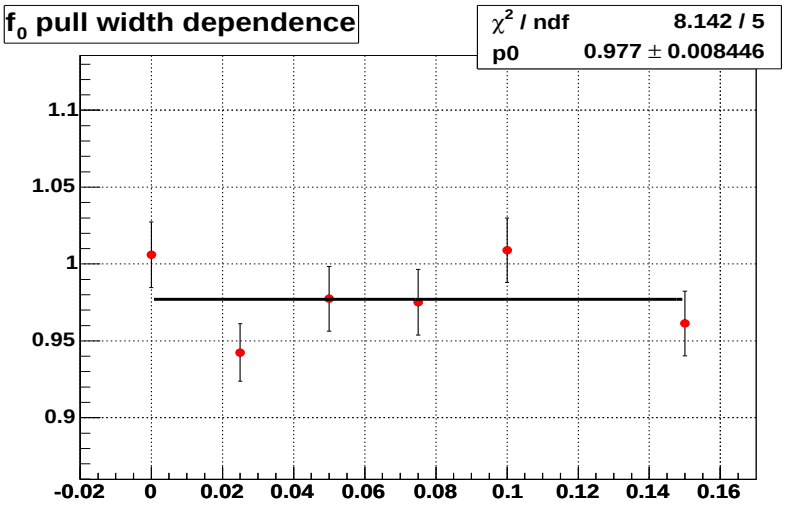

Figure 7.28: The dependence of constant fits to the pull widths dependences for f_0 of $b-$tagged events.

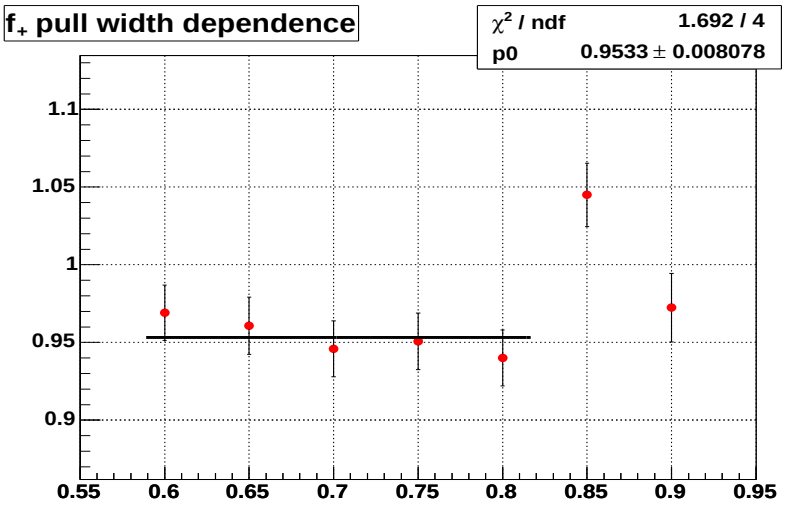

Figure 7.29: The dependence of constant fits to the pull widths dependences for f_+ of $b-$tagged events.

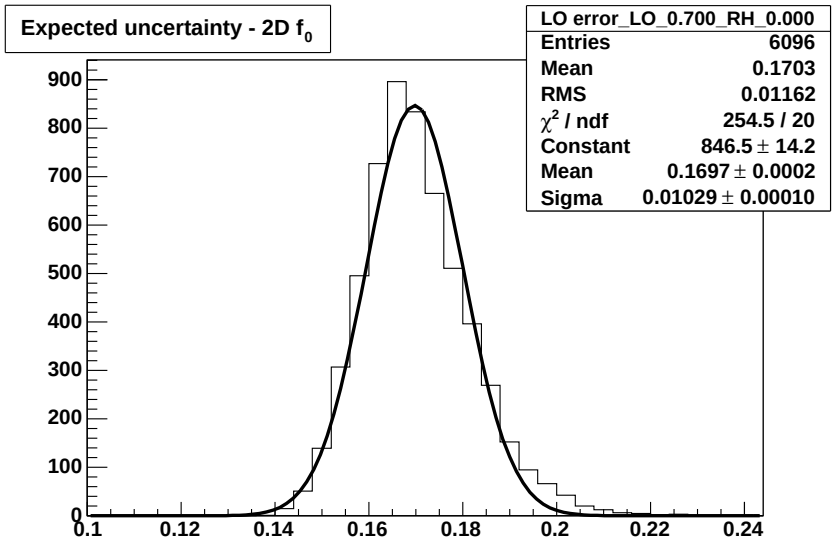

(a)

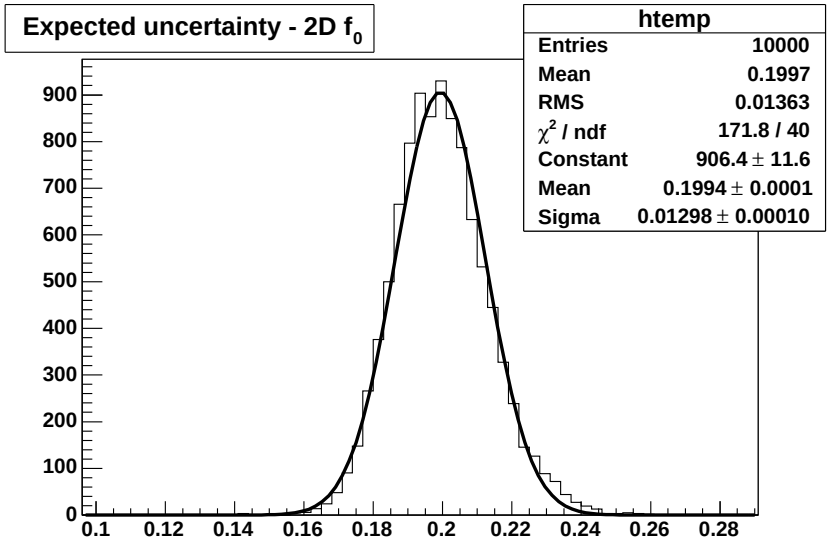

(b)

Figure 7.30: The expected uncertainty distribution for f_0^{2D} of pre−tagged (a) and b−tagged (b) events.

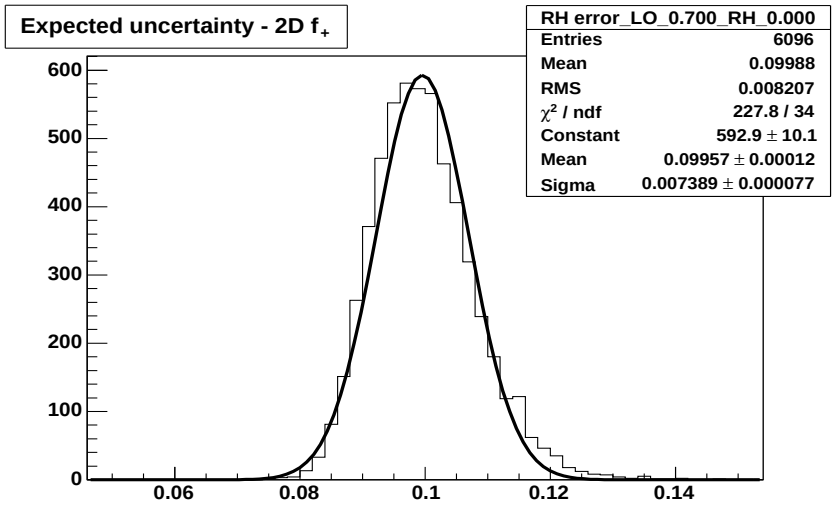

(a)

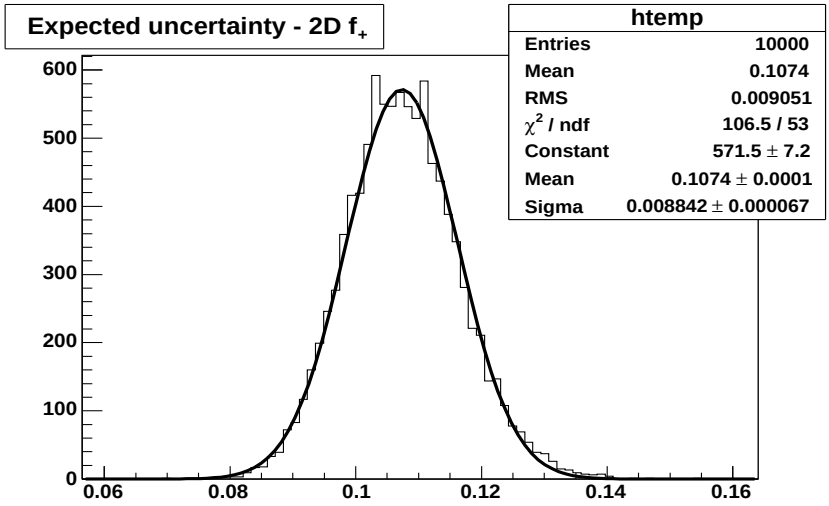

(b)

Figure 7.31: The expected uncertainty distribution for f_+^{2D} of pre−tagged (a) and b−tagged (b) events.

to be 0.17 for pre−tagged, 0.20 for $b-$tagged events and f_+^{2D} to be 0.10 for pre−tagged, 0.11 for $b-$tagged events (mean values of the fits to the distribution).

7.4 Systematic uncertainties

We evaluate systematic uncertainties using MC samples by performing one big pseudo-experiment where we use all events from a given MC sample. The background is included into the fit by randomly picking the events from background $\cos\theta^*$ distribution. The number of background events is determined such that it correspond to expected background to signal ratio for DIL $t\bar{t}$ selected events.

A few different systematic sources of systematic uncertainty are considered. They are described below and in the end combined into final systematic uncertainty of the measurement.

7.4.1 Jet energy scale

We evaluate the effect of uncertainty in the jet energy scale (JES) by applying $\pm 1\sigma$ shifts to energy corrections applied to jets (we apply level 5 jet energy corrections). After such shifts are applied, the number of events passing selection and reconstruction changes as well as shape of $\cos\theta^*$. The changes in reconstructed W helicity fractions together with assigned systematic uncertainty due to JES are shown in Table III.

sample (dataset,generator)	$f_0(1D)$	$f_+(1D)$
nominal (ttop75 - Pythia)	0.6486 ± 0.0062	-0.0263 ± 0.0032
JES + 1 σ	0.6792 ± 0.0061	-0.0070 ± 0.0032
JES - 1 σ	0.6131 ± 0.0064	-0.0461 ± 0.0032
Systematic uncertainty	0.033	0.020

sample (dataset,generator)	$f_0(2D)$	$f_+(2D)$
nominal (ttop75 - Pythia)	0.6688 ± 0.0128	-0.0120 ± 0.0067
JES + 1 σ	0.6604 ± 0.0126	0.0114 ± 0.0066
JES - 1 σ	0.6640 ± 0.0129	-0.0300 ± 0.0066
Systematic uncertainty	0.007	0.021

(a)

sample (dataset,generator)	$f_0(1D)$	$f_+(1D)$
nominal (ttop75 - Pythia)	0.6633 ± 0.0077	-0.0256 ± 0.0041
JES + 1 σ	0.6918 ± 0.0076	-0.0074 ± 0.0041
JES - 1 σ	0.6257 ± 0.0079	-0.0483 ± 0.0041
Systematic uncertainty	0.033	0.020

sample (dataset,generator)	$f_0(2D)$	$f_+(2D)$
nominal (ttop75 - Pythia)	0.7203 ± 0.0157	-0.0350 ± 0.0084
JES + 1 σ	0.7159 ± 0.0155	-0.0150 ± 0.0084
JES - 1 σ	0.7207 ± 0.0159	-0.0577 ± 0.0083
Systematic uncertainty	0.002	0.021

(b)

Table III: The reconstructed W helicity fractions for nominal and $\pm 1\sigma_{JES}$ samples for pre$-$tagged events (a) and $b-$tagged (b) events.

7.4.2 MC generators

We use GGWIG generator to generate signal templates and to generate sample used for the bias and uncertainty checks of the method. We also use Pythia to simulate some of the backgrounds. Since each generator use different hadronization model, the results between generators for the given process slightly differ.

Therefore we estimate what is the effect of using different generators on our measurement. For this purpose, we use 2 MC generators - Pythia and Herwig. The MC samples with input SM W helicity fractions are generated by both MC generators ($M_{top} = 175$ GeV). The difference between reconstructed fractions from both samples is assigned to be systematic uncertainty due to using different MC generators, see Table IV.

7.4.3 Initial and Final state radiation

Extra jets originating from the incoming partons and/or outgoing partons affect the measurement. These jets can be misidentified as jets coming from b-quarks or they can simply change the kinematics of the final state partons.

Since effect of the initial state radiation (ISR) and final state radiation (FSR) is correlated, it is studied simultaneously. Two Pythia samples are generated where it is increased (decreased) amount of ISR and FSR at the same time.

By doing the reconstruction on these "shifted" samples, we obtain shift in reconstructed fractions comparing to the fractions obtained using the nominal sample. The results are summarized in Table V.

MC generator (dataset)	$f_0(1D)$	$f_+(1D)$
Pythia (ttop75)	0.6486 ± 0.0062	-0.0263 ± 0.0032
Herwig (otop1s)	0.6839 ± 0.0066	-0.0079 ± 0.0035
Systematic uncertainty	0.035	0.018
MC generator (dataset)	$f_0(2D)$	$f_+(2D)$
Pythia (ttop75)	0.6688 ± 0.0128	-0.0120 ± 0.0067
Herwig (otop1s)	0.6868 ± 0.0136	-0.0018 ± 0.0072
Systematic uncertainty	0.018	0.010

(a)

MC generator (dataset)	$f_0(1D)$	$f_+(1D)$
Pythia (ttop75)	0.6633 ± 0.0077	-0.0256 ± 0.0041
Herwig (otop1s)	0.6951 ± 0.0082	-0.0075 ± 0.0045
Systematic uncertainty	0.032	0.018
MC generator (dataset)	$f_0(2D)$	$f_+(2D)$
Pythia (ttop75)	0.7203 ± 0.0157	-0.0350 ± 0.0084
Herwig (otop1s)	0.7303 ± 0.0168	-0.0219 ± 0.0091
Systematic uncertainty	0.010	0.013

(b)

Table IV: The reconstructed W helicity fractions for different MC generators for pre−tagged events (a) and b−tagged (b) events.

We use half of the difference between results obtained for samples with less and more ISR/FSR as the systematic uncertainty due to uncertainty in ISR/FSR.

7.4.4 Parton distribution functions

We determine the systematic uncertainty due to uncertainty in PDFs by using different set of PDFs MRST72 and MRST75. We compare the measured f_0 and f_+ values from these two MRST samples to that in the default ttop75 Pythia sample generated with CTEQ PDFs. Table VI shows the reconstructed W helicity fractions for different PDF systematic sample.

In addition, we consider the uncertainty in the parameters of the nominal PDFs. We measure $f_0(f_+)$ from CTEQ5L, MRST72, MRST75, CTEQ6L, CTEQ6L1, CTEQ6M and $\pm 1\sigma$ variation of the 20 CTEQ6M eigenvectors, 40 different weights are obtained per event using reweighting method as described in [46]. See Figures 7.32, 7.33.

We add in quadrature the difference between CTEQ6M 20 pairs of eigenvectors. The calculated systematic uncertainties are:

- For f_0 measurement (fixed $f_+ = 0.0$) : $\Delta f_0 = 0.004$
- For f_+ measurement (fixed $f_0 = 0.7$) : $\Delta f_+ = 0.002$
- For simultaneous measurement : $\Delta f_0 = 0.003$ and $\Delta f_+ = 0.003$

7.4.5 Background

We determine the systematic uncertainty due to fact that we do not know precisely the background amount and the shape the following way. Since

sample (generator,dataset)	$f_0(1D)$	$f_+(1D)$
nominal (Pythia - ttop75)	0.6486 ± 0.0062	-0.0263 ± 0.0032
ISR/FSR more (Pythia - otop03)	0.6613 ± 0.0096	-0.0175 ± 0.0050
ISR/FSR less (Pythia - otop04)	0.6854 ± 0.0096	-0.0150 ± 0.0051
Systematic uncertainty	0.025	0.010
sample (generator,dataset)	$f_0(2D)$	$f_+(2D)$
nominal (Pythia - ttop75)	0.6688 ± 0.0128	-0.0120 ± 0.0067
ISR/FSR more (Pythia - otop03)	0.6595 ± 0.0198	0.0011 ± 0.0104
ISR/FSR less (Pythia - otop04)	0.7430 ± 0.0199	-0.0350 ± 0.0105
Systematic uncertainty	0.042	0.018

(a)

sample (generator,dataset)	$f_0(1D)$	$f_+(1D)$
nominal (Pythia - ttop75)	0.6633 ± 0.0077	-0.0256 ± 0.0041
ISR/FSR more (Pythia - otop03)	0.6737 ± 0.0119	-0.0160 ± 0.0064
ISR/FSR less (Pythia - otop04)	0.6864 ± 0.0119	-0.0201 ± 0.0064
Systematic uncertainty	0.023	0.010
sample (generator,dataset)	$f_0(2D)$	$f_+(2D)$
nominal (Pythia - ttop75)	0.7203 ± 0.0157	-0.0350 ± 0.0084
ISR/FSR more (Pythia - otop03)	0.6980 ± 0.0243	-0.0150 ± 0.0131
ISR/FSR less (Pythia - otop04)	0.7786 ± 0.0244	-0.0572 ± 0.0131
Systematic uncertainty	0.041	0.021

(b)

Table V: The reconstructed W helicity fractions for different ISR/FSR systematic samples for pre−tagged events (a) and $b-$tagged (b) events.

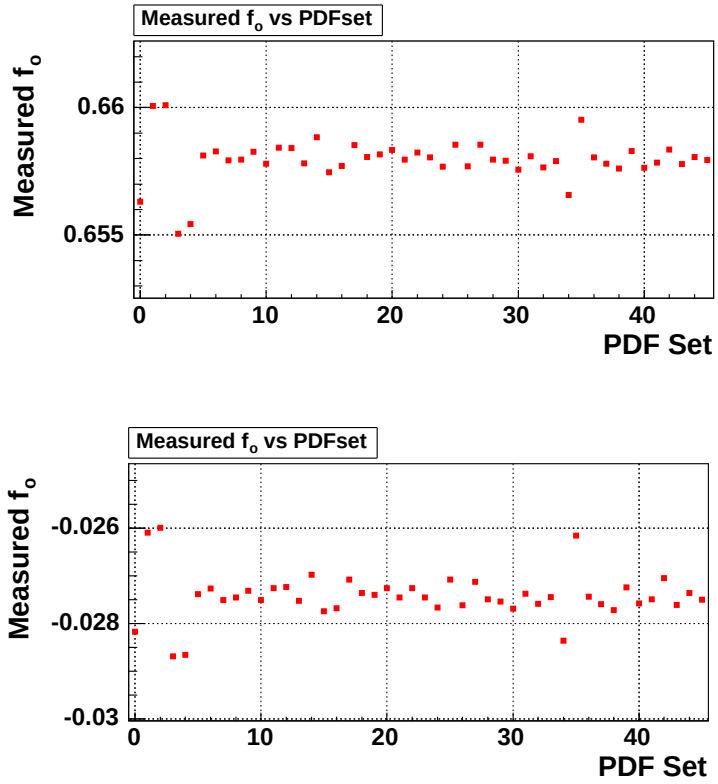

Figure 7.32: Top plot show the measurement the f_0 (fixed $f_+ = 0$) from CTEQ5L, MRST72, MRST75, CTEQ6L, CTEQ6L1, CTEQ6M and $\pm 1\sigma$ variation of the 20 CTEQ6M eigenvectors. And bottom plot is for the measurement the f_+ (fixed $f_0 = 0.7$) from 46 different PDF sets same as top plot.

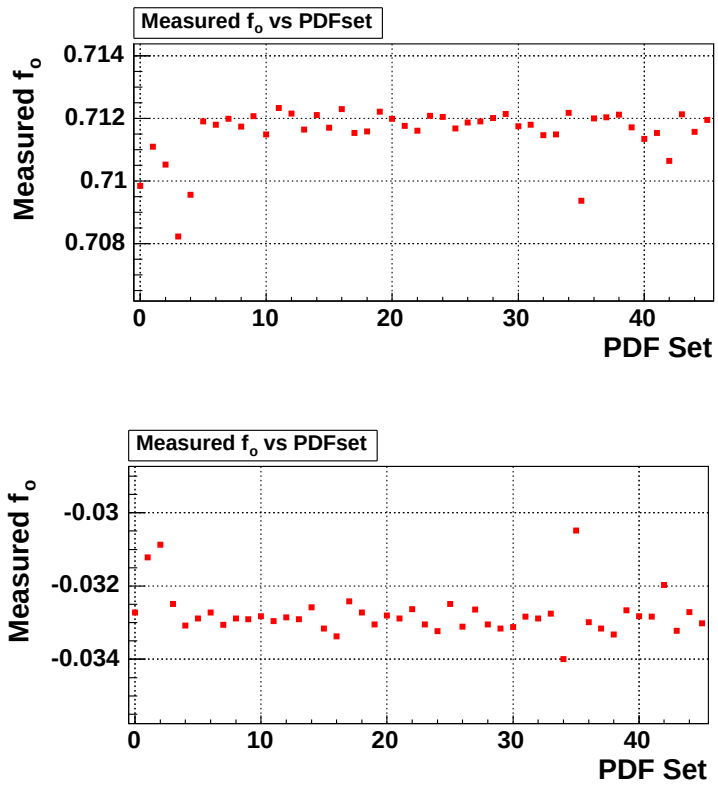

Figure 7.33: For the simultaneous measurement the f_0/f_+ from CTEQ5L, MRST72, MRST75, CTEQ6L, CTEQ6L1, CTEQ6M and $\pm 1\sigma$ variation of the 20 CTEQ6M eigenvectors. Top plot is for f_0 and bottom plot is for f_+.

sample	$f_0(1D)$	$f_+(1D)$
nominal CTEQ (ttop75)	0.6486 ± 0.0062	-0.0263 ± 0.0032
MRST72 (ttopgx)	0.6567 ± 0.0125	-0.0241 ± 0.0065
MRST75 (ttopgz)	0.6482 ± 0.0125	-0.0253 ± 0.0065
Systematic uncertainty	0.008	0.001
sample	$f_0(2D)$	$f_+(2D)$
nominal CTEQ (ttop75)	0.6688 ± 0.0128	-0.0120 ± 0.0067
MRST72 (ttopgx)	0.6866 ± 0.0255	-0.0180 ± 0.0134
MRST75 (ttopgz)	0.6599 ± 0.0256	-0.0070 ± 0.0134
Systematic uncertainty	0.027	0.011

(a)

sample	$f_0(1D)$	$f_+(1D)$
nominal CTEQ (ttop75)	0.6633 ± 0.0077	-0.0256 ± 0.0041
MRST72 (ttopgx)	0.6531 ± 0.0156	-0.0282 ± 0.0082
MRST75 (ttopgz)	0.6587 ± 0.0157	-0.0255 ± 0.0083
Systematic uncertainty	0.006	0.003
sample	$f_0(2D)$	$f_+(2D)$
nominal CTEQ (ttop75)	0.7203 ± 0.0157	-0.0350 ± 0.0084
MRST72 (ttopgx)	0.6947 ± 0.0314	-0.0257 ± 0.0168
MRST75 (ttopgz)	0.7004 ± 0.0316	-0.0257 ± 0.0169
Systematic uncertainty	0.006	0.000

(b)

Table VI: The reconstructed W helicity fractions for different PDF systematic samples for pre−tagged events (a) and $b-$tagged (b) events.

we allow to float the amount of background in the likelihood fit (see Eq. 7.3), we don't consider any background rate systematic uncertainty explicitly. However, we do consider the uncertainty in the shape of background templates. We evaluate it by changing the amount of each individual background by $\pm 1\sigma$ in the total background thus changing the overall shape of background template. As a systematic uncertainty, we combine all the shifts for each individual background in quadrature, see Table VIII.

7.4.6 Method

In our procedure, we use the templates to determine the W helicity fractions. These templates are parametrized. We evaluate the effect of limited statistics of the templates the following way.

We create 100 different fluctuated signal templates (for each W helicity fraction) by smearing the value in each bin according to Poisson distribution and obtain the parametrization by fitting them all with polynomial functions. After that, we perform 100 fits (always using different parametrization for all three signal templates) to the same high statistics sample (Pythia - ttop75). Plotting the results of the fit into one histogram, we obtain the distribution of reconstructed W helicity fraction. The width of this distribution determines the uncertainty in the reconstructed fraction given by the uncertainty in template parametrization and we use it as a measure of a systematic uncertainty. For the results, see Table IX. The distributions can be seen in Figure 7.34 and 7.35 for the 1D, 2D f_0 and f_+ fit of pre$-$tagged events and the distributions for $b-$tagged events are shown in Figure 7.36 and 7.37 for the 1D, 2D f_0 and f_+ fit.

Sample		$f_0(1D)$	$\Delta f_0(1D)$	$f_+(1D)$	$\Delta f_0(1D)$
Nominal background		0.6500 ± 0.0074	-	-0.0246 ± 0.0038	-
Diboson	$+1\sigma$	0.6498 ± 0.0074	0.0002	-0.0250 ± 0.0038	0.0004
	-1σ	0.6503 ± 0.0074		-0.0242 ± 0.0038	
DY$\to ee + \mu\mu$	$+1\sigma$	0.6544 ± 0.0074	0.0045	-0.0226 ± 0.0038	0.0021
	-1σ	0.6454 ± 0.0074		-0.0269 ± 0.0038	
DY$\to \tau\tau$	$+1\sigma$	0.6523 ± 0.0074	0.0023	-0.0241 ± 0.0038	0.0006
	-1σ	0.6477 ± 0.0074		-0.0253 ± 0.0038	
FAKES	$+1\sigma$	0.6415 ± 0.0074	0.0099	-0.0276 ± 0.0038	0.0034
	-1σ	0.6612 ± 0.0074		-0.0209 ± 0.0038	
Systematic uncertainty		0.011		0.004	

Sample		$f_0(2D)$	$\Delta f_0(2D)$	$f_+(2D)$	$\Delta f_0(2D)$
Nominal background		0.6637 ± 0.0153	-	-0.0081 ± 0.0080	-
Diboson	$+1\sigma$	0.6656 ± 0.0153	0.0019	-0.0094 ± 0.0080	0.0013
	-1σ	0.6618 ± 0.0153		-0.0068 ± 0.0080	
DY$\to ee + \mu\mu$	$+1\sigma$	0.6673 ± 0.0154	0.0037	-0.0077 ± 0.0080	0.0005
	-1σ	0.6600 ± 0.0152		-0.0086 ± 0.0079	
DY$\to \tau\tau$	$+1\sigma$	0.6692 ± 0.0154	0.0056	-0.0101 ± 0.0080	0.0019
	-1σ	0.6580 ± 0.0152		-0.0062 ± 0.0079	
FAKES	$+1\sigma$	0.6484 ± 0.0151	0.0181	-0.0041 ± 0.0078	0.0049
	-1σ	0.6846 ± 0.0154		-0.0139 ± 0.0080	
Systematic uncertainty		0.019		0.005	

Table VII: The reconstructed W helicity fractions assuming different pre−tagged background composition.

sample	$f_0(1D)$	$\Delta f_0(1D)$	$f_+(1D)$	$\Delta f_+(1D)$
nominal background	0.6644 ± 0.0080	–	-0.0263 ± 0.0042	–
dibosons	$+1\sigma$: 0.6638	0.0007	$+1\sigma$: -0.0265	0.0002
	-1σ: 0.6651		-1σ: -0.0261	
DY + LF	$+1\sigma$: 0.6676	0.0038	$+1\sigma$: -0.0242	0.0025
	-1σ: 0.6601		-1σ: -0.0291	
DY + HF	$+1\sigma$: 0.6654	0.0013	$+1\sigma$: -0.0256	0.0010
	-1σ: 0.6628		-1σ: -0.0275	
FAKES	$+1\sigma$: 0.6617	0.0062	$+1\sigma$: -0.0283	0.0046
	-1σ: 0.6741		-1σ: -0.0191	
Systematic uncertainty	0.0074		0.0053	

sample	$f_0(2D)$	$\Delta f_0(2D)$	$f_+(2D)$	$\Delta f_+(2D)$
nominal background	0.7298 ± 0.0162	–	-0.0402 ± 0.0086	–
dibosons	$+1\sigma$: 0.7286	0.0013	$+1\sigma$: -0.0398	0.0004
	-1σ: 0.7312		-1σ: -0.0406	
DY + LF	$+1\sigma$: 0.7288	0.0012	$+1\sigma$: -0.0376	0.0030
	-1σ: 0.7311		-1σ: -0.0436	
DY + HF	$+1\sigma$: 0.7290	0.0011	$+1\sigma$: -0.0391	0.0014
	-1σ: 0.7311		-1σ: -0.0419	
FAKES	$+1\sigma$: 0.7320	0.0054	$+1\sigma$: -0.0432	0.0071
	-1σ: 0.7213		-1σ: -0.0290	
Systematic uncertainty	0.0058		0.0078	

Table VIII: The reconstructed W helicity fractions assuming different $b-$tagged background composition.

sample	Δ (signal templates)	Δ (background templates)
1D f_0 fit	0.010	0.010
1D f_+ fit	0.006	0.004
2D f_0 fit	0.020	0.021
2D f_+ fit	0.012	0.009

(a)

sample	Δ (signal templates)	Δ (background templates)
1D f_0 fit	0.014	0.009
1D f_+ fit	0.006	0.004
2D f_0 fit	0.031	0.022
2D f_+ fit	0.015	0.011

(b)

Table IX: The systematic uncertainty due to uncertainty in signal and background templates for pre−tagged events (a) and b−tagged (b) events.

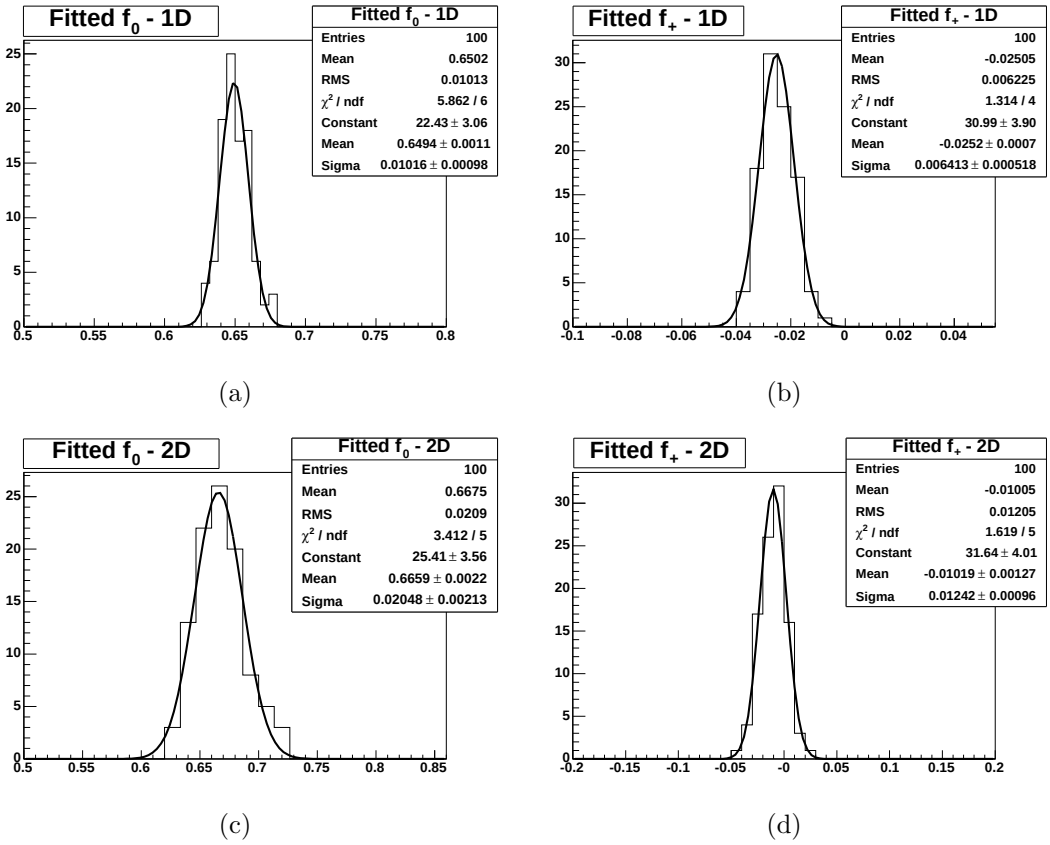

Figure 7.34: The distribution of reconstructed 1D f_0 (a), 1D f_+ (b), 2D f_0 (c) and 2D f_+ (d) of pre−tagged events for 100 fluctuated signal templates.

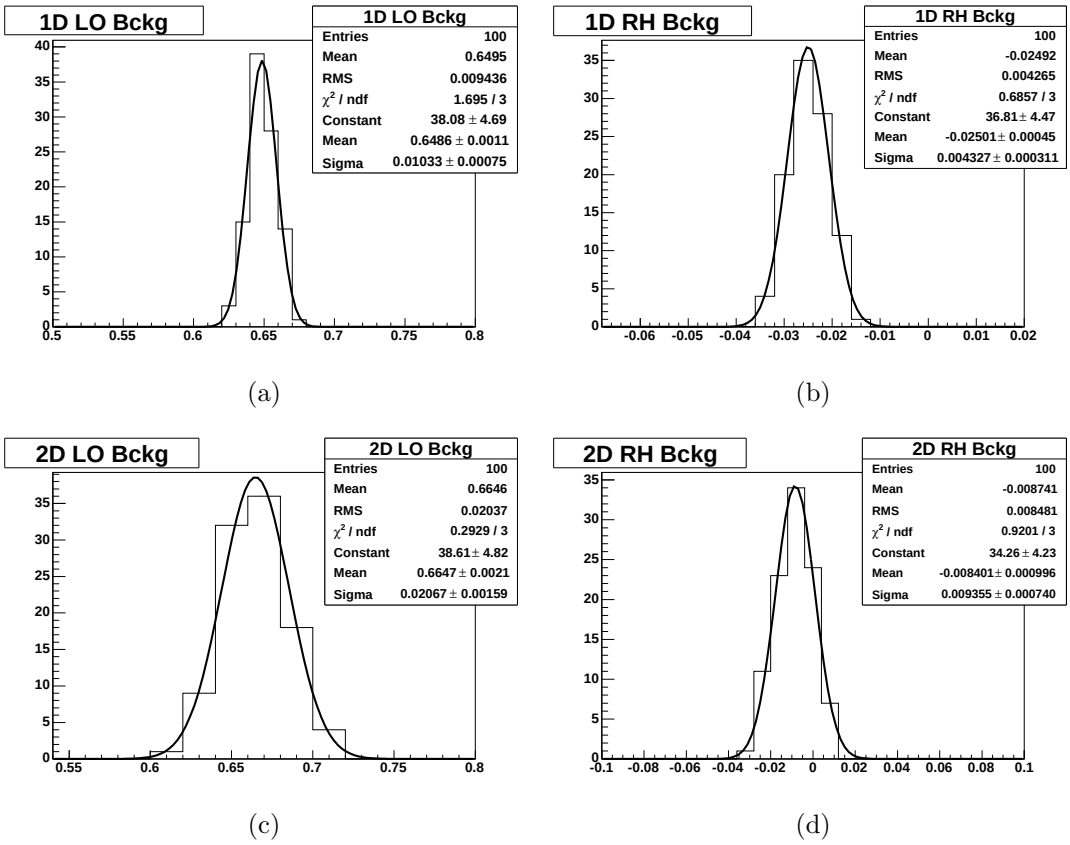

Figure 7.35: The distribution of reconstructed 1D f_0 (a), 1D f_+ (b), 2D f_0 (c), 2D f_+ (d) of pre−tagged events for 100 fluctuated background templates.

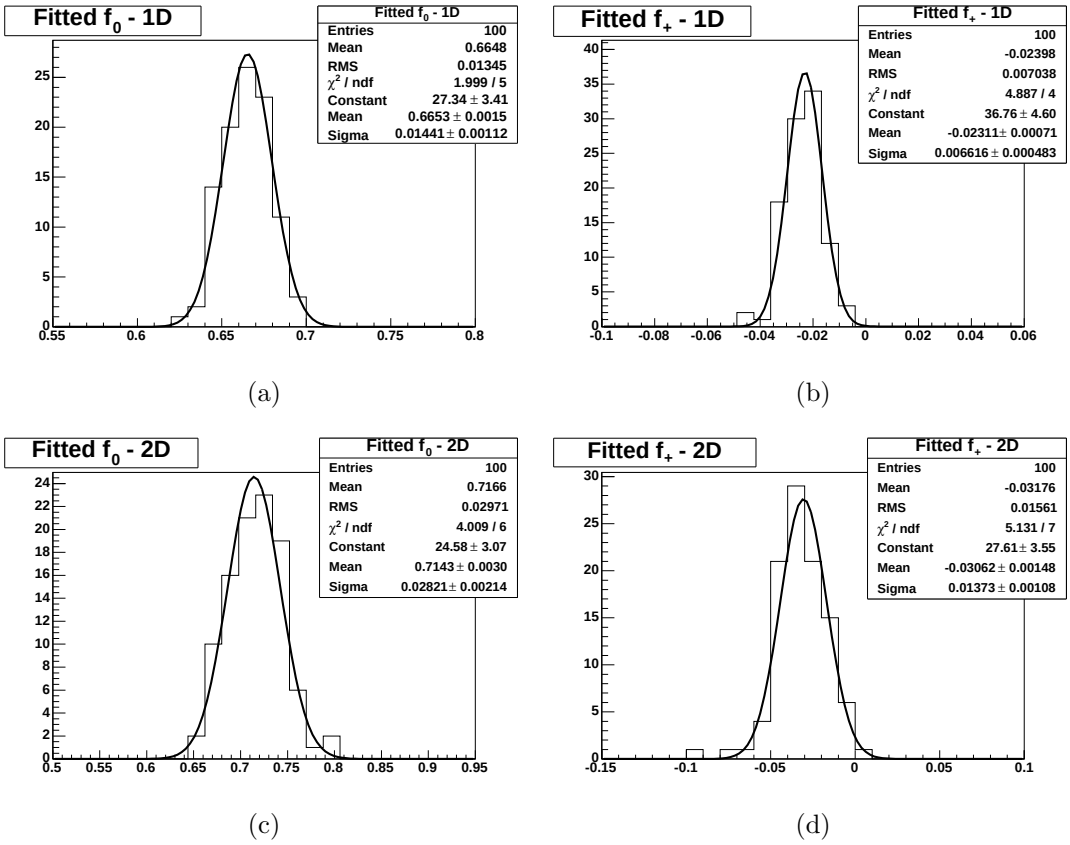

Figure 7.36: The distribution of reconstructed 1D f_0 (a), 1D f_+ (b), 2D f_0 (c) and 2D f_+ (d) of $b-$tagged events for 100 fluctuated signal templates.

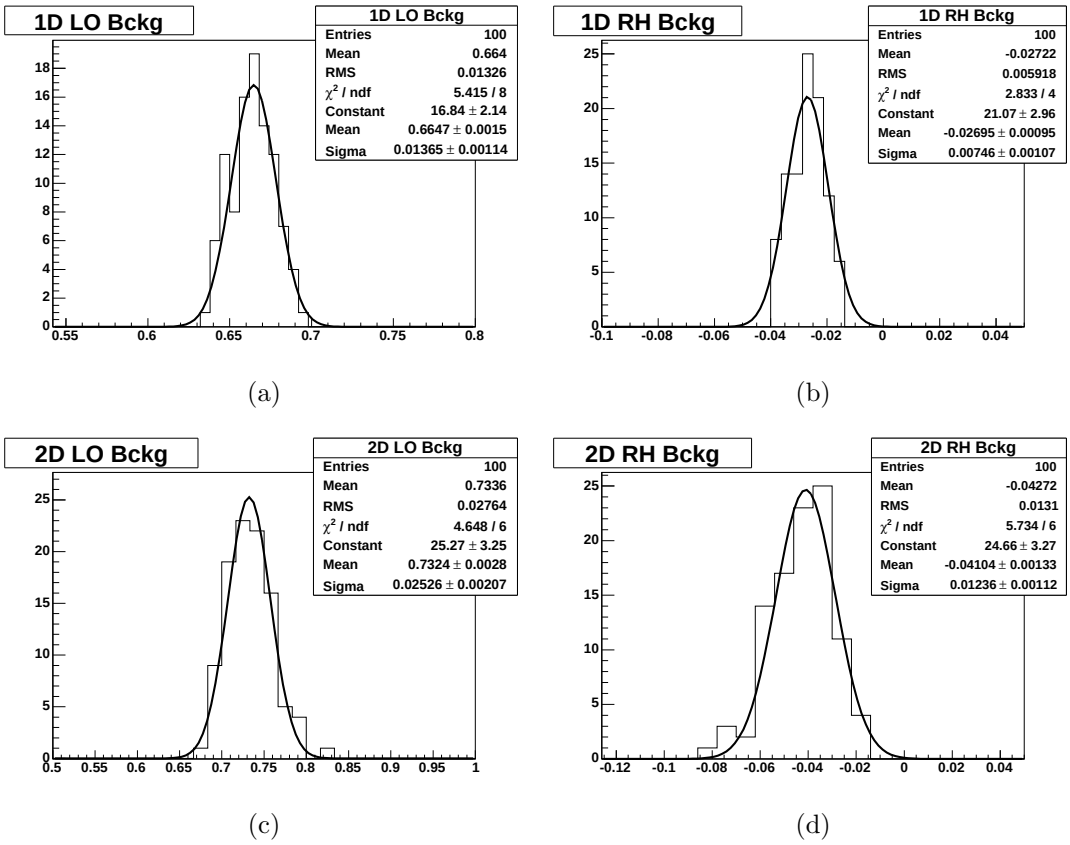

Figure 7.37: The distribution of reconstructed 1D f_0 (a), 1D f_+ (b), 2D f_0 (c), 2D f_+ (d) of $b-$tagged events for 100 fluctuated background templates.

7.4.7 Instantaneous luminosity dependence

We evaluate the effect of changing instantaneous luminosity over the period of CDF data taking using two different kind of MC signal samples: ttop75 which uses low luminosity profile (corresponding to first 1.2 fb^{-1} of data) and otop49 which uses so called "medium+high" luminosity profile (corresponding to selected high luminosity runs from data periods 10 to 17). Since the data run luminosities are somewhere in between, we take half of the difference between these results as a systematic uncertainty.

The results for both 1D and 2D fits are presented in Table X.

7.4.8 Summary of systematic uncertainties

The total systematic uncertainty is assumed to be independent sum of all partial systematic uncertainties due to different sources. As such, we determine it by summing the individual uncertainties in quadrature. The summary of uncertainties is in Table XI.

7.4.9 Top mass dependence

The W boson helicity fractions directly depend on m_{top} in SM, see Eq. 1.15. Although in our measurement we assume fixed top quark mass (m_{top} = 175 GeV), we estimate the dependence of the measured result as a function of top quark mass.

We use the template method where the samples used to make the templates are generated with m_{top} = 175 GeV. In order to correctly produce the result for different m_top (e.g. 172.5 GeV), we would need to repeat the whole analysis with the new templates. The corresponding samples do not exist for

MC samle (dataset)	$f_0(1D)$	$f_+(1D)$
low luminosity (ttop75)	0.6486 ± 0.0062	-0.0263 ± 0.0032
med+high luminosity (otop49)	0.6815 ± 0.0097	-0.0108 ± 0.0052
Systematic uncertainty	0.016	0.008
MC samle (dataset)	$f_0(2D)$	$f_+(2D)$
low luminosity (ttop75)	0.6688 ± 0.0128	-0.0120 ± 0.0067
med+high luminosity (otop49)	0.6971 ± 0.0201	-0.0095 ± 0.0107
Systematic uncertainty	0.014	0.001

(a)

MC samle (dataset)	$f_0(1D)$	$f_+(1D)$
low luminosity (ttop75)	0.6633 ± 0.0077	-0.0256 ± 0.0041
med+high luminosity (otop49)	0.6930 ± 0.0122	-0.0079 ± 0.0066
Systematic uncertainty	0.015	0.009
MC samle (dataset)	$f_0(2D)$	$f_+(2D)$
low luminosity (ttop75)	0.7203 ± 0.0157	-0.0350 ± 0.0084
med+high luminosity (otop49)	0.7243 ± 0.0250	-0.0195 ± 0.0136
Systematic uncertainty	0.002	0.008

(b)

Table X: The systematic uncertainty due to instantaneous luminosity effects for pre−tagged events (a) and $b-$tagged (b) events.

Source	Δf_0 (1D)	Δf_+ (1D)	Δf_0 (2D)	Δf_+ (2D)
Jet Energy Scale	0.033	0.019	0.007	0.014
Generators	0.036	0.018	0.019	0.010
ISR/FSR	0.025	0.010	0.042	0.018
PDF	0.010	0.002	0.027	0.011
Background shape	0.011	0.004	0.019	0.005
Template statistics				
Signal	0.010	0.006	0.020	0.012
Background	0.010	0.004	0.021	0.009
Instant. luminos. modeling	0.016	0.008	0.014	0.001
Total	0.060	0.030	0.063	0.030

(a)

Source	Δf_0 (1D)	Δf_+ (1D)	Δf_0 (2D)	Δf_+ (2D)
Jet Energy Scale	0.033	0.020	0.002	0.021
Generators	0.032	0.018	0.010	0.013
ISR/FSR	0.023	0.010	0.041	0.021
PDF	0.007	0.004	0.007	0.003
Background shape	0.007	0.005	0.006	0.008
Template statistics				
Signal	0.014	0.006	0.031	0.015
Background	0.009	0.004	0.022	0.011
Instant. luminos. modeling	0.015	0.009	0.002	0.008
Total	0.057	0.032	0.058	0.039

(b)

Table XI: Summary of the systematic uncertainties on the W helicity fractions measurement for pre−tagged events (a) and b−tagged (b) events. The total uncertainty is obtained by adding the individual contributions in quadrature.

the mass point of 172.5 GeV as of now. For the next round of the analysis, we plan to generate and use the samples with $m_{top} = 172.5$ GeV (or whatever mass will be recommended by top group since new Tevatron combined top mass is 173.3 GeV). For this round of the analysis, we estimate the effect of W helicity fraction dependence on top quark mass by using the MC samples with different m_{top} generated (ttop75 for $m_{top} = 175$ GeV, ytop72 for $m_{top} = 172.5$ GeV, ytop77 for $m_{top} = 177$ GeV), see Fig. 7.38 and 7.39.

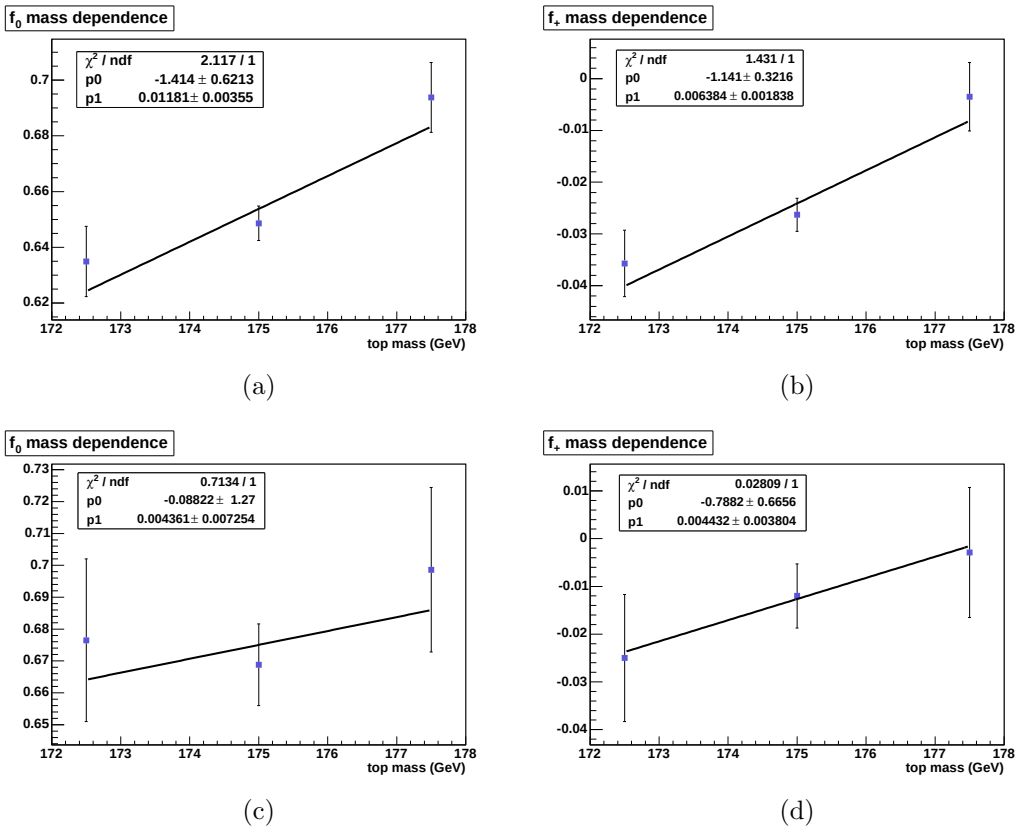

Figure 7.38: The dependence of reconstructed f_0^{1D} (a) and f_+^{1D} (b) on top quark mass for the case of single fraction fit before $b-$tagging requirement (second fraction is fixed). The dependence of reconstructed f_0^{2D} (c) and f_+^{2D} (d) on top quark mass for the case of simultaneous fit of both f_0 and f_+.

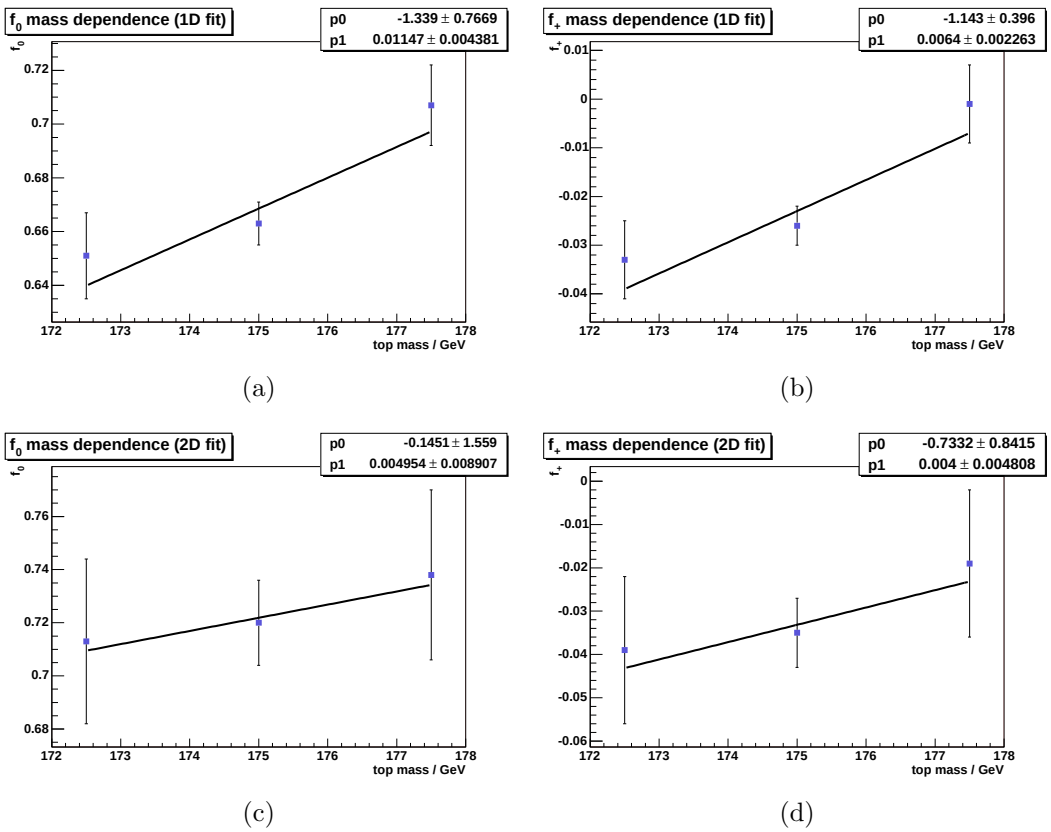

Figure 7.39: The dependence of reconstructed f_0^{1D} (a) and f_+^{1D} (b) on top quark mass for the case of single fraction fit after $b-$tagging requirement (second fraction is fixed). The dependence of reconstructed f_0^{2D} (c) and f_+^{2D} (d) on top quark mass for the case of simultaneous fit of both f_0 and f_+.

It can be seen that there is about 0.012 (pre$-$tag and $b-$tag) change in f_0 per 1 GeV change in top quark mass and similarly 0.006 (pre$-$tag and $b-$tag) change for f_+ in case of 1D fit. In case of 2D fit, the change is 0.004 (pre$-$tag and $b-$tag) for f_0 and 0.005 (pre$-$tag), 0.004 ($b-$tag) for f_+.

7.5 Results of W polarization measurement

The procedure which was extensively tested on MC samples is applied on CDF data corresponding to luminosity of 5.1 fb^{-1} (4.8 fb^{-1} after requiring the identification of one of the jets originating from a b quark) which is collected between March 2002 and June 2009 and corresponding to data periods P0 - P25. There are 343 pre−tagged candidate events and 137 b−tagged events passing DIL btag selection. Out of these, 304 pre−tagged events and 118 b−tagged events pass the $t\bar{t}$ kinematic reconstruction. The $\cos\theta^*$ distribution from data together with the SM expectations for pre−tagged and b−tagged candidate events shown in Figures 7.40 and 7.41.

First, we perform 1D measurement of f_0 fraction assuming SM expected value $f_+ = 0.0$ The NLL corresponding to 1D f_0 fit can be seen in Figure 7.42. The measured value of f_0 given by the minimum of NLL are $f_0^{1D} = 0.58 \pm 0.09$ for pre−tagged events and $f_0^{1D} = 0.59 \pm 0.11$ for b−tagged events. Applying correction determined in Sec. 7.3.1, we obtain the final results of $f_0^{1D} = 0.60 \pm 0.09$ for pre−tagged events and $f_0^{1D} = 0.62 \pm 0.11$ for b−tagged events.

Next, we perform 1D fit of f_+ fraction assuming SM expected value $f_0 = 0.7$. The NLL corresponding to 1D f_0 fit can be seen in Figure 7.43. The measured value of f_+ given by the minimum of the NLL are $f_+^{1D} = -0.07 \pm 0.04$ for pre−tagged events and $f_+^{1D} = -0.08\ ^{+\ 0.06}_{-\ 0.05}$ for b−tagged events. Applying correction determined in Sec. 7.3.2, we obtain the final results of $f_+^{1D} = -0.05 \pm 0.04$ for pre−tagged events and $f_+^{1D} = -0.07\ ^{+\ 0.06}_{-\ 0.05}$ for b−tagged events. The 1D fit results are summarized with systematic uncertainties in Table XII.

At the end, we perform 2D model independent fit of both f_0 and f_+ fractions simultaneously. The NLL corresponding to 2D f_0 and f_+ fit can be seen in Figure 7.45. The measured values of f_0 and f_+ given by the minimum of the NLL are $f_0^{2D} = 0.70\ ^{+\ 0.19}_{-\ 0.18}$ and $f_+^{2D} = -0.07\ ^{+\ 0.09}_{-\ 0.10}$ for pre−tagged events and $f_0^{2D} = 0.78\ \pm\ 0.21$ and $f_+^{2D} = -0.11\ ^{+\ 0.11}_{-\ 0.10}$ for b−tagged events. Applying correction determined in Sec. 7.3.3, we obtain the final results of $f_0^{2D} = 0.72\ ^{+\ 0.19}_{-\ 0.18}$ and $f_+^{2D} = -0.06\ ^{+\ 0.09}_{-\ 0.10}$ for pre−tagged events and $f_0^{2D} = 0.78\ \pm\ 0.21$ and $f_+^{2D} = -0.12\ ^{+\ 0.11}_{-\ 0.10}$ for b−tagged events. The 2D fit results are summarized with systematic uncertainties in Table XII.

7.5.1 Upper limit on f_+

Our measurement of f_+ is consistent with SM expectation (zero). By assuming SM value of $f_0 = 0.7$, we can determine the upper limit on f_+.

We follow the Bayesian procedure, where we assume constant *a priori* probability density for f_+ within physically possible range $< 0.0, 0.3 >$. Multiplying the likelihood distribution by prior probability density, we arrive at *a posterior* probability density. The value of f_+ below which the area of posterior probability density is $\geq 95\%$ determines the upper limit on f_+ at 95 % C.L. For the case of only taking into account the statistical uncertainty, the limit is $f_+ < 0.06$ (pre−tag) $f_+ < 0.08$ (b−tag), see Figure 7.46 and 7.48. When taking into account also systematic uncertainty by convoluting likelihood with Gaussian having mean zero and width equal to total systematic uncertainty of f_+ measurement, the results becomes: $f_+ < 0.07$ (pre−tag) $f_+ < 0.09$ (b−tag), see Figure 7.47 and 7.49.

	Pre−tagged Results (5.1 fb^{-1})	
	Before applying correction	After applying correction
f_0^{1D}	$0.58 \pm 0.09(\text{stat}) \pm 0.06(\text{syst})$	$0.60 \pm 0.09(\text{stat}) \pm 0.06(\text{syst})$
f_+^{1D}	$-0.07 \pm 0.04(\text{stat}) \pm 0.03(\text{syst})$	$-0.05 \pm 0.04(\text{stat}) \pm 0.03(\text{syst})$
f_0^{2D}	$0.70\ ^{+}_{-}\ ^{0.19}_{0.18}(\text{stat}) \pm 0.06(\text{syst})$	$0.72\ ^{+}_{-}\ ^{0.19}_{0.18}(\text{stat}) \pm 0.06(\text{syst})$
f_+^{2D}	$-0.07\ ^{+}_{-}\ ^{0.09}_{0.10}(\text{stat}) \pm 0.03(\text{syst})$	$-0.06\ ^{+}_{-}\ ^{0.09}_{0.10}(\text{stat}) \pm 0.03(\text{syst})$

(a)

	b−tagged Results (4.8 fb^{-1})	
	Before applying correction	After applying correction
f_0^{1D}	$0.59 \pm 0.11(\text{stat}) \pm 0.06(\text{syst})$	$0.62 \pm 0.11(\text{stat}) \pm 0.06(\text{syst})$
f_+^{1D}	$-0.08\ ^{+}_{-}\ ^{0.06}_{0.05}(\text{stat}) \pm 0.03(\text{syst})$	$-0.07\ ^{+}_{-}\ ^{0.06}_{0.05}(\text{stat}) \pm 0.03(\text{syst})$
f_0^{2D}	$0.78 \pm 0.21(\text{stat}) \pm 0.06(\text{syst})$	$0.78 \pm 0.21(\text{stat}) \pm 0.06(\text{syst})$
f_+^{2D}	$-0.11\ ^{+}_{-}\ ^{0.11}_{0.10}(\text{stat}) \pm 0.04(\text{syst})$	$-0.12\ ^{+}_{-}\ ^{0.11}_{0.10}(\text{stat}) \pm 0.04(\text{syst})$

(b)

Table XII: Summary of W boson helicity fraction measurements for pre−tagged (a) and b−tagged (b) events.

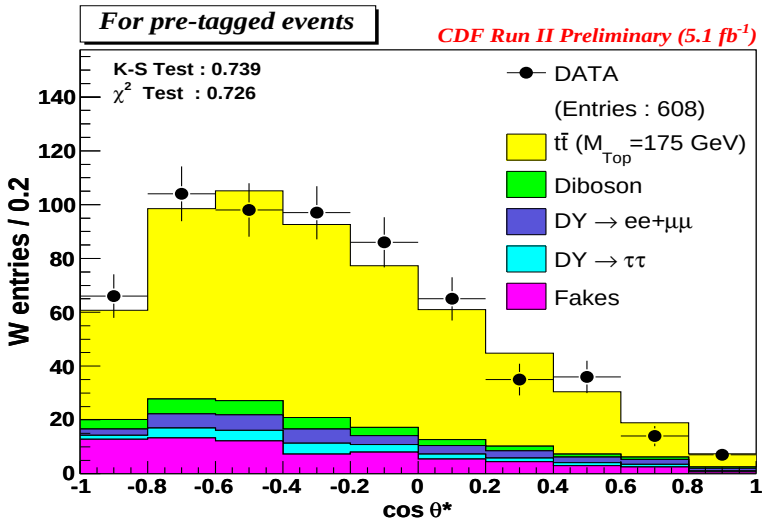

(a)

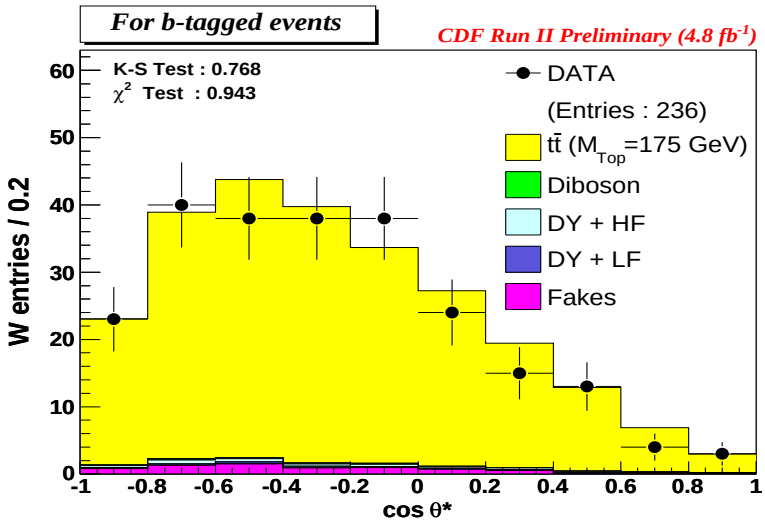

(b)

Figure 7.40: $\cos\theta^*$ distribution for data together with the SM expectations for pre−tagged (a) and b−tagged events (b).

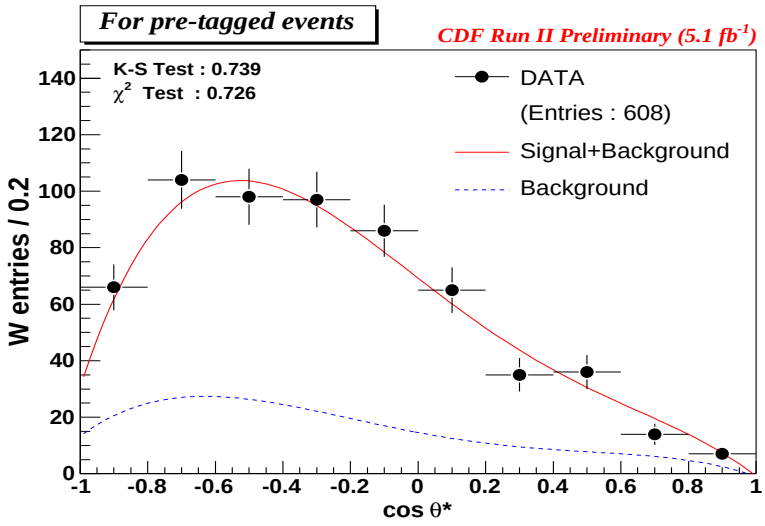

(a)

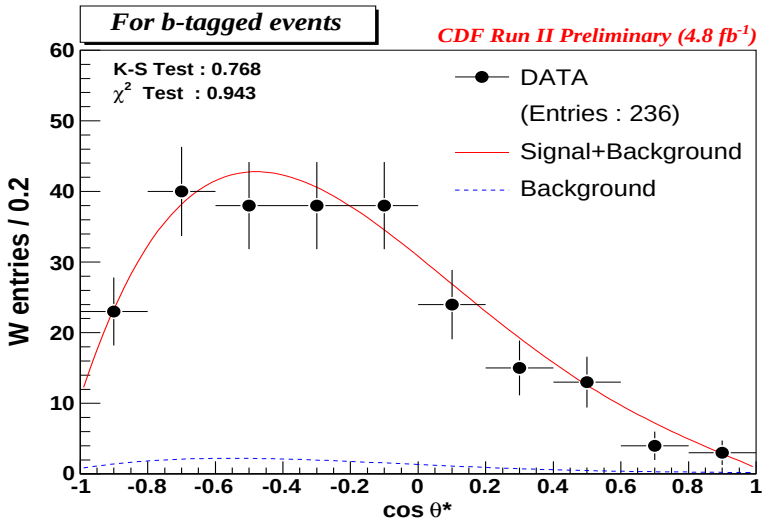

(b)

Figure 7.41: $\cos\theta^*$ distribution for data together with the SM expectations for pre−tagged (a) and b−tagged events (b).

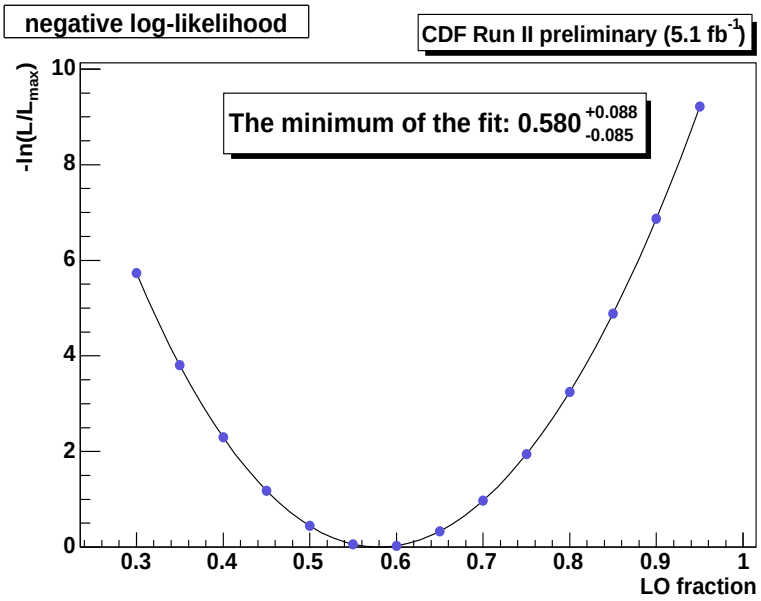

(a)

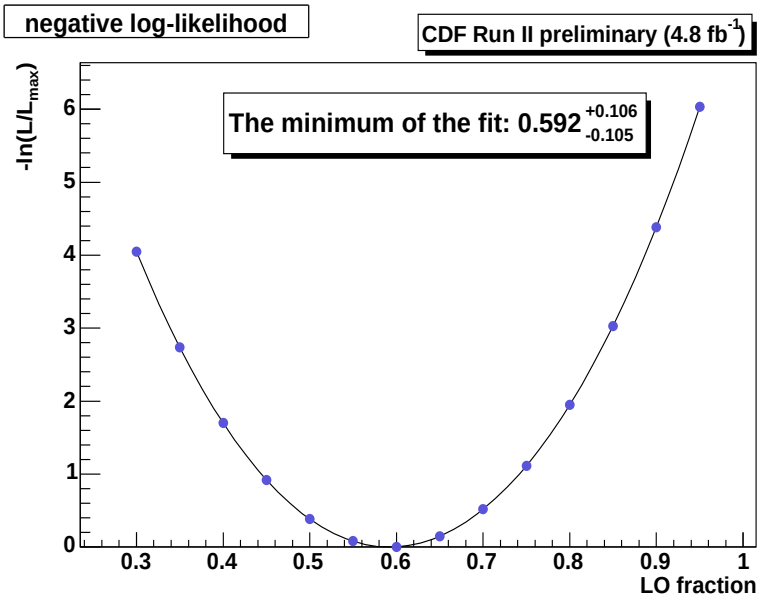

(b)

Figure 7.42: The NLL curve for 1D f_0 fit for pre−tagged (a) and b−tagged events (b).

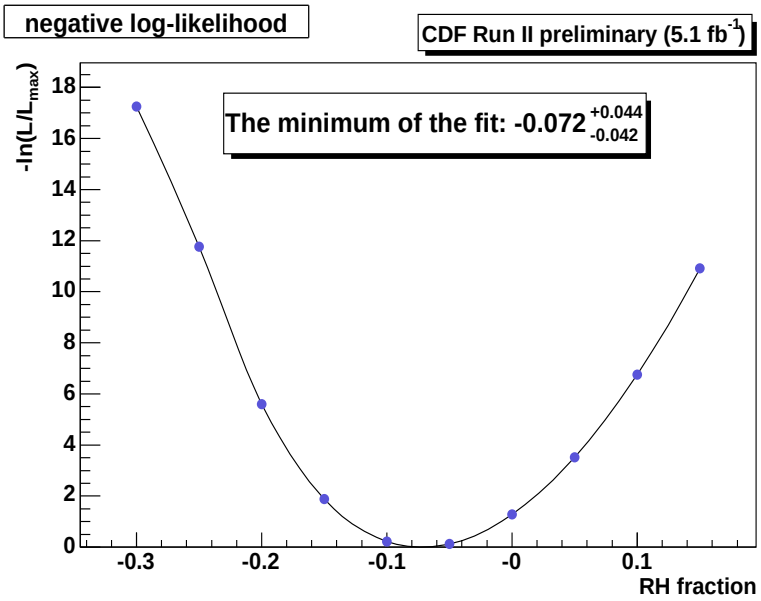

(a)

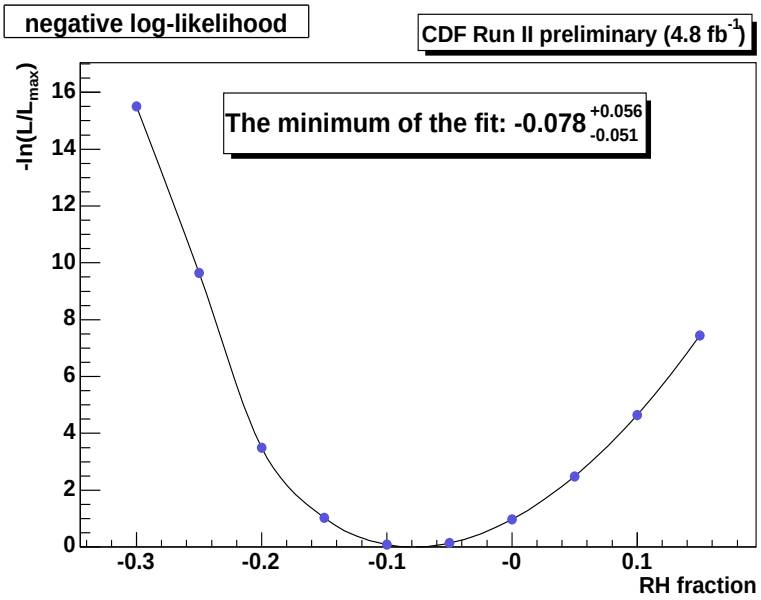

(b)

Figure 7.43: The NLL curve for 1D f_+ fit for pre−tagged (a) and b−tagged events (b).

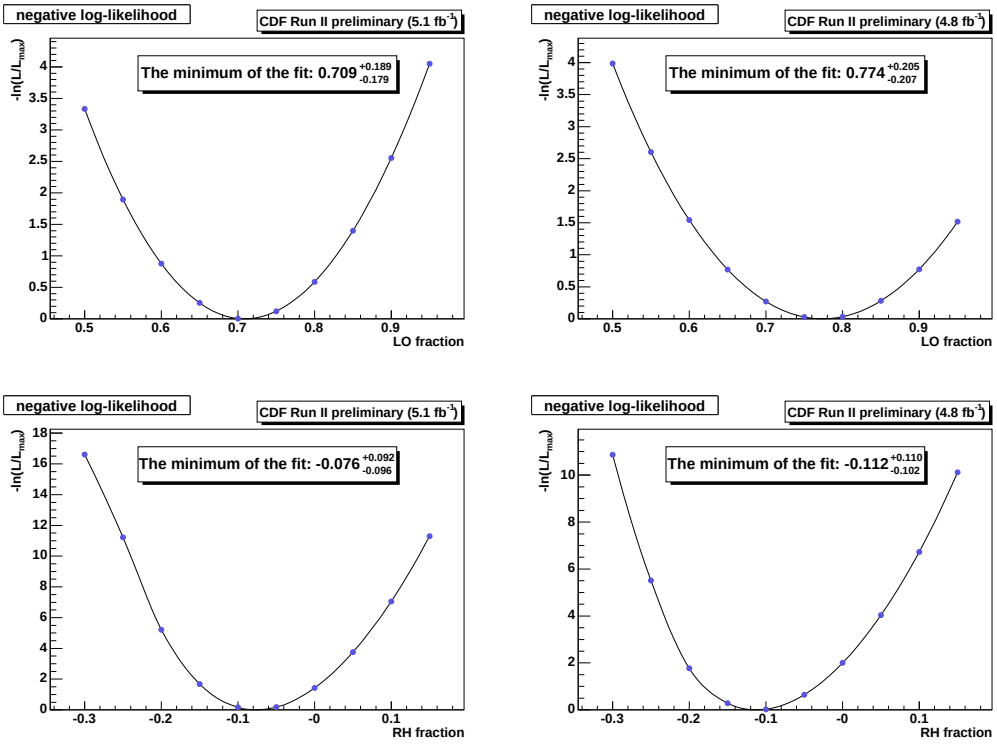

(a) (b)

Figure 7.44: The NLL 2D curve for simultaneous (f_0, f_+) fit for pre−tagged (a) and b−tagged events (b).

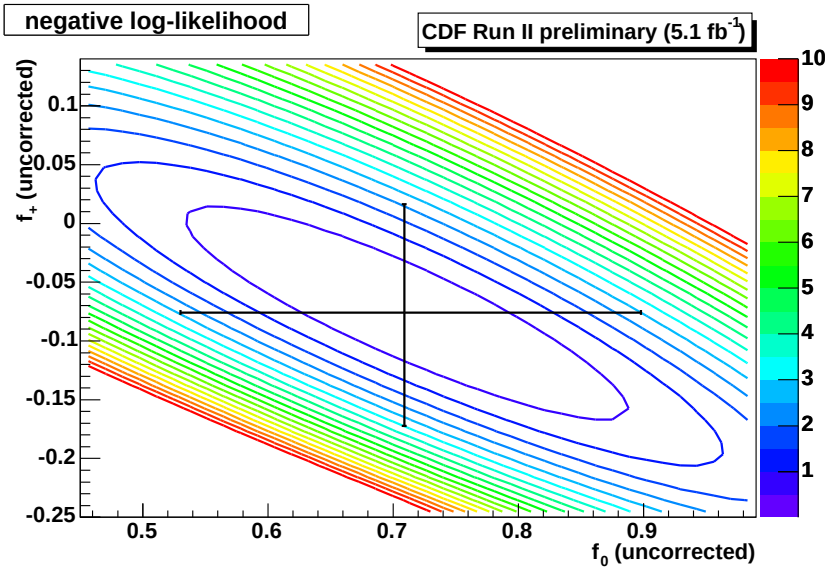

(a)

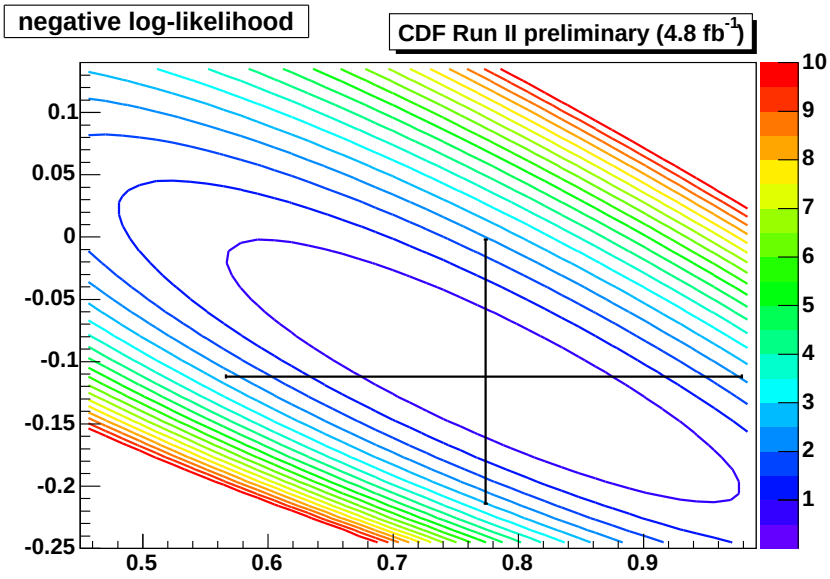

(b)

Figure 7.45: NLL 2D curve for simultaneous (f_0, f_+) fit for pre−tagged (a) and b−tagged events (b).

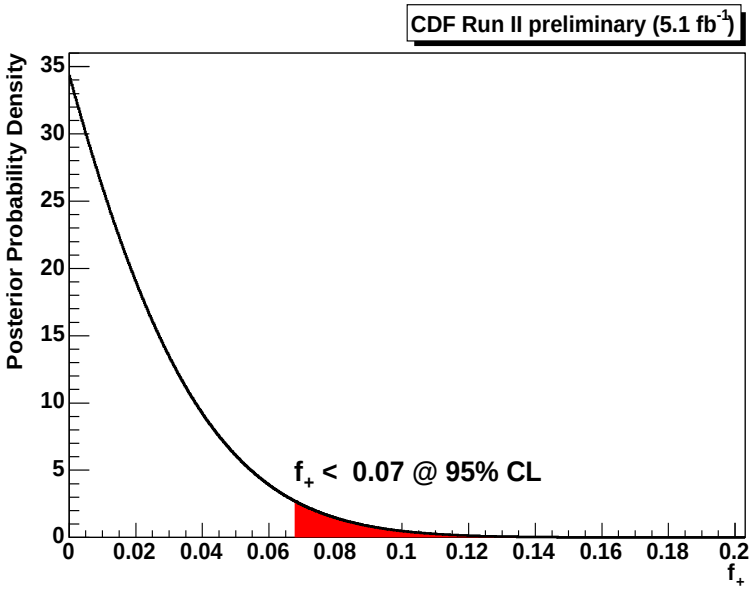

Figure 7.46: The posterior probability density determined for the both cases: without and with systematic uncertainty considered for pre−tag events.

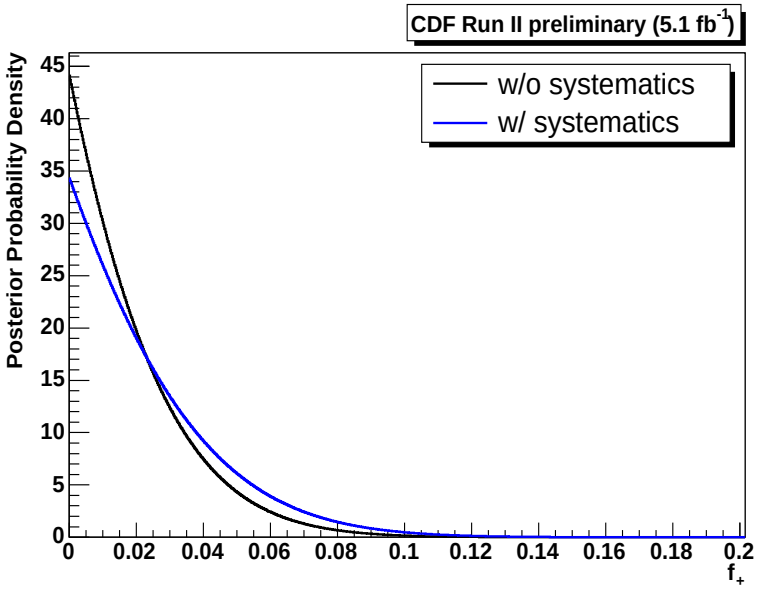

Figure 7.47: The posterior probability density with systematics included.

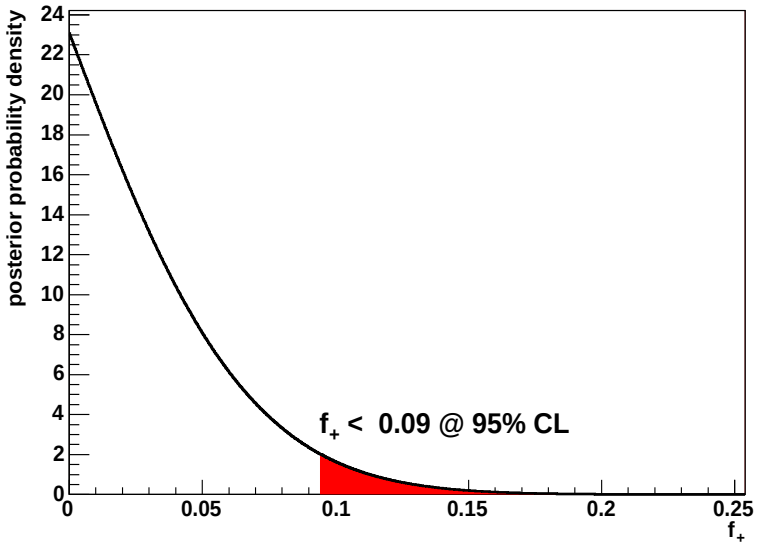

Figure 7.48: The posterior probability density determined for the both cases: without and with systematic uncertainty considered for $b-$tag events.

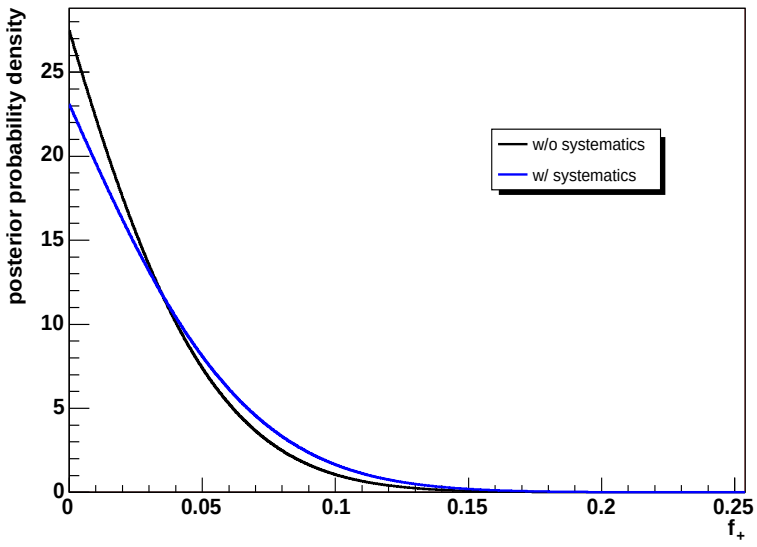

Figure 7.49: The posterior probability density with systematics included.

Chapter 8

Conclusion and Outlook

In this thesis, the measurement of the $t\bar{t}$ cross section using the top DIL selection in 5.1 fb^{-1} (4.8 fb^{-1} on $b-$tagging) of CDF data have been presented.

Assuming $m_t = 172.5$ GeV/c^2, the measured cross section for 343 signal candidate events before the secondary vertex $b-$tagging included with an estimated background of 105.80 ± 17.24 is:

$$\sigma_{t\bar{t}} = 7.40 \pm 0.58(\text{stat}) \pm 0.63(\text{syst}) \pm 0.45(\text{lumi}) \text{ pb}.$$

and the measured cross section for 137 signal candidate events after the secondary vertex $b-$tagging included with an estimated background of 9.75 ± 1.68 is found to be:

$$\sigma_{t\bar{t}} = 7.25 \pm 0.66(\text{stat}) \pm 0.47(\text{syst}) \pm 0.44(\text{lumi}) \text{ pb}.$$

which are consistent with a NNLO prediction of 7.4 ± 0.8 pb.

Figure 8.1 presents the measured $t\bar{t}$ production cross section on the theoretical expectation assuming the top quark mass is 172.5 GeV/c^2. It shows the

measurement agrees well with the Standard Model expectation within uncertainties. This measurement has an importance that the statical uncertainty becomes smaller than systematic uncertainty for the first time. The most recent the $t\bar{t}$ cross section measurements by CDF are shown in Figure 8.2.

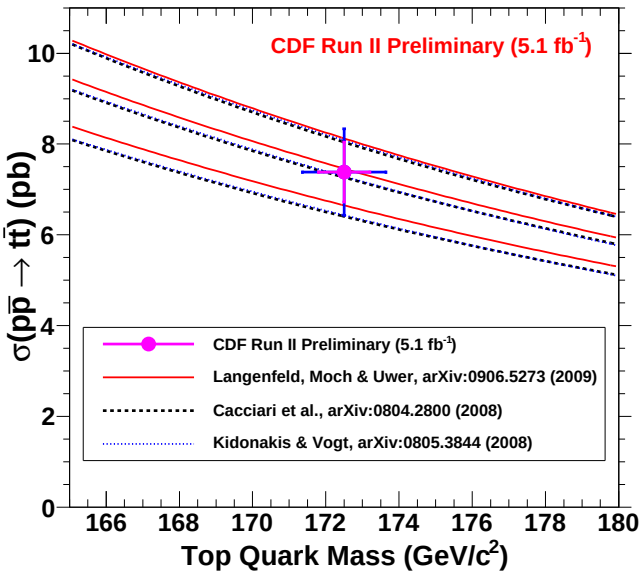

Figure 8.1: Measured $t\bar{t}$ production cross section on the theoretical curves as a function of the top mass

Meanwhile, the measurement of W boson polarization fractions in top decays from $t\bar{t}$ dilepton events using 5.1 fb^{-1} (with $b-$tagging : 4.8 fb^{-1}) of CDF data have been studied. The polarization fractions were determined by a comparison of angular distribution of leptons in W rest-frame ($cos\theta^*$) with templates corresponding to left-handed, right-handed an longitudinal fractions exclusively.

Two kinds of measurements have been performed. First, when one

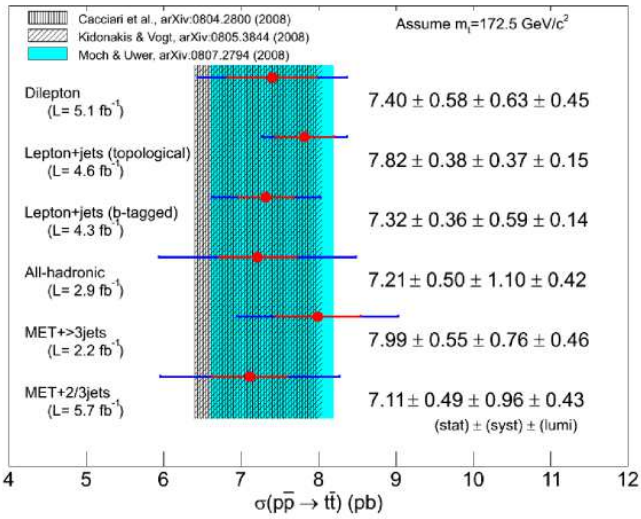

Figure 8.2: $t\bar{t}$ cross section measurements by CDF compared with theoretical predictions(shaded).

assumed one fraction (f_0, f_+ respectively) to have Standard Model expected value and determined the other fraction (f_+, f_0 respectively). We measure f_0 to be (assuming $f_+ = 0.0$):

$$\text{Before } b\text{−tagging} \quad : \quad f_0^{1D} = 0.60 \pm 0.09(\text{stat}) \pm 0.06(\text{syst})$$

$$\text{After } b\text{−tagging} \quad : \quad f_0^{1D} = 0.62 \pm 0.11(\text{stat}) \pm 0.06(\text{syst})$$

And f_+ (assuming $f_0 = 0.7$):

$$\text{Before } b\text{−tagging} \quad : \quad f_+^{1D} = -0.06 \pm 0.04(\text{stat}) \pm 0.03(\text{syst})$$

$$\text{After } b\text{−tagging} \quad : \quad f_+^{1D} = -0.07 \,^{+\,0.06}_{-\,0.05}(\text{stat}) \pm 0.03(\text{syst})$$

The 2D model independent simultaneous measurement of f_0 and f_+ gives

$$\text{Before } b\text{−tagging} : \quad \begin{aligned} f_0^{2D} &= 0.73 \,^{+\,0.18}_{-\,0.17}(\text{stat}) \pm 0.06(\text{syst}) \\ f_+^{2D} &= -0.08 \pm 0.09(\text{stat}) \pm 0.03(\text{syst}) \end{aligned}$$

$$\text{After } b\text{−tagging} \quad : \quad \begin{aligned} f_0^{2D} &= 0.78 \,^{+\,0.19}_{-\,0.20}(\text{stat}) \pm 0.06(\text{syst}) \\ f_+^{2D} &= -0.12 \,^{+\,0.11}_{-\,0.10}(\text{stat}) \pm 0.04(\text{syst}) \end{aligned}$$

All the result are consistent with Standard Model expectations. These results are first measurements of the W boson polarization using cos θ^* distribution in dilepton channel at CDF.

Table I shows recently published results of W boson polarization fractions at CDF and D0 experiment. And Table II presents Measurements of W boson polarization fractions using dilepton channel with 5.1 fb^{-1} of data (4.8 fb^{-1} on b−tagging). This results have competitive statistical and systematic uncertainties with previous results.

	CDF using L+jets channel (2.7 fb^{-1})	D0 using L+jets & DIL channel (5.4 fb^{-1})
f_0^{1D}	0.70 ± 0.07(stat) ± 0.04(syst)	0.71 ± 0.04(stat) ± 0.05(syst)
f_+^{1D}	−0.01 ± 0.02(stat) ± 0.05(syst)	0.01 ± 0.02(stat) ± 0.03(syst)
f_0^{2D}	0.88 ± 0.11(stat) ± 0.06(syst)	0.67 ± 0.08(stat) ± 0.07(syst)
f_+^{2D}	−0.15 ± 0.07(stat) ± 0.06(syst)	0.02 ± 0.04(stat) ± 0.03(syst)

Table I: Recently published results of W boson polarization fractions at CDF and D0

A precise measurement of W boson polarization is important because of the intimate relationship between the longitudinal W and the electroweak symmetry breaking mechanism in the standard model. It has been shown that one-loop supersymmetric QCD and electroweak corrections to the total width of $t \to Wb$ could increase the longitudinal fraction as predicted by the standard model by as much as a few percent [19]. Furthermore, a direct measurement

	Pre−tagged Results (5.1 fb^{-1})	b-tagged Results (4.8 fb^{-1})
f_0^{1D}	0.60 ± 0.09(stat)± 0.06(syst)	0.62 ± 0.11(stat) ± 0.06(syst)
f_+^{1D}	−0.06 ± 0.04(stat)± 0.03(syst)	$-0.07\ ^{+\ 0.06}_{-\ 0.05}$(stat) ± 0.03(syst)
f_0^{2D}	$0.73\ ^{+\ 0.18}_{-\ 0.17}$(stat) ± 0.06(syst)	$0.78\ ^{+\ 0.19}_{-\ 0.20}$(stat) ± 0.06(syst)
f_+^{2D}	−0.08 ± 0.09(stat)± 0.03(syst)	$-0.12\ ^{+\ 0.11}_{-\ 0.10}$(stat) ± 0.04(syst)

Table II: Measurements of W boson polarization fractions using dilepton channel with 5.1 fb^{-1} of data (4.8 fb^{-1} on $b-$tagging).

of the weak-current chirality from the tWb vertex is necessary to validate the $V-A$ form predicted by the standard model.

Until the end of 2011, CDF Run II of the Tevatron continues, CDF will obtain significantly larger amounts of luminosity. From greater statistics alone, the precision of this measurement will increase substantially over the value quoted here. So statistical uncertainty will be significantly reduced. And systematic uncertainties mainly attributed to the signal generator and jet energy scale. Therefore, improved Monte Carlo simulation study can lead to cut down the systematic uncertainty.

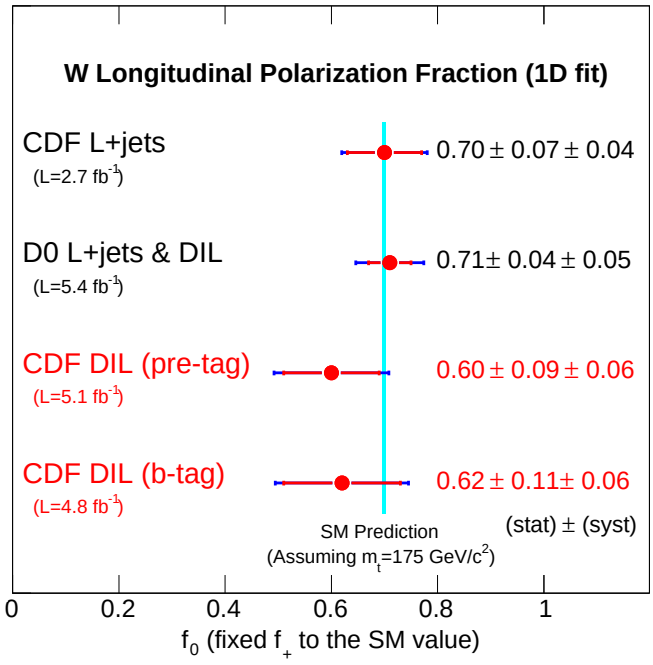

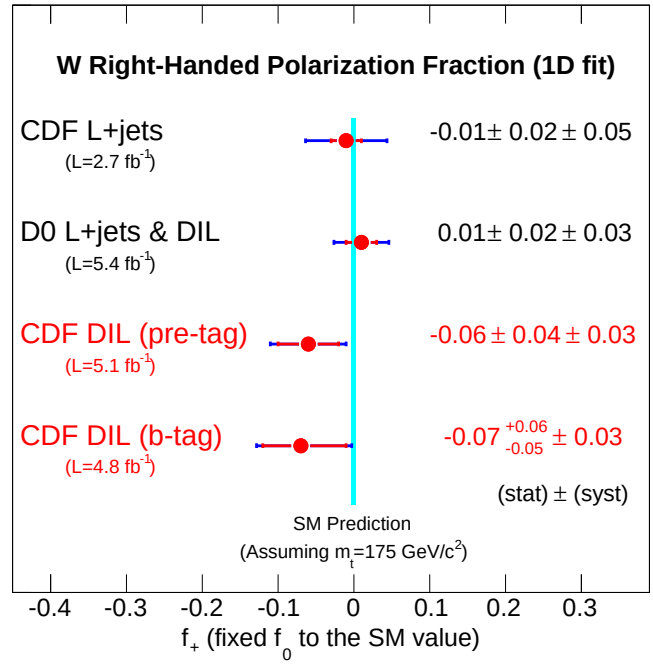

Figure 8.3: Comparison of measurements of W polarization fractions using 1D fit

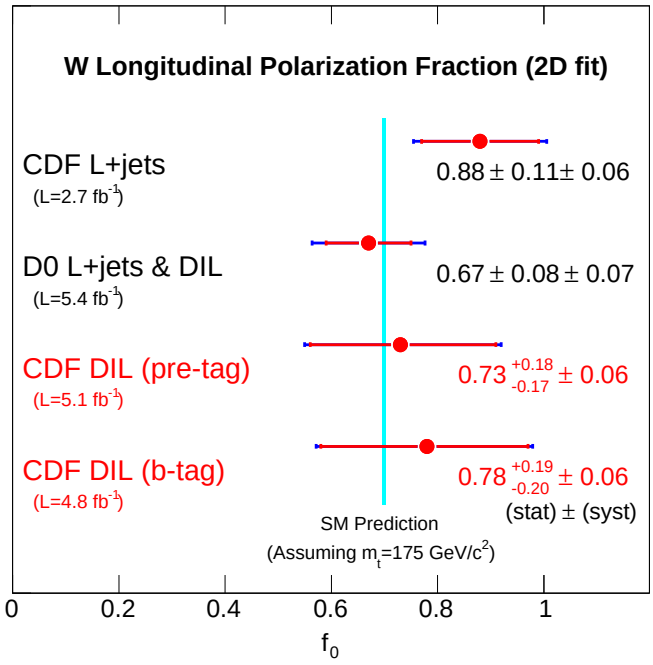

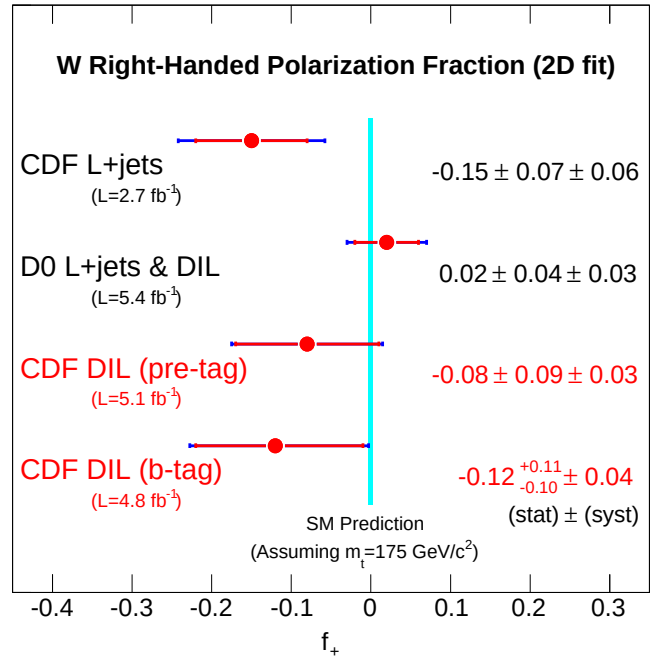

Figure 8.4: Comparison of measurements of W polarization fractions using 2D fit

Appendix A

Results of Monte Carlo Simulation

Tables of Monte Carlo events passing each step of the top DIL selection. These tables have been obtained by running the "topdil" selection macro in the topana_614_v12 package, which can be downloaded from `http://www-cdf.fnal.gov/~csmoon/internal/DIL/5.1fb/topcode`.

A.1 Pre−tagged Events

A.1.1 $t\bar{t}$ Signal Monte Carlo (ttop25)

Category	ALL	Zveto	Met	L-cut	0j	1j	≥2j	Ht	OS
DIL Category	ALL	ZVET	MET	dphi	0j	1j	¿=2j	Ht	OS
CEM-CEM	11576	8952	8018	7352	41	880	6431	6202	6195
CEM-NICEM	3666	1864	1705	1567	7	114	1446	1388	1305
PHX-CEM	5617	4411	3942	3613	19	447	3147	2996	2614
PHX-NICEM	836	384	347	318	1	26	291	276	234
ee inclusive	21695	15611	14012	12850	68	1467	11315	10862	10348
ee iso-iso	17193	13363	11960	10965	60	1327	9578	9198	8809
CMUP-CMUP	4044	3425	3052	2793	14	347	2432	2356	2356
CMUP-NICMUP	1309	792	733	690	0	34	656	639	605
CMUP-CMU	1742	1455	1284	1181	5	120	1056	1027	1027
CMUP-NICMU	287	173	161	149	1	7	141	137	129
CMUP-CMP	2450	2089	1861	1687	8	189	1490	1436	1436
CMUP-NICMP	460	248	234	215	0	12	203	198	179
CMUP-CMX	4169	3539	3211	2938	7	356	2575	2467	2467
CMUP-NICMX	693	369	339	315	0	15	300	283	257
CMX-NICMUP	624	370	340	314	0	18	296	289	271
CMUP-CMIO	1589	1322	1180	1083	6	138	939	908	907
CMX-CMX	1041	869	769	702	7	83	612	594	594
CMX-NICMX	303	152	142	130	0	13	117	108	98
CMX-CMU	750	637	569	528	3	69	456	431	431
CMX-NICMU	111	64	57	53	0	3	50	43	40
CMX-CMP	1105	931	851	782	3	88	691	664	664
CMX-NICMP	190	108	102	94	0	7	87	81	74
CMX-CMIO	698	598	526	474	1	55	418	403	403
mm inclusive	21565	17141	15411	14128	55	1554	12519	12064	11938
mm iso-iso	17588	14865	13303	12168	54	1445	10669	10286	10285
CEM-CMUP	13526	12802	11326	10228	50	1213	8965	8652	8640
CEM-NICMUP	2406	1645	1506	1389	0	82	1307	1260	1195
CMUP-NICEM	2151	1311	1191	1094	4	92	998	961	896
CEM-CMU	2952	2808	2486	2254	14	233	2007	1935	1930
CEM-NICMU	511	324	292	269	0	21	248	235	219
CEM-CMP	4142	3920	3453	3120	14	367	2739	2645	2644
CEM-NICMP	874	536	482	446	2	33	411	390	355
CEM-CMX	6864	6562	5769	5224	27	645	4552	4382	4375
CEM-NICMX	1178	762	670	610	1	35	574	543	514
CMX-NICEM	931	574	515	468	0	32	436	418	389
CEM-CMIO	2505	2312	2045	1869	6	242	1621	1559	1554
PHX-CMUP	3234	3155	2749	2487	6	308	2173	2072	1821
PHX-NICMUP	533	353	321	289	1	25	263	243	195
PHX-CMX	1510	1491	1271	1140	2	138	1000	938	827
PHX-NICMX	243	160	142	134	0	12	122	116	91
em inclusive	46195	38715	34218	31021	127	3478	27416	26349	25645
em iso-iso	37071	33050	29099	26322	119	3146	23057	22183	21791
total inclusive	71852	61278	54362	49455	233	5918	43304	41667	40885
total iso-iso	89455	71467	63641	57999	250	6499	51250	49275	47931

Table I: Pythia `ttop25` MC events, after each dilepton cut. The first column represents events with a good dilepton after conversion removal. The last columns gives the final number after all selection cuts.

A.1.2 WW Background Monte Carlo (ihht1a)

Category	ALL	Zveto	Met	L-cut	0j	1j	≥2j	Ht	OS
CEM-CEM	6501	4880	3750	3641	2787	666	188	125	125
CEM-NICEM	715	460	373	355	201	101	53	35	35
PHX-CEM	5296	4110	3157	3040	2359	520	161	109	95
PHX-NICEM	247	138	109	104	61	34	9	7	6
ee inclusive	12759	9588	7389	7140	5408	1321	411	276	261
ee iso-iso	11797	8990	6907	6681	5146	1186	349	234	220
CMUP-CMUP	2142	1712	1304	1257	970	221	66	48	48
CMUP-NICMUP	174	147	109	101	51	35	15	7	7
CMUP-CMU	862	699	511	495	381	90	24	20	20
CMUP-NICMU	57	50	38	36	18	16	2	1	1
CMUP-CMP	1235	1015	765	737	560	133	44	28	28
CMUP-NICMP	74	64	53	52	26	18	8	3	3
CMUP-CMX	2553	2049	1580	1528	1162	297	69	52	52
CMUP-NICMX	97	79	63	60	29	24	7	4	4
CMX-NICMUP	99	81	60	59	26	22	11	5	5
CMUP-CMIO	943	759	571	542	414	98	30	24	24
CMX-CMX	770	598	449	441	346	82	13	7	7
CMX-NICMX	57	38	32	31	12	15	4	2	2
CMX-CMU	458	376	284	276	222	41	13	9	9
CMX-NICMU	23	20	17	17	4	5	8	5	5
CMX-CMP	646	530	394	375	289	68	18	10	10
CMX-NICMP	26	19	13	12	3	6	3	1	1
CMX-CMIO	468	365	282	268	197	56	15	10	10
mm inclusive	10684	8601	6525	6287	4710	1227	350	236	236
mm iso-iso	10077	8103	6140	5919	4541	1086	292	208	208
CEM-CMUP	7374	7034	5085	4876	3705	916	255	169	168
CEM-NICMUP	371	321	251	248	129	80	39	19	19
CMUP-NICEM	379	300	228	219	109	73	37	24	24
CEM-CMU	1728	1659	1195	1142	892	190	60	35	35
CEM-NICMU	97	82	60	58	30	23	5	2	2
CEM-CMP	2153	2043	1478	1408	1068	267	73	43	42
CEM-NICMP	104	90	78	72	32	28	12	5	5
CEM-CMX	4486	4346	3196	3057	2369	533	155	102	102
CEM-NICMX	228	192	143	133	65	52	16	6	6
CMX-NICEM	197	162	119	114	62	35	17	9	9
CEM-CMIO	1648	1540	1136	1086	851	184	51	25	25
PHX-CMUP	2942	2888	2070	1981	1522	365	94	49	42
PHX-NICMUP	98	93	71	68	30	27	11	6	4
PHX-CMX	1581	1561	1130	1087	854	182	51	31	25
PHX-NICMX	83	77	58	56	20	26	10	3	3
em inclusive	25754	22388	16298	15605	11738	2981	886	528	511
em iso-iso	24113	21071	15290	14637	11261	2637	739	454	439
total inclusive	49197	40577	30212	29032	21856	5529	1647	1040	1008
total iso-iso	45987	38164	28337	27237	20948	4909	1380	896	867

Table II: Pythia `ihht1a` MC events, after each dilepton cut. The first column represents events with a good dilepton after conversion removal. The last columns gives the final number after all selection cuts.

A.1.3 WZ Background Monte Carlo (jhht1a)

Category	ALL	Zveto	Met	L-cut	0j	1j	≥2j	Ht	OS
CEM-CEM	15393	3067	2277	2128	687	1101	340	282	230
CEM-NICEM	1929	376	236	198	33	94	71	55	40
PHX-CEM	14098	3097	2388	2217	726	1144	347	271	169
PHX-NICEM	1109	193	112	100	30	32	38	33	23
eee inclusive	32529	6733	5013	4643	1476	2371	796	641	462
eee iso-iso	29491	6164	4665	4345	1413	2245	687	553	399
CMUP-CMUP	4785	1042	760	738	398	254	86	77	70
CMUP-NICMUP	584	126	75	69	13	32	24	15	12
CMUP-CMU	2280	491	375	360	207	127	26	21	20
CMUP-NICMU	121	34	17	16	4	4	8	7	5
CMUP-CMP	2825	603	443	426	256	130	40	37	30
CMUP-NICMP	163	43	27	22	11	7	4	4	4
CMUP-CMX	6259	1335	1017	979	547	336	96	84	66
CMUP-NICMX	360	71	32	29	8	10	11	8	7
CMX-NICMUP	371	64	38	37	15	15	7	6	5
CMUP-CMIO	2150	428	339	328	195	101	32	25	23
CMX-CMX	1878	408	307	299	170	96	33	28	23
CMX-NICMX	194	35	24	22	5	5	12	8	8
CMX-CMU	1219	266	205	200	111	67	22	16	11
CMX-NICMU	73	13	5	4	2	2	0	0	0
CMX-CMP	1478	332	256	241	142	67	32	30	26
CMX-NICMP	104	20	12	12	4	5	3	3	3
CMX-CMIO	1031	192	150	145	74	57	14	12	11
mm inclusive	25875	5503	4082	3927	2162	1315	450	381	324
mm iso-iso	23905	5097	3852	3716	2100	1235	381	330	280
CEM-CMUP	2073	1942	1501	1368	589	589	190	133	65
CEM-NICMUP	166	127	96	84	27	39	18	14	10
CMUP-NICEM	162	106	80	73	19	32	22	15	9
CEM-CMU	468	435	341	311	145	125	41	29	17
CEM-NICMU	38	30	26	23	6	10	7	6	3
CEM-CMP	556	531	427	394	178	157	59	40	24
CEM-NICMP	50	40	31	30	9	12	9	7	5
CEM-CMX	1326	1255	995	912	409	386	117	98	59
CEM-NICMX	84	51	47	40	8	23	9	6	3
CMX-NICEM	102	62	48	44	18	14	12	7	5
CEM-CMIO	489	446	349	313	126	131	56	45	19
PHX-CMUP	1144	1128	884	811	372	322	117	85	44
PHX-NICMUP	70	56	50	42	9	14	19	12	7
PHX-CMX	599	592	446	411	184	173	54	40	21
PHX-NICMX	48	36	28	25	8	11	6	3	1
em inclusive	8256	6837	5349	4881	2107	2038	736	540	292
em iso-iso	7499	6329	4943	4520	2003	1883	634	470	249
total inclusive	66660	19073	14444	13451	5745	5724	1982	1562	1078
total iso-iso	60895	17590	13460	12581	5516	5363	1702	1353	928

Table III: Pythia `jhht1a` MC events, after each dilepton cut. The first column represents events with a good dilepton after conversion removal. The last columns gives the final number after all selection cuts.

A.1.4 ZZ Background Monte Carlo (khht1a)

Category	ALL	Zveto	Met	L-cut	0j	1j	≥2j	Ht	OS
CEM-CEM	18052	3353	1851	1712	1154	369	189	174	153
CEM-NICEM	2628	473	181	150	42	58	50	45	42
PHX-CEM	15194	2412	1281	1193	831	244	118	102	82
PHX-NICEM	1191	196	75	65	22	20	23	14	10
ee inclusive	37065	6434	3388	3120	2049	691	380	335	287
ee iso-iso	33246	5765	3132	2905	1985	613	307	276	235
CMUP-CMUP	6030	1242	689	652	441	139	72	64	61
CMUP-NICMUP	959	217	78	69	18	29	22	18	17
CMUP-CMU	2671	508	293	274	182	67	25	22	21
CMUP-NICMU	200	47	24	23	4	8	11	7	7
CMUP-CMP	3567	708	380	353	241	86	26	24	22
CMUP-NICMP	273	74	22	18	7	8	3	3	3
CMUP-CMX	7021	1321	756	729	491	180	58	51	48
CMUP-NICMX	434	93	29	25	8	8	9	8	8
CMX-NICMUP	412	83	31	29	7	13	9	9	8
CMUP-CMIO	2393	468	270	259	179	56	24	20	19
CMX-CMX	2232	425	216	206	150	38	18	16	14
CMX-NICMX	307	74	23	19	6	12	1	1	1
CMX-CMU	1427	266	151	144	100	26	18	13	12
CMX-NICMU	111	25	8	8	4	4	0	0	0
CMX-CMP	1813	328	192	185	108	58	19	14	14
CMX-NICMP	131	21	10	7	4	2	1	1	1
CMX-CMIO	1229	256	135	127	93	27	7	6	6
mm inclusive	31210	6156	3307	3127	2043	761	323	277	262
mm iso-iso	28383	5522	3082	2929	1985	677	267	230	217
CEM-CMUP	601	555	341	271	50	145	76	67	41
CEM-NICMUP	83	71	36	27	6	9	12	9	7
CMUP-NICEM	74	60	33	29	3	14	12	9	7
CEM-CMU	141	137	73	56	7	34	15	13	11
CEM-NICMU	15	15	6	4	1	2	1	0	0
CEM-CMP	197	180	99	75	14	40	21	16	12
CEM-NICMP	22	17	9	6	1	1	4	3	1
CEM-CMX	342	318	180	150	52	65	33	26	13
CEM-NICMX	36	31	20	14	2	6	6	3	2
CMX-NICEM	29	25	16	11	2	6	3	1	1
CEM-CMIO	146	135	83	67	14	32	21	17	11
PHX-CMUP	264	260	128	100	31	47	22	16	10
PHX-NICMUP	35	35	18	11	1	3	7	4	3
PHX-CMX	156	156	83	67	17	34	16	11	6
PHX-NICMX	14	14	6	3	0	2	1	1	0
em inclusive	2401	2009	1131	891	201	440	250	196	125
em iso-iso	2076	1741	987	786	185	397	204	166	104
total inclusive	70676	14599	7826	7138	4293	1892	953	808	674
total iso-iso	63705	13028	7201	6620	4155	1687	778	672	556

Table IV: Pythia `khht1a` MC events, after each dilepton cut. The first column represents events with a good dilepton after conversion removal. The last columns gives the final number after all selection cuts.

A.1.5 $W\gamma$ Background Monte Carlo (Wgamma)

Category	ALL	Zveto	Met	L-cut	0j	1j	≥2j	Ht	OS
CEM-CEM	245	24	18	18	15	2	1	1	1
CEM-NICEM	48	6	3	3	2	1	0	0	0
PHX-CEM	269	109	78	68	51	15	2	0	0
PHX-NICEM	22	6	4	4	3	1	0	0	0
ee inclusive	584	145	103	93	71	19	3	1	1
ee iso-iso	514	133	96	86	66	17	3	1	1
CMUP-CMUP	0	0	0	0	0	0	0	0	0
CMUP-NICMUP	0	0	0	0	0	0	0	0	0
CMUP-CMU	0	0	0	0	0	0	0	0	0
CMUP-NICMU	0	0	0	0	0	0	0	0	0
CMUP-CMP	0	0	0	0	0	0	0	0	0
CMUP-NICMP	0	0	0	0	0	0	0	0	0
CMUP-CMX	0	0	0	0	0	0	0	0	0
CMUP-NICMX	0	0	0	0	0	0	0	0	0
CMX-NICMUP	0	0	0	0	0	0	0	0	0
CMUP-CMIO	0	0	0	0	0	0	0	0	0
CMX-CMX	0	0	0	0	0	0	0	0	0
CMX-NICMX	0	0	0	0	0	0	0	0	0
CMX-CMU	0	0	0	0	0	0	0	0	0
CMX-NICMU	0	0	0	0	0	0	0	0	0
CMX-CMP	0	0	0	0	0	0	0	0	0
CMX-NICMP	0	0	0	0	0	0	0	0	0
CMX-CMIO	0	0	0	0	0	0	0	0	0
mm inclusive	0	0	0	0	0	0	0	0	0
mm iso-iso	0	0	0	0	0	0	0	0	0
CEM-CMUP	124	17	13	12	6	4	2	0	0
CEM-NICMUP	24	5	3	3	3	0	0	0	0
CMUP-NICEM	14	2	1	1	1	0	0	0	0
CEM-CMU	42	3	1	1	0	1	0	0	0
CEM-NICMU	1	0	0	0	0	0	0	0	0
CEM-CMP	35	5	4	4	2	1	1	0	0
CEM-NICMP	7	2	2	1	1	0	0	0	0
CEM-CMX	104	19	16	16	10	6	0	0	0
CEM-NICMX	15	0	0	0	0	0	0	0	0
CMX-NICEM	10	0	0	0	0	0	0	0	0
CEM-CMIO	33	2	2	2	1	1	0	0	0
PHX-CMUP	59	59	41	38	31	5	2	0	0
PHX-NICMUP	4	4	3	2	0	2	0	0	0
PHX-CMX	44	44	29	29	23	5	1	0	0
PHX-NICMX	5	5	4	3	1	1	1	0	0
em inclusive	489	149	106	102	73	23	6	0	0
mu iso-iso	569	167	119	112	79	26	7	0	0
total inclusive	1153	312	222	205	150	45	10	1	1
total iso-iso	1003	282	202	188	139	40	9	1	1

Table V: Pythia `Wgamma` MC events, after each dilepton cut. The first column represents events with a good dilepton after conversion removal. The last columns gives the final number after all selection cuts.

A.2 $b-$tagged Events

A.2.1 $t\bar{t}$ Signal Monte Carlo (ttop25)

Category	ALL	Zveto	Met	L-cut	0j	1j	≥2j	Ht	OS
DIL Category	ALL	ZVET	MET	dphi	0j	1j	¿=2j	Ht	OS
CEM-CEM	11576	5128	4576	4173	0	364	3809	3718	3713
CEM-NICEM	3666	1095	1009	926	0	45	881	857	816
PHX-CEM	5617	2619	2333	2118	0	170	1948	1882	1646
PHX-NICEM	836	227	206	187	0	11	176	169	143
e - e	21695	9069	8124	7404	0	590	6814	6626	6318
iso-iso ee	17193	7747	6909	6291	0	534	5757	5600	5359
CMUP-CMUP	4044	1918	1721	1572	0	133	1439	1407	1407
CMUP-NICMUP	1309	486	444	419	0	18	401	395	374
CMUP-CMU	1742	845	744	679	0	57	622	611	611
CMUP-NICMU	287	98	92	86	0	2	84	82	75
CMUP-CMP	2450	1205	1074	978	0	76	902	877	877
CMUP-NICMP	460	158	150	141	0	8	133	133	117
CMUP-CMX	4169	2027	1839	1684	0	164	1520	1469	1469
CMUP-NICMX	693	215	199	187	0	4	183	175	158
CMX-NICMUP	624	221	199	185	0	6	179	177	166
CMUP-CMIO	1589	772	683	624	0	61	563	550	549
CMX-CMX	1041	503	446	415	0	33	382	372	372
CMX-NICMX	303	84	78	71	0	4	67	62	55
CMX-CMU	750	372	332	308	0	30	278	266	266
CMX-NICMU	111	39	35	31	0	0	31	28	27
CMX-CMP	1105	538	491	450	0	37	413	402	402
CMX-NICMP	190	64	58	53	0	1	52	51	46
CMX-CMIO	698	354	307	276	0	25	251	246	246
mu-mu	21565	9899	8892	8159	0	659	7500	7303	7217
iso-iso mm	17588	8534	7637	6986	0	616	6370	6200	6199
CEM-CMUP	13526	7356	6497	5870	0	470	5400	5262	5256
CEM-NICMUP	2406	957	870	798	0	35	763	740	700
CMUP-NICEM	2151	747	679	621	0	34	587	567	536
CEM-CMU	2952	1619	1432	1303	0	94	1209	1174	1172
CEM-NICMU	511	192	173	157	0	9	148	146	133
CEM-CMP	4142	2293	2029	1823	0	143	1680	1636	1635
CEM-NICMP	874	331	297	273	0	15	258	248	223
CEM-CMX	6864	3841	3374	3058	0	258	2800	2727	2723
CEM-NICMX	1178	465	410	378	0	12	366	352	333
CMX-NICEM	931	342	308	280	0	12	268	259	242
CEM-CMIO	2505	1310	1155	1041	0	93	948	926	922
PHX-CMUP	3234	1876	1630	1467	0	136	1331	1283	1125
PHX-NICMUP	533	205	186	170	0	10	160	150	121
PHX-CMX	1510	903	773	693	0	70	623	595	521
PHX-NICMX	243	96	85	82	0	1	81	78	60
e - mu	46195	22533	19898	18014	0	1392	16622	16143	15702
iso-iso em	37071	19198	16890	15255	0	1264	13991	13603	13354
total inclusive	89455	41501	36914	33577	0	2641	30936	30072	29237
total iso-iso	71852	35479	31436	28532	0	2414	26118	25403	24912

Table VI: Pythia `ttop25` MC events, after each dilepton cut. The first column represents events with a good dilepton after conversion removal. The last columns gives the final number after all selection cuts.

A.2.2 WW Background Monte Carlo (ihht1a)

Category	ALL	Zveto	Met	L-cut	0j	1j	≥2j	Ht	OS
CEM-CEM	6501	14	10	7	0	5	2	2	2
CEM-NICEM	715	8	6	6	0	2	4	3	3
PHX-CEM	5296	13	11	9	0	6	3	3	2
PHX-NICEM	247	0	0	0	0	0	0	0	0
ee inclusive	12759	35	27	22	0	13	9	8	7
ee iso-iso	11797	27	21	16	0	11	5	5	4
CMUP-CMUP	2142	8	6	6	0	2	4	2	2
CMUP-NICMUP	174	3	2	2	0	0	2	2	2
CMUP-CMU	862	0	0	0	0	0	0	0	0
CMUP-NICMU	57	1	1	1	0	1	0	0	0
CMUP-CMP	1235	3	3	3	0	2	1	1	1
CMUP-NICMP	74	0	0	0	0	0	0	0	0
CMUP-CMX	2553	9	9	8	0	5	3	2	2
CMUP-NICMX	97	0	0	0	0	0	0	0	0
CMX-NICMUP	99	1	1	1	0	1	0	0	0
CMUP-CMIO	943	2	2	2	0	2	0	0	0
CMX-CMX	770	1	1	1	0	1	0	0	0
CMX-NICMX	57	0	0	0	0	0	0	0	0
CMX-CMU	458	2	2	2	0	1	1	1	1
CMX-NICMU	23	1	1	1	0	0	1	1	1
CMX-CMP	646	2	1	1	0	1	0	0	0
CMX-NICMP	26	0	0	0	0	0	0	0	0
CMX-CMIO	468	1	1	1	0	0	1	0	0
mm inclusive	10684	34	30	29	0	16	13	9	9
mm iso-iso	10077	28	25	24	0	14	10	6	6
CEM-CMUP	7374	31	22	19	0	11	8	6	6
CEM-NICMUP	371	2	2	1	0	0	1	1	1
CMUP-NICEM	379	1	1	1	0	0	1	1	1
CEM-CMU	1728	2	1	1	0	0	1	1	1
CEM-NICMU	97	2	0	0	0	0	0	0	0
CEM-CMP	2153	4	1	1	0	0	1	1	1
CEM-NICMP	104	1	1	1	0	1	0	0	0
CEM-CMX	4486	13	9	9	0	6	3	3	3
CEM-NICMX	228	1	1	1	0	1	0	0	0
CMX-NICEM	197	2	2	2	0	1	1	1	1
CEM-CMIO	1648	2	1	1	0	0	1	1	1
PHX-CMUP	2942	11	9	7	0	2	5	4	4
PHX-NICMUP	98	1	1	1	0	1	0	0	0
PHX-CMX	1581	6	6	6	0	3	3	2	1
PHX-NICMX	83	1	0	0	0	0	0	0	0
em inclusive	25754	80	57	51	0	26	25	21	20
em iso-iso	24113	69	49	44	0	22	22	18	17
total inclusive	49197	149	114	102	0	55	47	38	36
total iso-iso	45987	124	95	84	0	47	37	29	27

Table VII: Pythia `ihht1a` MC events, after each dilepton cut. The first column represents events with a good dilepton after conversion removal. The last columns gives the final number after all selection cuts.

A.2.3 WZ Background Monte Carlo (jhht1a)

Category	ALL	Zveto	Met	L-cut	0j	1j	≥2j	Ht	OS
CEM-CEM	15393	33	15	11	0	7	4	3	3
CEM-NICEM	1929	7	2	0	0	0	0	0	0
PHX-CEM	14098	26	9	8	0	2	6	6	3
PHX-NICEM	1109	4	2	2	0	1	1	1	1
e - e	32529	70	28	21	0	10	11	10	7
iso-iso ee	29491	59	24	19	0	9	10	9	6
CMUP-CMUP	4785	14	6	6	0	2	4	4	4
CMUP-NICMUP	584	5	1	0	0	0	0	0	0
CMUP-CMU	2280	5	3	2	0	2	0	0	0
CMUP-NICMU	121	0	0	0	0	0	0	0	0
CMUP-CMP	2825	5	3	2	0	0	2	2	1
CMUP-NICMP	163	0	0	0	0	0	0	0	0
CMUP-CMX	6259	20	9	9	0	4	5	5	4
CMUP-NICMX	360	4	2	2	0	0	2	1	1
CMX-NICMUP	371	2	1	1	0	1	0	0	0
CMUP-CMIO	2150	3	1	1	0	1	0	0	0
CMX-CMX	1878	4	2	2	0	1	1	1	0
CMX-NICMX	194	1	0	0	0	0	0	0	0
CMX-CMU	1219	3	3	3	0	2	1	1	1
CMX-NICMU	73	0	0	0	0	0	0	0	0
CMX-CMP	1478	5	3	2	0	2	0	0	0
CMX-NICMP	104	1	1	1	0	1	0	0	0
CMX-CMIO	1031	2	0	0	0	0	0	0	0
mu-mu	25875	74	35	31	0	16	15	14	11
iso-iso mm	23905	61	30	27	0	14	13	13	10
CEM-CMUP	2073	9	8	7	0	2	5	5	3
CEM-NICMUP	166	3	2	2	0	0	2	2	1
CMUP-NICEM	162	0	0	0	0	0	0	0	0
CEM-CMU	468	1	0	0	0	0	0	0	0
CEM-NICMU	38	1	1	1	0	0	1	1	1
CEM-CMP	556	4	4	3	0	1	2	1	1
CEM-NICMP	50	0	0	0	0	0	0	0	0
CEM-CMX	1326	4	3	3	0	3	0	0	0
CEM-NICMX	84	1	1	1	0	0	1	1	0
CMX-NICEM	102	1	1	1	0	0	1	0	0
CEM-CMIO	489	2	2	2	0	0	2	2	1
PHX-CMUP	1144	8	6	5	0	2	3	3	2
PHX-NICMUP	70	0	0	0	0	0	0	0	0
PHX-CMX	599	2	2	2	0	1	1	1	1
PHX-NICMX	48	0	0	0	0	0	0	0	0
e - mu	8256	36	30	27	0	9	18	16	10
iso-iso em	7499	30	25	22	0	9	13	12	8
total inclusive	66660	180	93	79	0	35	44	40	28
total iso-iso	60895	150	79	68	0	32	36	34	24

Table VIII: Pythia `jhht1a` MC events, after each dilepton cut. The first column represents events with a good dilepton after conversion removal. The last columns gives the final number after all selection cuts.

A.2.4 ZZ Background Monte Carlo (khht1a)

Category	ALL	Zveto	Met	L-cut	0j	1j	≥2j	Ht	OS
DIL Category	ALL	ZVET	MET	dphi	0j	1j	¿=2j	Ht	OS
CEM-CEM	18052	135	29	18	0	3	15	11	11
CEM-NICEM	2628	31	5	3	0	1	2	2	2
PHX-CEM	15194	94	23	15	0	4	11	11	10
PHX-NICEM	1191	18	3	3	0	0	3	2	2
ee inclusive	37065	278	60	39	0	8	31	26	25
ee iso-iso	33246	229	52	33	0	7	26	22	21
CMUP-CMUP	6030	67	9	8	0	3	5	5	5
CMUP-NICMUP	959	22	6	3	0	0	3	2	1
CMUP-CMU	2671	22	5	5	0	1	4	4	4
CMUP-NICMU	200	5	1	1	0	0	1	0	0
CMUP-CMP	3567	35	6	4	0	3	1	1	1
CMUP-NICMP	273	10	0	0	0	0	0	0	0
CMUP-CMX	7021	47	7	5	0	1	4	3	3
CMUP-NICMX	434	14	3	2	0	0	2	2	2
CMX-NICMUP	412	7	2	2	0	0	2	2	1
CMUP-CMIO	2393	23	4	2	0	0	2	1	1
CMX-CMX	2232	22	5	3	0	0	3	3	3
CMX-NICMX	307	6	1	1	0	1	0	0	0
CMX-CMU	1427	11	2	2	0	0	2	1	1
CMX-NICMU	111	1	0	0	0	0	0	0	0
CMX-CMP	1813	12	3	3	0	1	2	2	2
CMX-NICMP	131	1	1	1	0	0	1	1	1
CMX-CMIO	1229	12	2	1	0	0	1	1	1
mm inclusive	31210	317	57	43	0	10	33	28	26
mm iso-iso	28383	251	43	33	0	9	24	21	21
CEM-CMUP	601	10	5	3	0	1	2	2	2
CEM-NICMUP	83	2	0	0	0	0	0	0	0
CMUP-NICEM	74	2	0	0	0	0	0	0	0
CEM-CMU	141	3	1	1	0	0	1	1	1
CEM-NICMU	15	2	1	0	0	0	0	0	0
CEM-CMP	197	5	3	2	0	0	2	1	1
CEM-NICMP	22	1	1	1	0	0	1	0	0
CEM-CMX	342	3	1	0	0	0	0	0	0
CEM-NICMX	36	6	4	1	0	0	1	1	1
CMX-NICEM	29	2	1	1	0	1	0	0	0
CEM-CMIO	146	1	0	0	0	0	0	0	0
PHX-CMUP	264	9	4	2	0	1	1	1	1
PHX-NICMUP	35	6	3	2	0	0	2	2	1
PHX-CMX	156	4	1	1	0	0	1	0	0
PHX-NICMX	14	1	0	0	0	0	0	0	0
em inclusive	2401	57	25	14	0	3	11	8	7
em iso-iso	2076	35	15	9	0	2	7	5	5
total inclusive	63705	515	110	75	0	18	57	48	47
total iso-iso	70676	652	142	96	0	21	75	62	58

Table IX: Pythia `khht1a` MC events, after each dilepton cut. The first column represents events with a good dilepton after conversion removal. The last columns gives the final number after all selection cuts.

Appendix B

CMX muon chamber drift velocity calibration

This chapter presents studies of the improvement of CMX muon chamber drift velocity calibration. Previous CMX drift velocity calibration based on 2002 measurement. And time dependent calibration was never implemented by anyone before. This could affect stub Z and Dz(track Z - stub Z) furthermore cause stubs to fail |R/Z| cut in stub reconstruction. I built up the calibration software that calculates time dependent CMX drift velocity by Gaussian fitting. These calibration set will be applied to the next version of analysis framework Gen-7 production and simulation data.

B.1 Data Period 0d

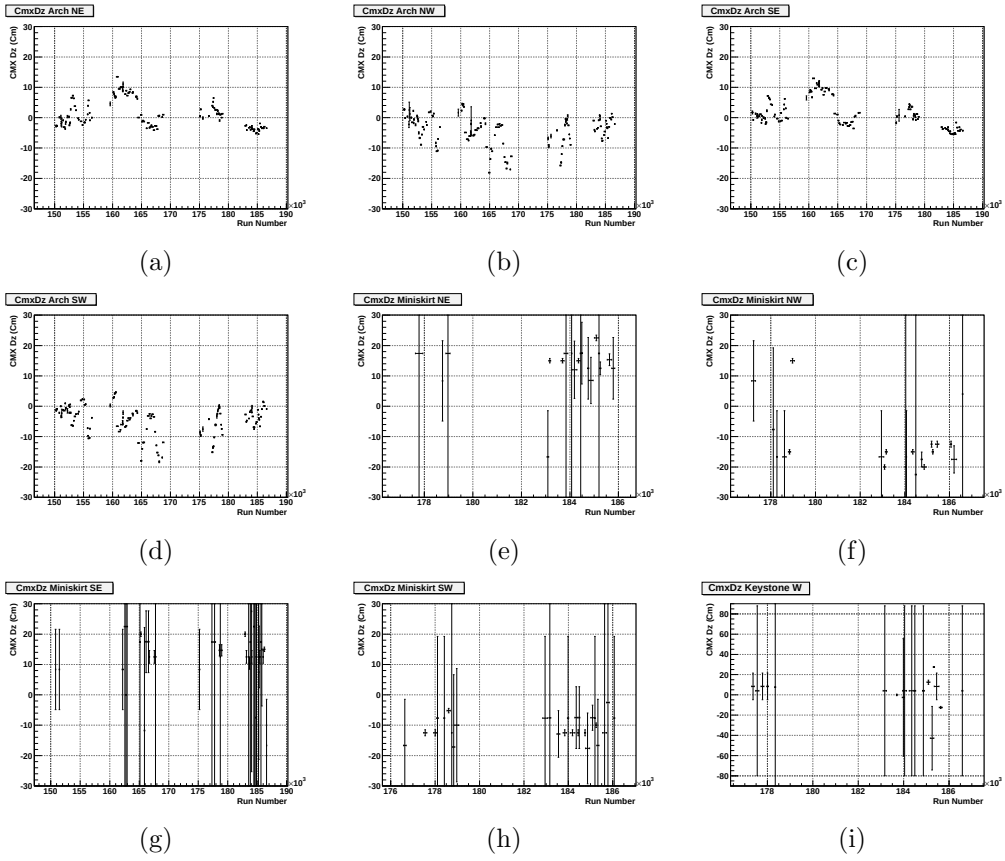

(a) (b) (c)

(d) (e) (f)

(g) (h) (i)

Figure B.1: The Dz (track Z - sub Z) distributions of CMX muon chamber as function of run number in data period 0d for the Arch north-east (a), the Arch north-west (b), the Arch south-east (c), the Arch south-west (d), the Miniskirt north-east (e), the Miniskirt north-west (f), the Miniskirt south-east (g), the Miniskirt south-west (h) and the Keystone west (i) part of the detector.

B.2 Data Period 0h

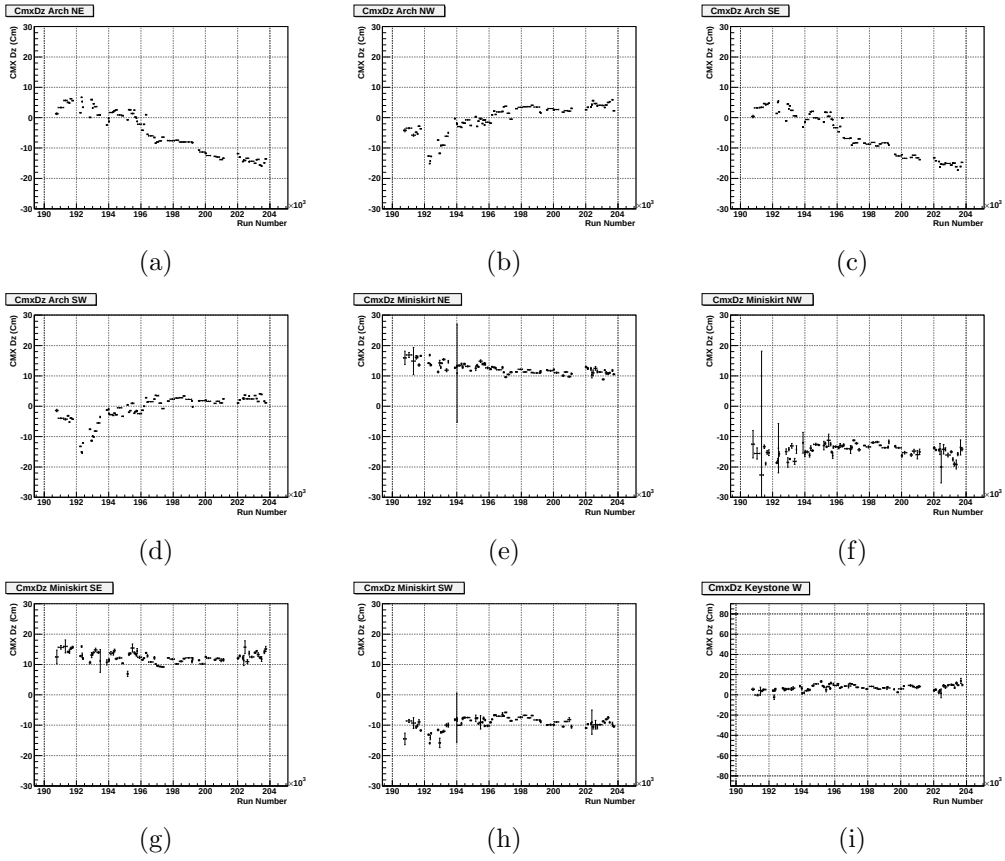

(a) (b) (c)

(d) (e) (f)

(g) (h) (i)

Figure B.2: The Dz (track Z - sub Z) distributions of CMX muon chamber as function of run number in data period 0h for the Arch north-east (a), the Arch north-west (b), the Arch south-east (c), the Arch south-west (d), the Miniskirt north-east (e), the Miniskirt north-west (f), the Miniskirt south-east (g), the Miniskirt south-west (h) and the Keystone west (i) part of the detector.

B.3 Data Period 0i

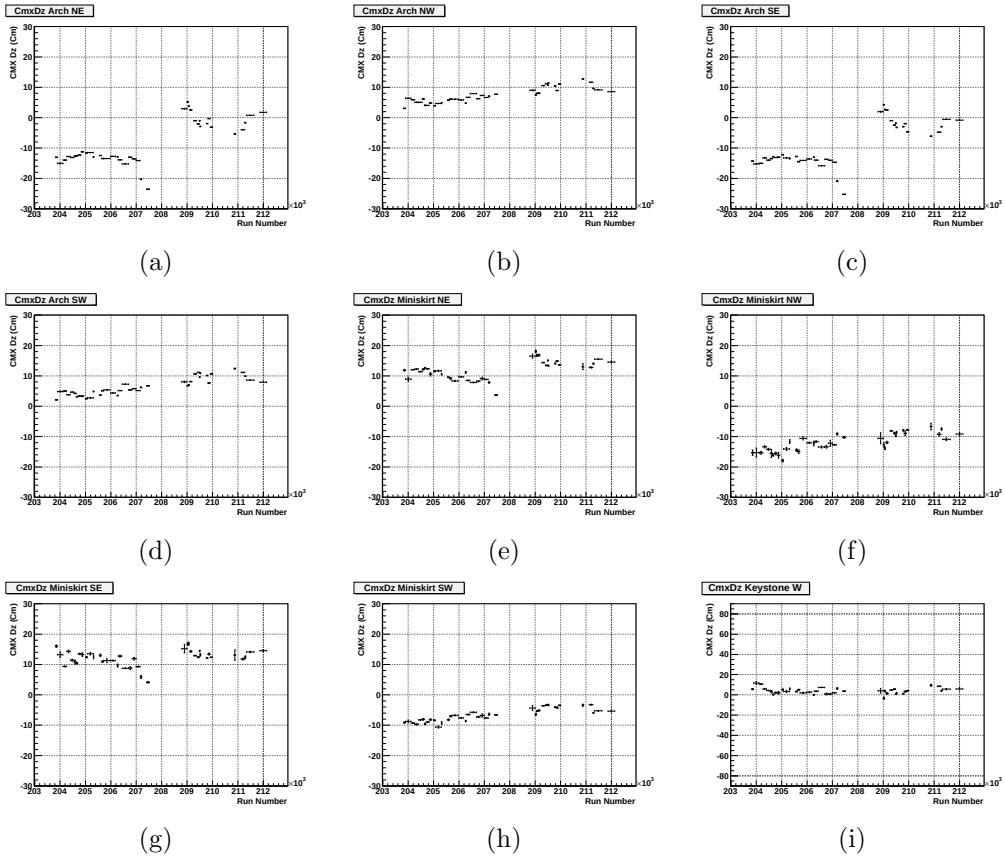

(a) (b) (c)

(d) (e) (f)

(g) (h) (i)

Figure B.3: The Dz (track Z - sub Z) distributions of CMX muon chamber as function of run number in data period 0i for the Arch north-east (a), the Arch north-west (b), the Arch south-east (c), the Arch south-west (d), the Miniskirt north-east (e), the Miniskirt north-west (f), the Miniskirt south-east (g), the Miniskirt south-west (h) and the Keystone west (i) part of the detector.

B.4 Data Period p08

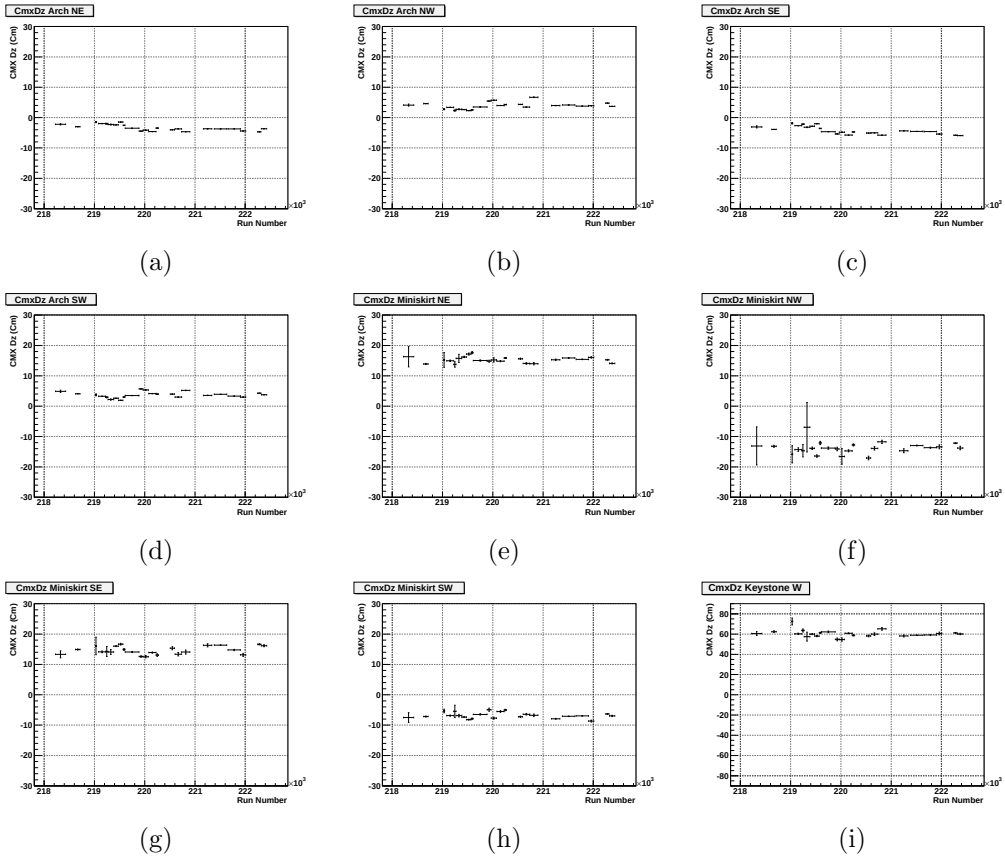

(a) (b) (c)

(d) (e) (f)

(g) (h) (i)

Figure B.4: The Dz (track Z - sub Z) distributions of CMX muon chamber as function of run number in data period p08 for the Arch north-east (a), the Arch north-west (b), the Arch south-east (c), the Arch south-west (d), the Miniskirt north-east (e), the Miniskirt north-west (f), the Miniskirt south-east (g), the Miniskirt south-west (h) and the Keystone west (i) part of the detector.

B.5 Data Period p09

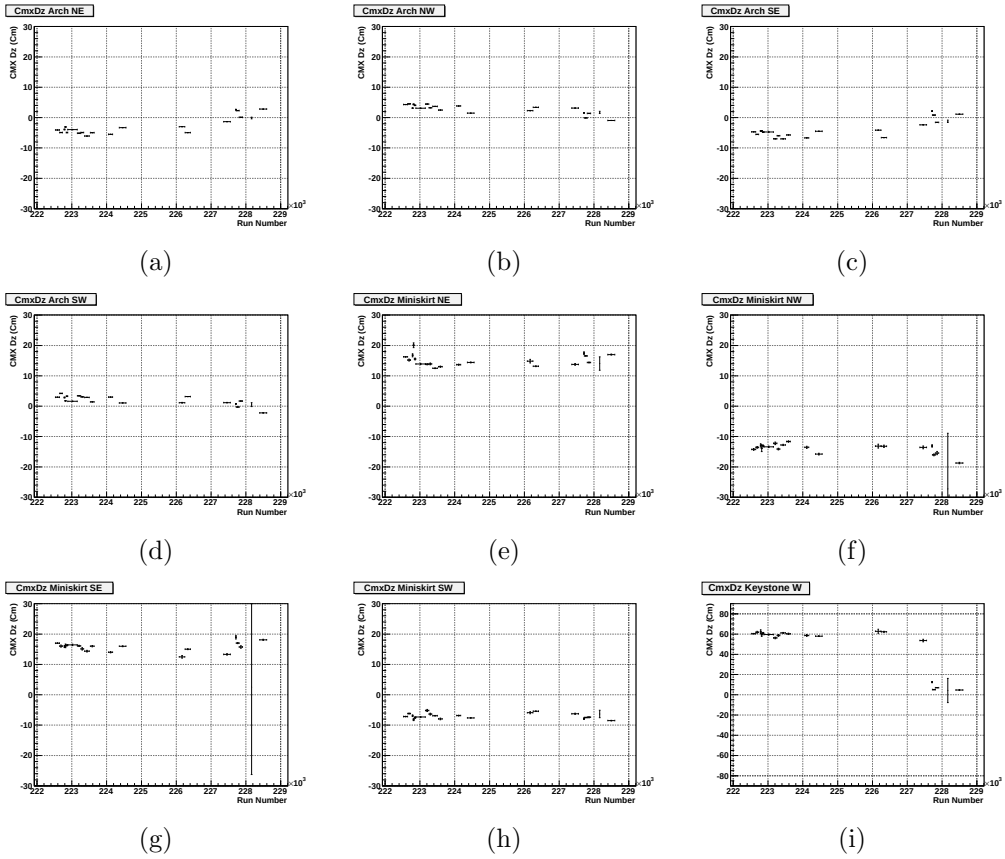

(a) (b) (c)

(d) (e) (f)

(g) (h) (i)

Figure B.5: The Dz (track Z - sub Z) distributions of CMX muon chamber as function of run number in data period p09 for the Arch north-east (a), the Arch north-west (b), the Arch south-east (c), the Arch south-west (d), the Miniskirt north-east (e), the Miniskirt north-west (f), the Miniskirt south-east (g), the Miniskirt south-west (h) and the Keystone west (i) part of the detector.

B.6 Data Period p10

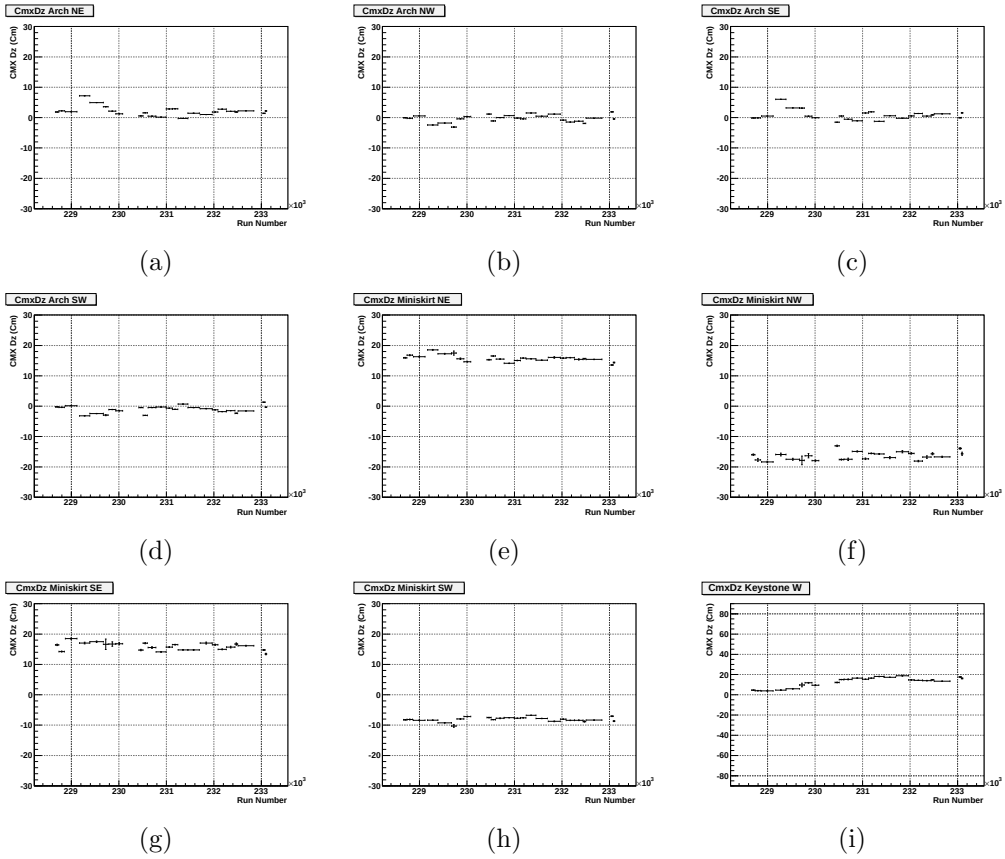

(a) (b) (c)

(d) (e) (f)

(g) (h) (i)

Figure B.6: The Dz (track Z - sub Z) distributions of CMX muon chamber as function of run number in data period p10 for the Arch north-east (a), the Arch north-west (b), the Arch south-east (c), the Arch south-west (d), the Miniskirt north-east (e), the Miniskirt north-west (f), the Miniskirt south-east (g), the Miniskirt south-west (h) and the Keystone west (i) part of the detector.

B.7 Data Period p11

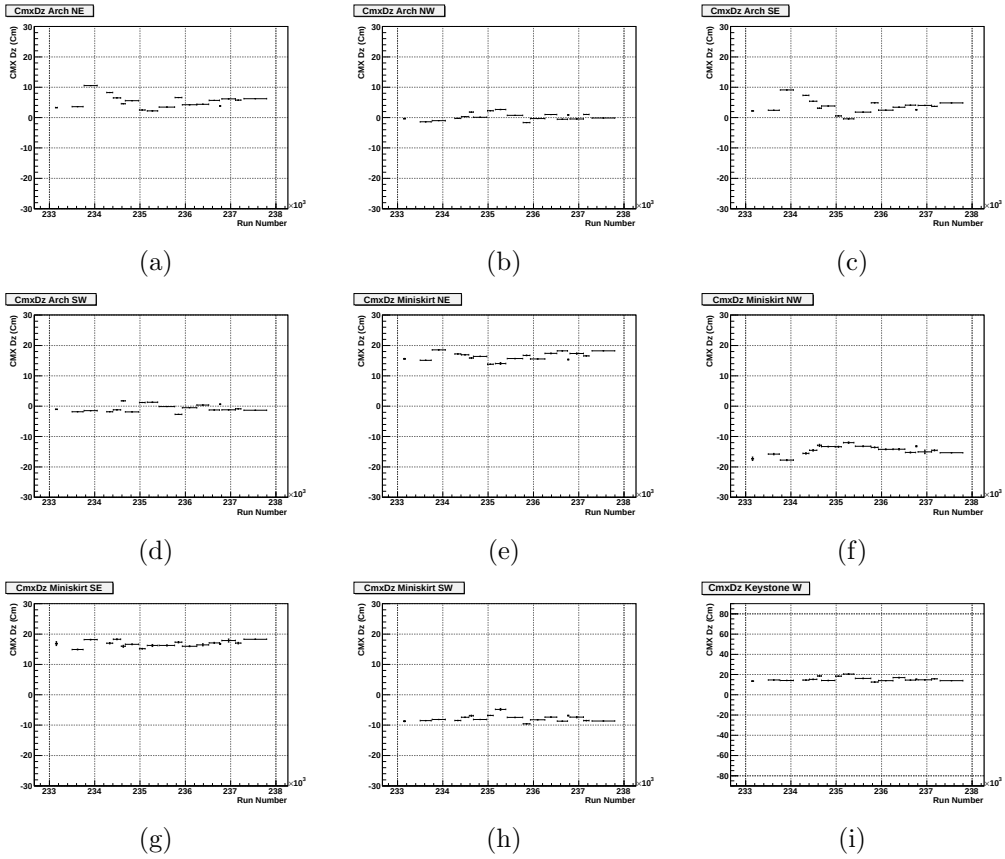

(a) (b) (c)

(d) (e) (f)

(g) (h) (i)

Figure B.7: The Dz (track Z - sub Z) distributions of CMX muon chamber as function of run number in data period p11 for the Arch north-east (a), the Arch north-west (b), the Arch south-east (c), the Arch south-west (d), the Miniskirt north-east (e), the Miniskirt north-west (f), the Miniskirt south-east (g), the Miniskirt south-west (h) and the Keystone west (i) part of the detector.

B.8 Data Period p12

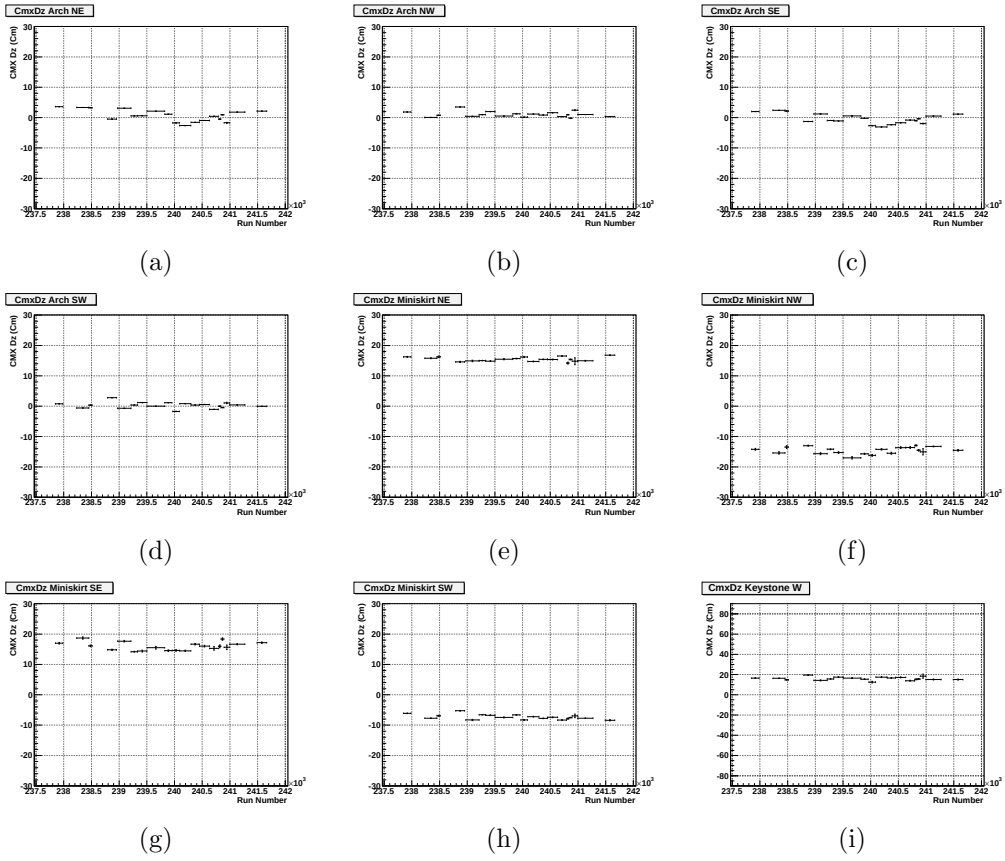

(a) (b) (c)

(d) (e) (f)

(g) (h) (i)

Figure B.8: The Dz (track Z - sub Z) distributions of CMX muon chamber as function of run number in data period p12 for the Arch north-east (a), the Arch north-west (b), the Arch south-east (c), the Arch south-west (d), the Miniskirt north-east (e), the Miniskirt north-west (f), the Miniskirt south-east (g), the Miniskirt south-west (h) and the Keystone west (i) part of the detector.

B.9 Data Period p13

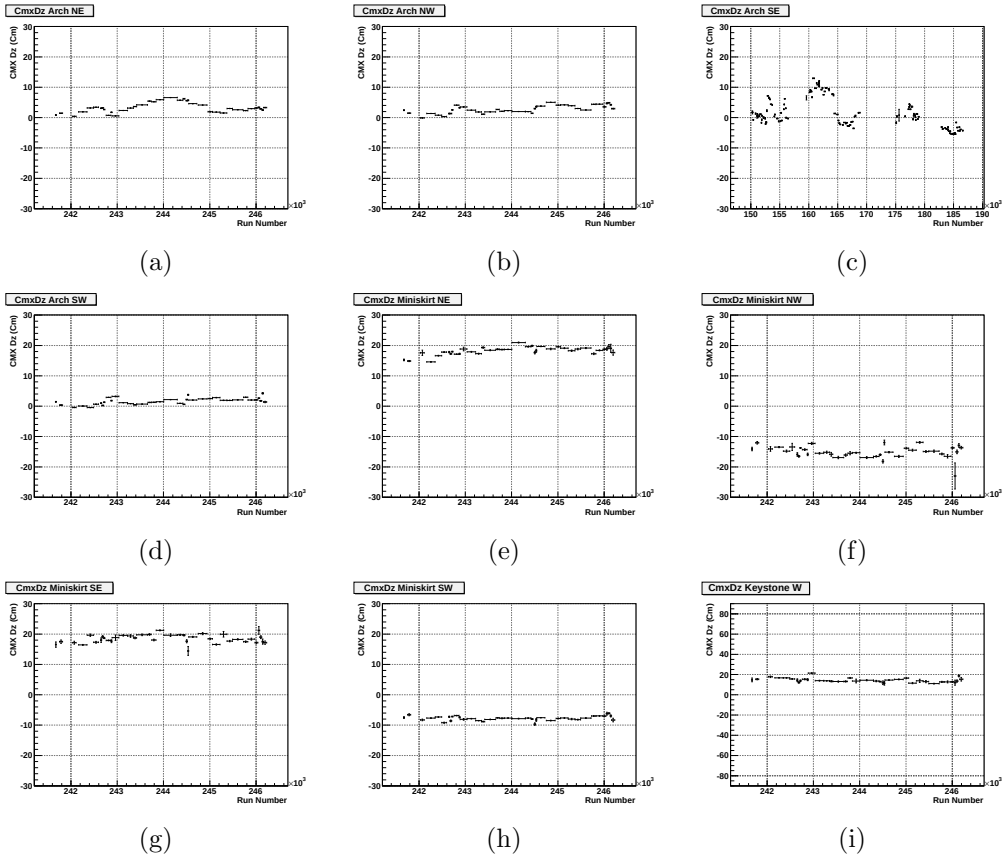

(a) (b) (c)

(d) (e) (f)

(g) (h) (i)

Figure B.9: The Dz (track Z - sub Z) distributions of CMX muon chamber as function of run number in data period p13 for the Arch north-east (a), the Arch north-west (b), the Arch south-east (c), the Arch south-west (d), the Miniskirt north-east (e), the Miniskirt north-west (f), the Miniskirt south-east (g), the Miniskirt south-west (h) and the Keystone west (i) part of the detector.

B.10 Data Period p14

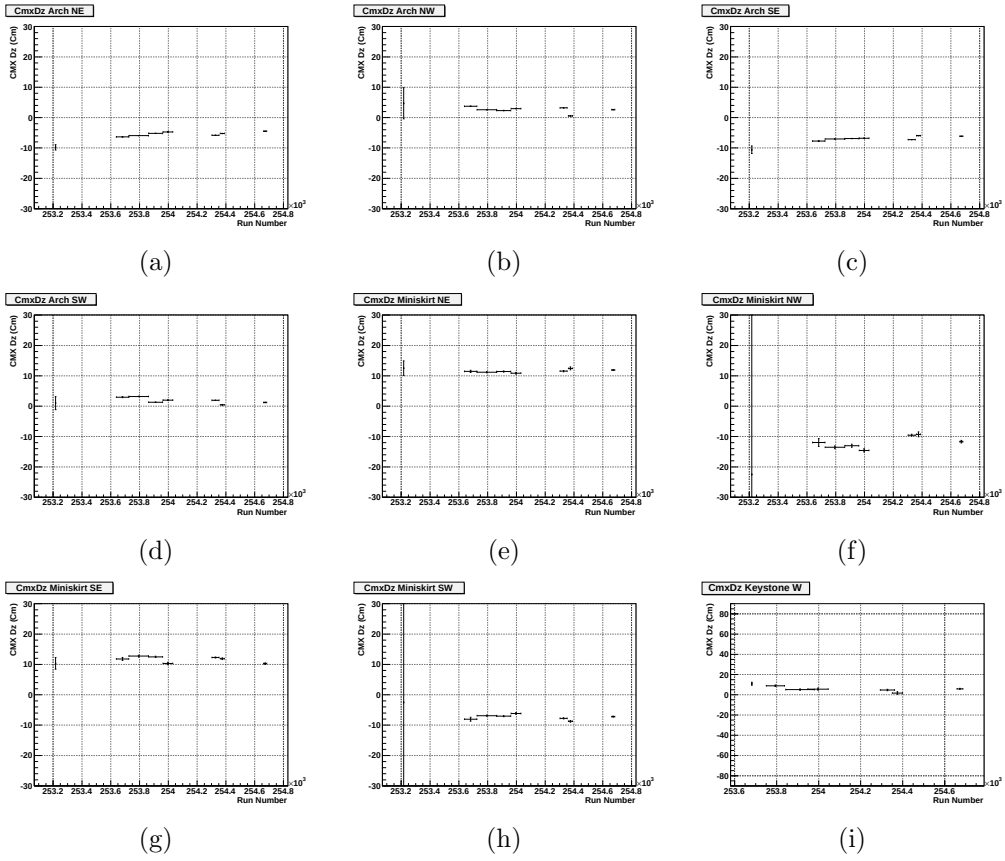

(a) (b) (c)

(d) (e) (f)

(g) (h) (i)

Figure B.10: The Dz (track Z - sub Z) distributions of CMX muon chamber as function of run number in data period p14 for the Arch north-east (a), the Arch north-west (b), the Arch south-east (c), the Arch south-west (d), the Miniskirt north-east (e), the Miniskirt north-west (f), the Miniskirt south-east (g), the Miniskirt south-west (h) and the Keystone west (i) part of the detector.

B.11 Data Period p15

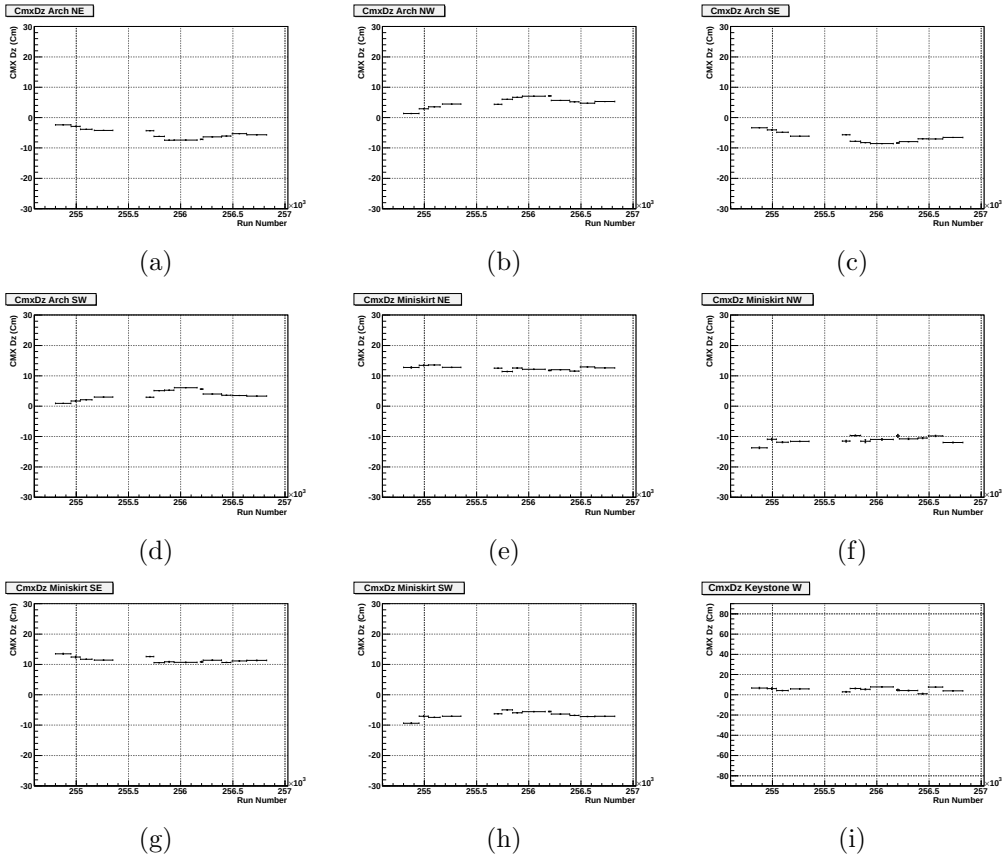

(a) (b) (c)

(d) (e) (f)

(g) (h) (i)

Figure B.11: The Dz (track Z - sub Z) distributions of CMX muon chamber as function of run number in data period p15 for the Arch north-east (a), the Arch north-west (b), the Arch south-east (c), the Arch south-west (d), the Miniskirt north-east (e), the Miniskirt north-west (f), the Miniskirt south-east (g), the Miniskirt south-west (h) and the Keystone west (i) part of the detector.

B.12 Data Period p16

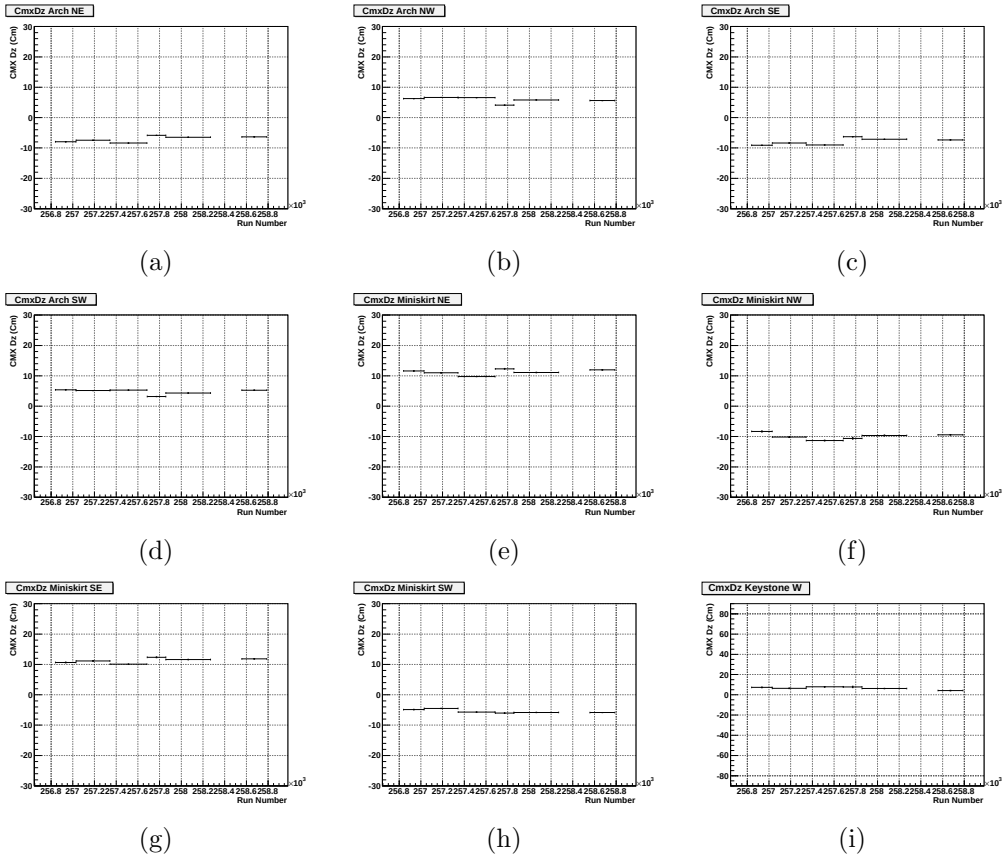

(a) (b) (c)

(d) (e) (f)

(g) (h) (i)

Figure B.12: The Dz (track Z - sub Z) distributions of CMX muon chamber as function of run number in data period p16 for the Arch north-east (a), the Arch north-west (b), the Arch south-east (c), the Arch south-west (d), the Miniskirt north-east (e), the Miniskirt north-west (f), the Miniskirt south-east (g), the Miniskirt south-west (h) and the Keystone west (i) part of the detector.

B.13 Data Period p17

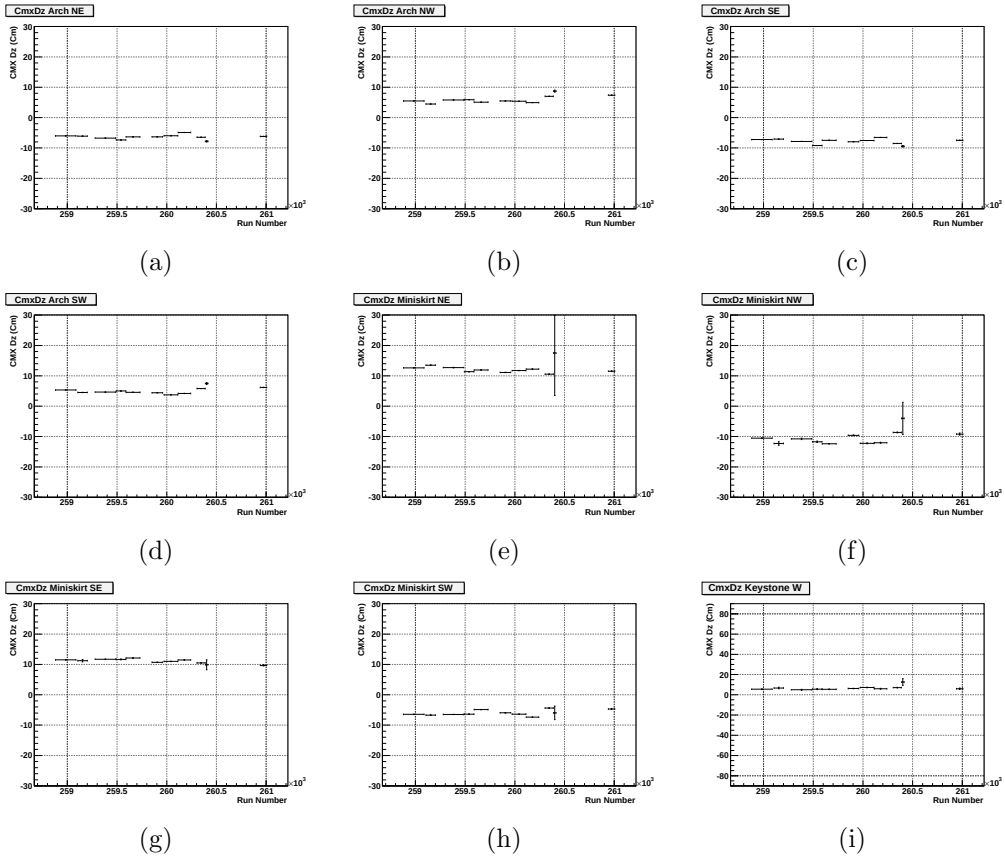

(a) (b) (c)

(d) (e) (f)

(g) (h) (i)

Figure B.13: The Dz (track Z - sub Z) distributions of CMX muon chamber as function of run number in data period p17 for the Arch north-east (a), the Arch north-west (b), the Arch south-east (c), the Arch south-west (d), the Miniskirt north-east (e), the Miniskirt north-west (f), the Miniskirt south-east (g), the Miniskirt south-west (h) and the Keystone west (i) part of the detector.

B.14 Data Period p18

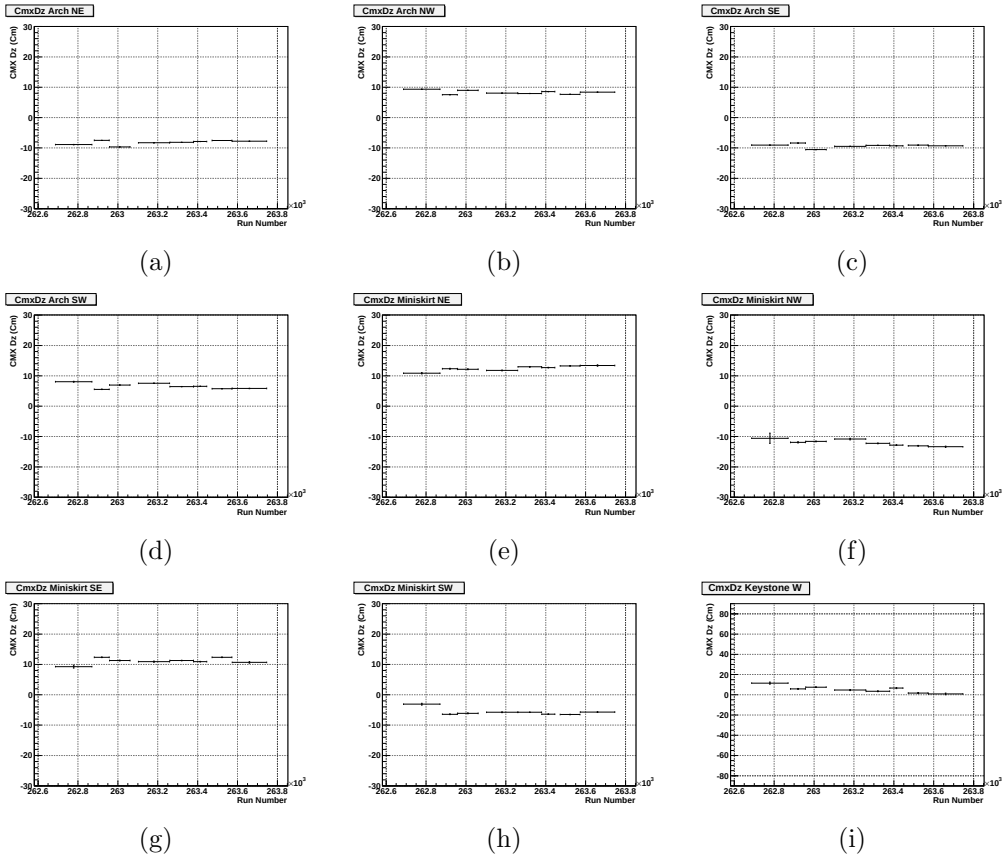

Figure B.14: The Dz (track Z - sub Z) distributions of CMX muon chamber as function of run number in data period p18 for the Arch north-east (a), the Arch north-west (b), the Arch south-east (c), the Arch south-west (d), the Miniskirt north-east (e), the Miniskirt north-west (f), the Miniskirt south-east (g), the Miniskirt south-west (h) and the Keystone west (i) part of the detector.

B.15 Data Period p19

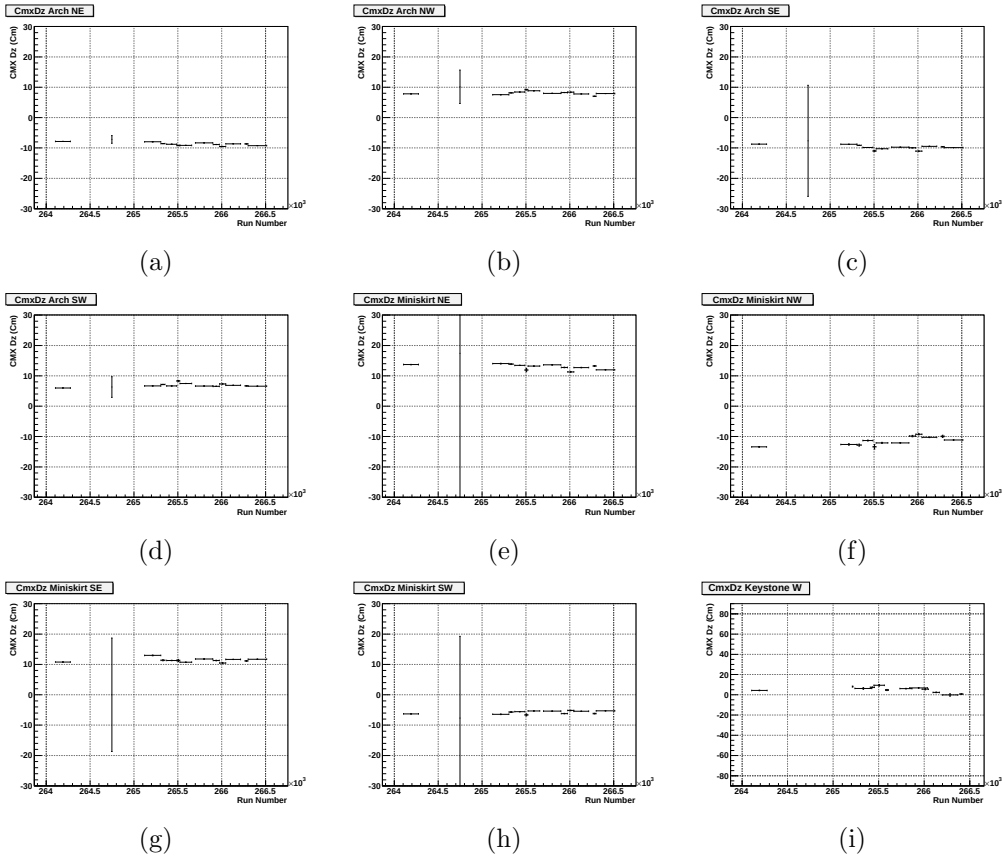

(a) (b) (c)

(d) (e) (f)

(g) (h) (i)

Figure B.15: The Dz (track Z - sub Z) distributions of CMX muon chamber as function of run number in data period p19 for the Arch north-east (a), the Arch north-west (b), the Arch south-east (c), the Arch south-west (d), the Miniskirt north-east (e), the Miniskirt north-west (f), the Miniskirt south-east (g), the Miniskirt south-west (h) and the Keystone west (i) part of the detector.

B.16 Data Period p20

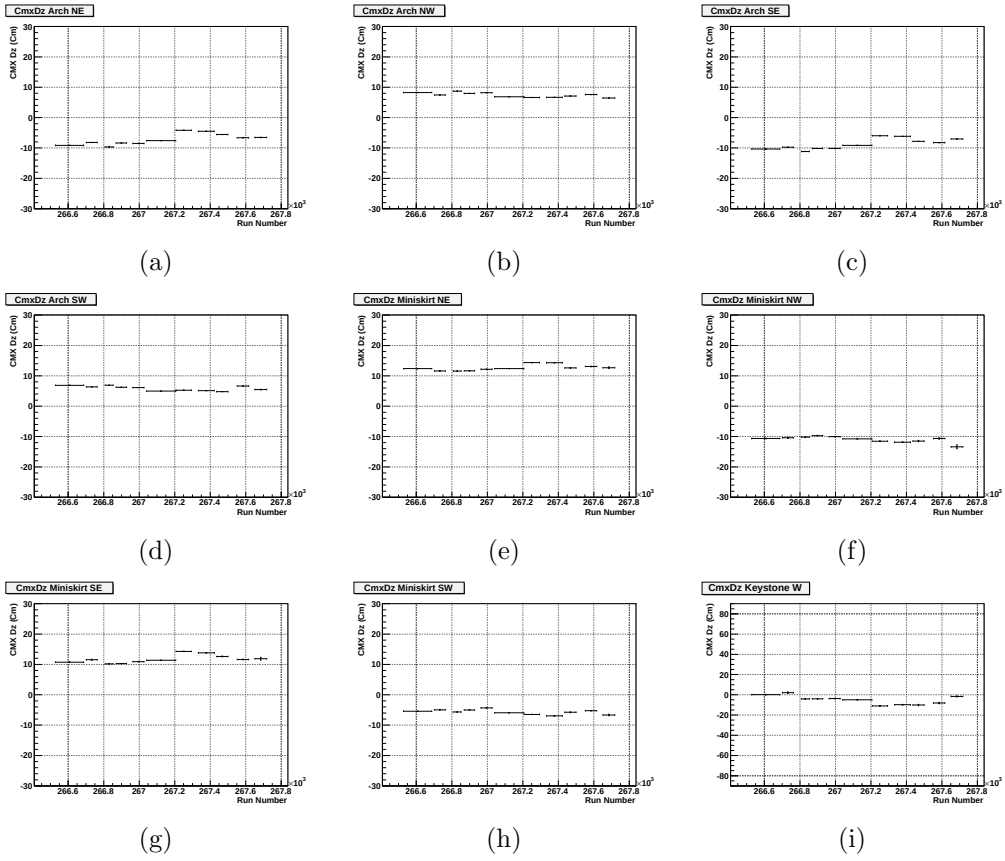

Figure B.16: The Dz (track Z - sub Z) distributions of CMX muon chamber as function of run number in data period p20 for the Arch north-east (a), the Arch north-west (b), the Arch south-east (c), the Arch south-west (d), the Miniskirt north-east (e), the Miniskirt north-west (f), the Miniskirt south-east (g), the Miniskirt south-west (h) and the Keystone west (i) part of the detector.

B.17 Data Period p21

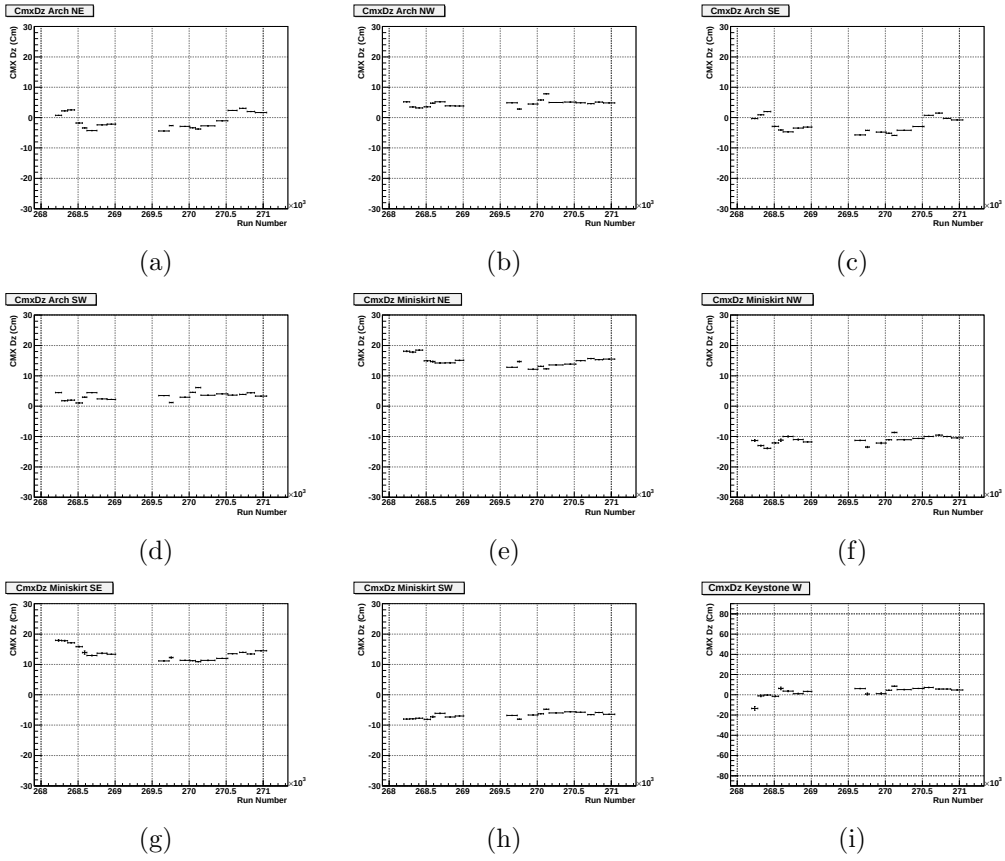

(a) (b) (c)

(d) (e) (f)

(g) (h) (i)

Figure B.17: The Dz (track Z - sub Z) distributions of CMX muon chamber as function of run number in data period p21 for the Arch north-east (a), the Arch north-west (b), the Arch south-east (c), the Arch south-west (d), the Miniskirt north-east (e), the Miniskirt north-west (f), the Miniskirt south-east (g), the Miniskirt south-west (h) and the Keystone west (i) part of the detector.

B.18 Data Period p22

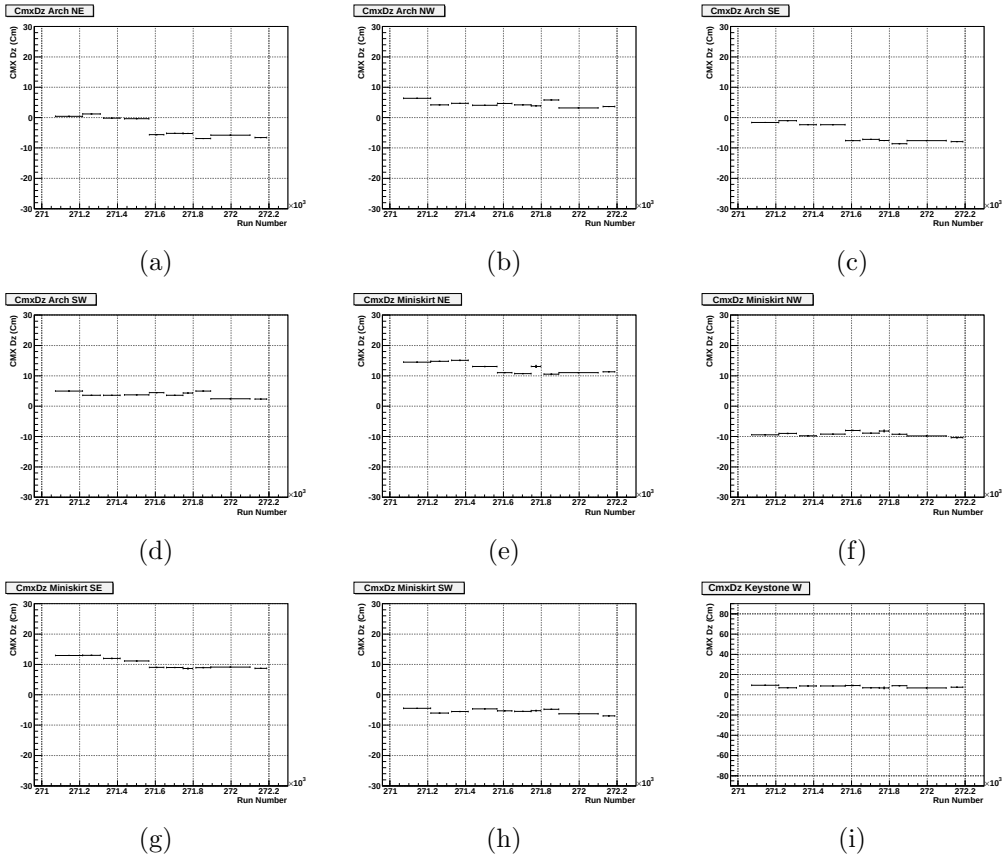

(a) (b) (c)

(d) (e) (f)

(g) (h) (i)

Figure B.18: The Dz (track Z - sub Z) distributions of CMX muon chamber as function of run number in data period p22 for the Arch north-east (a), the Arch north-west (b), the Arch south-east (c), the Arch south-west (d), the Miniskirt north-east (e), the Miniskirt north-west (f), the Miniskirt south-east (g), the Miniskirt south-west (h) and the Keystone west (i) part of the detector.

B.19 Data Period p23

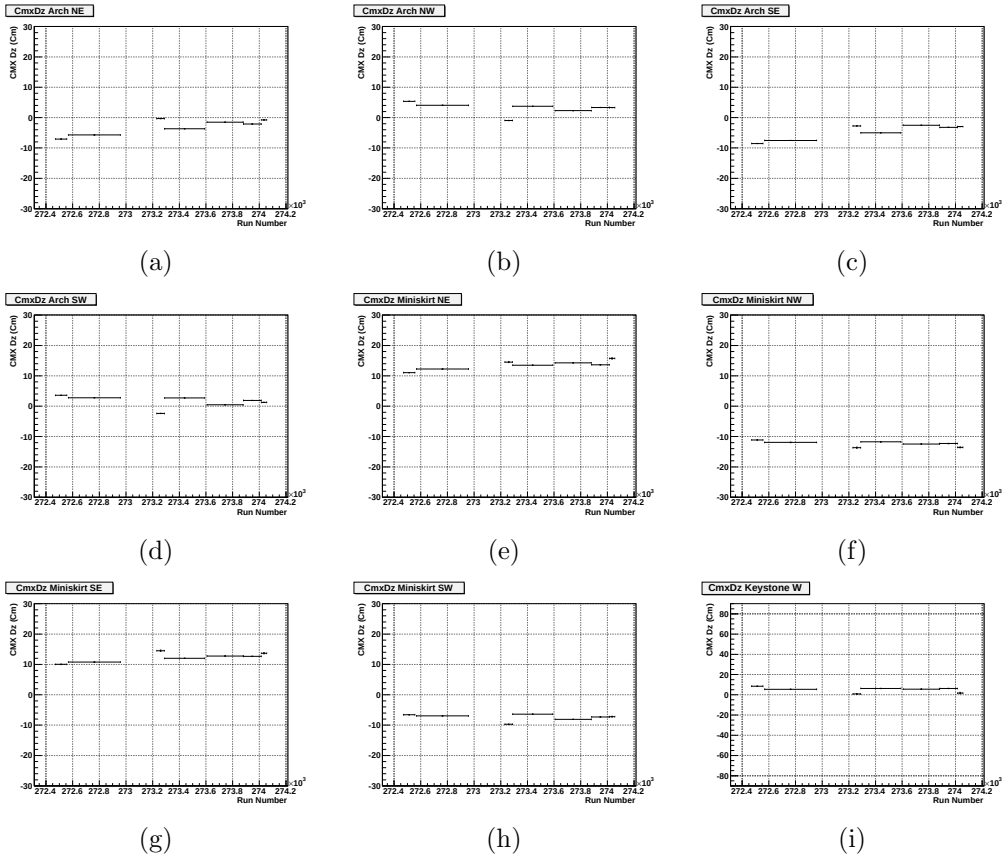

(a) (b) (c)

(d) (e) (f)

(g) (h) (i)

Figure B.19: The Dz (track Z - sub Z) distributions of CMX muon chamber as function of run number in data period p23 for the Arch north-east (a), the Arch north-west (b), the Arch south-east (c), the Arch south-west (d), the Miniskirt north-east (e), the Miniskirt north-west (f), the Miniskirt south-east (g), the Miniskirt south-west (h) and the Keystone west (i) part of the detector.

B.20 Data Period p24

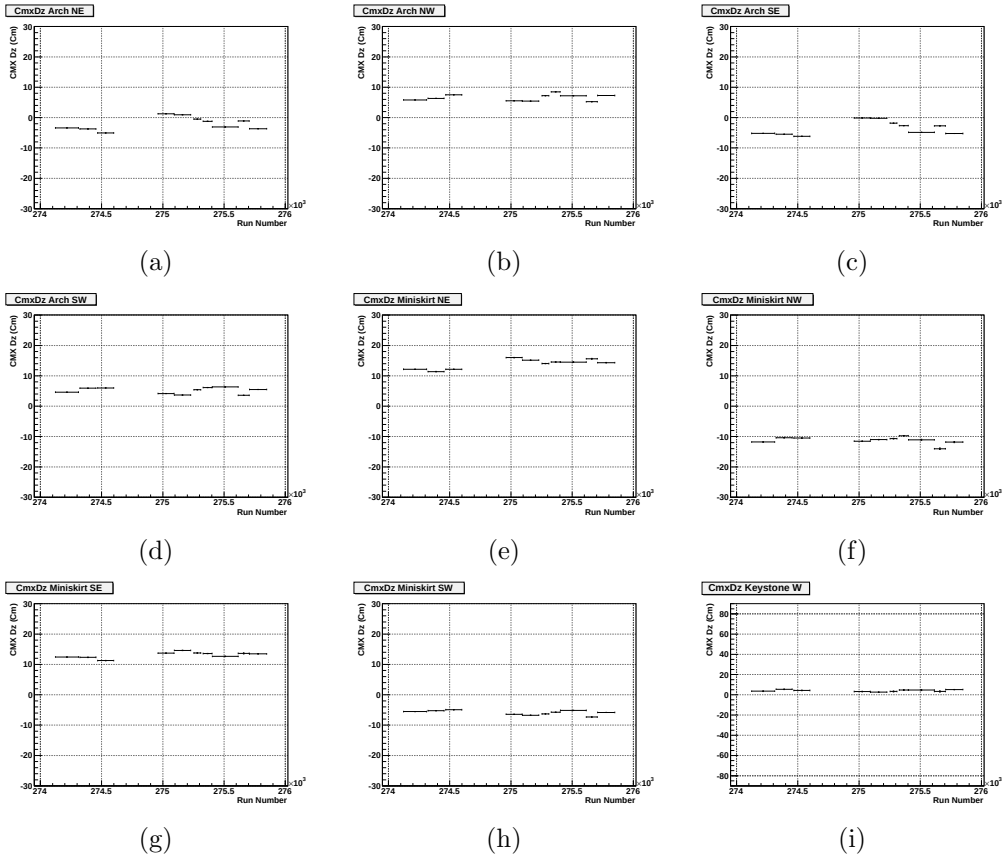

(a) (b) (c)

(d) (e) (f)

(g) (h) (i)

Figure B.20: The Dz (track Z - sub Z) distributions of CMX muon chamber as function of run number in data period p24 for the Arch north-east (a), the Arch north-west (b), the Arch south-east (c), the Arch south-west (d), the Miniskirt north-east (e), the Miniskirt north-west (f), the Miniskirt south-east (g), the Miniskirt south-west (h) and the Keystone west (i) part of the detector.

B.21 Data Period p25

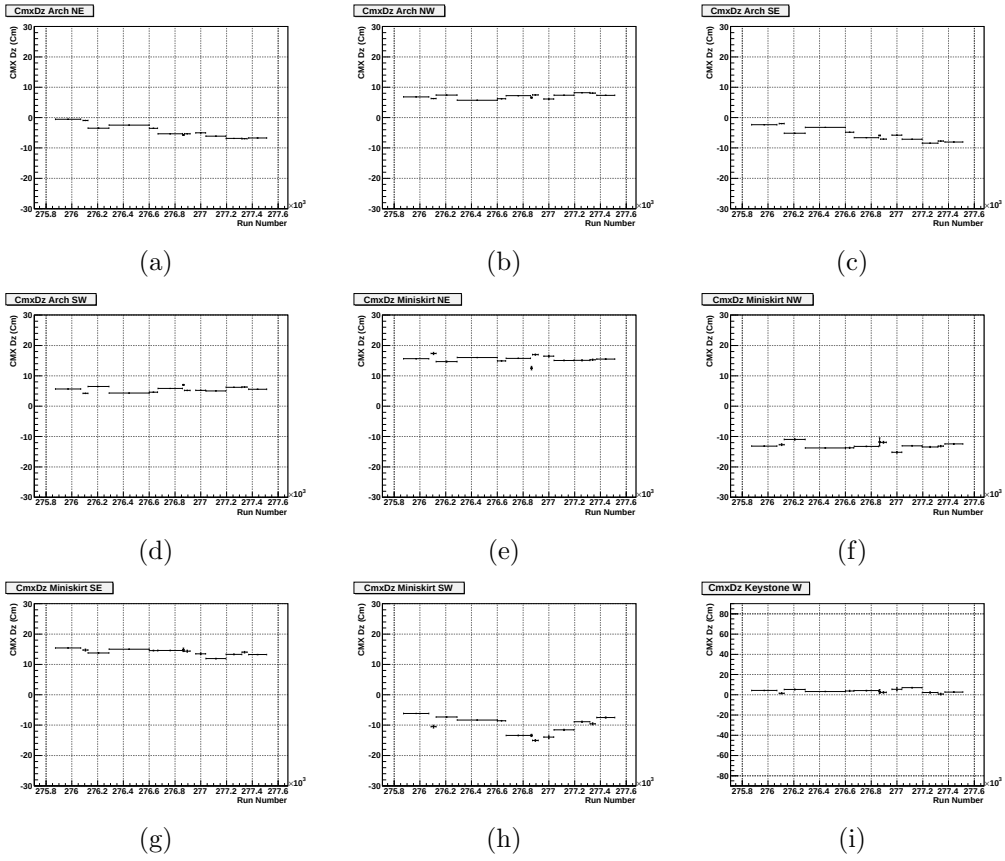

(a) (b) (c)

(d) (e) (f)

(g) (h) (i)

Figure B.21: The Dz (track Z - sub Z) distributions of CMX muon chamber as function of run number in data period p25 for the Arch north-east (a), the Arch north-west (b), the Arch south-east (c), the Arch south-west (d), the Miniskirt north-east (e), the Miniskirt north-west (f), the Miniskirt south-east (g), the Miniskirt south-west (h) and the Keystone west (i) part of the detector.

B.22 Data Period p26

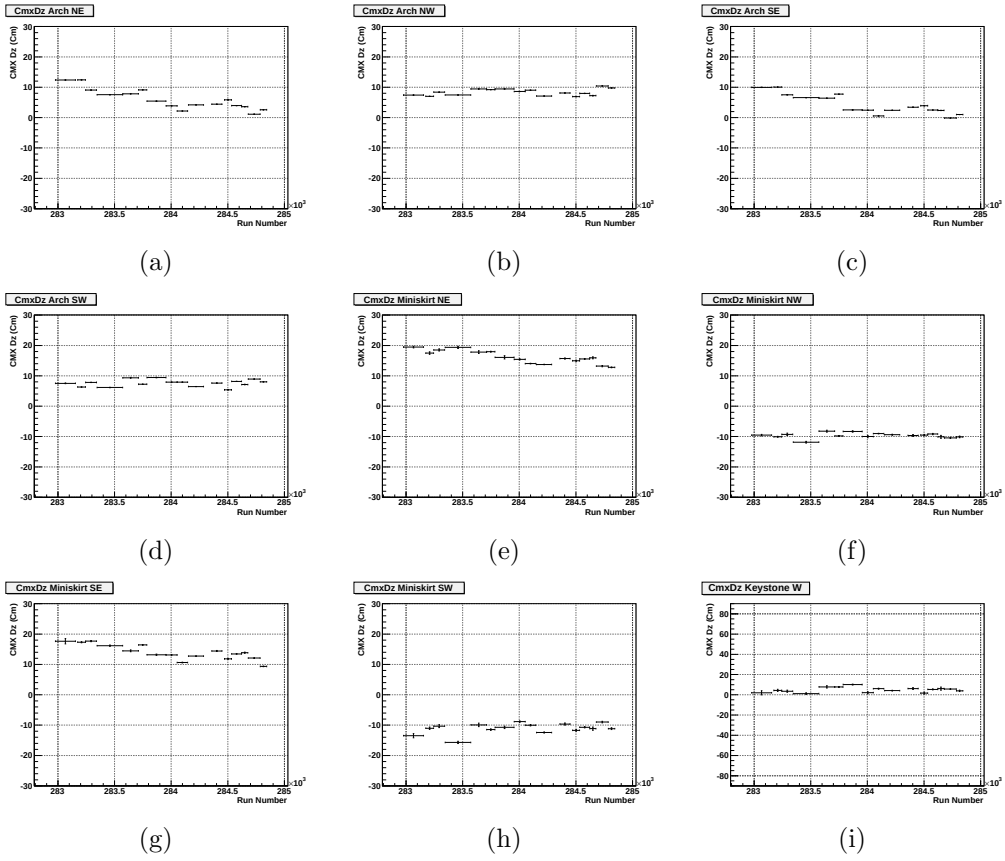

Figure B.22: The Dz (track Z - sub Z) distributions of CMX muon chamber as function of run number in data period p26 for the Arch north-east (a), the Arch north-west (b), the Arch south-east (c), the Arch south-west (d), the Miniskirt north-east (e), the Miniskirt north-west (f), the Miniskirt south-east (g), the Miniskirt south-west (h) and the Keystone west (i) part of the detector.

B.23 Data Period p27

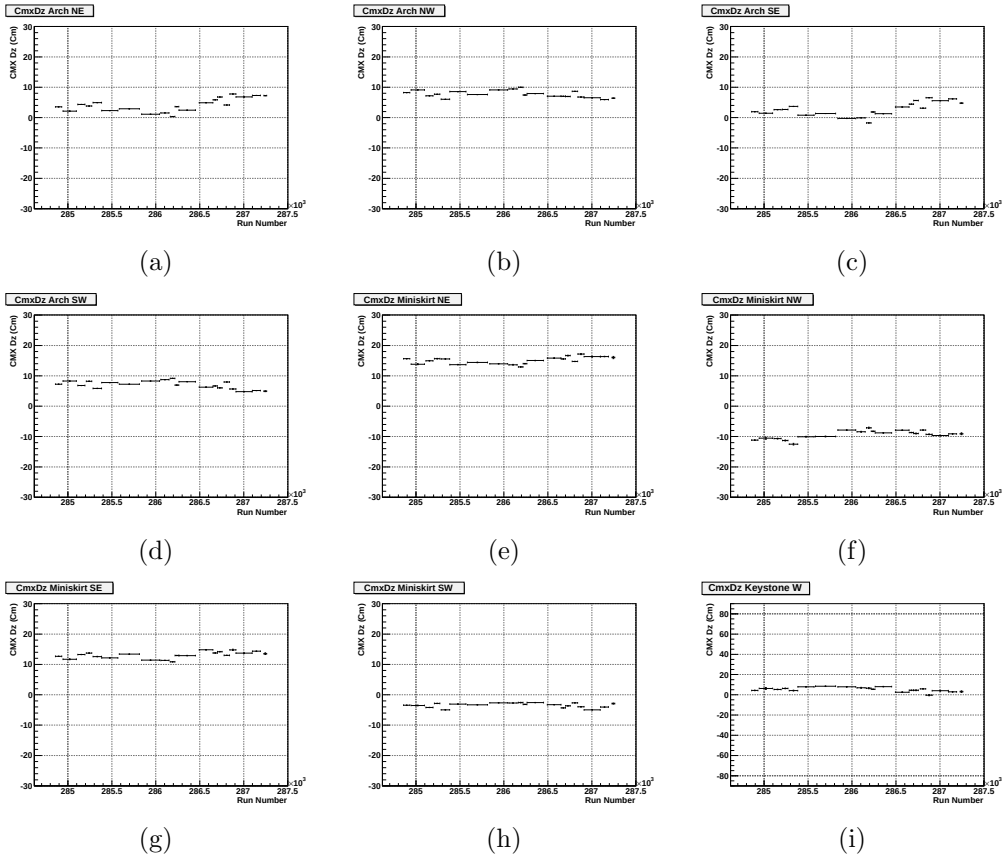

(a) (b) (c)

(d) (e) (f)

(g) (h) (i)

Figure B.23: The Dz (track Z - sub Z) distributions of CMX muon chamber as function of run number in data period p27 for the Arch north-east (a), the Arch north-west (b), the Arch south-east (c), the Arch south-west (d), the Miniskirt north-east (e), the Miniskirt north-west (f), the Miniskirt south-east (g), the Miniskirt south-west (h) and the Keystone west (i) part of the detector.

B.24 Data Period p28

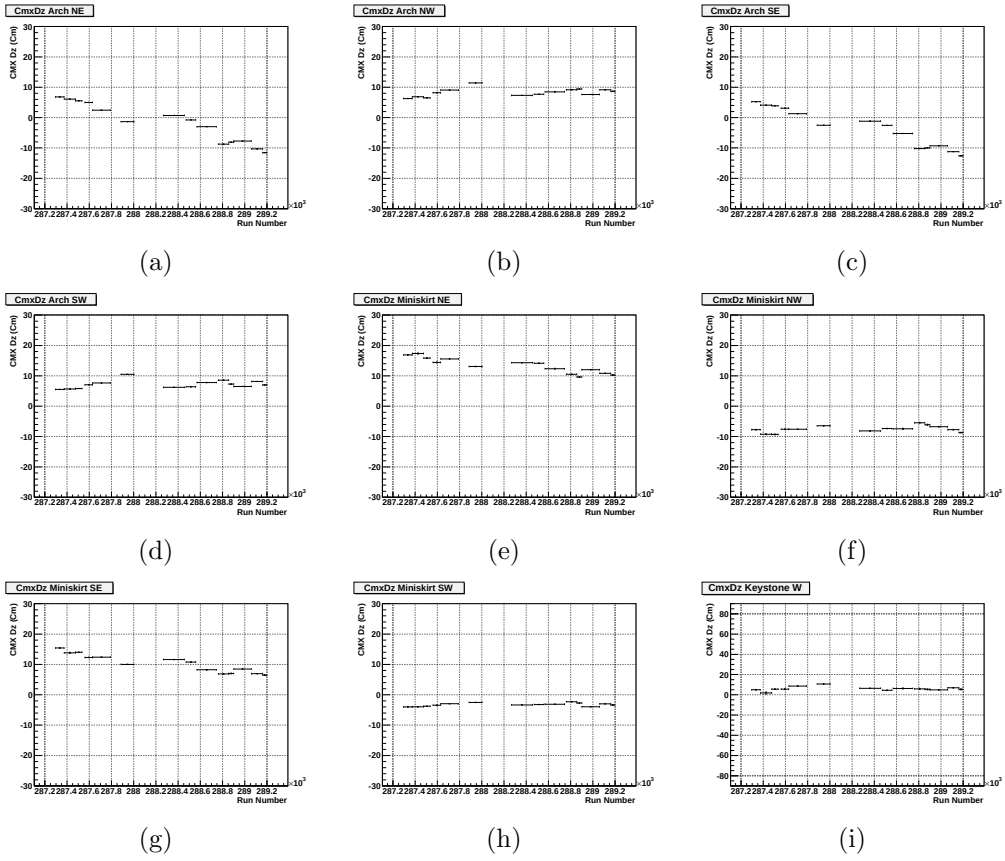

(a) (b) (c)

(d) (e) (f)

(g) (h) (i)

Figure B.24: The Dz (track Z - sub Z) distributions of CMX muon chamber as function of run number in data period p28 for the Arch north-east (a), the Arch north-west (b), the Arch south-east (c), the Arch south-west (d), the Miniskirt north-east (e), the Miniskirt north-west (f), the Miniskirt south-east (g), the Miniskirt south-west (h) and the Keystone west (i) part of the detector.

B.25 Data Period p29

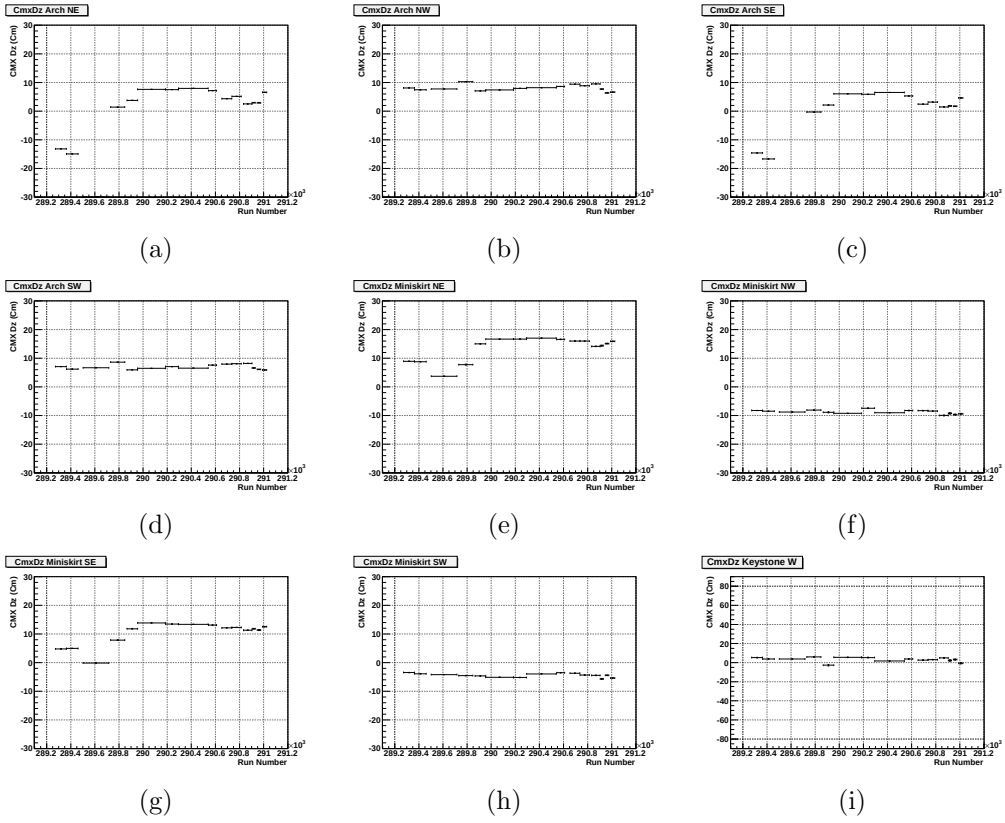

(a) (b) (c)

(d) (e) (f)

(g) (h) (i)

Figure B.25: The Dz (track Z - sub Z) distributions of CMX muon chamber as function of run number in data period p29 for the Arch north-east (a), the Arch north-west (b), the Arch south-east (c), the Arch south-west (d), the Miniskirt north-east (e), the Miniskirt north-west (f), the Miniskirt south-east (g), the Miniskirt south-west (h) and the Keystone west (i) part of the detector.

Bibliography

[1] Result of the Week in Fermilab Today
`http://www.fnal.gov/pub/today/archive_2010/today10-03-25.html`

[2] M. Cacciari *et al.*, J. High Energy Phys. 09 (2008) 127; N. Kidonakis and R. Vogt, Phys. Rev. D **78**, 074005 (2008); S. Moch and P. Uwer, Nucl. Phys. Proc. Suppl. **183**, 75 (2008).

[3] J. A. Aguilar-Saavedra, Phys. Rev. D **67** (2003) 035003 [Erratum-ibid. D 69 (2004) 099901] [hep-ph/0210112].

[4] F. del Aguila, M. Perez-Victoria and J. Santiago, Phys. Lett. B **492** (2000) 98 [hep-ph/0007160]; JHEP 0009 (2000) 011 [hep-ph/0007316].

[5] J. j. Cao, R. J. Oakes, F. Wang and J. M. Yang, Phys. Rev. D **68** (2003) 054019 [hep-ph/0306278].

[6] X. l. Wang, Q. l. Zhang and Q. p. Qiao, Phys. Rev. D **71** (2005) 014035 [hep-ph/0501145].

[7] A. Pomarol and J. Serra, Phys. Rev. D **78**, 074026 (2008) [0806.3247 [hep-ph]].

[8] W. Bernreuther, P. Gonzalez and M. Wiebusch, Eur. Phys. J. C **60** (2009) 197 [0812.1643 [hep-ph]].

[9] G. L. Kane, G. A. Ladinsky and C. P. Yuan, Phys. Rev. D 45 (1992) 124.

[10] M. Jezabek and J. H. Kuhn, Phys. Lett. B 329 (1994) 317 [hep-ph/9403366].

[11] M. Jezabek, Nucl. Phys. Proc. Suppl. 37B (1994) 197 [hep-ph/9406411].

[12] J. A. AguilarSaavedra, J. Bernabeu, Nucl. Phys. B **840** (2010) [1005.5382 [hep-ph]].

[13] D. Chakraborty, J. Konigsberg and D. L. Rainwater, Ann. Rev. Nucl. Part. Sci. **53** (2003) 301 [hep-ph/0303092].

[14] R. Meng, G.A. Schuler, J. Smith, and W.L. van Neerven. Nucl. Phys. B **339** (1990).

[15] D. Acosta *et al.*, (CDF Collaboration), Phys. Rev. Lett. **93**, 142001 (2004).

[16] T. Aaltonen *et al.*, (CDF Collaboration), Phys. Rev. D **79**, 112007 (2009).

[17] P. Nason, S. Dawson, and R. K. Ellis, Nucl. Phys. B **303**, 607 (1988).

[18] W. Beenakker, H. Kuijf, W. L. van Neerven, and J. Smith, Phys. Rev. D. **40**, 54 (1989).

[19] J. Cao *et al.*, "Supersymmetric effect in top quark decay into polarized W-boson", Phys. Rev. D **68**, 054019 (2003).

[20] T. Aaltonen *et al.* (CDF Collaboration), (submitted to Phys. Lett. B), hep-ex/0908.3914v3.

[21] T. Sjostrand, S. Mrenna, P. Skands, J. High Energy Phys. 05 (2006) 026. We use version 6.216.

[22] M.L. Mangano *et al.*, J. High Energy Phys. 07 (2003) 001. We use version 2.10;

[23] J. M. Campbell, R.K. Ellis, Phys. Rev. D **60**, 113006 (1999).

[24] W. Giele *et al.*, hep-ph/0204316.

[25] U. Baur, E.L. Berger, Phys. Rev. D **41**, 1476 (1990).

[26] U. Baur, T. Han, J. Ohnemus, Phys. Rev. D **48**, 5140 (1993).

[27] D. Lange, Nucl. Instrum. Methods Phys. Res., Sect. A 462, 152 (2001).

[28] T. Aaltonen *et al.*, (CDF Collaboration), hep-ex/0908.3914 (2010).

[29] The Tevatron ElectroWeak Working Group, hep-ex/0903.2503 (2009).

[30] Steve Kuhlmann, Preradiator Chamber Aging Tests, Internal CDF Note 1290, 1990. 35

[31] A. Bhatti, M.D.Shapiro, J. Lamoureux, DSTOWE, Internal CDF Note 3952, 2000. 62

[32] P. Azzi, G. Busetto, P. Gatti, A. Ribon, Histogram Tracking in the COT, Internal CDF Note 5562, 2001.

[33] Paolo Gatti, Performance of the new tracking system at CDF II, Internal CDF Note 5561, 2001.

[34] B.R.Ko, S.H.Oh, C.Wang, SVXII Standalone Tracking, Internal CDF Note 6440, 2003.

[35] Tim Nelson, Rick Snider, David Stuart, Forward Electron Tracking with the Phoenix- Mods Package, Internal CDF Note 6278, 2003.

[36] K. Bloom and W.-M. Yao, Outside-In Silicon Tracking at CDF, Internal CDF Note 5991, 2002.

[37] Yimei Huang, Chris Hays, and Ashutosh Kotwal, Inside-Out Tracking, Internal CDF Note 6706, 2003.

[38] D. Goldstein *et al*, Internal CDFNote 6588, July 2003 and Internal CDFNote 6830, July 2004.
M. Tecchio *et al*, Internal CDFNote 8741, April 2007 and Internal CDFNote 8040, February 2006.
N. Kimura *et al*, Internal CDFNote 9247, May 2008
C.S. Moon *et al*, Internal CDFNote 9635, Dec 2008

[39] E. J. Thomson *et al*, Internal CDFNote 5947, October 2003

[40] `http://www-cdf.fnal.gov/internal/dqm/goodrun/v31/goodv31.htm`

[41] Mark Rubier, private communications.

[42] `http://www-cdf.fnal.gov/internal/physics/top/RunIITopProp/gen6Sum06/lumi_v31.html`

[43] http:www-cdf.fnal.gov/~tecchio/internal/topntuple/DIL_topntuple.html

[44] A. D. Martin *et al.*, Phys. Lett. B **652**, 292 (2007).

[45] http://www-cdf.fnal.gov/ kimura/internal/DIL/Zveto/z_veto_DIL_addWW.html
http://www-cdf.fnal.gov/ kimura/internal/DIL/Val_METsig/val_met_sig.html

[46] How to estimate PDF acceptance uncertainties using Weighted MC: http://www-cdf.fnal.gov/internal/physics/joint_physics/instructions/ PDFUncertainties/pdf.html

[47] A. Ivanov *et al*, Internal CDFNote 9417, May 2009

[48] J. Antoš, Internal CDFNote 4165, Dec 1997

[49] http://www-cdf.fnal.gov/htbin/twiki/bin/view/WHElicity/GenSixGGWIGsamples

[50] T. Sjostrand, P. Eden, C. Friberg, L. Lonnblad, G. Miu, S. Mrenna and E. Norrbin, [arXiv:hepph/0010017]

[51] M. N. Coca, Ph. D Thesis, University of Rochester, 2005

[52] C.S. Moon, Internal CDFNote 10054, May 2010

[53] R. Lysák, Internal CDFNote 10333, Jan 2011

[54] C.S. Moon, Internal CDFNote 10381, Jan 2011

Acknowledgements

There is a long list of people whose help in this work must be acknowledged, and without whom it would never have been completed. I would like to thank those who contributed toward this thesis.

First of all, I would like to express my deepest thanks to my advisor, Prof. Soo-Bong Kim for providing the opportunity to conduct my research at Fermilab and supporting me to study in US. If it had not been for his guidance and continual encouragement, this dissertation could never have been accomplished.

I am grateful to the Top Dilepton working group. Special appreciation must go to Dr. Andrew F Beretvas Dr. Monica Tecchio and Dr. Alexei Varganov who have answered my countless questioons and have teached me the steps required to be a physicist. And I would like to say thank you to Prof. Hyunsoo Kim, Dr. Youngdo Oh, Prof. Yuji Takeuchi, Dr. Yen-Chu Chen, Prof. Jaroslav Antoš. I am especially thankful to my co-worker Dr. Roman Lysák and Dr. Naoki Kimura for all their help and time. They are great friend and collaborator.

I would like to thank the support of the CDF Collaboration and Fermilab Staff. Particularly, I would like to say thank you to CDF co-spokesperson Dr. Robert Martin Roser and Top group conveners Dr. Fabrizio Margaroli and Dr. Tom Schwarz. They show strong leadership made things clear and their careful advice guide me to find the correct way. Also, I owe a great debt of gratitude to Korean scientists in Fermilab. Their friendship, help and guidance let me had a great days in Fermilab.

I would like to express my appreciation to all members of Elementary Particle Physics Laboratory and friends at Seoul National University. Also I would like to show my thanks to my dissertation committee for valuable comments: Prof. H.C.Bang, Prof. H.D.Kim, Prof. S.H.Choi and Prof I.T.Yu.

Finally, I would like to express my best appreciation and a deep sense of gratitude to my parents and my brother.